Mixed Convective Flows for Future Operation of Power Generation Turbines



Oguzhan Murat

St Anne's College

University of Oxford

A thesis submitted for the degree of

Doctor of Philosophy

Hilary 2022

This thesis is for you, Mum.

Acknowledgements

Personal

I owe Professor Budimir Rosic my greatest debt of gratitude for his invaluable source of support and guidance throughout my DPhil at Oxford Thermofluids Institute. Besides all, I really appreciate his genuine personality and unparalleled mentorship. I will always remember his advice *"Do things in parallel!"* which seems to have worked just fine.

I must acknowledge the technical support from Wesley Ramm, with whom I very much enjoyed having fruitful and joyful both technical and utterly random conversations.

It has been an immense pleasure working and spending time together with some of the greatest minds in Oxford. I cannot list every individual but must mention Jamie, Mark, Simla, Dylan, Nikolas, Mohammed and Deepanshu who have made my time here more memorable.

It was good to know that my close friends -you know who you are- back home were just a phone call away whenever I needed. This is much appreciated.

I would like to thank my family for their seemingly endless support and always believing in me even when I had lost faith in myself.

Institutional

This project is sponsored by Mitsubishi Heavy Industries. I am particularly grateful for the regular meetings with Dr Uchida Sumiu, Dr Koichi Tanimoto and Ryo Egami who have provided invaluable feedback and expertise.

I am deeply indebted to the Ministry of National Education, the Republic of Turkey for the graduate scholarship.

Last but not least, I wish to acknowledge the continuous help from the technicians, staff and administration team at Oxford Thermofluids Institute.

What a turbulent life ...

Abstract

There has been a fast uptake of renewable sources in power generation in the recent years to mitigate the climate change. However, steam and gas turbines are expected to be in use to provide load levelling capacity when the demand cannot be met by the renewables due to their intermittent nature. This intermittency with renewables pose a grand challenge to the conventional power generation systems which are designed to provide a base load but now must adapt to the presence of renewables with frequent start-ups and shut-downs. Therefore, the focus in turbine design is shifting away from overall efficiency towards more operational flexibility.

The fundamental change in turbine design philosophy necessitates a thorough understanding of mixed convective flows during shut-down regimes which are responsible for non-uniform cooling leading to thermal stresses and compromise clearances which directly limit the operational flexibility. Numerical methods are needed to investigate these flows since the direct measurements are often not possible. A novel experimental facility that operates at engine realistic conditions has been designed and commissioned to simulate the mixed convective flows inside turbine casings. A number of experimental campaigns for various mixed convection scenarios have been performed and unique data sets have been generated, which have served as validation cases for the numerical methods. Subsequently, wall resolved large eddy simulations have been performed to gain a deeper insight into the flow field and heat transfer characteristics. A new universal RANS based model which incorporates and blends Reynolds stress and turbulent heat flux treatments has been developed and found to improve flow field and heat transfer predictions in buoyancy influenced flows.

Since the buoyant flows which cause non-uniform flow field and cooling are undesirable, the experimental facility has been modified with a blockage plate to create a local jet effect to suppress large thermal boundary layer development. The results have suggested that a simple modification to turbine casings could remarkably reduce flow field non-uniformity by suppressing the buoyant flows.

Additionally, the influence of cast surface roughness which are commonly encountered in turbomachinery industry on heat transfer, flow field and aerodynamics has been investigated with scale resolving simulations of multiple scaled-up roughness heights. It has been concluded that these rough surfaces have a significant impact on heat transfer, and cause similar velocity and temperature deficit which would potentially be simulated by a single low-order turbulence model.

Contents

List of Figures **x**

List of Tables **xiv**

Nomenclature **xv**

1 Introduction **1**
1.1 New Operational Realities 1
1.2 Cooling of Turbine Casings During Shut-Downs 3
1.3 Motivation 4
1.4 Thesis Scope 6
1.5 Thesis Outline 7

2 Literature Review **9**
2.1 Introduction 9
2.2 Convective Heat Transfer Fundamentals 9
2.3 Horizontal Concentric Annuli 12
2.3.1 Experimental Studies 12
2.3.2 Numerical Studies 16
2.4 Transient Analysis of Turbine Cooling 18
2.5 Reynolds Stress and Turbulent Heat Flux Modelling 19
2.5.1 Reynolds Stress Modelling 20
2.5.2 Turbulent Heat Flux Modelling 24
2.6 Cast Turbomachinery Casing Roughness 26
2.7 Conclusions 28

3 Experimental Facility **29**
3.1 Introduction 29
3.2 Simplified Turbine Casing Cavity 30
3.3 Contraction Nozzle Design 31
3.4 Test Section 32
3.5 Facility and Measurement Locations 35

3.6 Measurement Diagnostics 38
3.6.1 Linear Actuators 38
3.6.2 Temperature Measurements 38
3.6.3 Heat Flux Measurements 42
3.6.4 Hot-wire Anemometry Measurements 43
3.7 Conclusions 45

4 Experimental Campaigns **46**
4.1 Introduction 46
4.2 Campaigns 48
4.3 Radiation Correction 51
4.4 Measurements 53
4.4.1 Velocity Measurements 53
4.4.2 Temperature Measurements 53
4.4.3 Heat Flux Calculations 57
4.5 Conclusions 62

5 Large Eddy Simulations **63**
5.1 Introduction 63
5.2 Methodology 64
5.3 Velocity Profiles 68
5.4 Temperature Profiles 70
5.5 Flow Structures 76
5.6 Heat Transfer 82
5.7 Conclusions 89

6 New Model Development **90**
6.1 Introduction 90
6.2 Reynolds Stress Modelling 91
6.3 Turbulent Heat Flux Modelling 95
6.4 Model Implementation 96
6.5 Model Validation and Results 98
6.5.1 Methodology 98
6.5.2 Reynolds Stresses and Turbulent Heat Fluxes 99
6.5.3 Temperature Profiles 107
6.5.4 Heat Transfer 113
6.6 Conclusions 115

7 Flow Control **120**
7.1 Introduction . . . 120
7.2 Design Exercises . . . 121
7.2.1 Preliminary Design Modifications . . . 121
7.2.2 Preliminary Simulations . . . 123
7.3 Blockage Plate Experiments . . . 125
7.4 Blockage Plate Simulations . . . 131
7.5 Conclusions . . . 135

8 Turbine Casing Roughness **136**
8.1 Introduction . . . 136
8.2 Scan of Cast Iron Surface . . . 137
8.2.1 Scan of Cast Iron Patch . . . 137
8.2.2 Reconstruction of Rough Surface . . . 138
8.3 Precursor Simulation . . . 142
8.3.1 Precursor Simulation Methodology . . . 142
8.3.2 Precursor Simulation Validation . . . 143
8.4 Wall Resolved LES of Rough Walls . . . 146
8.4.1 Computational Methodology for Rough Walls . . . 146
8.4.2 Results . . . 149
8.5 Conclusions . . . 156

9 Conclusions and Future Work **157**
9.1 Introduction . . . 157
9.2 Experimental Campaigns . . . 157
9.3 Wall Resolved Large Eddy Simulations . . . 158
9.4 New Model Development . . . 159
9.5 Flow Control . . . 159
9.6 Turbine Casing Roughness . . . 160
9.7 Future Work . . . 160
9.8 Final Remarks . . . 162

Appendices

A Experimental and LES Results for Remaining Cases **164**
A.1 Case-A . . . 165
A.2 Case-D . . . 166
A.3 Case-E . . . 167
A.4 Case-G . . . 168

B NNR Temperature Results for Remaining Cases 169
B.1 Case-A 170
B.2 Case-E 171
B.3 Case-G 172

C Reynolds Stresses and Turbulent Heat Fluxes for Remaining Cases 173
C.1 Case-A 174
C.2 Case-D 176
C.3 Case-E 178
C.4 Case-G 180

D NNR Heat Transfer Profiles for Remaining Cases 182
D.1 Case-A 183
D.2 Case-E 184
D.3 Case-G 185

E Experimental and RANS Results for Case-2M and Case-DM 186
E.1 Case-2M 187
E.2 Case-DM 188

References 189

List of Figures

1.1 Share of primary energy [2] 1
1.2 Visualisation of the required flexibility of conventional systems [5] . 2
1.3 Heat transfer distribution on HP turbine casing 4
1.4 Turbine casing distortion due to large thermal stresses 4

2.1 HP Turbine casing cavity and a simplified model 10
2.2 Cast roughness in turbomachinery applications 10

3.1 Schematic of a simplified turbine casing 29
3.2 Velocity profile at the exit of contraction 30
3.3 PID controller layout 32
3.4 Distribution of surface thermocouples on the heated inner cylinder . 33
3.5 Experimental facility schematic with measurement locations 34
3.6 Operational range comparison of the experimental facility and a real turbine 36
3.7 CAD model of the facility with a section view 36
3.8 A photograph of the facility 37
3.9 Schematic of thermocouple probe 39
3.10 Heat transfer modes on a thermocouple bead 39
3.11 Thermocouple probe picture 42
3.12 HWA calibration box and the probe 44
3.13 HWA calibration 44

4.1 Mixed convective flow regimes 47
4.2 Selected experimental campaigns 49
4.3 Comparison of raw and time-averaged temperature data 50
4.4 Radiation correction for Case-1 at $\theta = 90°$ at Section 2 51
4.5 Radiation correction for Case-2 at $\theta = 90°$ at Section 2 52
4.6 Radiation correction for Case-3 at $\theta = 90°$ at Section 2 53
4.7 Velocity measurements at Section 0 54
4.8 Radial temperature profiles in Case-1 56
4.9 Radial temperature profiles in Case-2 57

4.10 Radial temperature profiles in Case-3 58
4.11 Viscous sub-layer thickness the heated inner cylinder 59
4.12 Near wall temperature profiles and R^2 values for increasing measurement points 60
4.13 Nusselt number distribution around the heated inner cylinder in Case-1 61

5.1 Computational domain 65
5.2 Computational mesh for LES 66
5.3 History of time-averaged energy imbalance in Case-1 67
5.4 Resolved turbulent kinetic energy at 90° at Section 3 67
5.5 Energy cascade at $r/L_g = 0.9\%$ at Section 3 68
5.6 Experimental and LES velocity profiles at Section 0 69
5.7 Experimental and LES temperature profiles in Case-1 71
5.8 Temperature contours in measurement sections in Case-1 72
5.9 Experimental and LES temperature profiles in Case-2 73
5.10 Temperature contours in measurement sections in Case-2 74
5.11 Experimental and LES temperature profiles in Case-3 75
5.12 Temperature contours in measurement sections in Case-3 76
5.13 Flow structures and their footprints in Case-1 77
5.14 Flow structures and their footprints in Case-2 79
5.15 Flow structures and their footprints in Case-3 81
5.16 Nusselt number distribution around the heated inner cylinder . . . 87
5.17 Heated inner cylinder time-averaged Nusselt number contours . . . 88

6.1 Different types of convective flow regimes 90
6.2 Mesh used in RANS simulations 99
6.3 Reynolds stresses in Case-1 101
6.4 Turbulent heat fluxes in Case-1 102
6.5 Reynolds stresses in Case-2 103
6.6 Turbulent heat fluxes in Case-2 104
6.7 Reynolds stresses in Case-3 105
6.8 Turbulent heat fluxes in Case-3 106
6.9 Temperature profiles in Case-1 109
6.10 Temperature profiles in Case-2 110
6.11 Temperature profiles in Case-D 111
6.12 Temperature profiles in Case-3 112
6.13 Heat transfer distribution in Case-A (a) Nusselt number comparison (b) Error 117
6.14 Heat transfer distribution in Case-1 (a) Nusselt number comparison (b) Error 118

6.15 Heat transfer distribution in Case-D 119
6.16 Heat transfer distribution in Case-3 119

7.1 Flow control design exercises 121
7.2 Plate location in Design 3 and 4 122
7.3 Temperature field in each design 124
7.4 Schematic of the modified rig with blockage plate 125
7.5 A photograph of the modified rig with blockage plate 125
7.6 Radial temperature profiles in Case-AM 127
7.7 Radial temperature profiles in Case-1M 128
7.8 Radial temperature profiles in Case-2M 129
7.9 Radial temperature profiles in Case-DM 130
7.10 Computational mesh for blockage plate 131
7.11 Experimental and RANS temperature profiles in Case-AM 132
7.12 Experimental and RANS temperature profiles in Case-1M 133
7.13 Case-1 (no blockage) and Case-1M (blockage) temperature field comparison 134
7.14 Velocity field in the blockage region 135

8.1 Re-construction of rough surface 137
8.2 Histogram of the scanned rough surface 138
8.3 Reconstruction of initial rough surface with singular value decomposition 139
8.4 Close-up views of (a) Rough surface (b) Scaled +25% (c) Scaled +50% 141
8.5 Computational domain and methodology 142
8.6 Energy cascade at $x/\theta_0 = 5880$ and $y^+ = 145$ 144
8.7 Validation case heat flux comparison against Kays and Crawford's correlation [142] 145
8.8 Mean velocity $< u >^+$ and temperature $< \theta >^+$ profiles 146
8.9 FFT of rough surfaces 147
8.10 Near wall mesh schematic 148
8.11 Resolved TKE and energy spectra of u' 150
8.12 Mean velocity and temperature profile comparison 150
8.13 Velocity and temperature function ratio for Scaled +50% Case . . . 151
8.14 Skin friction profile comparison 152
8.15 Heat transfer profile comparison 152
8.16 Instantaneous temperature field comparison 153
8.17 Reynolds stresses and turbulent heat fluxes 154
8.18 Velocity profiles 155

A.1 Experimental and LES temperature profiles in Case-A 165

A.2 Experimental and LES temperature profiles in Case-D 166
A.3 Experimental and LES temperature profiles in Case-E 167
A.4 Experimental and LES temperature profiles in Case-G 168

B.1 NNR temperature profiles in Case-A 170
B.2 NNR temperature profiles in Case-E 171
B.3 NNR temperature profiles in Case-G 172

C.1 Reynolds stresses in Case-A 174
C.2 Turbulent heat fluxes in Case-A 175
C.3 Reynolds stresses in Case-D 176
C.4 Turbulent heat fluxes in Case-D 177
C.5 Reynolds stresses in Case-E 178
C.6 Turbulent heat fluxes in Case-E 179
C.7 Reynolds stresses in Case-G 180
C.8 Turbulent heat fluxes in Case-G 181

D.1 Nusselt number comparison for Case-2 183
D.2 Nusselt number comparison for Case-E 184
D.3 Nusselt number comparison for Case-G 185

E.1 Experimental and RANS temperature profiles in Case-2M 187
E.2 Experimental and RANS temperature profiles in Case-DM 188

List of Tables

3.1 Rig dimensions (P: Parameter, D: Dimension) 35
3.2 Thermocouple details 41

4.1 Experimental campaigns 48
4.2 Test section inner and outer wall temperatures 49
4.3 Boundary layer characteristics at Section 0 55
4.4 Uncertainty of each variable 61

5.1 Fluid properties 65
5.2 Grid resolutions 66
5.3 Nusselt number comparison at measurement locations on the heated inner cylinder 85

8.1 Roughness details 144
8.2 Kolmogorov length and time scales 147
8.3 LES spatial and temporal resolution 149

Nomenclature

Abbreviations

CFD	Computational fluid dynamics
CFL	Courant–Friedrichs–Lewy number
CR	Contraction ratio
FEA	Finite element analysis
LES	Large eddy simulation
MHI	Mitsubishi Heavy Industries
NNR	New Nonlinear RANS
OTI	Oxford Thermofluids Institute
PID	Proportional integral derivative
RANS	Reynolds-averaged Navier-Stokes
RC	Refinement coefficient
RMS	Root mean square
SGS	Subgrid scale
SVD	Singular value decomposition

Greek Letters

α	Thermal diffusivity (m^2/s)
β	Thermal expansion coefficient (K^{-1})
Δ	Cell size ($\sqrt[3]{cell\ volume}$) or grid spacing (m)
ϵ	Emissivity
θ	Angle (°) or circumferential direction
θ	Angle (°) or circumferential direction

θ	Momentum thickness (m)
μ	Dynamic viscosity (kg/ms)
ν	Kinematic viscosity (m^2/s)
ρ	Density (kg/m^3)
δ	Kronecker delta
δ^*	Displacement thickness (m)
κ	von Karman constant
κ	Wavelength (mm^{-1})
Δt	Time step (s)
η_k	Kolmogorov length scale (m)
λ_η	Kolmogorov length scale (m)
Λ	NNR model coefficient
Ω	Vorticity (1/s)
ω	Specific dissipation rate (1/s)

Roman Letters

B	Bias error
C_p	Specific heat capacity (J/kgK)
C_f	Skin friction coefficient
d	Closest wall distance, (m)
D	Fractal dimension
$D_{i,o}$	Inner, outer diameter (m)
D_h	Hydraulic diameter (m)
f	Frequency (Hz)
g	Gravitational acceleration (m/s^2)
Gr	Grashof number
H	Hurst exponent
H	Shape factor
k	Thermal conductivity (W/mK)
k	Turbulent kinetic energy (m^2/s^2)

L_d	Downstream contraction length (m)
L_e	Entrance length (m)
L_g	Gap width (m)
L_t	Test section length (m)
Nu	Nusselt number
P	Pressure (bar)
Pr	Prandtl number
$q^{''}$	Heat flux (W/m^2)
r	Radial distance (m)
R_a	Arithmetic roughness height (m)
R_b	Bellmouth radius (m)
$R_{i,o}$	Inner, outer radius (m)
R_ku	Kurtosis
R_n	Contraction nose radius (m)
R_q	Root mean square of elevation (m)
R_{sk}	Skewness
Re	Reynolds number
Ri	Richardson number
S	Strain rate (1/s)
St	Stanton number
T	Temperature (K)
u	Velocity (m/s)
u_τ	Friction velocity (m/s)
$u'T'$	Turbulent heat flux (mK/s)
$u'u'$	Reynolds stress (m^2/s^2)
V	Variable

Superscripts and Subscripts

$^+$	Scaling by wall units
$< \ >$	Spanwise and time averaged
$\overline{(\ )}$	Time-averaged

$(\quad)_b$	Thermocouple bead
$(\quad)_{i,o}$	Inner or outer
$(\quad)_{eff}$	Effective surrounding
$(\quad)_t$	Turbulent
$(\quad)_{S,L}$	Small or large bead thermocouple
$(\quad)_{EXP}$	Experimental results
$(\quad)_{LES}$	LES results

Chapter 1

Introduction

1.1 New Operational Realities

As the global warming has reached alarming levels with the Earth's temperature being 1.1 °C higher compared to the late 1800s [1], 193 parties including the European Union (EU) have joined the Paris agreement which is a legally binding treaty for the participant countries to commit to minimise the green house gas emissions.

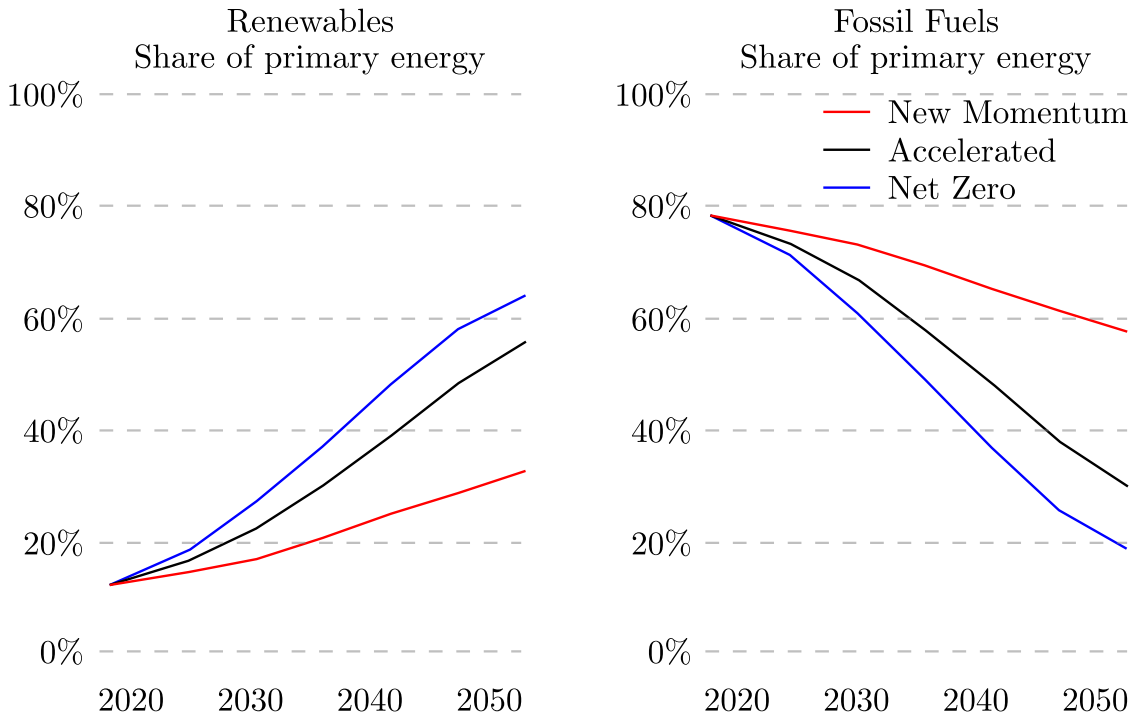

Figure 1.1: Share of primary energy (reproduced from [2])

The goal is to keep the global temperature rise below 2 °C, and to pursue an ambitious target of 1.5 °C above the pre-industrial levels, as well as to address the negative impacts that the climate change has caused so far [3, 4]. The short-term effects of global carbon neutralisation movement with the Paris agreement have

been apparent in power generation and transportation sectors the most, creating a competitive business environment which leads to faster technology development.

In British Petrol's (BP) Global Energy Outlook 2022, three scenarios have been identified to explore the potential pathways to 2050, namely *New momentum*, *Accelerated* and *Net Zero*. *New momentum* refers to the current speed of progress in tackling the global warming, and its trajectory in future decarbonisation. *Accelerated* and *Net zero* are the pathways to a substantial fall in carbon emissions with strict climate policies. With these three different scenarios, the energy mix, energy demand and electrification trends are explored in the context of the energy transition to 2050 [2]. The BP report suggests that the fossil fuels will likely be used in power generation even with the *Net zero* scenario as shown in Fig. 1.1. The same figure also depicts the fast uptake of renewable sources in power generation by 2050, reaching a share of more than 60 % in the *Net zero* scenario.

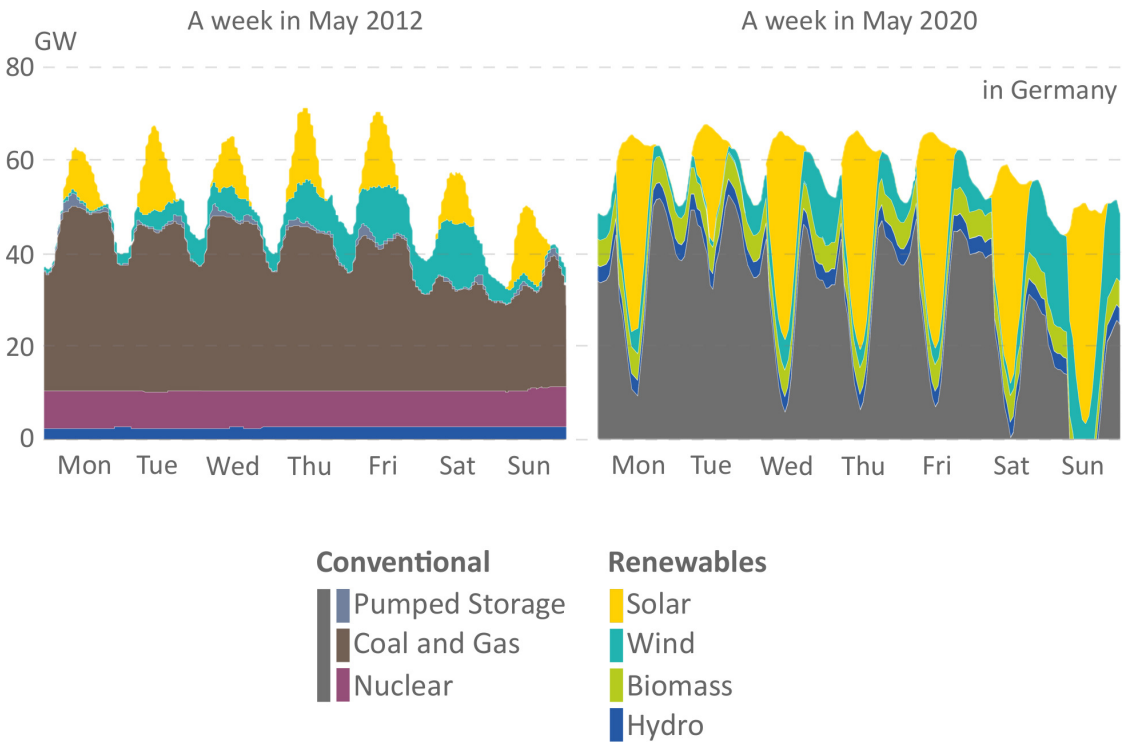

Figure 1.2: Visualisation of the required flexibility of conventional systems [5]

The efforts in minimising the CO_2 emissions are noteworthy. However, meeting

the power demand with the renewables at all times may not be possible due to the intermittent nature of the renewable sources. This intermittency will ultimately lead to a grand challenge of continuous electricity supply. Therefore, the conventional power generation systems will be required for load levelling. As opposed to the actual design philosophy of steam and gas turbines which have been the core of base load, these conventional systems will be required to operate flexibly when the supply from the renewables does not meet the demand. This new operational reality for conventional systems is visualised by comparing power generation by renewables and conventional sources over a week in 2012 and 2020 (projection at the time of publication) in Germany as seen in Fig. 1.2 [5]. Therefore, the conventional power generation systems will be required to operate flexibly with frequent start-ups and shut-downs depending on the availability of renewable sources.

1.2 Cooling of Turbine Casings During Shut-Downs

With the increasing presence of renewables in power generation, steam and gas turbines will be expected to adapt to the flexible operations. When an engine is shut, turbine casings are exposed to buoyant flows which arise from the temperature differences between engine components.

Depending on the operating condition, mixed type of convection occurs with various dominance levels of natural convection. Since the strong inertial forces are not present when the engine is shut, the buoyant flows may reach upto the outer casing, which cause non-uniform temperature distribution (i.e., the temperature of upper half is greater than the lower half). The non-uniform temperature distribution ultimately cause non-uniform cooling on the turbine casings. In Fig. 1.3, the non-uniformity in heat transfer coefficient (h) distribution on high pressure (HP) casing cylinder after a shut-down is shown. Considering the mass of thick turbine casings, cooling of these components may take days [6]. The non-uniform temperature distribution may lead to severe fatigues on the casings due to large thermal stresses, e.g., cat's back distortion as illustrated in Fig. 1.4 where the casing bows. The

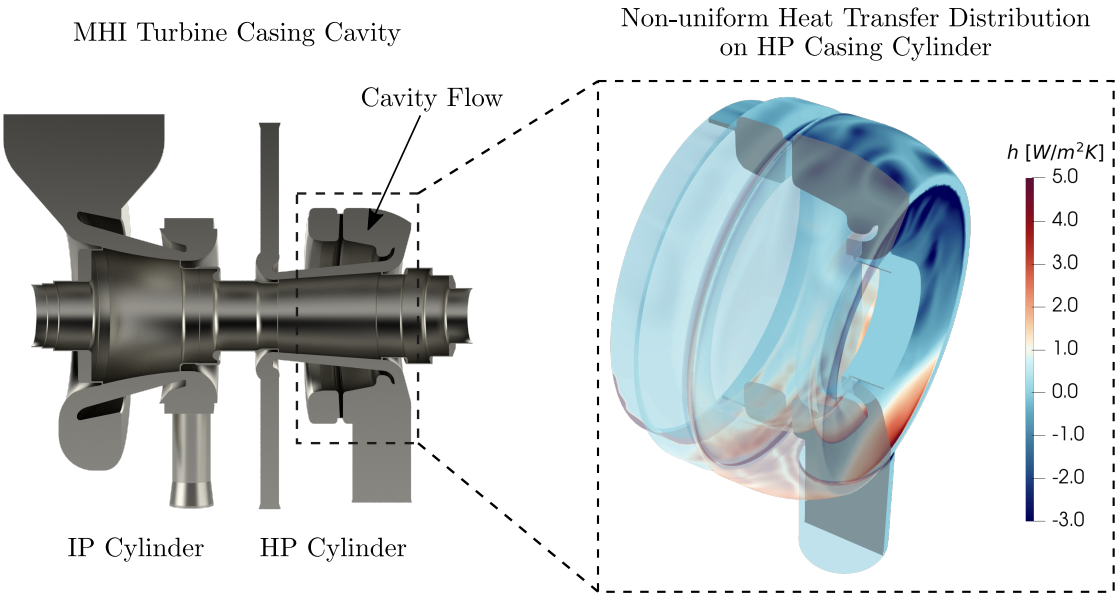

Figure 1.3: Heat transfer distribution on HP turbine casing

distortions on casings may result in closure of labyrinth clearances and reduction in clearances between moving and static parts of an engine. Increasing the clearances to tackle the effects of rubbing and binding of components due to distortion leads to undesirable performance losses [7].

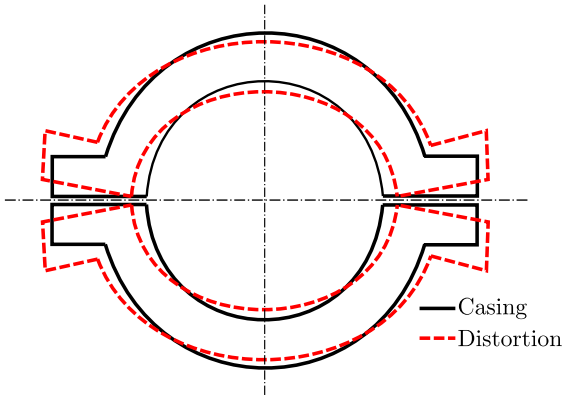

Figure 1.4: Turbine casing distortion due to large thermal stresses (reproduced from [8])

1.3 Motivation

In the foreseeable future, renewables will be the dominant component of power generation. The new realities with operational flexibility for steam and gas turbines

need to be acknowledged, and the mitigation strategies for transforming conventional systems to adapt to the presence of renewables need to be identified to ensure a swift transition to a sustainable future.

From an engineering perspective, the flow physics of mixed (natural and forced convection) types of flows occurring inside turbine casing cavities during shut-down regimes must be thoroughly investigated to account for thermal stresses and compromised clearances in steam and gas turbines. This is vital to enable flexible operations of the conventional power generation systems with frequent start-ups and shut-downs. Due to the limited access to the flow field and harsh operating conditions, the direct measurements inside turbine casing cavities are often not possible. Considering the transient nature of shut-down regimes, computational fluid dynamics (CFD) tools with conjugate heat transfer analyses are also not trivial for simulating an entire shut-down duration due to time disparity with between convection and conduction time scales as reported in the study of He and Oldfield [9]. Even for flow field analyses for investigations of individual time instances during shut-down regimes, the unavailability of extensive turbine shut-down data leads to a sole dependence on CFD tools. These computational tools require experimental validations, otherwise the confidence in the numerical predictions would remain too low to rely on. Accurate predictions with the CFD tools are also essential for finite element analyses (FEA) of the turbine casings since heat transfer coefficient (htc) boundary conditions could be obtained from CFD simulations. To the best of author's knowledge, mixed type of flows with real engine representative conditions and geometrical features for turbine casing cavity flows have not been experimentally investigated with detailed flow field measurements. The lack of experimental studies has also hindered the development of advanced turbulence models to be used in power generation industry at design stage for quick predictions with reasonable computational cost. Therefore, the first step towards enabling flexible operations of steam and gas turbines is to develop a unique experimental facility which can operate at engine realistic conditions. Subsequently, performing and validating scale resolving simulations to gain deeper inside into flow field, and advancing the

computationally less demanding turbulence models for improved accuracy would contribute to enabling flexible operation of future power turbines.

1.4 Thesis Scope

In power generation industry, the main consideration in turbine design is shifting away from a focus on overall efficiency towards more operational flexibility. Due to the liabilities imposed by the international agreements, the growing public awareness on climate change and more importantly the negative impacts of global warming on every aspect of life, the technical challenges which delay or hinder the transition to a greener future must be promptly addressed by the global engineering and scientific community.

As mentioned previously, flexible operations of steam and gas turbines along with renewables will be required for load levelling, which may lead to radical changes in turbine design. Therefore, the improved understanding of mixed type of flows with various buoyancy dominance during shut-down regimes is prerequisite. To this end, the aim of this thesis is to improve our understanding of mixed type of flows in turbine casing cavities using both experimental and numerical methods to enable flexible operations. The scope of this thesis consists of the following items:

- To design a novel experimental facility which is capable of operating at engine representative conditions is presented
- To conduct accurate and detailed measurement diagnostics on the facility
- To perform and validate scale resolving simulations of experimental campaigns
- To asses the performance and highlight the deficiencies of widely used low order turbulence model
- To develop a turbulence model treatment for improved flow field and heat transfer predictions

- To test design modifications for more uniform cooling
- To investigate casing roughness effects on heat transfer and aerodynamics

1.5 Thesis Outline

This thesis will first review the existing literature on natural and mixed type of flows which are relevant to turbine flexible operations, and highlight the lack of available experimental data sets for understanding the nature of such flows, and also for advance turbulence modelling development. A new facility will then be introduced to generate the required experimental validation cases, which will be followed by the scale resolving simulations to gain deeper understanding of the mixed type of flows. The validated simulations will also provide further information on variables such as Reynolds stresses and turbulent heat fluxes which would not be available from the experimental campaigns. These data will then be used to emphasize the shortcomings of conventional turbulence modelling techniques for mixed type of flows, and also to develop a new model to overcome the inadequacies of such techniques. Following the experimental and numerical investigations, various design modifications to the facility will be numerically and experimentally explored to improve the flow field uniformity, which may be applied to real turbine casings. Finally, the surface characteristics of cast turbine casings, and their effects on heat transfer and aerodynamics, which are of great importance and cannot be ignored as will be discussed, will be studied with scale resolving simulations.

A short outline of each chapter is as follows:

Chapter 2 reviews the literature on natural and mixed convection type of flows, and surface roughness. A brief overview on numerical methods is included. Conventional turbulent heat flux and Reynolds stress models are discussed.

Chapter 3 presents the novel experimental facility design. Details of the measurement diagnostics including temperature, velocity measurements as well as

radiation correction methodology are discussed. Characteristics of experimental campaigns are given.

Chapter 4 lists the experimental campaigns conducted. Velocity, temperature and heat flux measurements are given for three selected cases which cover a wide range of mixed convection type.

Chapter 5 explains the methodology of large eddy simulations (LES). A number of LES are validated against the experimental data. The validated LES results are used to gain a deeper insight into the flow field, and also to obtain the Reynolds stress and the turbulent heat flux information which are then used to asses the performance of RANS based turbulence models.

Chapter 6 details a new model which incorporates and blends a Reynolds stress and turbulent heat flux models. The results from the new model are compared against the data from experiments, LES and conventional RANS.

Chapter 7 presents a design modification with a blockage plate to suppress buoyant flows. The effectiveness of the proposed modification is experimentally and numerically assessed.

Chapter 8 investigates the effects of cast turbine casing roughness based on a surface scan on heat transfer and aerodynamics with scale resolving simulations.

Chapter 9 gives a summary of the thesis and some suggestions for future work.

Chapter 2

Literature Review

2.1 Introduction

Combustion chamber of a gas turbine and casing cavity of a high-pressure steam turbine can be represented as horizontal concentric annulus to investigate the flow behaviour and heat transfer characteristics for natural and mixed convection types of flows as shown in Fig. 2.1 where an HP turbine casing [10] and a simplified casing cavity model are shown. In particular, during a shut-down regime, gland seal establishes a cross-flow which goes through HP steam turbine annulus cavity formed by inner and outer casings, hence resulting in a mixed type of convection.

Today, casting is still heavily used to manufacture the large and/or sophisticated parts of industrial devices. Of particular interest are the casings of gas/steam turbines, industrial compressors and turbocharger volutes (Fig. 2.2) where other manufacturing techniques such as machining are not applicable. The casting process causes irregular textures on casing surfaces, and these roughness elements are known to increase the skin friction and the local heat transfer [11].

2.2 Convective Heat Transfer Fundamentals

Convective heat transfer, or simply, convection, is a heat transfer mechanism which occurs due to motion of fluids. Convection can be mainly classified as natural and forced convection. In natural convection, fluid motion is driven by buoyancy forces which arise from temperature gradients in the fluid. In forced convection, an external source, such as a fan or a pump, causes the fluid motion. In some circumstances, both forced and natural convection may occur concurrently, which is known as mixed convection.

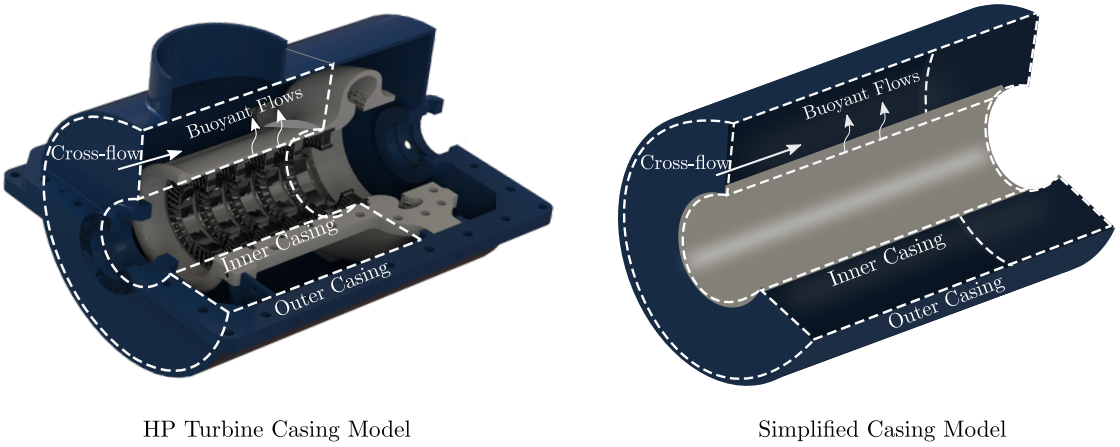

HP Turbine Casing Model Simplified Casing Model

Figure 2.1: HP Turbine casing cavity and a simplified model

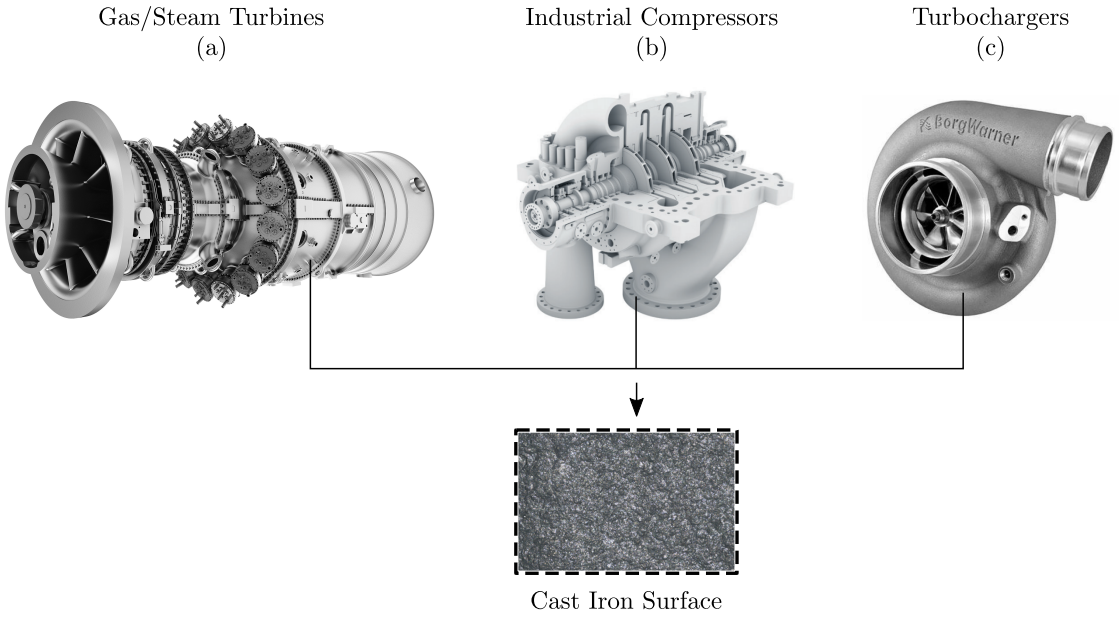

Figure 2.2: Cast roughness in turbomachinery applications (a) GE 9HA gas turbine, (b) MAN Energy Solutions axial compressor, (c) BorgWarner-Turbocharger

In Eq. 1.1 - 1.5, the relevant non-dimensional numbers are given. Nusselt number (Nu) is of paramount importance in heat transfer studies, particularly for convective heat transfer. Nu is effectively a non-dimensionlised heat transfer coefficient, which represents the relative heat transfer enhancement over conduction due to motion of a fluid. In more practical terms, Nu is a key parameter for determining surface temperature distribution in turbine thermal design. In natural convective flows, Grashof number (Gr) approximates the ratio of buoyancy forces to viscous forces, which is analogous to Reynolds number (Re) in forced convective

flows, the ratio of inertial forces to viscous forces. Another important dimensionless number in natural convective flows is Rayleigh number (Ra) which is defined as the product of Grashof number and Prandtl number (Pr). In mixed type of flows, Richardson number (Ri) is a dimensionless number which expresses the effect of buoyancy with respect to shear and can be defined combining the Grashof number and Reynolds number. Hence, Richardson number can be used to determine the dominance of either natural or forced convection in mixed type of flows. In mixed type of flows, natural convection becomes dominant when $Ri > 16$, whilst forced convection is dominant when $Ri < 0.3$ [12]. When $0.3 < Ri < 16$, both plays important role, thus none of them is negligible.

$$Nu = \frac{hD_i}{k} \tag{2.1}$$

$$Gr = \frac{g\beta(T - T_\infty)L_g^3}{v^2} \tag{2.2}$$

$$Re = \frac{uD_h}{v} \tag{2.3}$$

$$Ra = \frac{g\beta(T - T_\infty)L_g^3}{v\alpha} = GrPr \tag{2.4}$$

$$Ri = \frac{g\beta(T - T_\infty)L_g}{u^2} = \frac{Gr}{Re^2} \tag{2.5}$$

where L_g denotes the gap width, D_h is the hydraulic diameter, for a concentric annulus, $D_h = D_o - D_i$.

Although there exists a considerable body of literature on natural convection enclosed in annuli, to the best of author's knowledge, mixed convection (with cross-flow which is diagonal to the gravitational field) types of flows in horizontal concentric annuli for turbine cavity flows has not been experimentally investigated with detailed flow field measurements. The majority of experimental studies concerning mixed types of flows has been on fully developed duct and pipe flows (for instance [13–15]) which do not reflect or remind the developing flows inside turbine cavities. Therefore, the literature review in the following sections will focus mostly on natural convective flows in horizontal concentric annuli which are more relevant to the present study.

2.3 Horizontal Concentric Annuli

Buoyant flows due to temperature gradients in horizontal concentric annuli exhibit various interesting flow patterns, some of which are turbulent plume reaching cold outer cylinder, stable stratified flow and transitional flow [16] which may occur in a wide range of engineering applications such as solar thermal collectors, cable cooling, nuclear reactors and shut-down periods of steam and gas turbines.

2.3.1 Experimental Studies

One of the first attempts to investigate heat transfer in horizontal cylindrical annuli configuration belongs to Beckmann [17] who conducted experiments using air, H_2 and CO_2 as working fluid with Grashof numbers based on inner cylinder diameter, D_i, up to 10^7. He also first proposed a definition for the dimensionless effective conductivity, K_{eff}/k, which has been used in many studies as equivalent thermal conductivity, K_{eq}.

$$K_{eq} = \frac{K_{eff}}{k} = \frac{Qln(D_o/D_i)}{2\pi L_s \Delta T k} \tag{2.6}$$

where K_{eff} is the conductivity of a stationary fluid that would cause the same heat transfer as the convection case. However, it was later noticed that there had been some accuracy problems in Beckmann's measurements. Liu et al. [18] conducted experiments using fluids with high Prandtl numbers to reach higher Rayleigh numbers based on inner cylinder diameter, Ra_{D_i} up to nearly 10^9, and proposed effective conductivity ratio correlation which is a function of Prandtl number, Pr and Grashof number based on gap width between cylinders, Gr_{L_g}. It is also stated in their study that equivalent thermal conductivity should reach unity at low Ra_{L_g}.

Liu et al. [18] also investigated the flow patterns using photographic techniques and observed laminar flow oscillations with $Ra_{L_g} = 4 \times 10^7$. Grigull and Hauf [19] performed experiments to investigate the temperature field and flow patterns in

horizontal circular annuli filled with air, using a Mach-Zehnder interferometer. It was proposed that the flow forms kidney-shape recirculation zones of which the centre tends to migrate towards the upper region of the annulus as Gr_{L_g} increases. For the first time, three distinct regions; the pseudo-conductive region ($Gr_{L_g} < 2.4 \times 10^3$), the transition region ($2.4 \times 10^3 < Gr_{L_g} < 3 \times 10^4$) and the fully developed convective region ($Gr_{L_g} > 3 \times 10^4$), were identified by Grigull and Hauf [19] who also concluded that the solution strongly depends on Gr_{L_g} in the fully developed convective region, while it is independent of Gr_{L_g} in the pseudo-conductive region. A correlation for Nusselt number based on gap width, Nu_{L_g} was proposed for fully developed convective flow for $2.1 \leq D_o/D_i \leq 6.3$ and $Pr = 0.7$.

In study of Lis [20], pressurized nitrogen and sulphur hexafluoride were used at pressures varying from 0.7 to 40 atm to reach high Rayleigh numbers up to 10^{10} in the annulus. Schlieren method was used to investigate the flow qualitatively. Oscillations in thermal-plume above heated inner cylinder were observed at $Ra_{D_i} = 5.5 \times 10^5$. Bishop et al. [21] concluded that the mean equivalent thermal conductivity is a function of Ra_{D_i}. Bishop et al. [22] conducted experiments on natural convection in cylindrical annuli with relative gap widths ($L/2r_i$) of 0.423, 0.731 and 1.35 for heat transfer measurements and flow visualizations. The flow started to oscillate at Gr_{D_i} of 6.6×10^5, 5.6×10^5 and 1.35×10^5 for relative gap widths of 0.423, 0.731 and 1.35, respectively. Itoh et al. [23] introduced a new correlation for characteristic length to be used in Rayleigh number calculations, $(R_i R_o)^{1/2} ln(R_i/R_o)$ and a correlation based on their experimental results consisting of the new characteristic length and Ra_{D_i} for $Ra_{D_i}[0.5\sqrt{D_0/D_i} ln(D_o/D_i)]^3 \geq 7.1 \times 10^3$.

Raithby and Hollands [24] presented heat transfer equations using semi-empirical conduction layer models, and proposed the expressions for equivalent thermal conductivity and Nusselt number. Although the heat transfer equation of Raithby and Hollands [24] included Ra_{L_g}, Pr and diameter ratio, it was valid for only laminar flows.

Kuehn and Goldstein [25] performed experimental and numerical study on natural convection in concentric annuli with Ra_{L_g} varying from 2.11×10^4 to 9.76×10^5 using Mach-Zehnder interferometer. The experiments were conducted

using water and air at atmospheric pressure with $D_o/D_i = 0.8$. In all tests with air, the flow was found to be steady with $Ra_{L_g} < 10^5$ at which the inner cylinder boundary layer was similar to a boundary layer of a single horizontal cylinder. With tests with water, thermal boundary layer was observed around the inner cylinder and the outer cylinder with exception of near the bottom at $Ra_{L_g} = 2.33 \times 10^5$. The maximum heat transfer was observed on top of the outer cylinder where the rising thermal plume impinged on the outer cylinder surface. Kuehn and Goldstein [26] further investigated natural convection with the same experimental set-up with pressurized nitrogen and presented temperature distributions and local heat transfer coefficients up to $Ra_{L_g} = 7.7 \times 10^7$ as well as qualitative results. With Rayleigh numbers of 9.5×10^3 and 1.02×10^5, steady boundary layers on both cylinders were observed. Recirculation zones almost occupied the entire annuli and caused temperature reversal in the central portion. The thermal plume above the inner cylinder oscillated at $Ra_{L_g} = 2 \times 10^5$ for the first time without any regularity which was also observed by [18] and [20]. On the outer cylinder boundary layer, oscillations were found to be regular around $Ra_{L_g} = 5 \times 10^5$. For $Ra_{L_g} \geq 1.5 \times 10^6$, irregular oscillations were found and thought as the onset of turbulence. At $Ra_{L_g} = 1.6 \times 10^7$, the upper portion of the thermal plume was found to be turbulent. The whole plume was turbulent at $Ra_{L_g} = 2 \times 10^7$ at which inner cylinder boundary layer was still laminar. When Ra_{L_g} was increased to 8×10^7, the boundary layer at the upper half of the inner cylinder became turbulent. However, the turbulence decayed as the flow moved towards lower portion of the annuli on outer cylinder surface, which caused the lower portion to be virtually steady. The empirical heat transfer correlations from their previous study [27] were modified.

Based on their experimental observations on natural convection at Rayleigh numbers up to $1.8x10^9$ between concentric cylinders with a diameter ratio of 3.37, Bishop [28] concluded that the expansion number $\beta\Delta T$ must be taken into account when determining heat transfer. Therefore, the expansion number was included in the equivalent conductivity equation. It was also recommended that volume

averaged temperature should be used to evaluate thermodynamic and transport properties, which was defined as;

$$T_{ref} = 0.335T_i + 0.664T_o \tag{2.7}$$

McLeod and Bishop [29] performed an experimental study on natural convection in a concentric annuli with helium at cryogenic temperatures. Heat transfer rates, time-averaged temperature and its fluctuations were obtained for Ra numbers based on gap width between cylinders, varying from 8×10^6 to 2×10^9 using a spectral density analysis of instantaneous temperature measurement technique which was firstly employed by Fresner [30]. The equivalent thermal conductivity was defined using modified Rayleigh number, Ra^*, which includes the diameter ratio effect which was proposed by Raithby and Hollands's [24]. However, the proposed correlation is only valid for $0.2 \leq \beta\Delta T \leq 1.0$, $6 \times 10^6 \leq Ra_{L_g} \leq 2 \times 10^9$, $Pr = 0.688$ and $3.0 \leq D_o/D_i \leq 5.0$. Temperature measurements were performed at circumferentially placed locations with 30° intervals, e.g $\phi = 0°$ being a line above inner cylinder. At $\phi = 30^o$ and 60, temperature of the fluid close to cold outer cylinder was higher than that of the fluid near the hot inner cylinder. This phenomenon is known as temperature inversion which arises from strong recirculation. Increasing Rayleigh number from 1.2×10^7 to 1.18×10^9 resulted in a significant escalation in turbulence at $\phi = 0^o$ which caused the temperature gradient at that location to become more uniform at a value close to that of $\phi = 30°$ due to enhanced mixing. At other measurement lines, 30°, 60°, 90° and 120°, there were not any significant changes in temperature gradients, except locations that were close to inner and outer surfaces where there were a remarkable decrease in thermal boundary layers which caused the temperature gradients to be steeper. It was also found out that more developed turbulence could exist with increasing the expansion number for a constant Rayleigh number.

2.3.2 Numerical Studies

There have been a numerous investigations of natural convection numerically in enclosed cavity. However, most of them, horizontal annulus in particular, were limited to low Rayleigh numbers flows ([31], [32] and [33]).

Farouk and Guceri [34] performed two-dimensional simulations for buoyancy-driven flows in horizontal annuli using $k-\epsilon$ model proposed by Launder and Spalding [35]. Diameter ratio, D_o/D_i, of 2 and air at atmospheric pressure were used. Up to $Ra_{L_g} = 10^2$, velocities were not found to be high enough to affect the temperature field, which means heat transfer occurred due to pure conduction. For Ra_{L_g} between 10^2 and $3x10^4$, existence of the transition region was reported. When Ra_{L_g} was increased from 10^6 to 10^7, the ratio of turbulent viscosity to molecular viscosity escalated from 4 to 14. The turbulent viscosity was remarkable only in the upper half of the annulus, which indicates that the turbulence did not exist in the lower half. Equivalent thermal conductivities, K_{eq}, of $Ra_{L_g} = 10^6 and 10^7$ were presented. Satisfactory agreement with experimental results of Kuehn and Goldstein [26] was observed for $Ra_{L_g} = 10^6$, whilst $k-\epsilon$ under-predicted K_{eq} values for $Ra_{L_g} = 10^7$.

Desai and Vafai [36] investigated two and three dimensional turbulent natural convection in a horizontal annulus for Ra_{L_g} ranging from 10^6 to 10^9 using $k-\epsilon$ model with wall function approach . For $Ra_{L_g} = 10^6 - 10^8$ with $D_o/D_i = 2.6$, recirculating kidney-shaped pattern was observed and the basic flow field structure was defined as follows; the increase in inner cylinder thermal boundary layer thickness; the rise of thermal plume above the inner cylinder towards the outer cylinder; mixing of the thermal plume and the outer cylinder thermal boundary layer; completion of recirculation after separation of the outer boundary layer. Maximum kinetic energy regions occurred near the top of outer cylinder where the thermal plume impinged and near the rotation centre of recirculating flow. The delay in the inner cylinder boundary layer separation was observed as Rayleigh number increased, which in return caused the heat transfer to be more uniform around the inner cylinder except the top region from which the thermal plume departs. The effect of D_o/D_i was also investigated with maintaining the gap width, L_g constant. It

was noticed that the heat transfer becomes greater when the diameter ratio is decreased since the recirculation zone path becomes longer, which causes the bulk temperature to increase. Desai and Vafai [36] also concluded that in the core region, two dimensionality is valid. However, near the end wall, the temperature distribution was significantly affected by the viscous shear of the end wall, which indicated three dimensionality of the fluid mechanism exists at such regions.

Kenjereš and Hanjalić [16] proposed Algebraic Flux Model (AFM) for turbulent heat flux modelling (which will be discussed in the following section) for which temperature variance $\overline{\theta'^2}$ needed to be calculated. The performance of the adopted model was tested using three equation model $k-\epsilon-\overline{\theta'^2}$ on turbulent thermal convection in concentric and eccentric horizontal annuli cases. The model was able to reproduce the flow behaviour such as stagnant region in the lower half and the rising thermal plume above the inner cylinder. Substantial improvement on predicting temperature profiles and Nusselt number distribution were achieved compared to the standard $k-\epsilon$ model.

Fukuda et al. [37] extensively investigated natural convection in horizontal annuli using direct numerical simulation, DNS for Ra_{L_g} up to 1.72×10^7 and large eddy simulation, LES for Ra_{L_g} up to 1.18×10^9 to provide valuable insight into temperature field and flow patterns. Stratified flows were observed in the lower portion of the annulus. Temperature inversion occurred, which had been previously observed in the literature (e.g. [24]). Both DNS and LES under-predicted temperature distribution on the top of the annulus for $Ra_{L_g}=1.22\times10^7$, however, good agreements between DNS/ LES and experimental results were achieved at other locations. According to the authors, the discrepancies at higher Rayleigh numbers might have arisen from the way the representative temperature is calculated. For instance, if the temperature at which the thermophysical properties are obtained is calculated by using arithmetic average, Rayleigh number becomes 7.23×10^6, whereas Rayleigh number becomes even greater at $Ra_{L_g}=1.22\times10^7$ if the volumetrically averaged temperature is used. Thus, it was concluded that Rayleigh number used in the experiments might actually be lower than the real value.

2.4 Transient Analysis of Turbine Cooling

Marinescu et al. [38] conducted the first field turbine measurements with optical pyrometers which tracked the rotor temperature, as well as multiple thermocouples installed on inner and outer casing for natural cooling analyses over 96 hours after a shut-down of an operational steam turbine. These measurements were then used to develop and validate a new numerical procedure with finite element analysis which adopts an equivalent fluid overconductivity replacing the fluid gross gross buoyancy. The numerical method was able to capture the cooling characteristics of turbine components over 96 hours time period with good accuracy.

Stein et al. [39] highlighted that the turbine inner casings as well as rotors suffer from high thermal stresses due to cycling operations of large steam turbines used in solar thermal power plants, and proposed a method to reduce the temperature gradients (and therefore thermal stresses) using heat shields.

CFD based convective heat transfer analyses commonly employ heat transfer coefficient which is assumed to be mostly independent of wall temperature. This assumption, however, has been shown to be prone to large errors for forced convective flows with certain conditions as investigated by Maffuli and He [40, 41], and Zhang and He [42]. Fadl et al. [43] emphasized the deficiency of this assumption for natural convective flows where the near wall temperature is dictated by the wall temperature, and the necessity for conjugate heat transfer (CHT) analyses for coupling the fluid-solid domains. For the first time, a loosely coupled CHT methodology with multi-scale methodology initially developed and tested by He and Fadl [44] for transient forced convective flows was applied to transient natural convectve flows in order to mitigate significant computational time requirements due to temporal accuracy required in commercial codes. The methodology with dual time stepping adopted in source term was found to increase the accuracy compared to quasi-steady flow models (e.g., [45, 46]) without any significant additional computational expense. The authors applied their methodology to LES, which requires much stringent temporal resolution, for transient natural convection problem, and stated that direct coupling of conjugate heat transfer with LES approach leads to over

and underpredictions of wall temperature and heat flux, respectively when the solid mesh is not adequately generated for high frequency disturbances, which was addressed by the loosely coupled LES conjugate heat transfer analysis [47].

2.5 Reynolds Stress and Turbulent Heat Flux Modelling

Although large eddy simulations offer improved accuracy over conventional Reynolds-averaged Navier-Stokes (RANS) simulations, it may not always be possible adopt scale resolving simulations for complex engineering problems in industry where the time is the greatest constraint. Even among the scientific community, computationally less expensive simulations with RANS are preferred if the mean flow characteristics are of interest. Therefore, the turbulence modelling in RANS simulations is important, which may not provide a required degree of accuracy if not treated adequately.

In RANS decomposition, the instantaneous flow variables are decomposed into a mean and a fluctuating components as shown in Eq. 2.8.

$$u_i = \overline{U_i} + u_i' \ , \quad T = \overline{T} + T' \tag{2.8}$$

where the instantaneous, mean and fluctuations are denoted by plain (no accent), bar and prime, respectively.

When the Reynolds averaging is applied to the Navier-Stokes equations, the following set of equations for incompressible flows are obtained for the momentum and the energy equations, respectively.

$$\frac{\partial \overline{U_i}}{\partial t} + \frac{\partial (\overline{U}_j \overline{U}_i)}{\partial x_j} = -\frac{1}{\rho}\frac{\partial P}{\partial x_i} + \frac{\partial}{\partial x_j}\left[v\frac{\partial \overline{U}_i}{\partial x_j} - \overline{u_i' u_j'} \right] + \overline{S}_U \tag{2.9}$$

$$\frac{\partial \overline{T}}{\partial t} + \frac{\partial (\overline{U}_j \overline{T})}{\partial x_j} = \frac{\partial}{\partial x_j}\left[\alpha \frac{\partial \overline{T}}{\partial x_j} - \overline{u_j' T'}\right] + \frac{\tau_{ij}}{\rho C_p}\frac{\partial \overline{U}_i}{\partial x_j} + \overline{S}_T \tag{2.10}$$

where $\tau_{ij} = \mu\left[\frac{\partial \overline{U}_i}{\partial x_j} + \frac{\partial \overline{U}_j}{\partial x_i} - \frac{2}{3}\delta_{ij}\frac{\partial \overline{U}_k}{\partial x_k}\right]$.

These equations Eq. 2.9 and Eq. 2.10 contain additional unknowns, namely $\overline{u_i' u_j'}$ and $\overline{u_j' T'}$, called Reynolds stresses and turbulent heat fluxes, respectively, which lead to the closure problem as there are now more unknowns than the equations in the system. Therefore, modelling is required for the Reynolds stresses and the turbulent heat fluxes [48].

2.5.1 Reynolds Stress Modelling

Individual terms for Reynolds stresses, $\overline{u_i' u_j'}$, are given in Eq. 2.11 which includes nine terms. These nine terms are effectively represented by six terms since $\overline{u'v'} = \overline{v'u'}$, $\overline{u'w'} = \overline{w'u'}$ and $\overline{v'w'} = \overline{w'w'}$. These stresses are crucial for the prediction of mean flow (e.g., velocity) as evidently $\tilde{u} \neq \overline{U_i}$ for turbulent flows where the momentum transfer due to the fluctuating field cannot be ignored [49].

$$\overline{u_i' u_j'} = \begin{bmatrix} \overline{u'u'} & \overline{u'v'} & \overline{u'w'} \\ \overline{v'u'} & \overline{v'v'} & \overline{v'w'} \\ \overline{w'u'} & \overline{w'v'} & \overline{w'w'} \end{bmatrix} \tag{2.11}$$

Besides scale resolving simulations which come at a great computational resource, Reynolds stress models [48] are also often avoided since transport equations (six additional equations in total) are required for each individual Reynolds stresses shown in Eq. 2.11, which scales up the computational requirements. Due to the increased equations to be solved, the Reynolds stress model are known to exacerbate convergence problems in complex flows although they could offer improved accuracy [7, 48, 50].

More computationally affordable and robust option is the turbulent (or eddy) viscosity model which is based on the turbulent (or eddy) viscosity hypothesis. The linear eddy viscosity (more commonly called as Boussinesq hypothesis or approximation) hypothesis form the foundations of Spalart-Allmaras which is one equation model [51], and the commonly used two equation models (e.g., $k-\omega$ SST) [52]. The Boussinesq hypothesis assumes that there is a linear relation between the Reynolds stresses and the mean rate of strain [53] as given in Eq. 6.1. The linear eddy viscosity models, however, are known to fail in predicting Reynolds stresses in flows where strong streamline curvature, rotation and mixing are present.

$$\overline{u_i' u_j'} = -2v_t S_{ij} + \frac{2}{3} k \delta_{ij} \tag{2.12}$$

where v_t is the turbulent viscosity, S_{ij} is the strain rate, k is the turbulent kinetic energy, and δ_{ij} is the Kronecker delta. The strain rate is defined as in Eq. 2.13.

$$S_{ij} = \frac{1}{2}\left(\frac{\partial \overline{U_i}}{\partial x_j} + \frac{\partial \overline{U_j}}{\partial x_i}\right) \tag{2.13}$$

Unlike the laminar viscosity, ν, which is a fluid property, the turbulent (or eddy) viscosity, ν_t, is a flow property which must be modelled. The turbulent viscosity can be approximated as a function of the turbulent kinetic energy, k, and the turbulence dissipation rate, ϵ, or the specific dissipation rate, ω. The transport equations for k and ω are given in Eq. 2.14 and Eq. 2.15.

$$\frac{\partial}{\partial t}(k) + \frac{\partial}{\partial x_i}(k u_i) = \frac{\partial}{\partial x_j}\left(\Gamma_k \frac{\partial k}{\partial x_j}\right) + P_k - Y_k + S_k + G_b \tag{2.14}$$

$$\frac{\partial}{\partial t}(\omega) + \frac{\partial}{\partial x_i}(\omega u_i) = \frac{\partial}{\partial x_j}\left(\Gamma_\omega \frac{\partial \omega}{\partial x_j}\right) + \frac{\alpha\alpha^*}{\nu_t} P_k - Y_\omega + S_\omega + G_{\omega b} \tag{2.15}$$

where Y_k and Y_ω are dissipation of k and ω, S_k and S_ω are source terms, Γ_k and Γ_ω are the effective diffusivities for k and ω, which are defined as:

$$\Gamma_k = \nu + \frac{\nu_t}{\sigma_k} \tag{2.16}$$

$$\Gamma_\omega = \nu + \frac{\nu_t}{\sigma_\omega} \tag{2.17}$$

where σ_k and σ_w the turbulent Prandtl numbers for the turbulent kinetic energy and the specific dissipation rate.

The turbulent viscosity in Eq. 2.16 and 2.17 is calculated as defined in Eq. 2.18 for $k-\omega$ SST model where a limiter is included to avoid overprediction of the turbulent viscosity with standard $k-\omega$. Further details regarding the coefficients in the limiter can be found in [52].

$$\nu_t = \frac{k}{\omega} \frac{1}{max\left(\frac{1}{\alpha^*}, \frac{SF_2}{a_1\omega}\right)} \tag{2.18}$$

In Eq. 2.14 and Eq. 2.15, P_k represents the production of turbulent kinetic energy which can be defined using the Reynolds stress tensor:

$$P_k = -\overline{u_i' u_j'} \frac{\partial u_i}{\partial x_j} \tag{2.19}$$

The Reynolds stress anisotropy, a_{ij}, can be expressed in a non-dimensional form as:

$$a_{ij} = \frac{\overline{u_i{}' u_j{}'}}{k} - \frac{2}{3}\delta_{ij} \tag{2.20}$$

where the last term is the isotropic part.

Absence of anisotropy in turbulent viscosity calculations with the Boussinesq hypothesis leads to inaccurate predictions of Reynolds stress in complex turbulent flows where the flow is strongly three dimensional. This is the main deficiency of linear eddy viscosity models since the turbulent flows are anisotropic by nature. This approximation particularly fails in swirling flows and flows over curved surfaces where significant changes exist in the mean strain rate [54–56].

Nisizima and Yoshizawa [57] performed one of the earliest Reynolds anisotropy developments for $k-\epsilon$ model for turbulent channel and Couette-Poiseuille flows, and they reported an improved predictions of turbulence intensities with the non-linear model compared to the standard $k-\epsilon$ model. Craft et al. [58] developed a cubic $k-\epsilon$ model with an additional transport equation to the their earlier model [59] to account for non-equilibrium effects with low Reynolds number phenomena. A quadratic extension of $k-\epsilon$ was proposed by Speziale [60], which was shown to predict more accurate normal Reynolds stresses compared to the convectional linear relation with $k-\epsilon$. In addition, the model was able to produce turbulent secondary flows in non-circular ducts, as well as the flow separation phenomena. Apsley et al. [61] examined the performance of non-linear models in complex flows. It was found that the quadratic constitutive relation in stress-strain led to improved normal stress anisotropy, whereas the cubic model increased the sensitivity to the curvatures. Gatski and Jongen [62] reviewed various non-linear models, and concluded that five tensors (terms in general tensor notation) are able to represent anisotropy in most cases sufficiently. Fadhila et al. [63] recently reported a new non-linear eddy viscosity model for $k-\omega$ turbulence model using a quadratic stress-strain relation

for Reynolds stress tensor. The main advantage of their proposed model is that the anisotropy magnitude scales with the turbulent Reynolds number. A realisability condition was also included to avoid negative turbulent kinetic energy at the beginning of a simulation. Furthermore, anisotropy coefficients were obtained from DNS data, and subsequently new constants were proposed. Extensive validations were performed with boundary layer, curvature and swirl flows, which proved that the model remarkably enhanced the accuracy of predictions.

2.5.2 Turbulent Heat Flux Modelling

Simultaneous presence of buoyancy driven flows and the flows with relatively strong momentum imposes further complications to be addressed. As discussed, the non-linear eddy viscosity models offer improved predictions of Reynolds stresses. Similar modifications towards second moment closures are available to account the influence of temperature gradients with different orientations for improved heat transfer predictions.

The turbulent heat flux term, $\overline{u_i'T'}$, in Eq. 2.10 which is analogous to the Reynolds stress term, $\overline{u_i'u_j'}$, requires a model to close the system. The most straightforward method for modelling the turbulent heat flux term is to assume that the turbulent heat flux is proportional to the mean temperature gradient, which is known as Simple Gradient Diffusion Hypothesis (SGDH) given in Eq. 2.21.

$$\overline{u_i'T'} = -\frac{\nu_t}{Pr_t}\frac{\partial \overline{T}}{\partial x_i} \tag{2.21}$$

where the first component on the right hand side, $\frac{\nu_t}{Pr_t}$, is the eddy diffusivity which consists of eddy viscosity and predefined turbulent Prandtl number.

Although the SGDH model is widely used (also employed in ANSYS Fluent), it is well-known that this model does not yield accurate results for flows where the influence of buoyancy is present. Hanjalić [64] investigated the potential and limitations of a number of closure levels of one point turbulence models for buoyant flows. It was concluded that the isotropic eddy diffusivity fails in predicting accurate

turbulent heat fluxes in vertical heated wall and Rayleigh–Bénard convection setting. Particularly in buoyant driven flows over vertical heated walls, the SGDH model suffers from under-prediction of turbulent heat flux parallel to the wall since parallel to the wall the temperature gradient is significantly smaller than the wall normal component.

Daly and Harlow [65] proposed the Generalised Gradient Diffusion Hypothesis (GGDH) which takes into account the temperature gradient normal to the gravitational field. The turbulent heat flux calculation by GGDH model is defined in Eq. 2.22.

$$\overline{u_i' T'} = -C \frac{k}{\epsilon} \overline{u_i' u_j'} \frac{\partial \overline{T}}{\partial x_j} \tag{2.22}$$

where the C is a model constant, $C = 0.15$.

As seen in Eq. 2.22, the GGDH model does not require any additional transport equation to be solved while offering improved predictions if the near-wall turbulence is adequately captured [66]. Therefore, the treatment of eddy viscosity may alter the results since the model includes a dedicated term for the Reynolds stress.

Pilkington et al. [67] recently modified the GGDH model to include the buoyancy effect via enabling the model constant, C, vary in the flow field, which is given in Eq. 2.23.

$$C = 0.15 \left(1 + tanh \left| \frac{u}{v} \right| sgn \left(g_j \frac{\partial T}{\partial x_j} \right) \right) \tag{2.23}$$

where $tanh\left|\frac{u}{v}\right|$ is responsible for determining whether the flow is over horizontal or vertical surface, which allows the model to switch to $C = 0.15$ for a flow over a vertical wall.

The model also identifies if the flow is above or below a heated surface with $sgn\left(g_j \frac{\partial T}{\partial x_j}\right)$ which becomes positive for flows above heated surfaces. The perfor-

mance of GGDH+ model was assessed with experimental and LES results, and it was concluded that the model performs in the thermally stratified regions the best.

More advanced turbulent heat flux models are available such as Algebraic Flux Model (AFM) [16] and Differential Flux Model (DFM) [68]. These models, however, require additional transport equations to be solved, which further increase the computational requirements, and therefore may not be desirable in complex engineering flows.

2.6 Cast Turbomachinery Casing Roughness

Roughness studies date back to 1850's with the pioneering works of Hagen [69] and Darcy [70] which were followed by Colebrook [71], Nikuradse [72] and Schlichting [73]. Grinvald and Nukora [74] categorised roughness in two types: discrete (regular) and continuous (irregular). The discrete type is comprised of linear scales of discrete elements and their combinations (e.g. height, length, width and spacing), whereas the continuous type exhibits random surface elevations which are defined by statistical moments (e.g., standard deviation, skewness and kurtosis). The latter, in the context of turbomachinery casings, leads to unforeseeable flow interactions which alter the flow field and heat transfer characteristics.

Although there is a large body of literature on experimental and numerical studies of flow over regular roughness shapes (e.g., cubes, spheres) ([75–81] among others) realistic irregular roughness has not been investigated extensively as much due to the complexity of acquiring surface topology and the requirement of heavy computational resources.

In the past two decades, the focus in roughness studies started shifting towards the irregular roughness to further investigate the effect of relatively small surface textures and the interactions of various length scales on the turbulent motion, momentum and heat transfer. Artificially (mathematically) created irregular roughness research has become popular among researchers to propose a universal correlation to account for roughness effect by systematically testing multiple rough

surfaces. In the literature, these artificially created surfaces were achieved using randomly distributed ellipsoids ([82]), superimposition of sinusoidal functions ([83]), linear combinations of a Gaussian random matrices ([84, 85]), random phase Fourier modes ([86]), power spectrum and probability density function of height function ([87]).

For realistic irregular roughness, Schultz and Flack [88] performed turbulence measurements for a wide range of Reynolds numbers ($Re_\theta = 2180 - 27100$) covering an extensive roughness range from hydrodynamically smooth to fully rough regimes. Brzek et al. [89] performed near-wall measurements in a wind tunnel setting with a 24 grit aluminium oxide abrasive sheet and a 60 grit sand paper to investigate the surface roughness effects and viscous shear stresses on the transitionally rough regime. The breakdown of the viscous stresses in a zero pressure gradient boundary layer were presented by 2D LDA measurements for the first time. Cardillo et al. [90] conducted a DNS of a turbulent boundary layer at $Re_\theta = 2077 - 2439$ on a smooth and a rough surface for which laser measurements were used to obtain the topographical data of the surface used in the study of Brzek et al. [89]. The DNS results were validated against the velocity and wall shear stress measurements in [88] and [89]. In terms of qualitative observations, the iso-contours of instantaneous velocity showed that the surface roughness caused the thickening of the turbulent boundary layer. Increased turbulence led to enhanced mixing within the boundary layer. Compared to the DNS results for smooth case [91], there was a 4% increase in the velocity deficit.

Yuan and Piomelli [92] carried out large eddy simulations for turbulent open channel flows with realistic roughness obtained from hydraulic turbine blades to test applicability of existing correlations with different surface topographies. Based on a scan of graphite surface Busse et al. [93] performed DNS of turbulent flow over a realistic irregular surface. Low-pass Fourier filtering were systematically applied to the surface scan to investigate the influence of of data filtering levels on the mean flow and turbulence characteristics. DNS of 17 industrially relevant irregular rough surfaces based on surface scan was performed by Thakkar et al.

[94]. The roughness levels scaled to represent the same physical roughness height in the transitionally rough regime. Although the friction Reynolds number and the roughness height was the same for all surfaces, the downward shift of the logarithmic law occurred at different levels, which indicates that the u^+ displacement is also effected by surface topography, along with the roughness height. The surface properties which have the highest impact on the hydrodynamic drag, the turbulent kinetic energy and the velocity defect profiles were identified and used in the roughness model optimization. Notably, one of the surfaces used in [94] is a cast surface which is of a particular interest in the present study. However, the DNS study of Thakkar et al. [94] did not include heat transfer phenomenon which is of great importance in the field of turbomachinery.

2.7 Conclusions

Although pure natural convection has been extensively investigated with both experimental and numerical methods, mixed type of convection which refers to the concurrent occurrence of natural and forced convection has not been thoroughly studied. The gap in the literature for the mixed type of flows hinders the advanced turbulence model developments. The previous works on the simple Reynolds stress and turbulent heat flux models which do not require any additional transport equation to be solved have been reviewed for a new model development. Additionally, despite an extensive literature on surfaces with both regular and irregular roughness topographies, the literature still lacks for cast roughness based on a surface scan and its effect on heat transfer and aerodynamics.

These areas of research have been identified and investigated in this thesis with both experimental and numerical methods to enable flexible operation of future power generation turbines.

Chapter 3

Experimental Facility

3.1 Introduction

To be able to test novel design ideas and even simple modifications, or to gain deeper insight into the mixed convective flow field in turbine casing cavities, given that the direct measurements on real engines are not trivial, numerical tools are needed. However, if there is not any representative validation data available, the confidence in the results will be too low to rely on. This would also hamper the numerical model developments. Therefore, a new facility which is capable of simulating engine realistic conditions is a prerequisite to understand the physics of mixed types of flows, to validate the CFD predictions and also to enable the development of advance turbulence models.

A novel experimental facility has been designed, built and commissioned at Oxford Thermofluids Institute (OTI) to investigate mixed convection types of flows in turbine casing cavities during shut-down regimes.

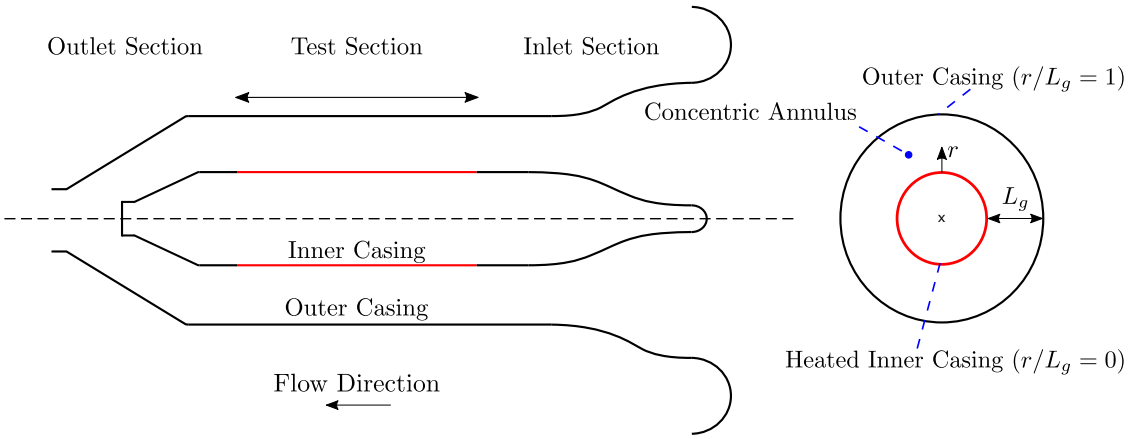

Figure 3.1: Schematic of a simplified turbine casing

3.2 Simplified Turbine Casing Cavity

As highlighted in Fig. 2.1, a horizontal concentric annulus can be considered as a simplified geometry of turbine casing cavities. Buoyant flows can be simulated with a heated inner cylinder. In order to create mixed convection types of flows, cross-flow needs to be introduced to the buoyant flow field. Schematic of a simplified turbine casing including these features is shown in Fig. 3.1. There are mainly three sections, namely, inlet, test and outlet sections. At the inlet section, a contraction nozzle is used to guide the flow to keep the boundary layer attached. There is a heated inner cylinder with isothermal conditions at the test section. Subsequently, the outlet section guides the flow to leave the domain.

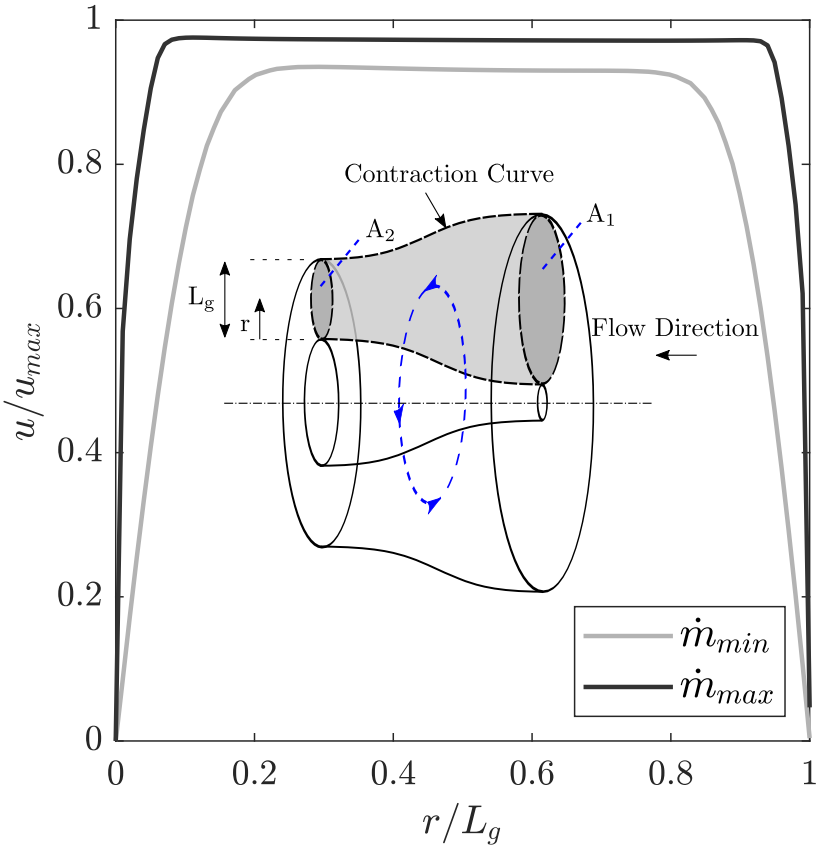

Figure 3.2: Velocity profile at the exit of contraction

3.3 Contraction Nozzle Design

The facility could be considered as an open circuit wind tunnel which requires a contraction nozzle at inlet. There are a number of parameters to be considered when designing a contraction to avoid boundary layer separation and achieve low turbulence uniform flow downstream of the contraction, the most important of which is the contraction ratio, $CR = A_1/A_2$, as can be seen in Fig. 3.2. Contraction curve was achieved using the two matched cubics method proposed by Morel [95, 96], details of which can be found in the study of Fang [97] where he used a combination of two matched cubics to achieve an optimised contraction curve for contractions with square ends. This method is used for conventional wind tunnel inlet contraction design. In the present study where the rig features an annulus, a slightly different methodology was followed. First, the contraction curve was obtained as if it was for a contraction (no annulus) with a circular end. The obtained contraction curves ($CR = 4$ for the highlighted subfigure on Fig. 3.2) were then revolved around the center of axis of the facility to form an annulus, which is illustrated in Fig. 3.2.

Preliminary simulations with steady $k - \omega$ SST [98] turbulence model were performed to test the effectiveness of the contraction design. In the simulations, the contraction was preceded by a straight annulus. Figure 3.2 demonstrates the velocity profile at the exit of the contraction for the proposed $\dot{m}_{min}$ and $\dot{m}_{max}$ in the experiments, which indicates that the velocity profile is uniform in the core region, and remains symmetrical between inner and outer cylindrical walls. Mid-gap ($r/L_g = 0.5$) velocities at various circumferential locations were measured using hot-wire anemometry (HWA) probe, and the flow was found to be sufficiently uniform around the circumference with a maximum deviation of less than 5%, which further confirms the adequate design for a contraction nozzle with concentric annulus end sections. Once the design was finalised, the model was converted to a large assembly, and the individual parts were 3D printed using inhouse *Makerbot Replicator Z18* [99].

3.4 Test Section

The inlet section consists of inner and outer cylinders. The outer cylinder is made up of multiple mild steel parts. The outer surface of outer cylinder is covered with a flexible ceramic heat shield -*ZircoFlex* [100] to minimise the heat loss from the system. Copper was selected for the inner cylinder to ensure high thermal conductivity. The inner surface of the inner cylinder is covered with a self-adhesive silicone heater mat rated for 32 A 5 kW. Purpose built proportional, integral, and derivative (PID) controller is used to adjust the current going through the heater mat to keep the temperature of the inner cylinder constant at a set value. The PID controller box is shown in Fig. 3.3. There are 9 thermocouples attached on the copper cylinder to record and to control the surface temperature via the PID controller. Locations of the thermocouples are given in Fig. 3.4 where two low conductivity ($k = 0.26$ W/mK) calcium silicate -*Monolux* [101] insulation inserts at each end of the copper cylinder are also highlighted. Thermocouples *TC-1* and *TC-5* are used for the power regulation by the PID controller. At the outlet, there is an industrial fan attached to the rig to suck the air from the inlet through the test section, the speed of which is varied to simulate different mixed convection scenarios.

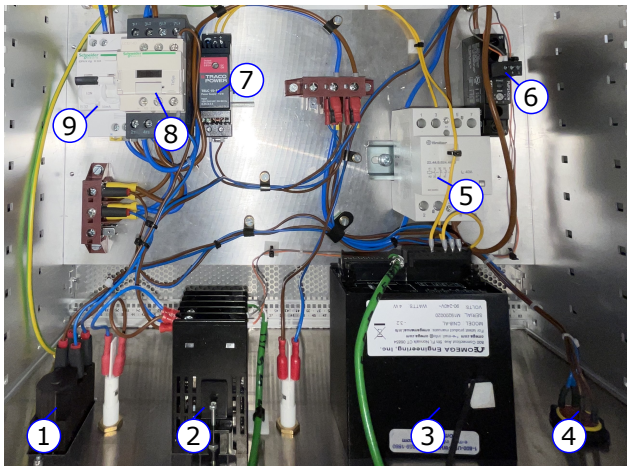

1 - Latching power switch
2 - Temperature controller
3 - Limit controller
4 - Emergency push button
5 - Contactor
6 - Solid state relay
7 - AC/DC power supply
8 - Contactor
9 - Circuit breaker/overcurrent protection

Figure 3.3: PID controller layout

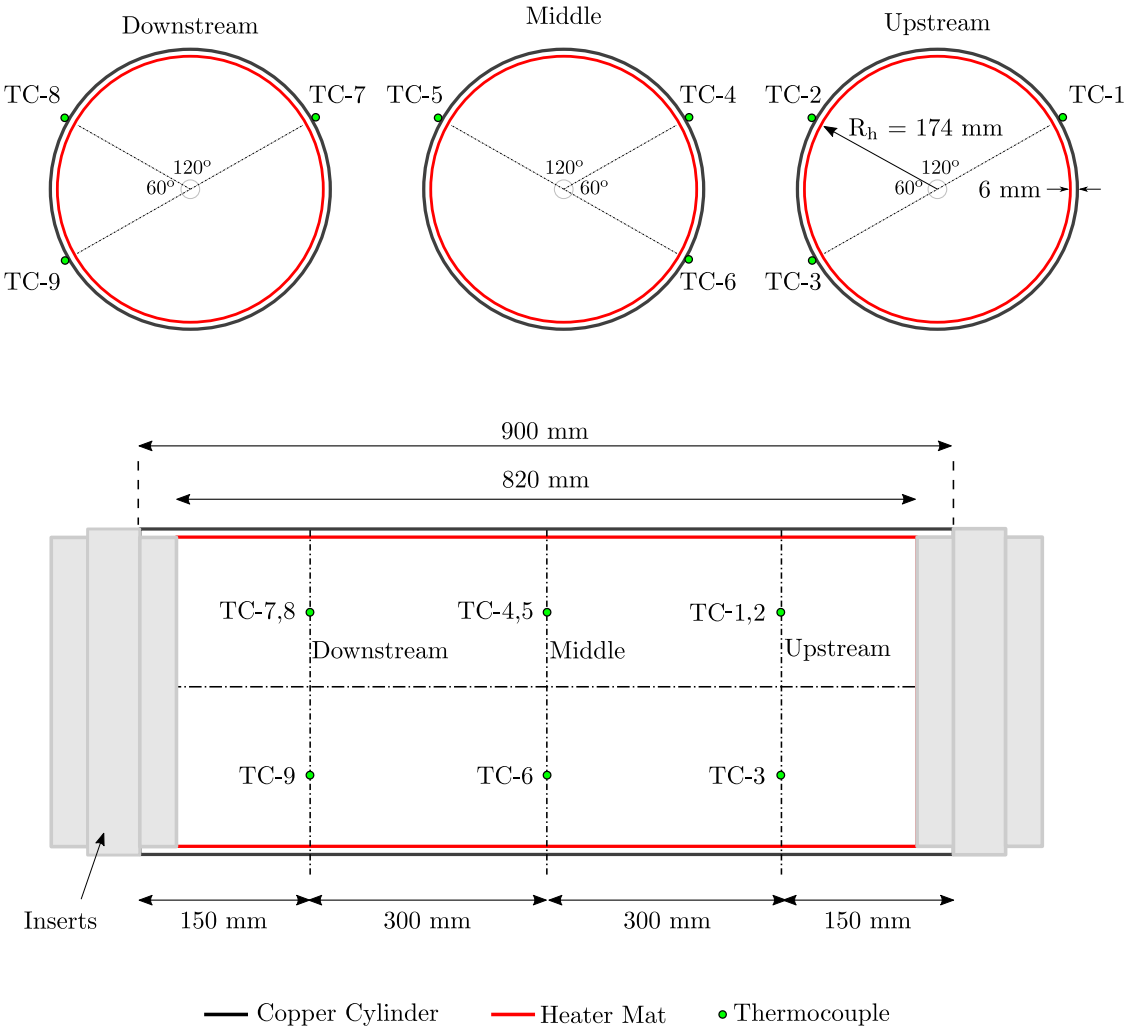

Figure 3.4: Distribution of surface thermocouples on the heated inner cylinder

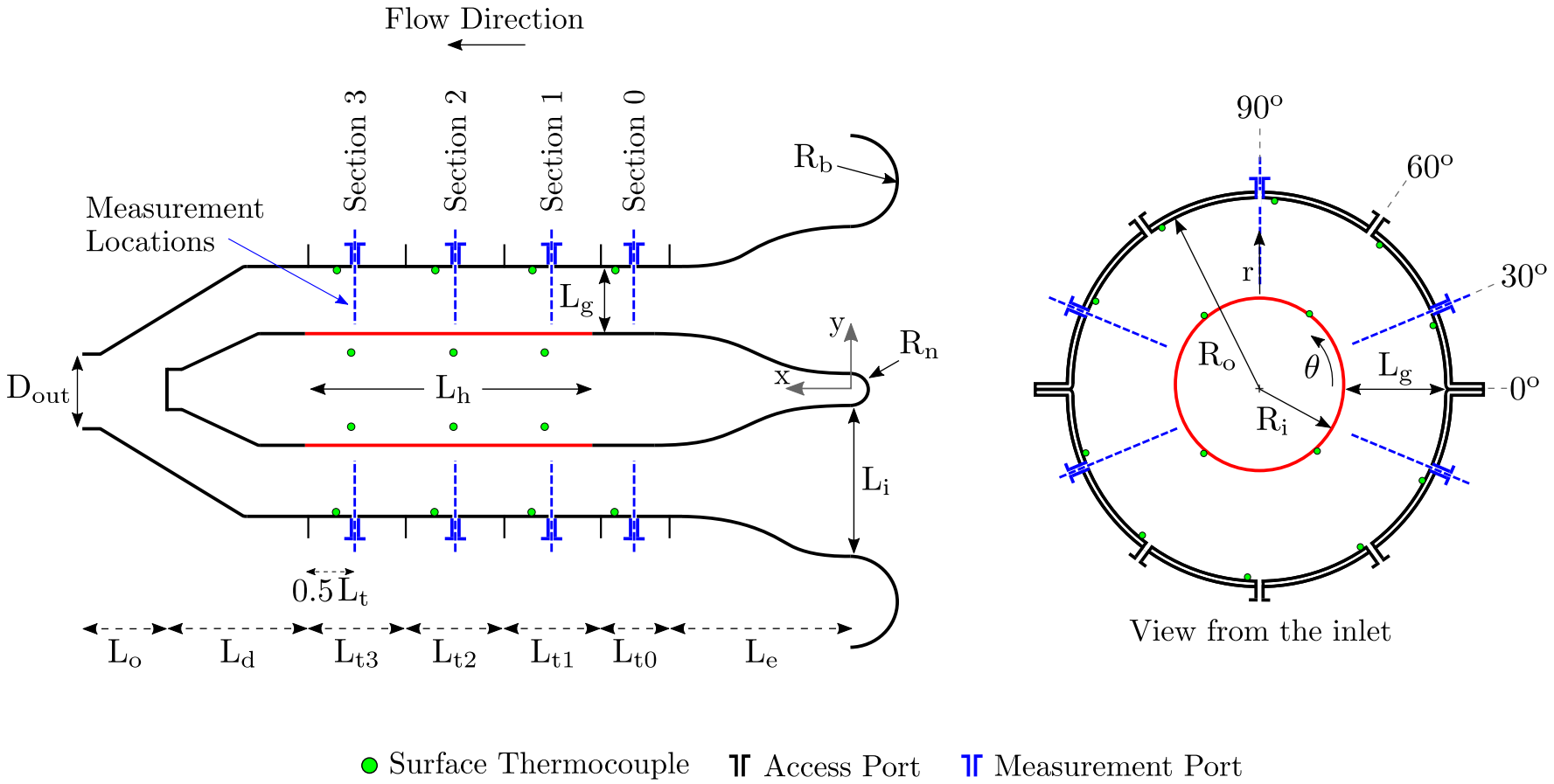

Figure 3.5: Experimental facility schematic with measurement locations

Table 3.1: Rig dimensions (P: Parameter, D: Dimension)

P	D (mm)	P	D (mm)	P	D (mm)	P	D (mm)
R_i	180	R_n	70	L_e	720	L_d	425
R_o	400	L_i	440	L_{t_0}	250	L_o	390
R_b	150	L_g	220	$L_{t_{1,2,3}}$	300	D_{out}	200

3.5 Facility and Measurement Locations

There are a total number of 36 access ports which are distributed axially and circumferentially on the experimental facility. 30 of them are placed in the test section, and the remaining ones are at Section 0. The detailed schematics of the facility with measurement locations are shown in Fig. 3.5. The corresponding dimensional details are tabulated in Table 3.1.

The outer cylinder was split vertically and horizontally to provide the rig modularity, and to enable future modifications. The test section is divided into three sections, namely Section 1, 2 and 3. The additional section, Section 0, is placed upstream of the test section, where the hot-wire anemometry (HWA) measurements were performed to obtain the inlet velocity profiles, and ultimately to calculate the mass flow rates. The copper cylinder in the test section was spray painted matte black to reduce the reflectivity of the copper for radiation effects.

It is important that any experimental facility matches the real scenario as close as possible. The facility in the present study is able to operate at pure natural, pure forced and a wide range of mixed type of convection conditions. Figure 3.6 compares the operational ranges of the facility and a real turbine (data provided by Mitsubishi Heavy Industries (MHI)). As seen in the figure, the facility is able to operate at engine realistic conditions.

A photograph of the final facility assembly can be seen in Fig. 3.8.

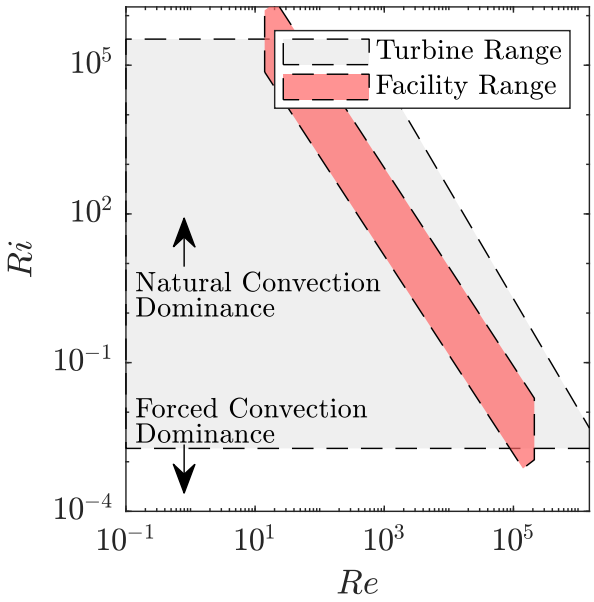

Figure 3.6: Operational range comparison of the experimental facility and a real turbine

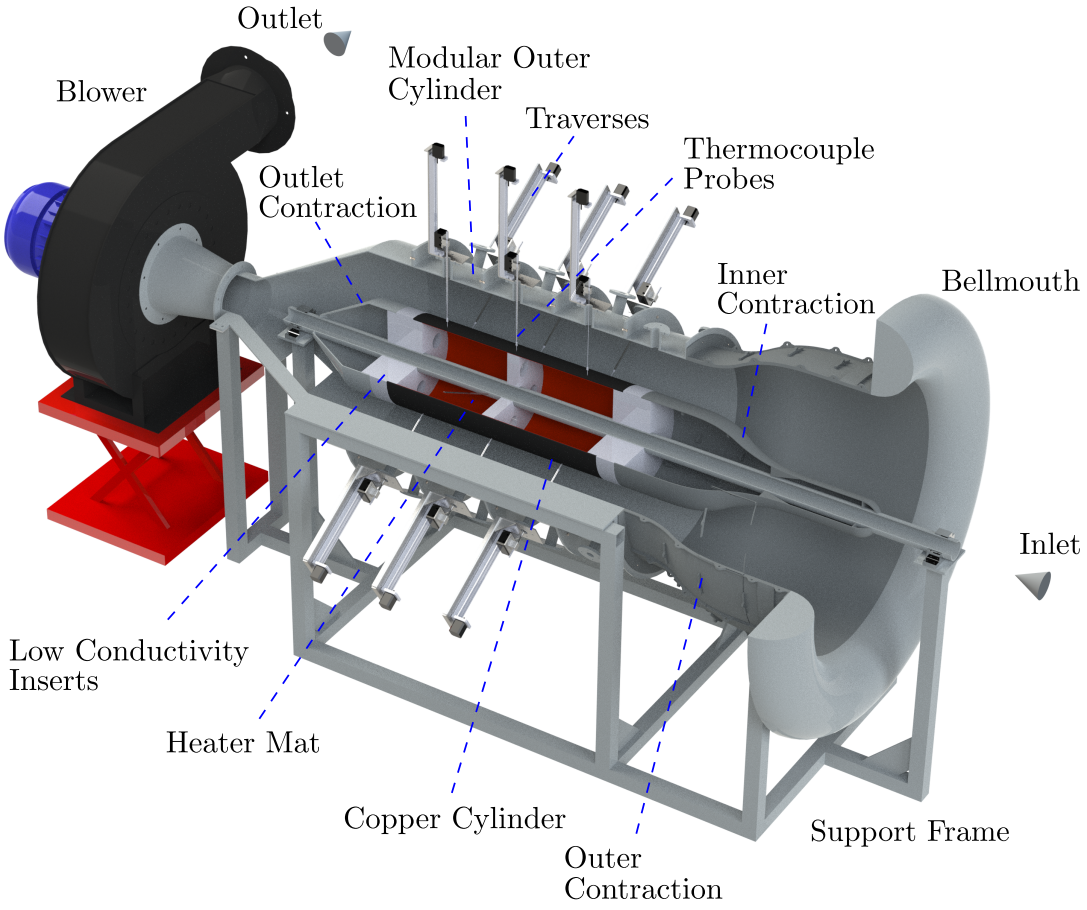

Figure 3.7: CAD model of the facility with a section view

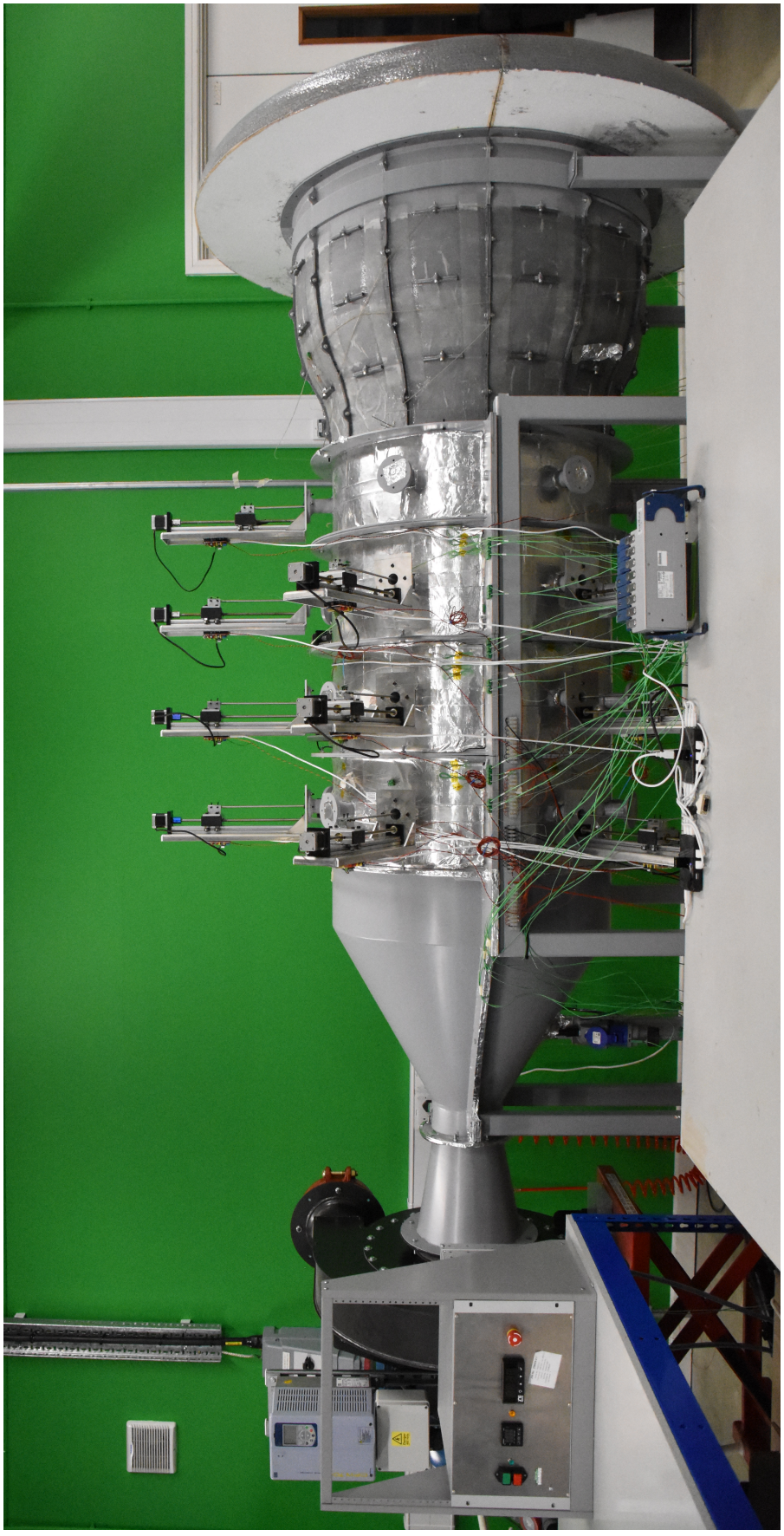

Figure 3.8: A photograph of the facility

3.6 Measurement Diagnostics

3.6.1 Linear Actuators

Each traverse unit consists of a metal bracket, a linear actuator motor which is controlled by an *Arduino-UNO* microcontroller [102], and a steel tube with an outer diameter of $OD = 6$ mm, which houses thermocouples (and HWA probe at Section 0). The linear actuators have an accuracy of 0.05 mm, which were used to traverse the probes with a high resolution stepping of 0.1 mm from the heated inner cylinder to ensure that large near wall gradients are accurately captured.

3.6.2 Temperature Measurements

Detailed temperature measurements were taken at $\theta = 30°$, $90°$, $150°$, $210°$ and $330°$ in Section 1, 2 and 3. K-type thermocouples with exposed beads for faster response times were used for the temperature measurements. The temperature readings were taken by *National Instruments* NI-9212 [103] data acquisition modules. The unsteady data were acquired over a period of 120 seconds with a sampling rate of 50 Hz. Multiple surface thermocouples (40 in total) were placed on the inner and outer cylinders as shown in Fig. 3.5 to determine the boundary conditions to be used in the simulations. The temperature data from both thermocouple probes and surface thermocouples were acquired after the facility had reached a steady-state. In order to ensure that a steady-state condition was reached, surface thermocouples on the outer cylinder were checked as the readings from those were found to reach steady-state last.

The schematic of thermocouple is shown in Fig. 3.9. Steel tubes were used to prevent thermocouples from oscillations which would have affected the flow field and temperature readings. The thermocouples were guided through a collet where a needle was used to set the distance (0.2 mm) between the thermocouple bead and the wall to avoid contact in between.

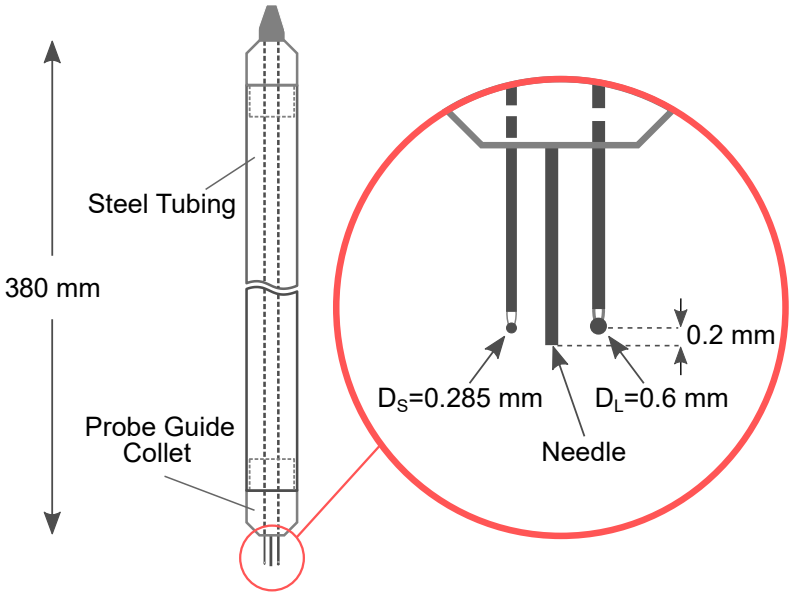

Figure 3.9: Schematic of thermocouple probe

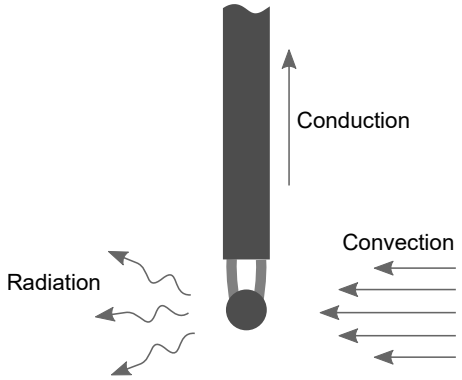

Figure 3.10: Heat transfer modes on a thermocouple bead

When a thermocouple is located in a high temperature environment, temperature measurement may remarkably be affected by a number of error sources, some of which are heat conduction through the thermocouple wires and radiation. These errors, therefore, cause temperature readings to diverge from the true gas temperature.

There are several ways to avoid the error sources, particularly radiation, such as coating the bead of thermocouple with highly reflective material, or using suction pyrometer. These methods, however, have certain limitations as they may not be cost effective, non-intrusive or suitable for certain probe sizes. Multiple thermocouple method was proposed by Daniels [104]. In his study, the probe

consists of sets of thermocouples with different diameters, the temperature readings are plotted as a function of the bead size. The readings are then extrapolated to the zero mm bead diameter which theoretically indicates the true fluid temperature. However, this method could disturb the flow field with multiple thermocouples occupying too much space. On the other hand, with fewer thermocouples, accuracy of the extrapolation may not reliable. Several other studies on the use of two thermocouples with unequal bead size but same properties have been reported in the literature([105], [106], [107])for estimating the radiation errors.

The heat transfer modes that occur on a thermocouple are radiative heat transfer from/to surroundings, conduction through the thermocouple wires and convection as illustrated in Fig. 3.10. Blevins and Pitts [108] proposed an idealised steady state energy balance equation (Eq. 3.1) for exposed bead thermocouples by neglecting heat dissipation due to conduction.

$$h(T_f - T_b) = \epsilon_b \sigma ({T_b}^4 - {T_\infty}^4) \tag{3.1}$$

where T_∞ is the effective surrounding temperature, T_b is the thermocouple temperature, T_f is the true fluid temperature, ϵ_b is the emissivity of the thermocouple bead, h is the convective heat transfer coefficient and σ is the Stefan-Boltzman constant.

When Whitaker's correlation [109] for external flow over a sphere is used, Nusselt number yields as follow:

$$Nu = 2 + (0.4Re^{0.5} + 0.06Re^{0.666})Pr^{0.4} \tag{3.2}$$

In order to check the sensitivity of the two thermocouple approach to the selection of Nusselt number correlation, another model for forced convective flows over spheres proposed by Achenbach [110] was used, and the results were found to be similar to the Whitaker's correlation with a maximum deviation of 2.1 %.

When Eq. 3.1 is solved for T_∞:

$$T_\infty = \sqrt[4]{\frac{h(T_b - T_f) + \epsilon_b \sigma {T_b}^4}{\epsilon_b \sigma}} \tag{3.3}$$

Since Eq. 3.3 for T_∞ would be the same for any thermocouples with close proximity to each other, two thermocouples could be related to each other in the form of following equation:

$$T_\infty = \sqrt[4]{\frac{h(T_{b,1} - T_f) + \epsilon_{b,1} \sigma {T_{b,1}}^4}{\epsilon_{b,1} \sigma}} = \sqrt[4]{\frac{h(T_{b,2} - T_f) + \epsilon_{b,2} \sigma {T_{b,2}}^4}{\epsilon_{b,2} \sigma}} \tag{3.4}$$

Solving Eq. 3.4 for the true fluid temperature T_f if the emissivity is the same for both thermocouples:

$$T_f = \frac{h_2 T_{b,2} - h_1 T_{b,1} + \epsilon({T_{b,2}}^4 - {T_{b,1}}^4)}{h_2 - h_1} \tag{3.5}$$

Two K-type thermocouples with unequal diameters, details of which are tabulated in Table 3.2, were selected to conduct radiation corrections. The larger thermocouple has been chosen based on recommendations of Tagawa and Ohta [105] which state that diameter ratio should be around 2 or 3 to maintain adequate difference in thermocouples' frequency responses. The bead diameters of the thermocouples in this study are $D_S = 0.285$ mm and $D_L = 0.600$ mm, and the diameter ratio is $D_L/D_S = 2.1$. The thermocouple picture can be seen in Fig. 3.11.

Table 3.2: Thermocouple details

TC	Bead Diameter (mm)	Type	Wire Material	Emissivity
D_S	0.285	K	Nickel Chromium-Aluminium	0.75
D_L	0.600	K	Nickel Chromium-Aluminium	0.75

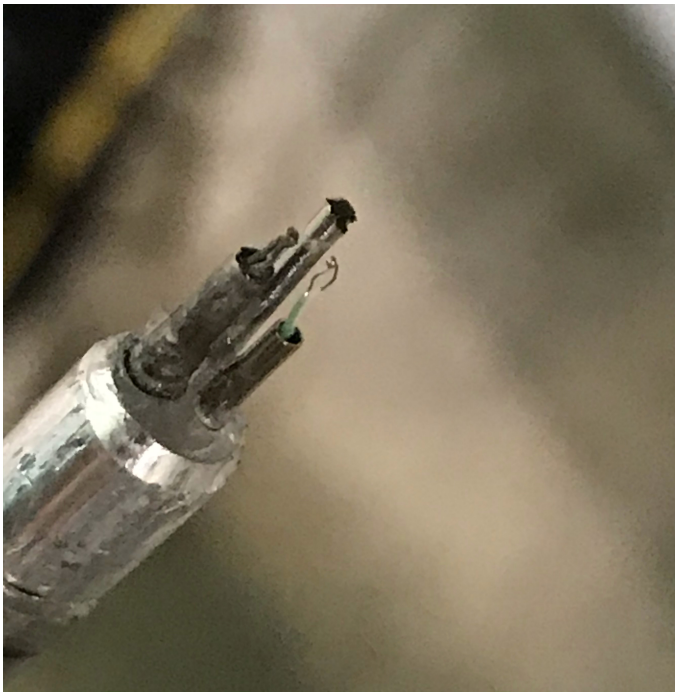

Figure 3.11: Thermocouple probe picture

3.6.3 Heat Flux Measurements

The heat transfer from the wall is defined by temperature gradient near the wall. In the conductive viscous sub-layer, temperature gradient remains linear [54]. Since the conduction is dominant heat transfer mode in this region, Fourier's law [111] given in Eqn. 3.6 can be used to calculate the heat flux using the linear temperature gradient [67, 112, 113].

$$q^{''} = -k\frac{dT}{dr} \tag{3.6}$$

As mentioned previously, linear actuators were traversed starting from the heated inner cylinder towards outer casing with sufficiently small resolution (0.1 mm). Therefore, even large temperature gradients occurring in the thin viscous sub-boundary layers were successfully captured at all traverse locations. However, the heat transfer calculations may not be possible when the viscous sub-layer ($y^+ < 5$) are not thick enough to fit sufficient number of measurement points, which will be

further discussed in Section 4. Wall heat fluxes at traverse locations on the heated cylinder were calculated using the linear temperature gradient near the wall, to which an average of 4-12 measurement points were fitted. The goodness of each fit was assessed using linear regression analysis. Alternative to the linear best fitting method, exact integral method could be used to evaluate the wall heat flux. This method employing multiple integrations of Reynolds averaged energy equations was proposed by Ebadi et al. [114]. Pilkington [7] used both methods to calculate the wall heat fluxes, and concluded that the results were very similar.

3.6.4 Hot-wire Anemometry Measurements

Velocity measurements were performed with a *DANTEC Dynamics* boundary layer hot-wire anemometry (HWA) (constant temperature anemometry (CTA) type) probe [115]. The measurements were taken at $\theta = 30°$, $90°$, $150°$, $210°$ and $330°$ at Section 0 which is the upstream of the test section where the flow field is not affected by the buoyant flows, therefore isothermal. In the test section, the flow field is mostly influenced by the buoyant flows which may lead to large temperature fluctuations. Therefore, it was not possible to perform HWA measurements in the test section.

The data was logged using NI-9209 [116] C series voltage input module. As HWA is an indirect measurement technique, probe calibration is required to relate voltage (V) readings to velocity magnitudes. *DANTEC Dynamics* Streamline Pro [117] shown in Fig. 3.12 was used to calibrate the boundary layer probe. A number of velocities ranging from 0.02 to 5 m/s were set on the calibrator and the corresponding voltages from the probe were acquired. 4th order polynomial fitting which is seen in Fig. 3.13 was then used to convert the voltages into the velocities in the actual experiments.

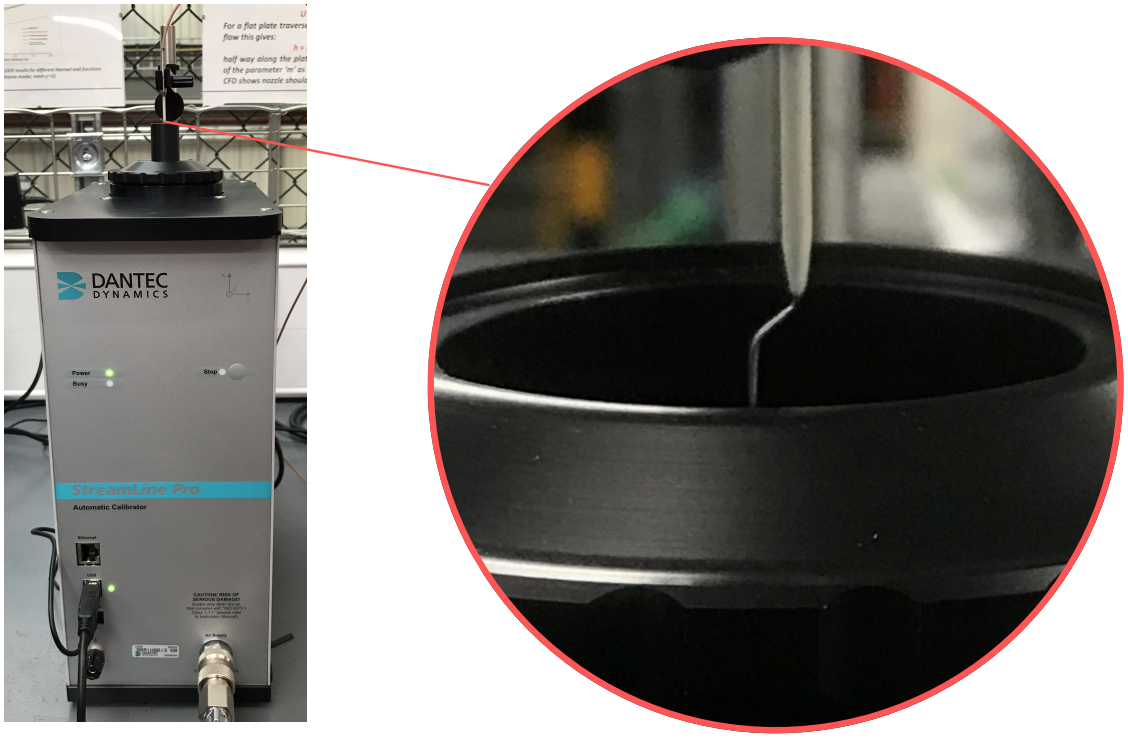

Figure 3.12: HWA calibration box and the probe

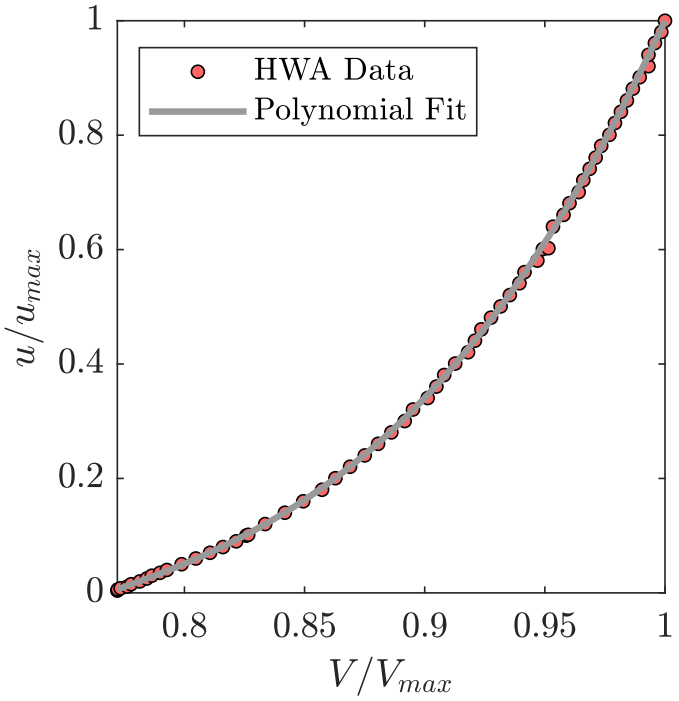

Figure 3.13: HWA calibration with a polynomial fit

3.7 Conclusions

A novel experimental facility which has been developed for investigations of mixed (natural and forced) convective types of flows has been presented. The range of facility operating conditions has been compared against Mitsubishi Heavy Industries (MHI) turbine, and found to simulate engine realistic conditions in terms of Richardson and Reynolds numbers.

Geometrical features have been identified for the facility to replicate a region of interest in a real engine. The design of contraction nozzle for guiding the incoming air has been presented and shown to provide satisfactory flow uniformity at the outlet (upstream of the test section).

The detailed information of measurements locations which were distributed axially and circumferentially has been illustrated on the schematics of the facility. The details of measurement diagnostics which includes temperature, heat flux and velocity measurements have been given. Finally, calibration of the boundary layer hot-wire probe has been presented.

Chapter 4

Experimental Campaigns

4.1 Introduction

It is vital to have experimental data to validate CFD predictions of any application. As mentioned previously in Section 3.2, the test section is comprised of a horizontal concentric annulus. As opposed to pure natural convection and pure forced convection in a horizontal annulus, mixed convection flow fields have not been extensively studied.

In pure natural convection, there is a boundary layer starting to develop from the bottom of the heated cylinder, which then forms a thermal plume at the upper half. The developed thermal plume then impinges on the outer cylinder where the heat transfer is enhanced with large temperature gradient. After impingement, the fluid cools down and is directed to the bottom half. In pure forced convection, the boundary layer progressively thickens along the heated cylinder and forms circumferentially uniform thickness. When a buoyant flow field is disturbed by a cross flow (inertial force), which makes the case mixed type of convection, complex flow interactions occur with strong three dimensionality. These flow regimes are illustrated in Fig. 4.1. As seen in the figure, the influence of buoyant flow varies depending on how strong the cross flow is. If the speed of cross flow is sufficiently reduced, Richardson number (Ri) increases, and the flow field starts to remind a natural convection case. With much lower Ri, thermal plume does not form and the boundary layer becomes more uniform around a given circumference.

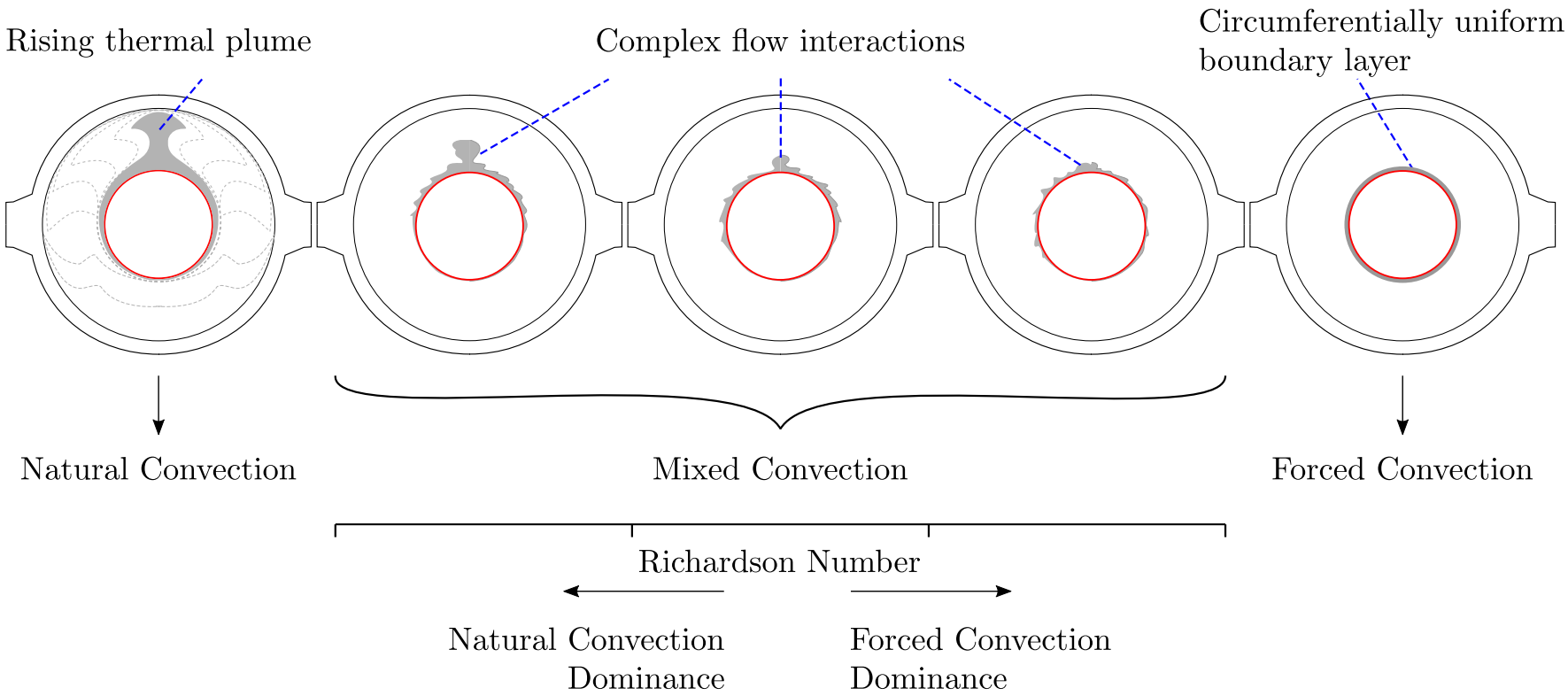

Figure 4.1: Mixed convective flow regimes

4.2 Campaigns

Since the literature lacks for experiments for mixed convection types of flows in turbine casing cavities, 7 experimental campaigns were performed with various Richardson numbers ranging from 0.472 to 0.016 to cover a wide range of different flow regimes including natural and forced convection dominant regimes to generate a data set for CFD validations, to reveal characteristics of the flow field.

Table 4.1: Experimental campaigns

All Cases	Selected Cases	Gr	Re	Ri
Case-A	-	1.83×10^8	1.95×10^4	0.472
Case-B	*Case-1*	1.86×10^8	2.75×10^4	0.246
Case-C	*Case-2*	1.83×10^8	3.95×10^4	0.117
Case-D	-	1.75×10^8	4.73×10^4	0.078
Case-E	-	2.06×10^8	6.56×10^4	0.048
Case-F	*Case-3*	1.96×10^8	7.87×10^4	0.032
Case-G	-	1.90×10^8	1.09×10^5	0.016

All experimental cases with respective non-dimensional numbers are tabulated in Table 4.1. Based on the assessments of individual cases' results, 3 cases were identified to be presented in greater detail. The selected cases are Case-B, Case-C and Case-F which were found to represent various regimes including natural and forced convection dominant flows where the effects of the less dominant type are still present to a certain degree.

Hereafter, the selected Cases-B, C and F will be referred as Case-1, Case-2 and Case-3 which are marked on the facility/real engine comparison plot in Fig. 4.2. The details of the inner and outer casing temperatures in each case are given in Table 4.2. The temperature results from the remaining cases are given in Appendix A. Case-1 and Case-3 represent the natural and forced convection dominant cases, respectively.

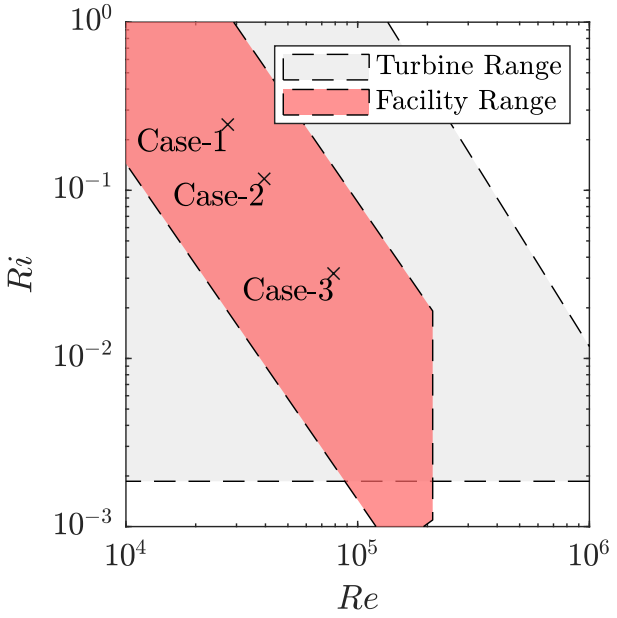

Figure 4.2: Selected experimental campaigns

Table 4.2: Test section inner and outer wall temperatures

Test Section		Case-1 (K)	Case-2 (K)	Case-3 (K)
Heated inner cylinder		422.5	422.5	426.5
Section 1 Outer Casing	Lower Half	315.5	313.6	308.1
	Upper Half	314.5	312.8	307.1
Section 2 Outer Casing	Lower Half	320.6	318.1	313.1
	Upper Half	318.6	317.1	313.1
Section 3 Outer Casing	Lower Half	316.1	316.1	311.1
	Upper Half	317.6	315.1	311.1

The dominant mode was judged by presence of apparent presence of rising thermal plume. Case-2 lies in between the other two cases in terms of flow characteristics. For instance, there is not a thermal plume development but a distinct thickening of boundary layer in Case-2 as will be discussed in the upcoming sections.

Sampling duration of any raw data is critical to ensure that the adequate time is passed for converged time-averaged variable. In Figure 4.3, raw temperature

readings from $\theta = 90°$ and $150°$ at $r/L_g = 0.09$ in Section 3 in Case-1 are shown. Raw temperature readings are shown by black lines whilst light red lines indicate the cumulative average of the raw data. $\theta = 90°$ in Case-1 were particularly selected since the flow field tends to be highly unsteady in the plume region at the upper half of the annulus which can be deduced from the large fluctuations as opposed to the readings at $\theta = 150°$ where laminar flow is present in the lower half of the annulus.

In Figure 4.3, the unsteady temperature data, which was non-dimensionalised using Eq. 4.1, was logged for 240 seconds. Based on the mean data, it was deduced that averaging over 120 seconds would be sufficiently enough to obtain accurate time-averaged data since the maximum temperature deviation in the mean values remained below 1 K beyond 120 seconds.

$$T^* = \frac{T - T_\infty}{T_i - T_\infty} \tag{4.1}$$

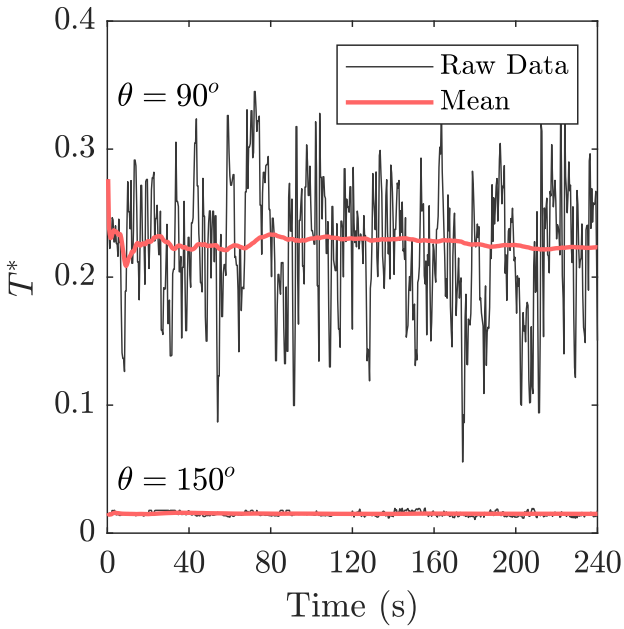

Figure 4.3: Comparison of raw and time-averaged temperature data

4.3 Radiation Correction

The experimental facility is capable of reaching upto 475 K on the inner cylinder with the current set-up. With these relatively high temperatures, the thermocouple readings may be biased due to radiation from the thermocouple bead. Therefore, the temperature readings must be corrected. The methodology described in Section 3 was followed to account for the radiation effects.

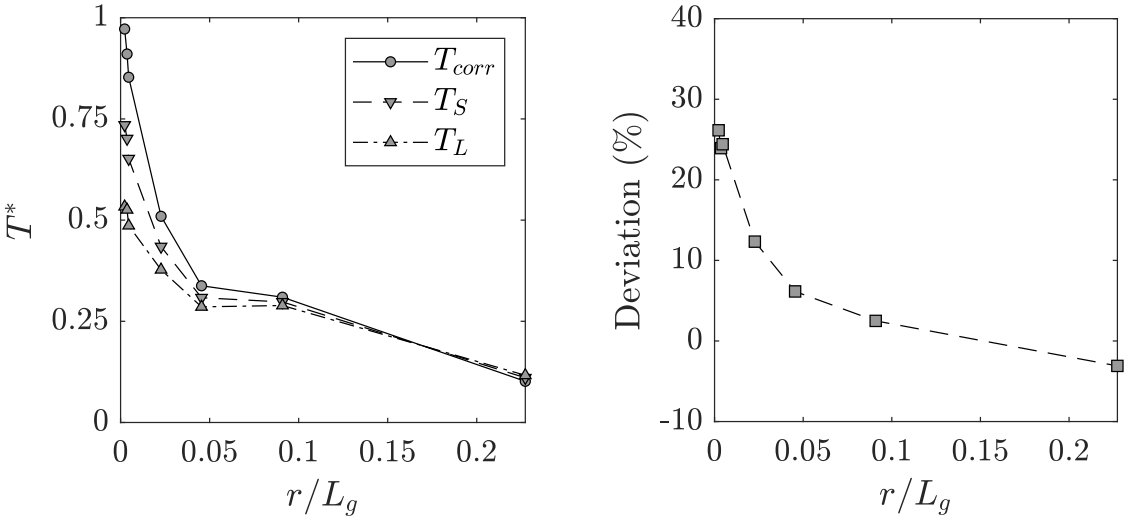

Figure 4.4: Radiation correction for Case-1 at $\theta = 90°$ at Section 2

The radiation influence would increase with increasing the temperature difference between the fluid and the surrounding temperature since the radiative heat transfer scales with the fourth power of temperature. Additionally, errors are proportional to the thermocouple bead size, and inversely proportional to the velocity [106]. As the measurements were conducted at numerous radial locations with various cross-flow speeds, the associated errors would not be expected to be constant but rather vary along the radial direction. Overall, it is important to account for the radiation effects in the temperature measurements.

In Figures 4.4, 4.5 and 4.6, the temperature readings from two thermocouples with unequal diameters, T_S and T_L, along with the corrected temperatures, T_{corr}, are presented for Case-1, Case-2 and Case-3, respectively. Errors in small bead thermocouple readings are also shown for each case. Errors were calculated with regards to the readings in degrees Celsius (°C) instead of Kelvin (K) which would

have resulted in much lower values. Results are presented at near-wall region up to $r/L_g = 0.2$ with fewer measurement locations for visual clarity.

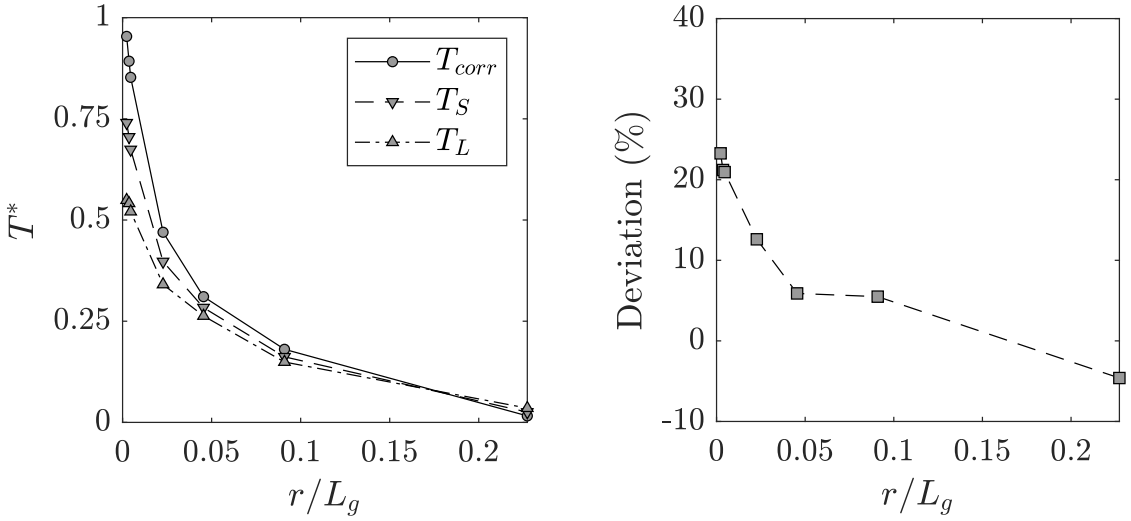

Figure 4.5: Radiation correction for Case-2 at $\theta = 90°$ at Section 2

It is evident that the small diameter bead thermocouple yields more accurate readings than the large diameter thermocouple since the heat loss due to radiation decreases with decreasing the bead surface area. Further reduction in bead diameter would have resulted in less errors but it would be too fragile to handle during the probe development phase. In all Cases, the maximum error occurred in the near-wall region, reading up to $\text{deviation}_{\text{max}} = 33\%$ in Case-3. It is important to note that the readings did not approximate to the heated cylinder temperature (far less than $T^* \ll 1$). This is due to a very thin sub-layer arising from a relatively high flow speed. As traversing away from the heated wall, the difference in temperature readings was reduced so does the error. This could be attributed to the lower temperatures and the increased convective heat transfer. It can also be deduced that the error is not strong function of flow speed with moderate temperatures.

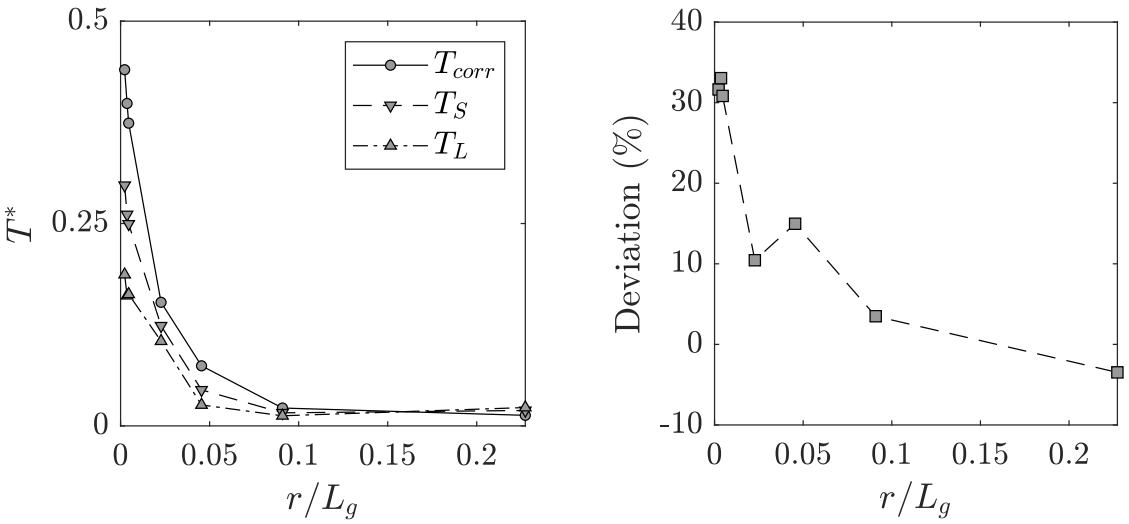

Figure 4.6: Radiation correction for Case-3 at $\theta = 90°$ at Section 2

4.4 Measurements

4.4.1 Velocity Measurements

Velocity measurements were performed using the calibrated boundary layer hot-wire probe as presented in Chapter 3 at various circumferential locations at Section 0 which marks the upstream of the test section. In Fig. 4.7, non-dimensionlised velocity profiles for each case are given. In Table 4.3, the displacement thickness, δ^*, the momentum thickness, θ, and the shape factor, $H = \delta^*/\theta$, are given for each case. As seen in the table, H reduces as the Reynolds number increases. Relatively low H values compared to typical laminar boundary layer profiles (e.g., $H_{flat\ plate} = 2.59$ [118]) indicate that the boundary layer separation was avoided. Overall, the velocity profiles confirmed that the inlet contraction was adequately designed since the boundary layer remains attached and uniform circumferentially. Additionally, these velocity measurements were particularly important for the mass flow rate calculations which would be used in CFD simulations.

4.4.2 Temperature Measurements

Radial temperature profiles in Section 1, 2 and 3 in Case-1, 2 and 3 are presented in Fig. 4.8, 4.9 and 4.10, respectively. The circumferential measurement locations

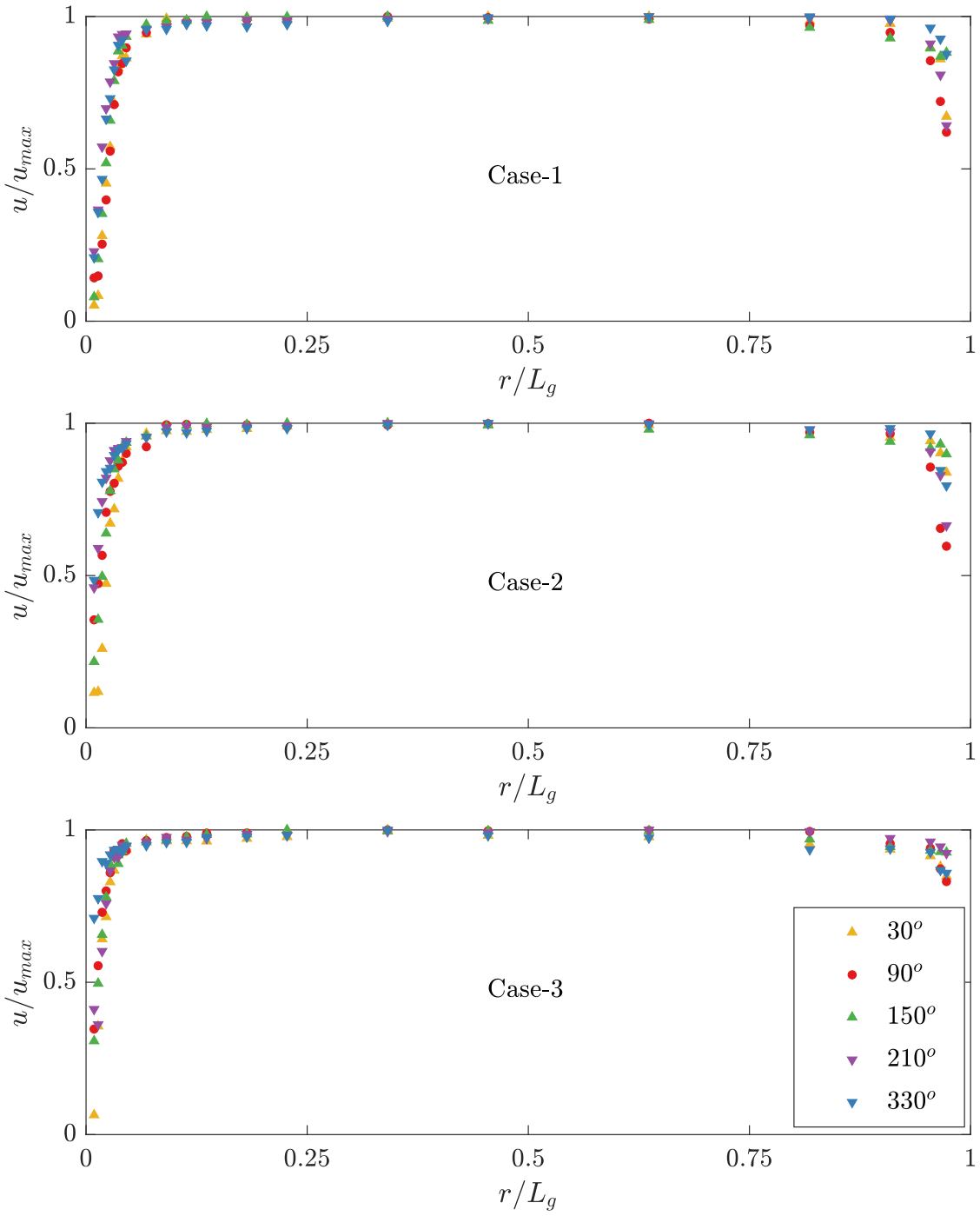

Figure 4.7: Velocity measurements at Section 0

are $\theta = 30°, 90°, 150°, 210°$ and $330°$ which cover the entire circumference. In all figures, every third measurement point were marked for better visualisation.

In Fig. 4.8, the temperature measurements for Case-1, where $Ri = 0.246$, are given. Section 1 exhibits a very similar temperature profiles at all circumferential

Table 4.3: Boundary layer characteristics at Section 0

Case	δ^* (mm)	θ (mm)	H
Case-1	8.87	5.81	1.53
Case-2	6.78	5.30	1.28
Case-3	4.25	3.55	1.19

locations, resulting in a uniform boundary layer around the heated inner cylinder with a weak buoyancy effect. As the flow progresses, a large increase in the boundary layer thickness is present at 90°, where the thermal plume departure from the heated wall occurs, in Section 2. Further downstream in Section 3, the boundary layer thickening at 90° further continues and reaches beyond the mid-gap location ($r/L_g = 0.5$). The boundary layer growth at each side at 150° and 210° can also be visually inspected, which are now distinguishable from the lower half of the annulus. Throughout the test section, 210° and 330° exhibits thin temperature boundary layers since the buoyancy force pushes the flow upward (up-against the wall) which inhibits the boundary layer growth as opposed to the upper half of the annulus.

In Case-2, the Richardson number is reduced to $Ri = 0.117$ by increasing the Reynolds number with almost identical Grashof number as Case-1. The temperature measurements for Case-2 are presented in Fig. 4.9. Radial temperature profiles at Section 1 are very similar to those in Case-1 with a thin boundary layer around the heated cylinder. The boundary layer thickens at 90° in Section 2 due to the buoyancy effect. However, these buoyant forces are not as pronounced as in Case-1 since the inertial forces are increased with the cross-flow. Comparing the measurements at each side ($150° - 210°$ and $30° - 330°$), it can be deduced that the buoyancy appears to have a very weak influence in these regions.

In Section 3, the boundary layer thickness continues to increase at 90°. Temperature profiles at $30° - 150°$ are not remarkably different from those at $210° - 330°$, indicating that the buoyancy effect remains to be suppressed. It is interesting to note that the temperature field at Section 3 of Case-3 reminds those at Section 2 of Case-2.

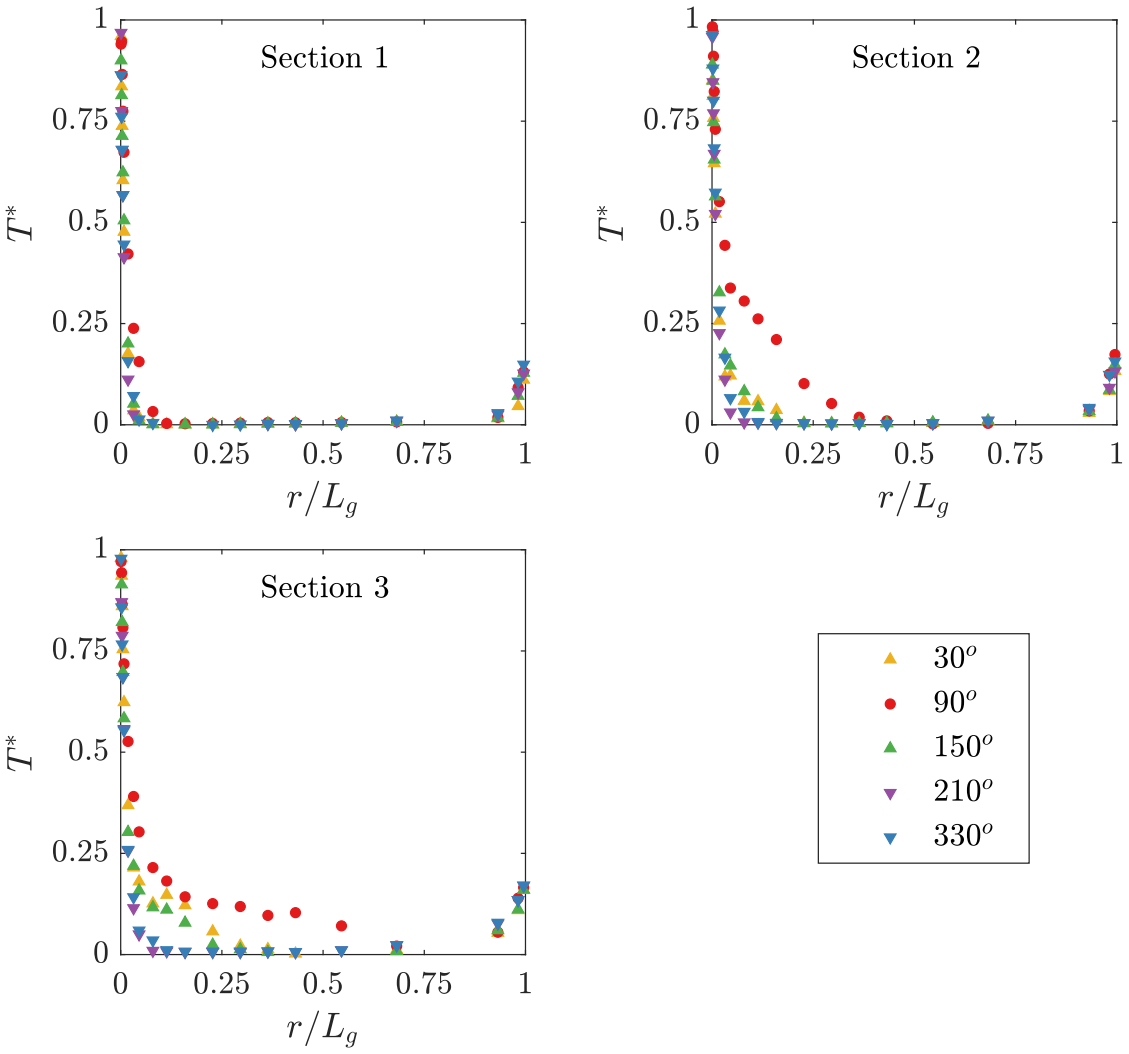

Figure 4.8: Radial temperature profiles in Case-1

In other words, a similar field to Section 2 of Case-2 could have achieved with Case if the test section was sufficiently longer to allow the boundary layer to further develop. This observation denotes that the boundary layer development is delayed with lower Richardson number in Case-2. Overall, $\theta = 90°$ appears to be the only region which the buoyant flows are strong enough to influence the flow field significantly.

The temperature measurements for Case-3 are given in Fig. 4.10. Case-3 represents the lowest Richardson number ($Ri = 0.032$) among the cases considered, which implies that stronger momentum of the fluid in the axial direction is expected in Case-3 with a very similar Grashof numbers to those in Case-1 and Case-2. At each individual section, almost identical temperature readings among the circumferential

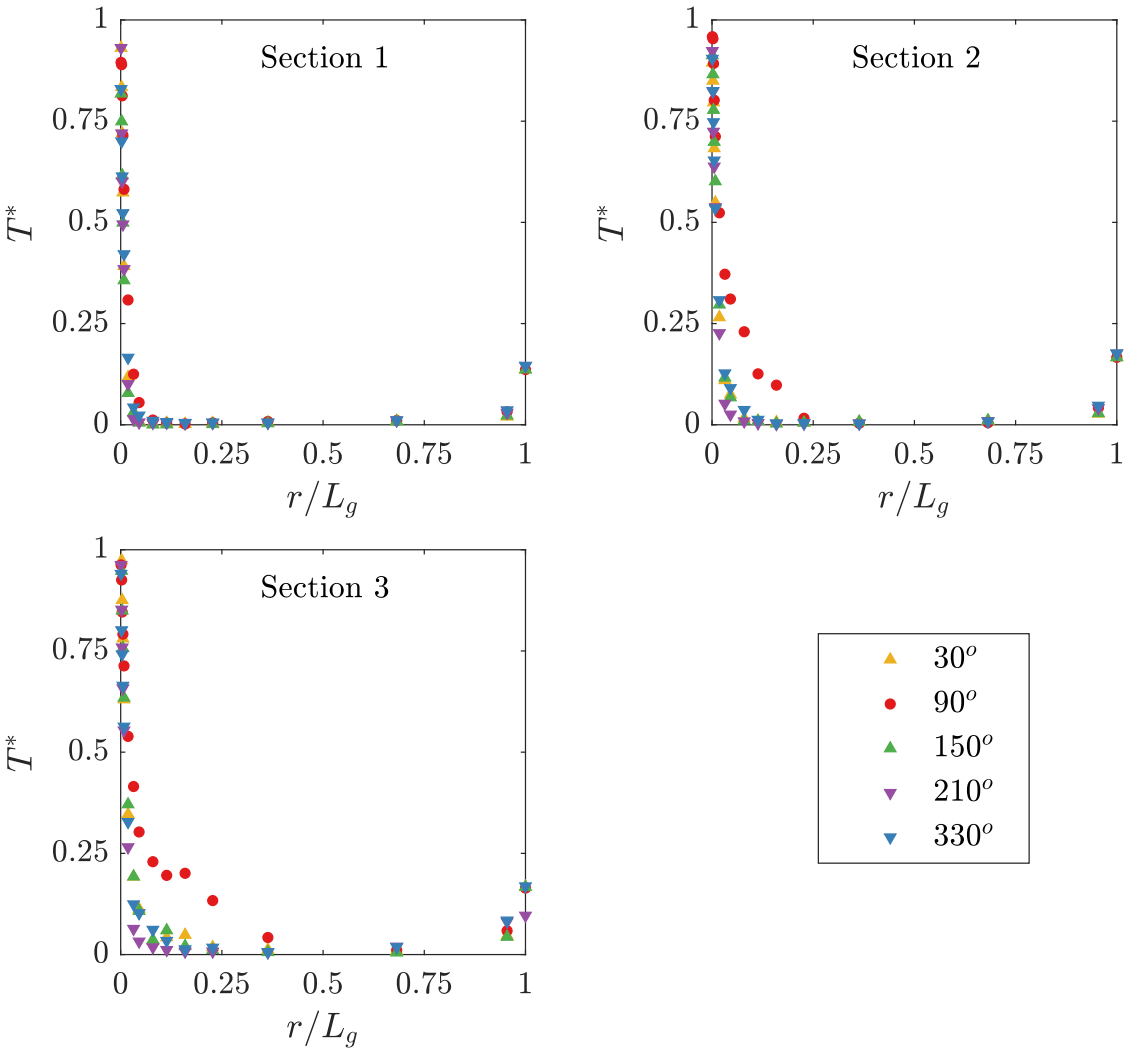

Figure 4.9: Radial temperature profiles in Case-2

measurement locations are seen. Although the boundary layer around the inner cylinder is slightly thickened as the flow progresses from Section 1 to Section 3, there is no sign of plume development at 90° which elucidates the dominance of forced convection. Hence, the buoyancy effect is suppressed with a sufficiently strong cross-flow, resulting in identical boundary layers in the entire circumference.

4.4.3 Heat Flux Calculations

As already discussed in Chapter 3, the local wall heat flux can be determined using the linear temperature gradient in the conductive viscous sub-layer [112]. Therefore, the term dT/dr in the Fourier's law [111], which effectively defines the

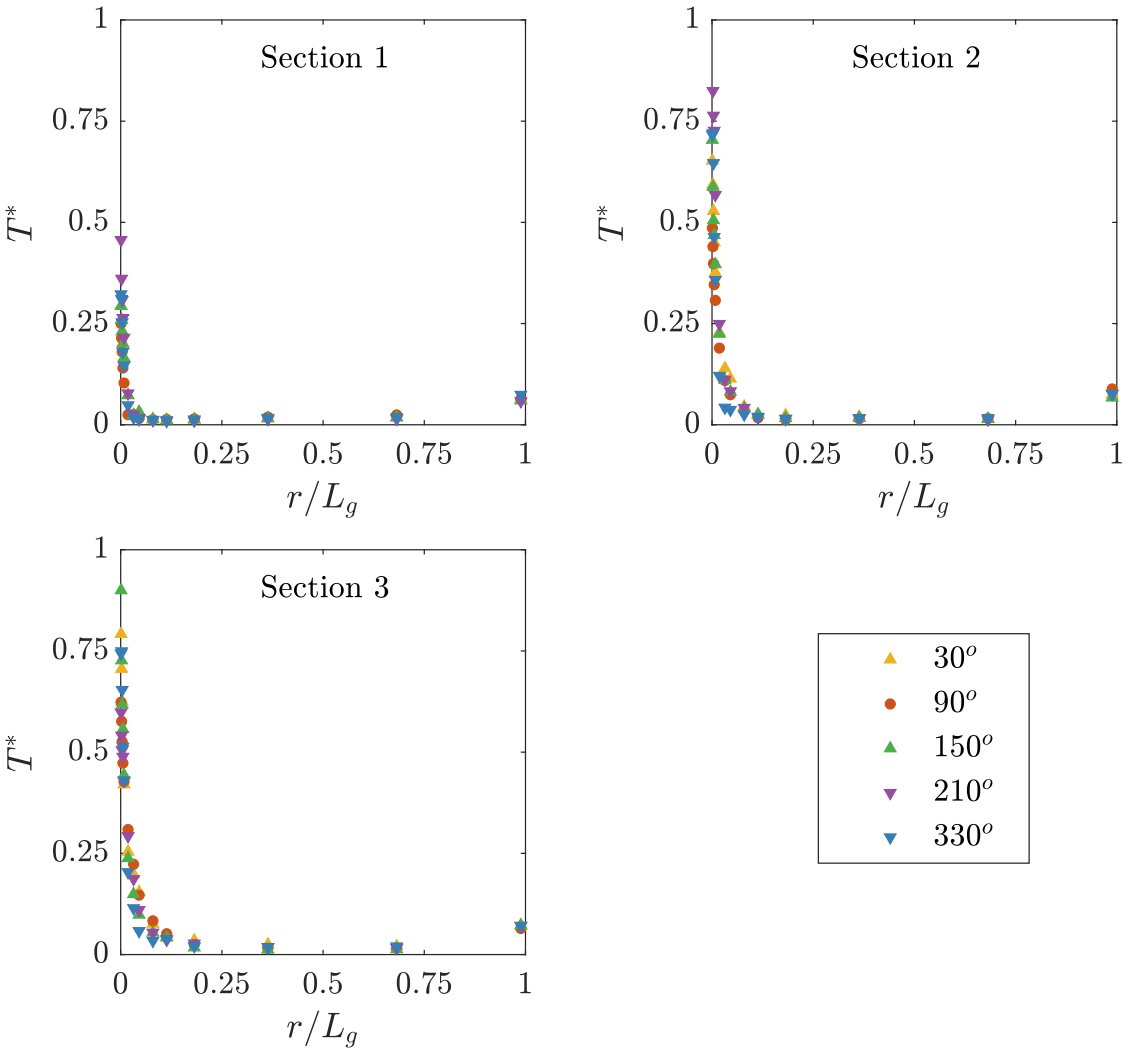

Figure 4.10: Radial temperature profiles in Case-3

rate of heat transfer, must be calculated. This is, however, not a straightforward step since the gradient may vary remarkably depending on the selection of traverse measurement points. A least-squares linear regressions analysis [119, 120] can be performed to decide the start and end traverse points which are then used to calculate the temperature gradient. In the regression analysis, R^2 coefficient is used to asses the goodness of the fit, which varies between 0 and 1 ($R^2 = 1$ indicates a perfect fit). Another parameter which should be taken into account is the thickness of viscous sub-layer, $y^+ \approx 5$. This is particularly important since beyond this point the dominance of viscous forces reduces, and Reynolds shear stress effect starts to be more pronounced.

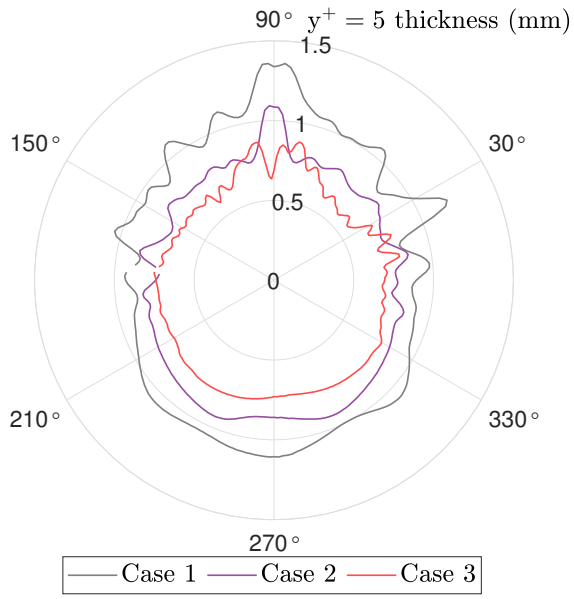

Figure 4.11: Viscous sub-layer thickness around the heated inner cylinder

The viscous sub-layer thickness decreases with increasing flow speed. In other words, the number of measurement points that can be fitted in the conductive layer decreases, which leads to a large uncertainty in the calculations. Figure 4.11 shows the viscous sub-layer thickness obtained from wall resolved LES around the heated inner cylinder in three cases. As expected, largest Reynolds number case, Case-3, yields the thinnest sub-layer thickness. Considering the thermocouple bead diameter, $D = 0.285$ mm, the closest traverse location to the wall (at $r = 0.2$ mm) was excluded from the measurements to avoid the wall proximity effect as the fluid between the thermocouple bead and the wall accelerates, which increases the convective heat transfer, therefore may lead to an inaccurate wall heat flux calculation. Therefore, temperature measurements were used only for Case-1 to calculate the wall heat flux since the viscous sub-layer was large enough to fit sufficient number of measurement points with high R^2 values.

In Fig. 4.12, the near wall temperature readings and R^2 values from the linear regression analyses are given for 30°, 90° and 330° which covers the right vertical half of the annulus. The points used in the wall heat flux calculations are highlighted. Fahy [113] performed the same linear regression analysis to calculate the wall heat flux in a pure natural convection case, and determined the measurement points

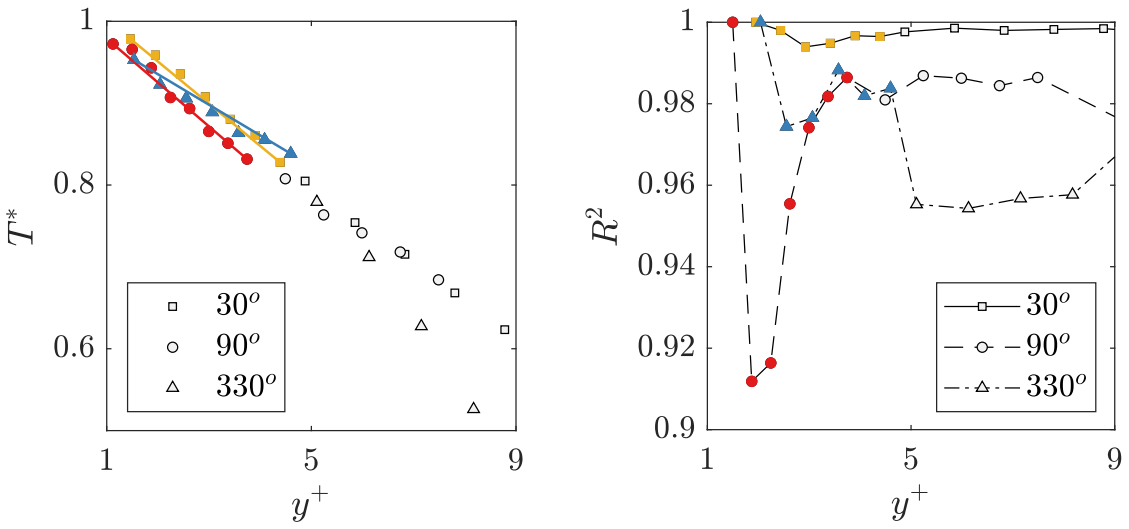

Figure 4.12: Near wall temperature profiles and R^2 values for increasing measurement points (Filled markers show the points used in linear fitting in the conductive sub-layer)

based on a location where R^2 indicated a significant drop. In the present study, the measurement point selection was determined based on $y^+ < 5$ and drop in R^2 value. The reduction in R^2 was clear at 330°, which appeared at $y^+ < 5$. Although R^2 values 30° and 90° continued to plateau beyond $y^+ = 5$, the end point selections were limited by $y^+ = 5$ to ensure that the selected points remained in the viscous sub-layer.

$$Nu = \frac{q'' D_i}{(T_i - T_\infty)k} \tag{4.2}$$

The heat transfer results are presented in Nusselt number which is calculated using Eq. 4.2. The associated bias errors for variable used in Nusselt number calculations are given in Table 4.4. Uncertainty analysis for Nusselt number calculation were performed using the root sum square method [121] as shown in Eq. 4.3. Uncertainty varied between different measurement points depending on the number of points used in the linear fittings. Overall, the uncertainty varied between 2 and 22% in the Nusselt number calculations.

$$B_{Nu} = \sum_n \sqrt{\left(\frac{\partial Nu_{D_i}}{\partial V_n}\right)^2 {B_{V_n}}^2} \tag{4.3}$$

The Nusselt number distribution around the heated inner cylinder at different sections in Case-1 is given in Fig. 4.13. At Section 1, the lower half (at 210°

Table 4.4: Uncertainty of each variable

Variable	Uncertainty	Variable	Uncertainty
Traverse Thermocouple	±0.5 K	Heated Cylinder Diameter	±1 mm
PID Thermocouple	±0.5 K	Traverse	±0.05 mm

and 330°) exhibited enhanced heat transfer compared to the upper half, which is attributed to the thinner temperature boundary layer at the lower half due to the buoyant flows. Progressive heat transfer increase from Section 1 to Section 3 is seen at each upper side at 30° and 150°. It is also interesting to note that there is a remarkable heat transfer escalation at the top at 90° as opposed to pure natural convection cases [25, 26, 113] where the top exhibits a much lower heat transfer rates than the bottom due to the thermal plume causing a smaller gradient at the top. These heat transfer characteristics will be discussed in Chapter 5 in greater details with complementary scale resolving simulations.

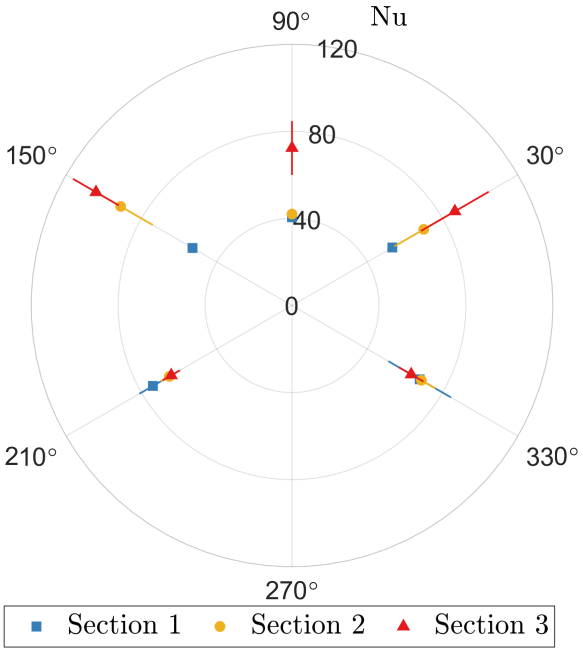

Figure 4.13: Nusselt number distribution around the heated inner cylinder in Case-1 (Solid lines represent the error bars)

4.5 Conclusions

Various mixed convection types of flow regimes have been highlighted and compared against conventional flow fields with pure natural and pure forced convection. An experimental campaign, a total number of 7 experimental tests, has been performed, which covers a wide range of Richardson numbers. 3 cases have been identified, which would be representative of 3 different flow regimes, Case-1 for natural convection dominant, Case-2 for equally balanced, Case-3 for forced convection dominant mixed type of flows. Details of each case have been shown, and radiation corrections have been conducted for all cases. Velocity measurements taken at the upstream of the test section, which further validated the adequate inlet contraction, have been presented.

The temperature measurements have been compared at three sections in the test section to track the boundary layer development in each test case. With decreasing Richardson numbers, the effect of buoyant forces have become progressively less pronounced, leading to a uniform temperature boundary layer at a given circumference. Additionally, the wall heat flux measurements have been performed for Case-1.

The key importance of this chapter is that these results have been presented for the first time in the literature. Therefore, they will contribute to the improved understanding of mixed type of flows, and will act as validation test cases for numerical predictions and enable advanced turbulence model developments.

Chapter 5

Large Eddy Simulations

5.1 Introduction

The first application of large eddy simulation (LES) methodology, which dates back to 1963, belongs to Smagorinsky [122] who employed LES to investigate atmospheric flows. Since then, LES has been used for both fundamental and engineering flows. With recent advancements and increased availability of high performance computing servers, LES has gained further popularity among engineering community to solve complex flow problems for which direct numerical simulations (DNS) are computationally not affordable. Conventional turbulence models with Reynolds-Averaged Navier-Stokes (RANS) often fails in predicting unsteady complex flow interactions accurately. Hence, LES is a preferred methodology over RANS and DNS to allow resolving of turbulent structures with an unsteady manner at a reasonable computational cost [123].

Experimental campaigns presented in Chapter 4 help one to gain an overall idea of the flow field. However, much more detailed information is required to gain deeper understanding of the flow physics. Therefore, wall resolved large eddy simulations were performed for each experimental campaign for further investigations with temperature, wall shear stress contours and iso-surfaces which were not possible to obtain from the experimental campaigns. The detailed results will be presented in this chapter for the selected cases, namely Case-1, Case-2 and Case-3. The remaining results will be given along with experimental comparisons in Appendix A.

5.2 Methodology

Wall resolved lage eddy simulations for all experimental campaigns were performed with ANSYS Fluent 2020 R1 [52]. The semi-implicit method for pressure linked equations (SIMPLE) algorithm was used for pressure-velocity coupling in a segregated manner. For spatial discretisation, second-order scheme was used for pressure, while bounded central differencing scheme was employed for momentum and energy equations. Bounded second-order implicit scheme was chosen for the temporal discretisation. Dynamic Smagorinsky model [124] was used for subgrid scale modelling.

The computational domain used in the simulations is illustrated in Fig. 5.1. As seen in the figure, CFD domain involves an additional region at the upstream of the bellmouth, referred as *entrance region*, to allow boundary layer development over the bellmouth. This region was included to simulate the experiments with exactly the same physical conditions.

The velocity profiles obtained from the hot-wire probe measurements at Section 0 in Chapter 4 were used to calculate the mass flow rates for each case. The mass flow rates which were used as outlet boundary conditions are $\dot{m}_1 = 0.46$ kg/s, $\dot{m}_2 = 0.67$ kg/s and $\dot{m}_3 = 1.31$ kg/s for Case-1, Case-2 and Case-3, respectively. At the inlet boundaries, ambient conditions were applied, which read as $T_{\infty,1}$=295.65 K, $T_{\infty,2}$=296.35 K and $T_{\infty,3}$=294.65 K. The fluid (air) was assumed to be incompressible ideal gas, and the fluid properties that were calculated using the ambient conditions which are tabulated in Table 5.1. The Boussinesq approximation was used to account for density changes due to local temperature variation. In the test section (Section 1, 2 and 3), inner and outer walls were treated as isothermal walls, the details of which are already given in Table 4.2 in Chapter 4 whereas adiabatic boundary condition was applied to the remaining walls in the domain.

Structured hexahedral type mesh was used for the LES. The close-up view of mesh can be seen in Fig. 8.10 where the entrance region is excluded for visual clarity. The total number of mesh nodes are 2.96 $\times 10^7$ in Case-1 and Case-2, and 2.53 $\times 10^7$ for Case-3. For wall resolved LES (no wall function was employed), the

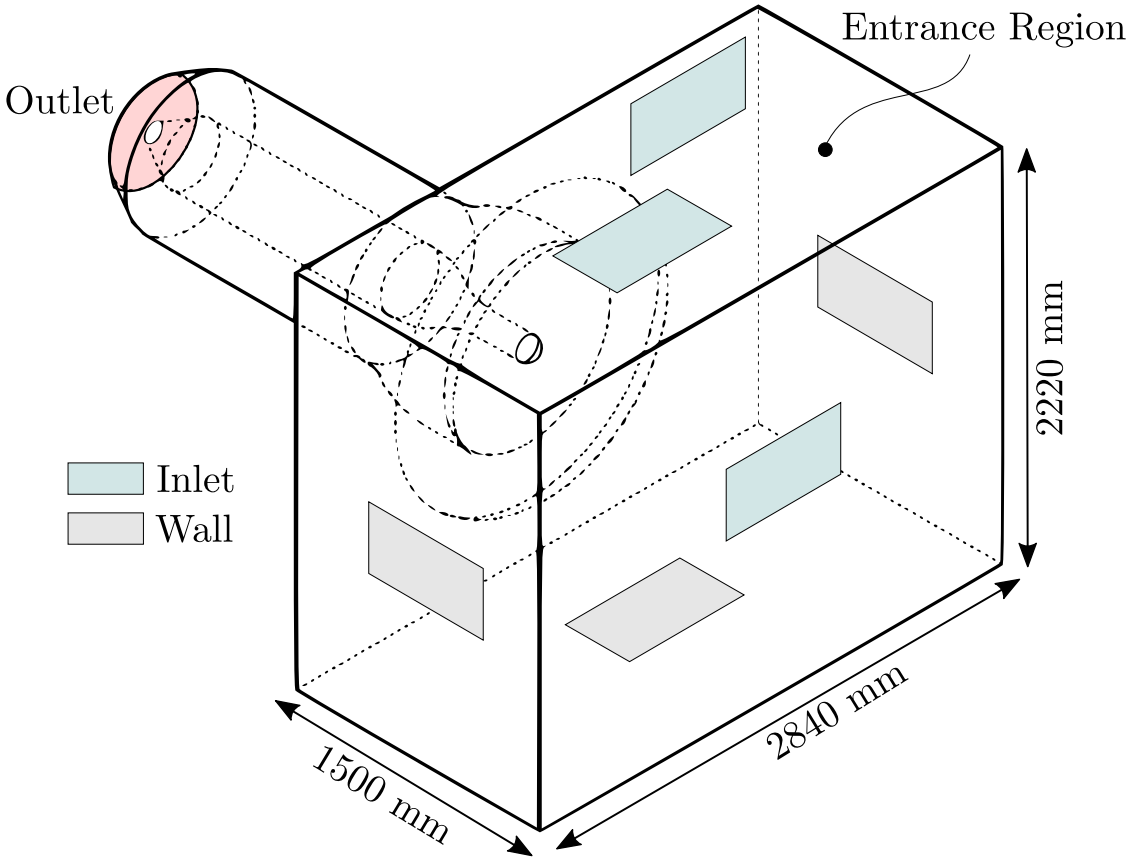

Figure 5.1: Computational domain

Table 5.1: Fluid properties

Case	k (W/mK)	C_p (J/kgK)	μ (kg/ms)	Pr	β (1/K)
Case-1	0.02587	1006.91	1.84×10^{-5}	0.7144	3.39×10^{-3}
Case-2	0.02592	1006.93	1.84×10^{-5}	0.7143	3.39×10^{-3}
Case-3	0.02579	1006.84	1.83×10^{-5}	0.7146	3.41×10^{-3}

mesh nodes were clustered towards the inner and outer walls to maintain $r^+ \ll 1$. The detailed information on grid resolutions in each case is tabulated in Table 5.1. The grid resolutions can be examined by the ratio of cell size, $\Delta = \sqrt[3]{Cell\ Volume}$, to Kolmogorov length scale, $\eta = (\nu^3/\epsilon)^{0.25}$. The ratio, Δ/η remained below 8, 7 and 6 in Case-1, Case-2 and Case-3, respectively, which indicates the adequacy of the grid resolution [7, 49].

Kolmogorov times scales, $t_\eta = (\nu/\epsilon)^{0.5}$, were calculated as $t_{\eta,1} = 6.1 \times 10^{-3}$ s,

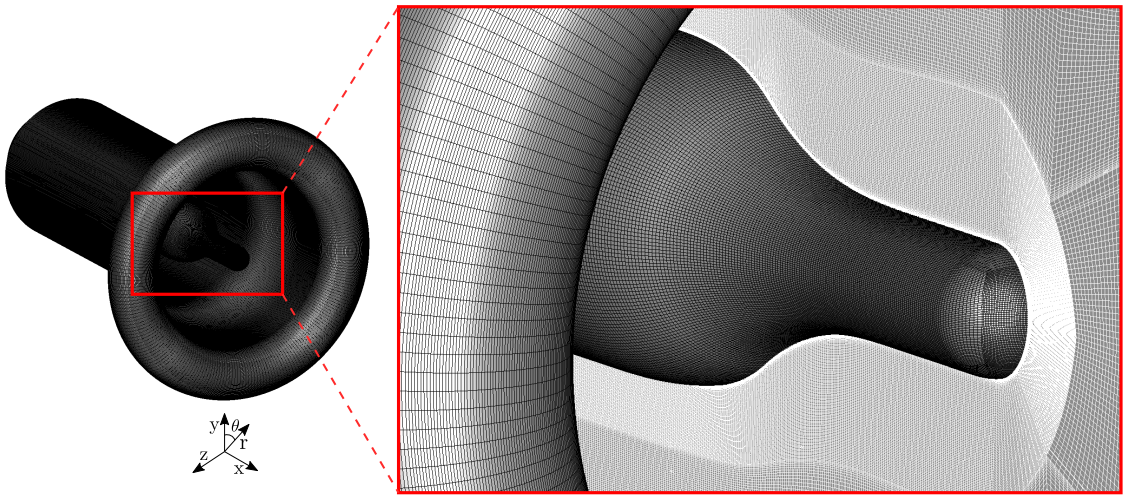

Figure 5.2: Computational mesh for LES

$t_{\eta,2} = 3.7 \times 10^{-3}$ s and $t_{\eta,3} = 1.4 \times 10^{-3}$ s. Considering the Courant-Fruedrichs-Lewy (CFL) condition based on the grid resolution, and the Kolmogorov time scales, conservative time steps of $\Delta t_1 = 2 \times 10^{-3}$ s, $\Delta t_2 = 1.5 \times 10^{-3}$ s and $\Delta t_3 = 5 \times 10^{-4}$ s were chosen for Case-1, Case-2 and Case-3, respectively.

Table 5.2: Grid resolutions

				$0 < r/L_g < 0.33$		$0.33 < r/L_g < 0.66$		$0.66 < r/L_g < 1$	
				Δr^+		Δr^+		Δr^+	
Case	Δx^+	$R_i\Delta\theta^+$	$R_o\Delta\theta^+$	Min	Max	Min	Max	Min	Max
Case-1	17.07	18.22	40.51	0.29	3.45	3.45	7.58	1.16	9.52
Case-2	19.58	20.91	46.47	0.33	3.95	3.95	8.71	1.33	10.92
Case-3	23.53	25.02	55.61	0.31	4.18	4.18	30.4	1.24	24.3

It is crucial that unsteady simulations are run sufficiently long for well-established convergence and time-averaged quantities. In the presented simulations, a number of instantaneous flow variables across the domain were monitored to check the convergence. Figure 5.3 shows a history of instantaneous and time averaged energy imbalance normalised by the sum of heat transfer from the heated inner cylinder and the enthalpy from upstream of the test section in Case-1. The simulation was first

run for 4000 time steps (9 through-flow in the test section) to let the initial transients decay. The unsteady data was then sampled over 12000 time steps. For Case-2 and Case-3, the statistics were collected for 11500 and 8000 time steps, respectively.

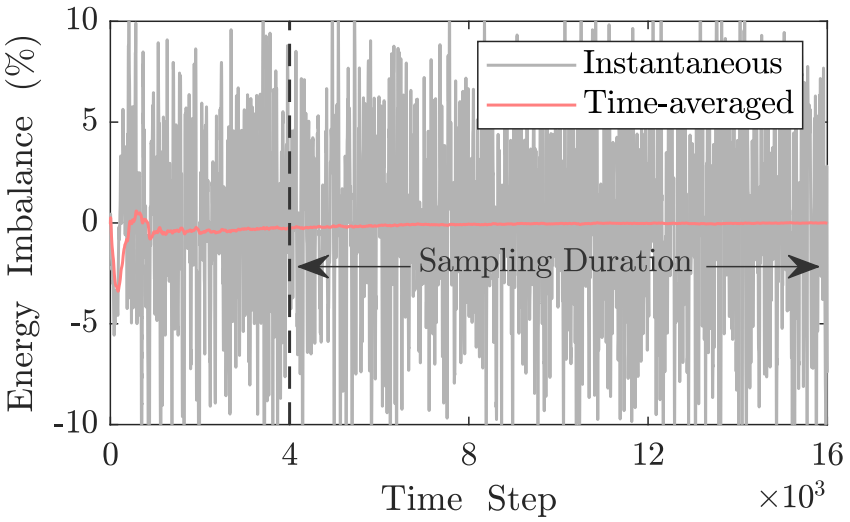

Figure 5.3: History of time-averaged energy imbalance in Case-1

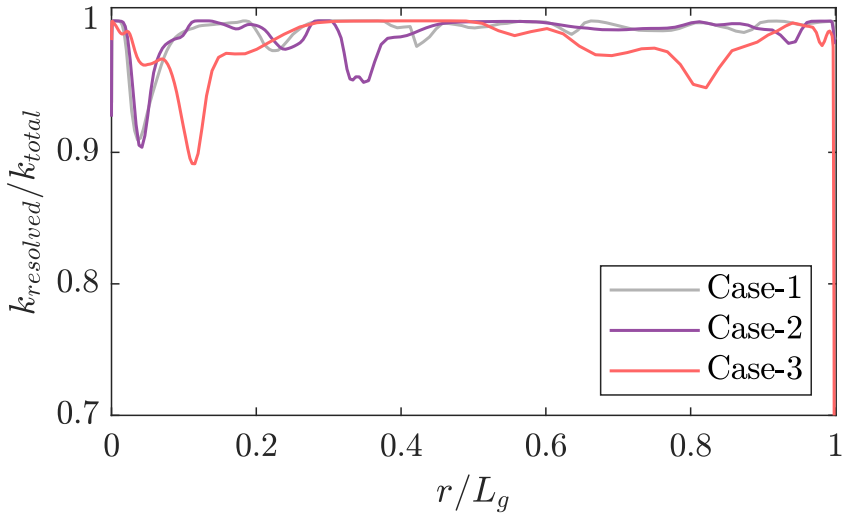

Figure 5.4: Resolved turbulent kinetic energy at 90° at Section 3

In Fig. 5.4, the amount of resolved turbulent kinetic energy, $k_{resolved}/k_{total}$, at 90° at Section 3 is given for each case. It can be deduced that sufficient amount of turbulent kinetic energy was resolved in each case with more than average of

95%. Figure 5.5 shows the energy spectra of the streamwise velocity fluctuations recorded at $r/L_g = 0.9\%$ at Section 3. As seen from the figure, the simulation data for each case agrees well with the Kolmogorov's -/3 slope in the inertial sub-range. These observations further improve the validity of the simulations.

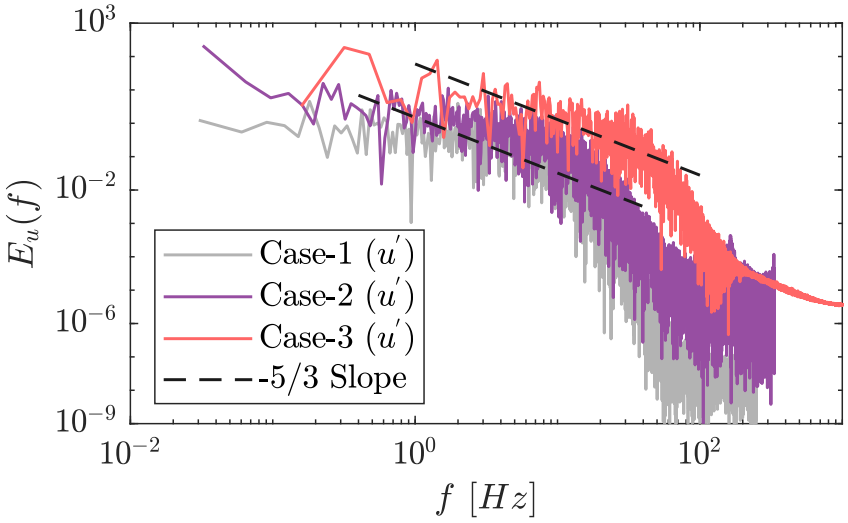

Figure 5.5: Energy cascade at $r/L_g = 0.9\%$ at Section 3

5.3 Velocity Profiles

Non-dimensionalised LES velocity profiles at circumferential measurement locations at the upstream of test section, Section 0, are given in Fig. 5.6 where the corresponding experimental velocity measurements are also plotted with markers.

LES velocity predictions agree well with the experimental data in all cases, confirming the circumferentially uniform boundary layer. The accurately predicted upstream profiles further increase the confidence in the numerical methodology. Additionally, these good agreements between experimental and numerical results suggest that the experimentally measured velocity profiles could be used as inlet boundary condition at Section 0, which would lead to reduction in total number of grid nodes in simulations with the exclusion of entrance region, therefore would require less computational resources.

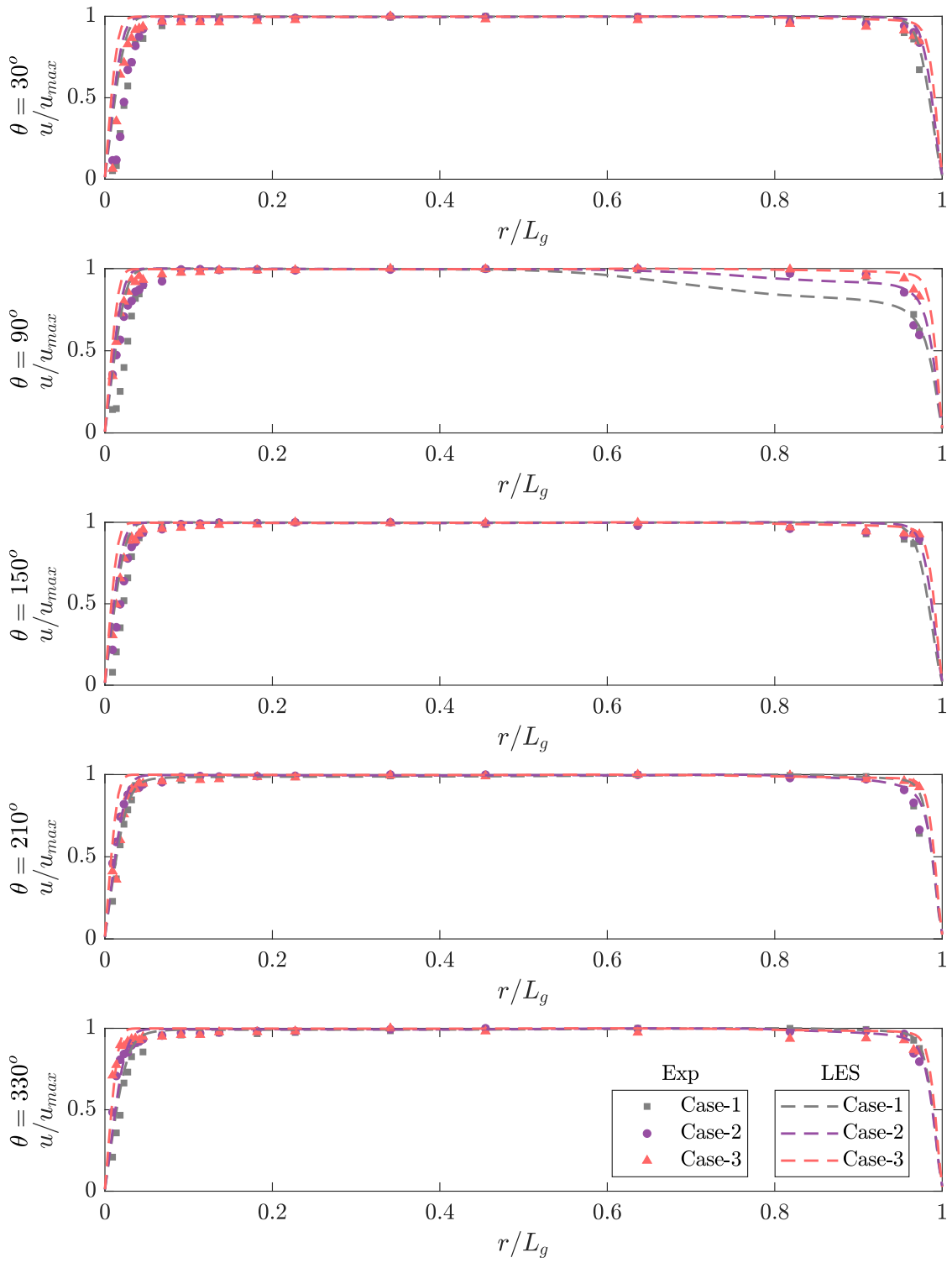

Figure 5.6: Experimental and LES velocity profiles at Section 0

5.4 Temperature Profiles

The temperature profiles are presented in a non-dimensional form given in Eq. 5.1. Comparisons of experimental and LES temperature profiles are given in Fig. 5.7, Fig. 5.9 and Fig. 5.11 for Case-1, Case-2 and Case-3, respectively.

$$T^* = \frac{\overline{T} - T_\infty}{T_i - T_\infty} \tag{5.1}$$

In order to visualise the flow fields at measurement locations in each case, temperature contours from LES are presented in Fig. 5.8, Fig. 5.10 and Fig. 5.12 for Case-1, Case-2 and Case-3, respectively.

Case-1 exhibits a thin uniform boundary layer around the heated inner cylinder in Section 1, which is accurately captured by LES as seen in Fig. 5.7. In Section 2, the boundary layer thickness is remarkably increased at the top of the cylinder (90°) where the flow is lifted up by the buoyancy forces, which can also be seen in Fig. 5.8. Although it is not quantitatively distinguishable in Fig. 5.7, the boundary layer growth at each side at 30° and 150° are seen in the temperature contours. Despite some overpredictions at the the thermal plume region, LES results overall agree well with the experimental data. As the flow progresses, the thermal plume further develops at 90°, creating a large boundary layer as also seen in the temperature contour in Fig. 5.8. The buoyancy effect is also present at 30° and 150° with thicker boundary layers compared to those at Section 1 and 2. Throughout the test section, the lower half of the annulus at 210° and 330° remains to be much thinner than the upper half. Both qualitative and quantitative temperature results do not reveal regarding the near-wall temperature gradients in the lower half. More can be inferred from the heat flux observations which will be discussed in the following section. The agreement between experiment and LES is excellent in the lower half.

LES results in Case-2 is compared against the experimental data in Fig. 5.9, and the temperature contours are presented in Fig. 5.10. Similar to Case-1, the boundary layer appears to be uniform around the heated inner cylinder in Section

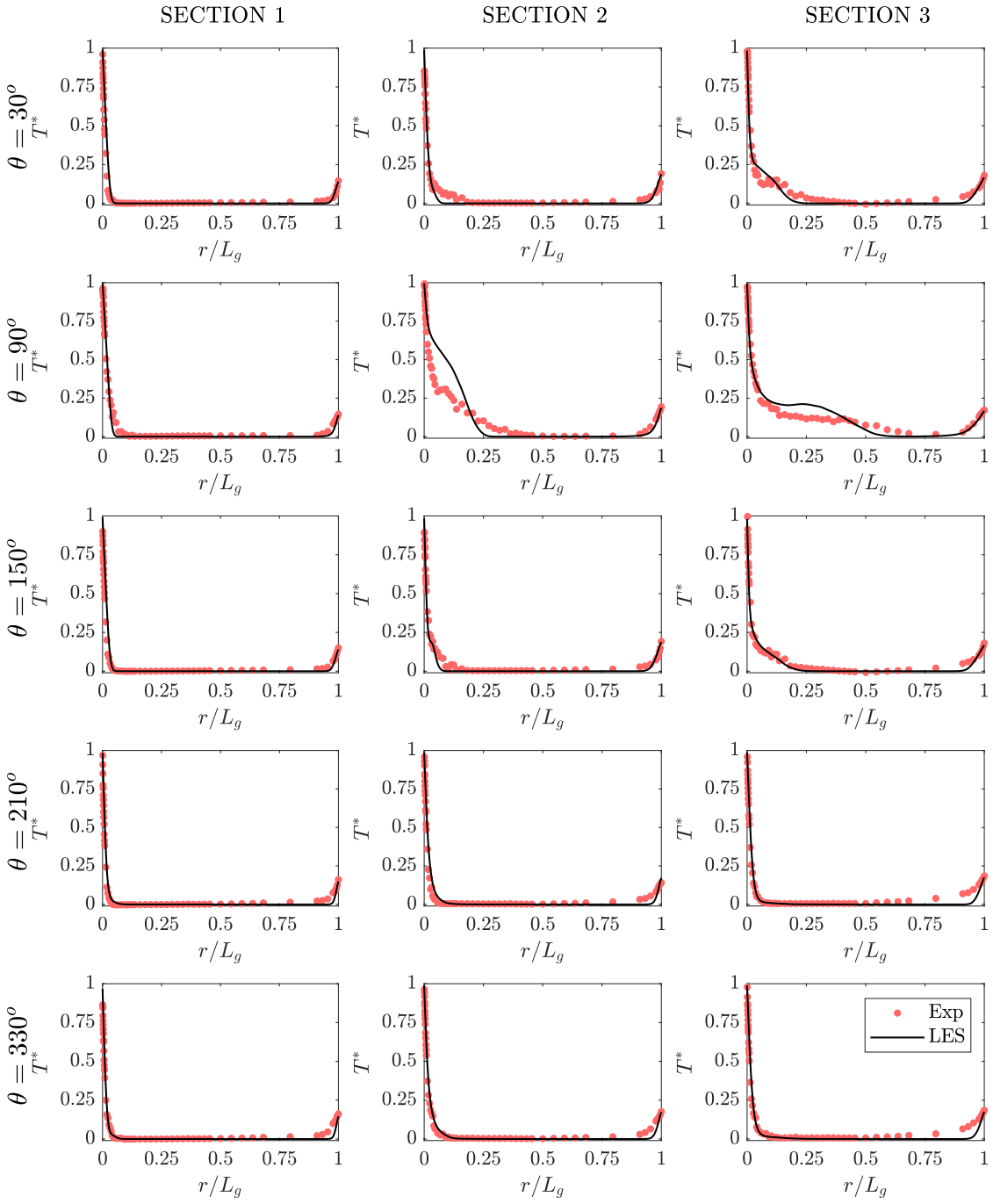

Figure 5.7: Experimental and LES temperature profiles in Case-1

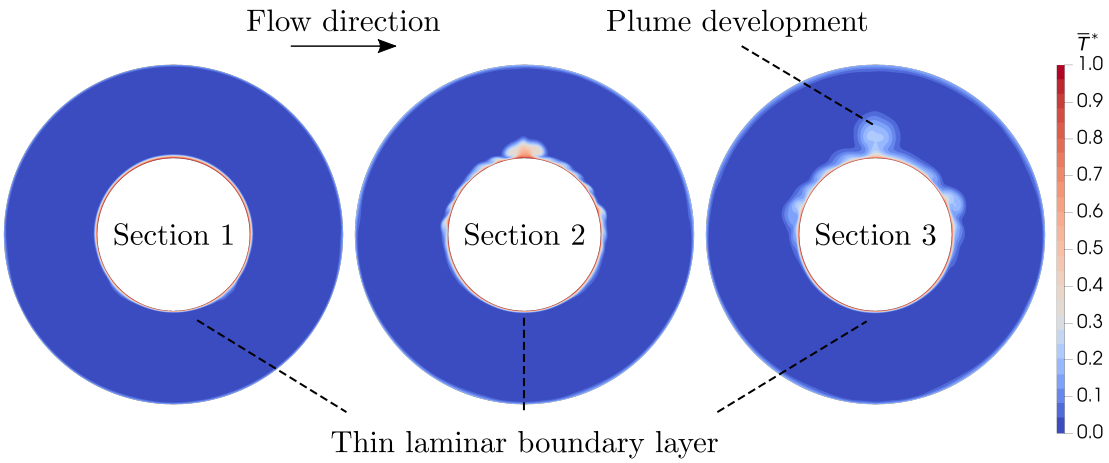

Figure 5.8: Temperature contours in measurement sections in Case-1

1, which is accurately predicted by LES. Thickening of the boundary layer at 90° in Section 2 is not as pronounced as that in Case-1, but is still distinguishable from the remaining circumference. Laminar flow region in the lower annulus in Section 2 is present, and captured accurately by LES. Further downstream at Section 3, the boundary layer continues to develop at the top of the heated inner cylinder, for which LES agrees well with the experimental data. However, the thermal plume is not developed distinctively. In fact, this region resembles Section 2 in Case-1 (as already highlighted in Chapter 4 with the experimental). The similarity in flow fields between Section 2 Case-1 and Section 3 Case-2 is much clear in the temperature contours in Fig. 5.8 and Fig. 5.10. Considering that the Grashof numbers are almost identical in Case-1 and Case-2, it can be deduced that the increased Reynolds number caused a delay in the thermal boundary layer development in Case-2. In the lower half of the annulus, the temperature field in Case-2 looks visually almost identical to Case-1, indicating that increasing Reynolds number does not impose significant changes in the flow field. With all these flow field features, Case-2 represents an instance where both buoyant and inertial force effects co-exist in a balanced manner.

Case-3 adopts the highest Reynolds number, therefore the lowest Richardson number. The cross-flow speed was deliberately increased to a degree where a thermal plume does not form at the top of the heated inner cylinder. As expected, Section

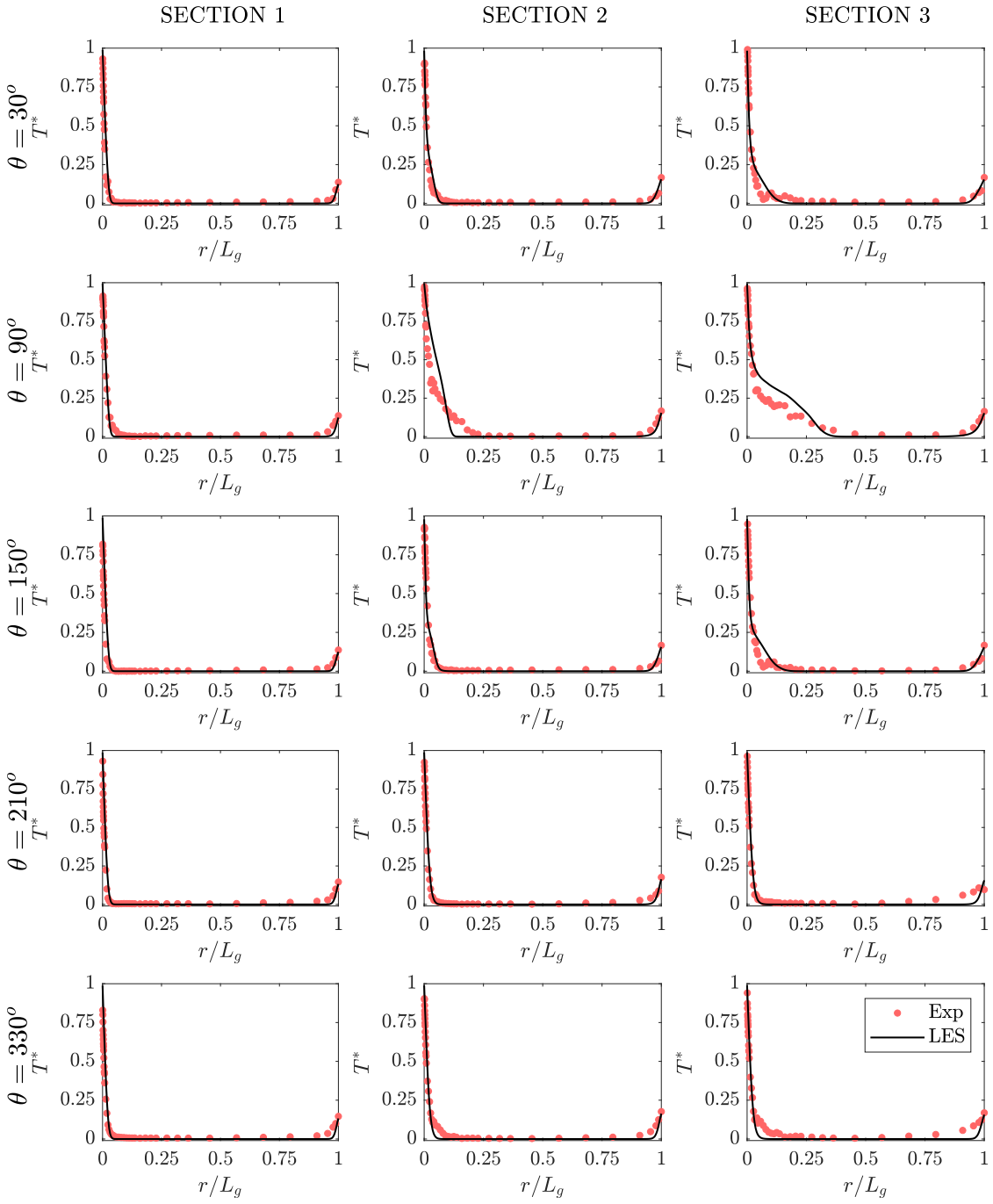

Figure 5.9: Experimental and LES temperature profiles in Case-2

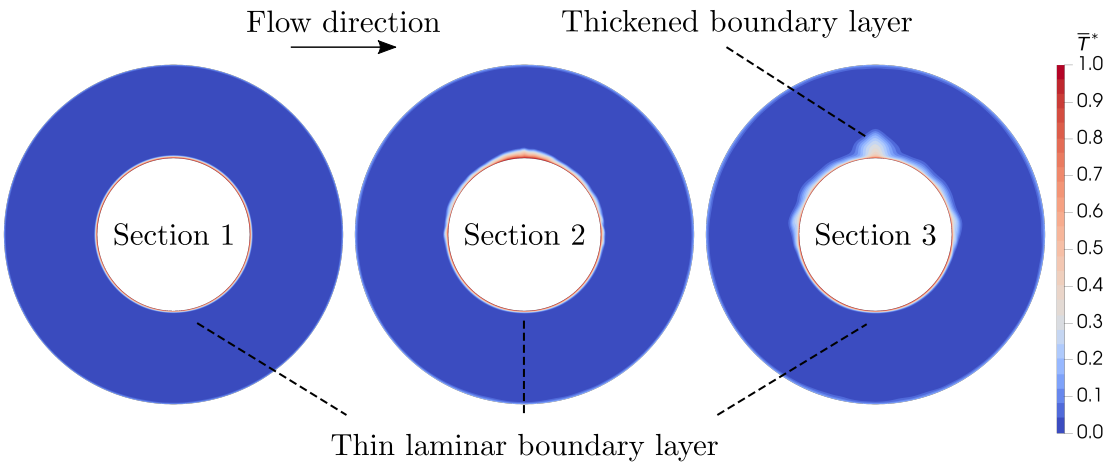

Figure 5.10: Temperature contours in measurement sections in Case-2

1 still presents a uniform temperature boundary layer around the inner cylinder. As opposed to Case-1 and Case-2, there is now no clear sign of buoyant field in Section 2 as seen in both Fig. 5.11 and 5.12. The upward flow distortion due to the buoyancy disappears with the presence of strong inertial force. The dominance of forced convection continues to be present in Section 3 as the results does suggest any considerable change in the boundary layer thickness. The lower half of the annulus presents a very similar temperature profile to those in Case-1 and Case-2 with a thin boundary layer. Quantitative results show that thin boundary layers in Case-3 are well predicted by the scale resolving simulation.

Comparing the temperature contours of each case, it is evident that the progressive escalation in inertial forces that are perpendicular to the gravitational field results in distinct flow regimes in the upper half of the annulus along the test section. Some regions resemble a pure natural convection with a rising thermal plume at the top [16, 25], whereas some regions demonstrate pure forced convective flow features with uniform boundary layer around the inner cylinder. All these various flow fields are accurately captured with wall resolved large eddy simulations.

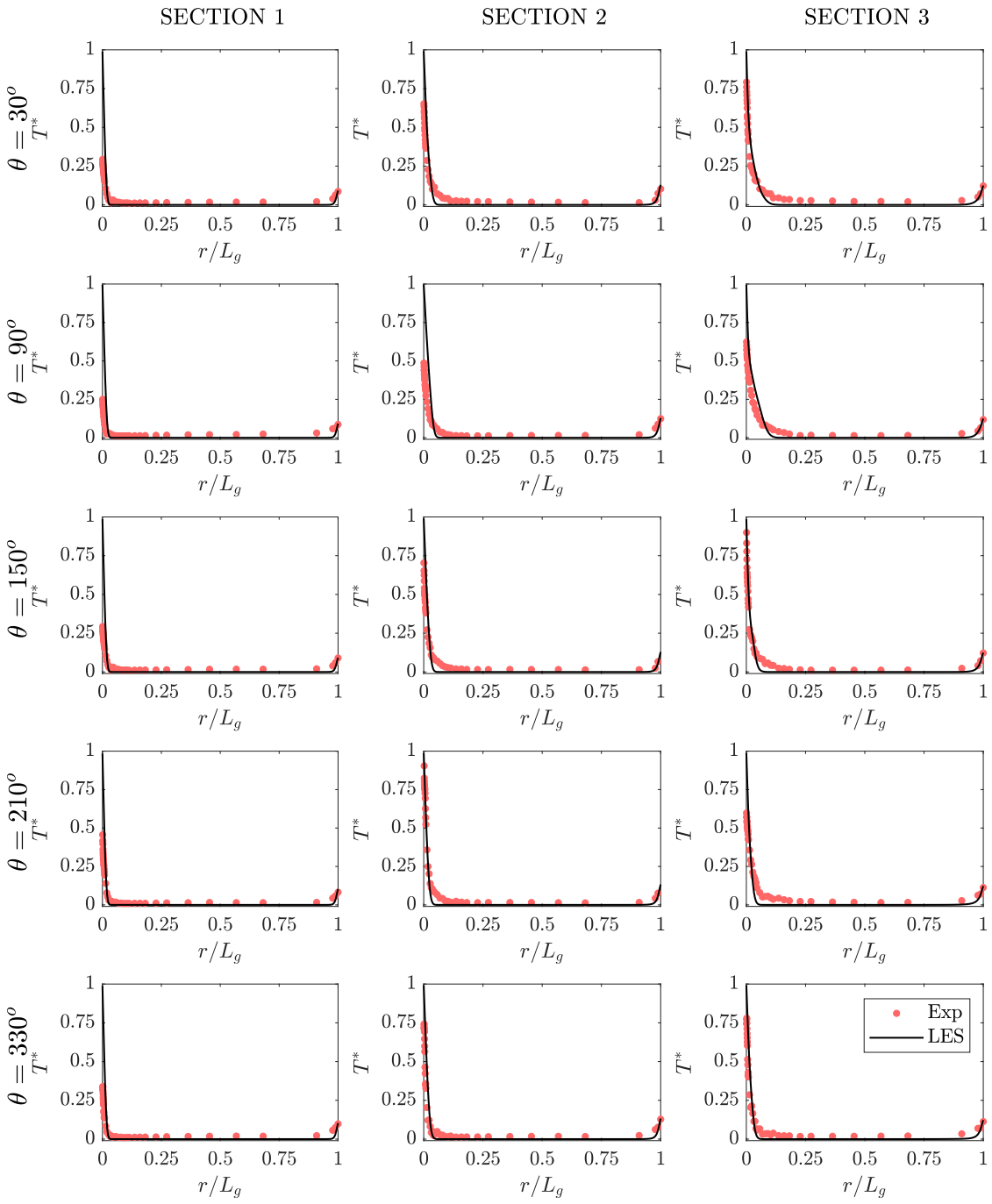

Figure 5.11: Experimental and LES temperature profiles in Case-3

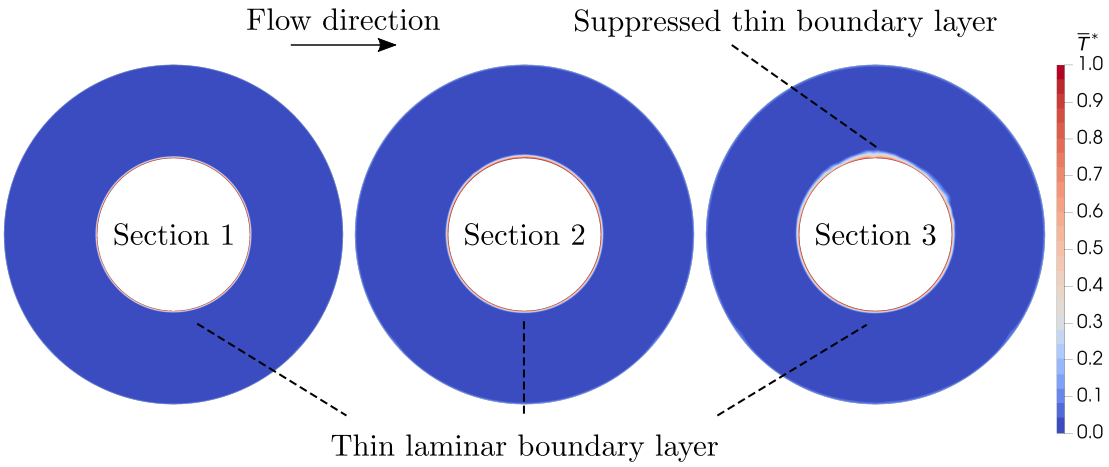

Figure 5.12: Temperature contours in measurement sections in Case-3

5.5 Flow Structures

Internal flows in straight circular and rectangular channels demonstrate a stable behaviour with a pack of moving layers when Reynolds number is sufficiently low. This well ordered fluid movement is known as laminar flow [54]. With higher Reynolds numbers, strong mixing (turbulent flow) arises from the momentum transfer among the fluid particles which was visualised by Osborne Reynolds in his pioneering work on fluid motion in pipe flows [125]. Besides the internal flow itself, the boundary layer on a body immersed in a moving fluid can also be classified as laminar or turbulent. The transition from laminar to turbulent flow (referred as laminar-turbulent transition or onset of turbulence) takes place if the characteristic length (i.e., length of a flat plate) sufficiently long since the Reynolds number is proportional to the characteristic length. Additionally, surface topography, a tripped boundary layer, high turbulence intensity in the incoming bulk flow can lead to early transition. Over a flat plate, the transition mechanism is initiated by a two dimensional boundary layer instabilities known as Tollmien-Schlichting (T-S) waves. These instabilities then form into three dimensional vortices which are followed by turbulent spots, and then fully turbulent flow [54, 126]. For a flow over a heated surface, buoyancy forces may trigger the transition with counter-rotating pairs of vortices [127] which form elongated stream-wise vortices [128].

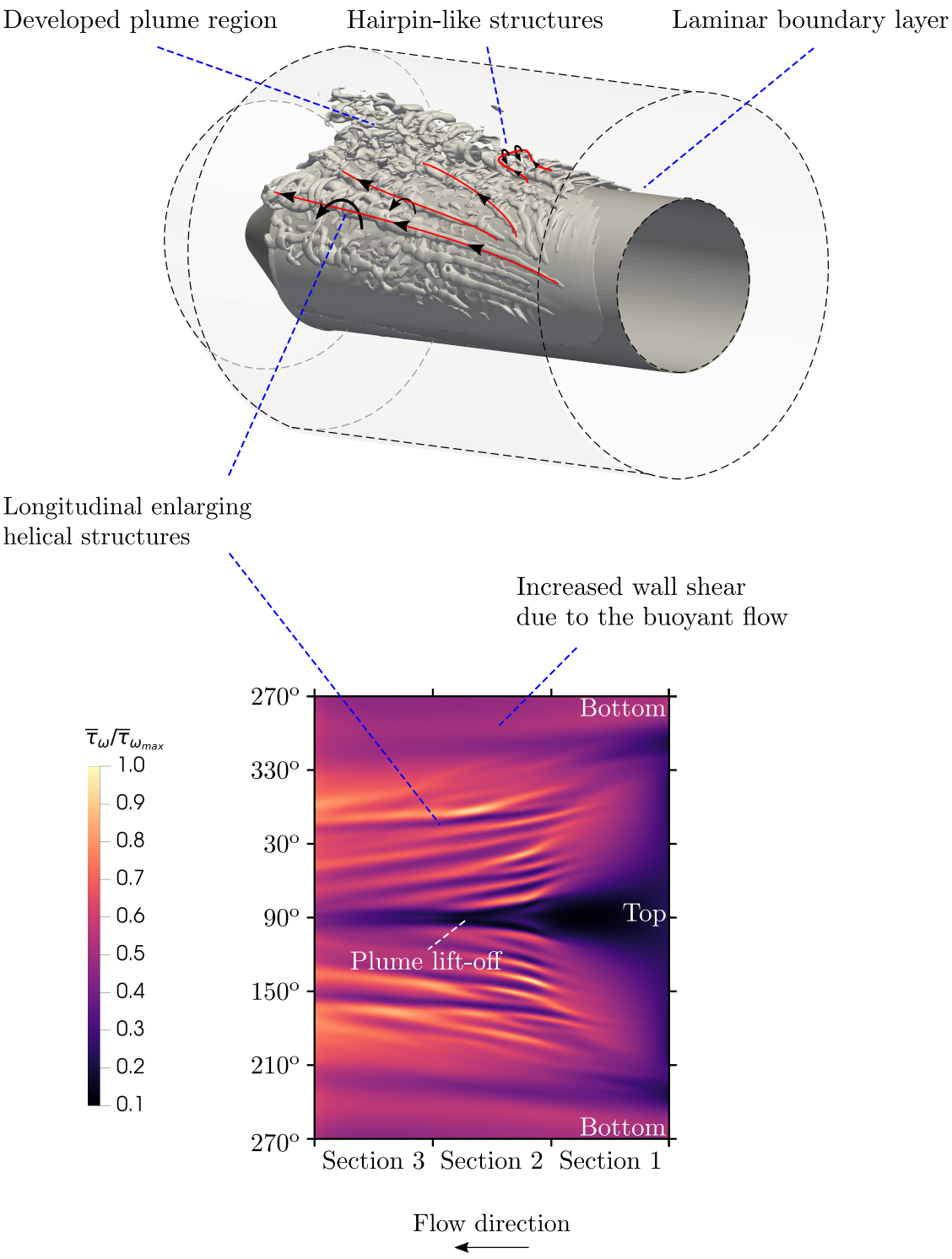

Figure 5.13: Flow structures and their footprints in Case-1

For a mixed type of convection flow, buoyancy forces that are perpendicular to streamwise flow may present various flow structures simultaneously depending on the operating conditions which may act as a triggering mechanism for early transition to turbulence. These flow structures can be visualised by iso-surfaces. In the present study, the iso-surfaces are created by second invariant of velocity calculated by vorticity and strain-rate magnitude, $Q = 0.5(\omega^2 - S^2)$.

The iso-surfaces, which were created with $Q = 200$, are shown in Fig. 5.13, 5.14 and 5.15 for Case-1, Case-2 and Case-3, respectively. Along with the iso-surfaces, the time-averaged wall shear stress contours for each case are also presented in the figures to be able to track the footprints of the structures on the heated inner cylinder. The wall shear stress contours are shown on unwrapped inner cylinder surfaces for better visualisation. The surfaces were unwrapped along the streamwise direction at the bottom at 270°.

Case-1 which represents the highest Richardson number in the cases considered in the present study exhibits a laminar boundary layer at the beginning of test section where the buoyancy forces are not strongly pronounced in the upper half. As the flow progresses, near-wall vortices create vortex legs [129] where the shear is increased. These vortices then form the legs of hairpin-like structures which immediately lift-up, and freshly formed fluid layer ejects through the hairpin legs. These structures cause early transition to turbulence. Once the hairpin vortices lift-up, they create ring shape structures which then break up upon interacting with the outer flow [130]. The lift-up of the coherent structures due to the buoyancy forces is responsible for the thermal plume departure from the inner heated cylinder as seen in the decreased wall shear stress at the top at 90°. At each side of the heated cylinder between $0° - 70°$ and $110° - 180°$, some of the low momentum fluid lifts-off due to the buoyancy and is stretched towards the downstream by the cross-flow.

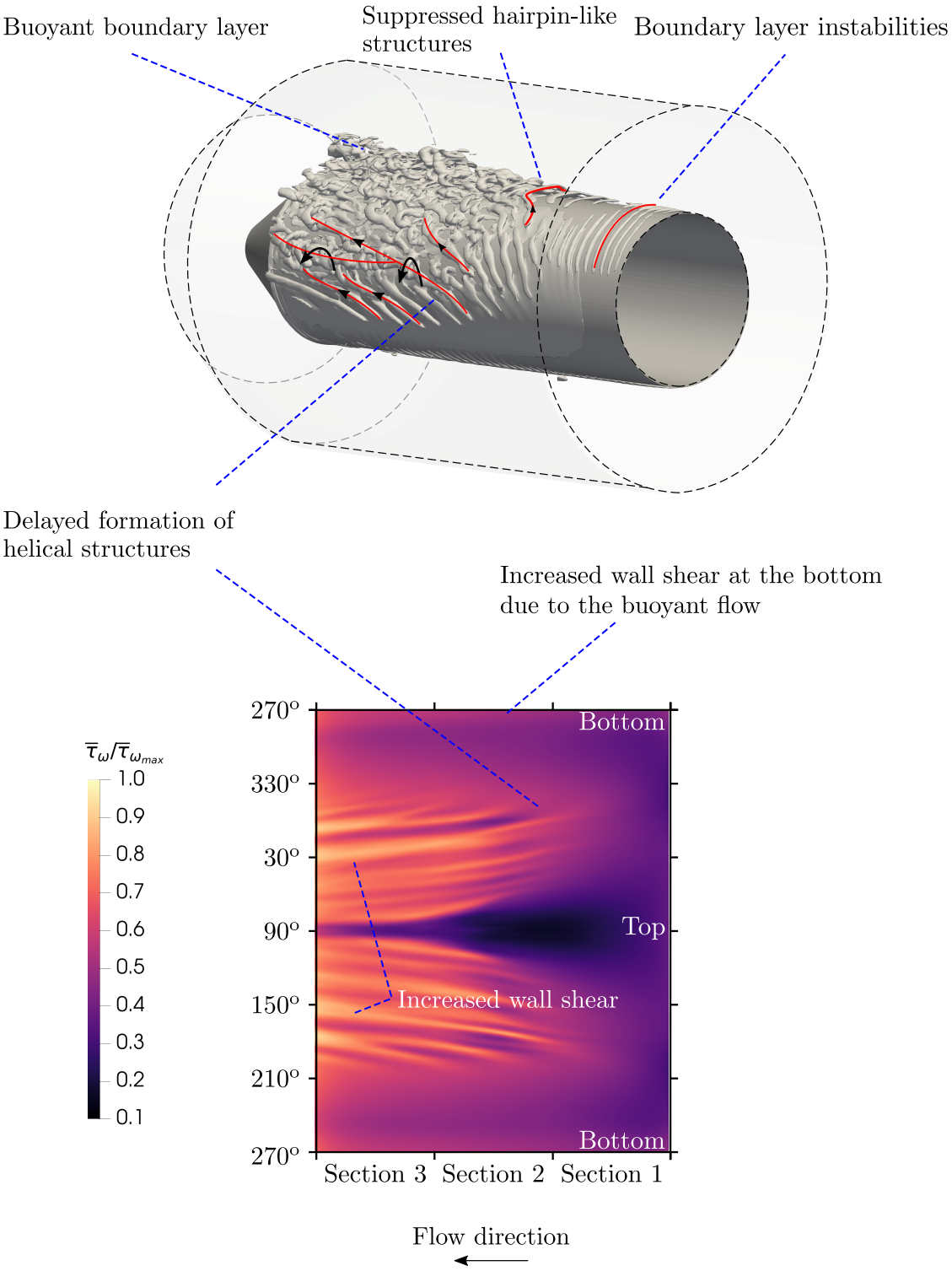

Figure 5.14: Flow structures and their footprints in Case-2

After the detachment, the flow shows tendency to migrate downwards due to a decrease in temperature, and then re-join the near wall low momentum fluid that moves upwards. These rolling up processes with detachment and reattachments create helical structures which enlarge along the streamwise direction as highlighted in Fig. 5.13. A similar helical motion were also suggested in the studies of Mojtabi and Caltagirone [131] and Ciampi et al. [14]. These flow structures can be tracked by looking at their footprints on the heated inner cylinder as illustrated in the same figure where the stretched streaks are seen.

With increased speed of cross-flow in Case-2, the boundary instabilities occur at the beginning of the test section as opposed to Case-1 where the flow was laminar as discussed. The boundary layer streaks are directed towards the top of the heated inner cylinder, which contribute to the formation of hairpin-like structures. As seen in Fig. 5.10, these structures are suppressed by the increased cross-flow effect, therefore are not able to further develop to form a thermal plume which was present in Case-1. Despite the absence of a well developed thermal plume, the reduced wall shear stress at 90° indicates that the buoyancy forces still influence the flow field. Further downstream at the top, a three dimensionality is present due to the buoyancy forces interacting with the streamwise inertial forces. Unlike Case-1 where the formation of helical structures started relatively early, the occurrence of these vortices is delayed. Therefore, the alternations in wall hear stress are also delayed, creating increased wall shear which suggest that the flow remains rather attached to the wall in the regions of 30° and 150° as opposed to Case-1 which exhibited reduced wall shear stress in the same region. Since the buoyant flow at the bottom does not manage to migrate towards the top, they increase the wall shear stress at the bottom at 270° along the streamwise direction as can be seen in the wall shear stress contour in Fig. 5.14.

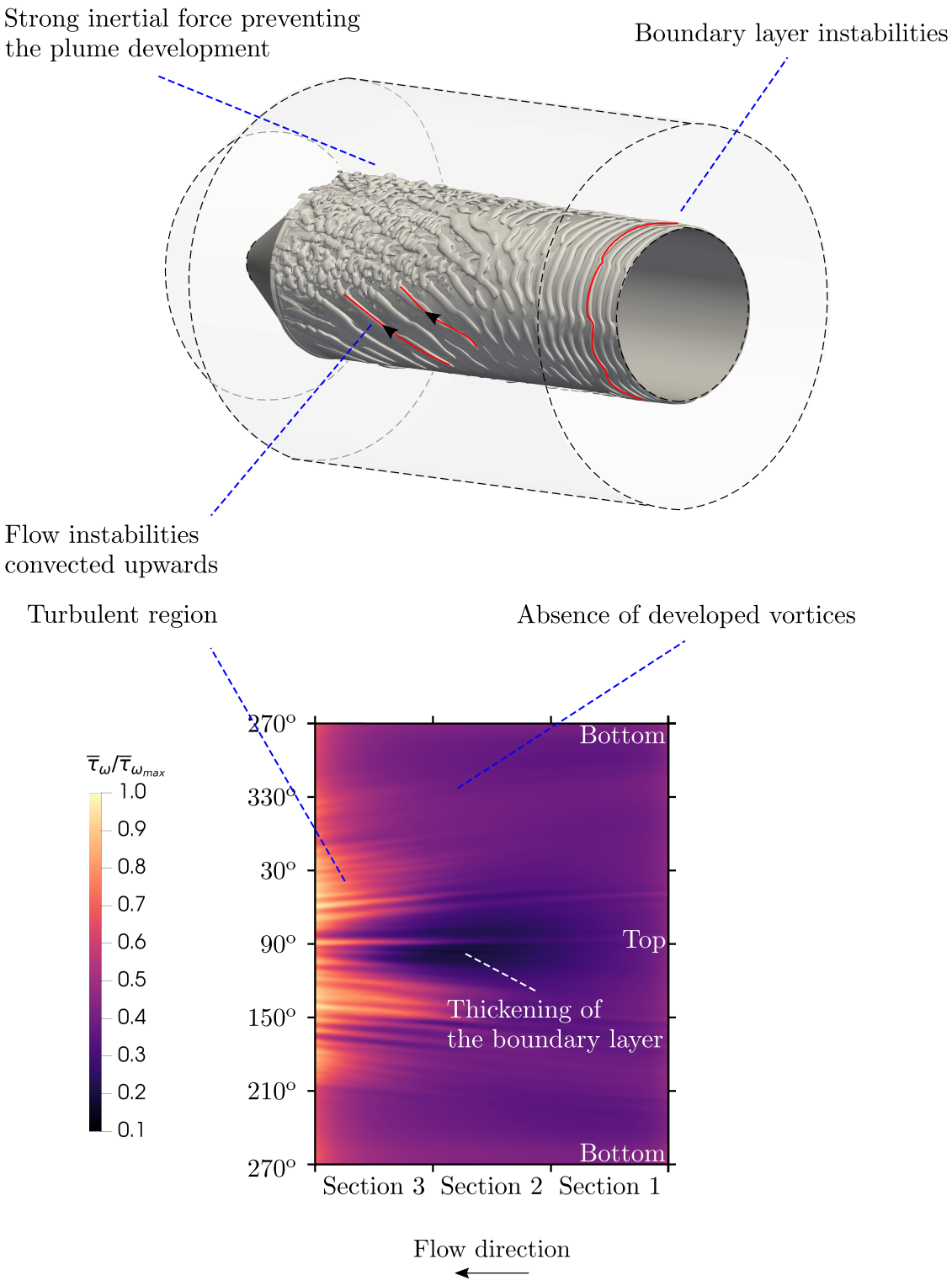

Figure 5.15: Flow structures and their footprints in Case-3

The cross-flow speed is further increased in Case-3 which adopts a very similar a Grasof number to Case-1 and Case-2, therefore has the lowest Richardson number amongst all cases. The boundary layer instabilities resembling the Tollmien-Schilichting (T-S) waves on a flat plate that were present in Case-2 are now further pronounced at the beginning of the test section, covering the entire circumference. These instabilities can be seen in Fig. 5.15. It is important to note that these instabilities resembling the T-S waves were also observed in the numerical (LES) tests of the facility for pure aerodynamics (no heating) investigations.

The strong inertial force prevents the thermal plume development at the top of the heated inner cylinder in the entire test section. Suppressed thin boundary layer at Section 3 shown in Fig. 5.11 is also seen in the iso-surfaces in Fig. 5.12. However, the decreased wall shear stress at the upper half at around 90° suggests that there is a thickening of the boundary layer duo to buoyancy. The shear stress distribution remains relatively uniform until the beginning of turbulent region towards the downstream of test section. On each side, there are low momentum buoyant flows near the heated inner cylinder which are convected upwards. However, these near-wall fluid movements remain as instabilities as seen in Fig. 5.15 where the wall shear stress contour indicates that there is no clear sign of developed vortices.

5.6 Heat Transfer

In addition to the time-averaged temperature field, the instantaneous flow field and the time-average wall shear stress contours, the wall heat transfer may give further perspective for the flow field. Table 5.3 gives a detailed information on Nusselt number distribution at each circumferential and axial measurement location in the test section. Since the experimental heat transfer could not be obtained for Case-2 and Case-3 as explained in Chapter 4, only LES results are presented for Case-2 and Case-3, whereas both experimental and LES heat transfer results as well as LES errors are available for Case-1 in Table 5.3. The heat transfer distribution around

the entire circumference at each section is illustrated in Fig. 5.16. Additionally, the heated inner cylinder Nusselt number contours are shown in Fig. 5.17 which provides better visualisation of the heat transfer profiles for each case.

In Section 1, the heat transfer profile at the bottom transfer correlates with the Richardson number. With increasing Ri number (decreasing cross-flow speed), the heat transfer deviates from uniform profile at the lower half, particularly at the bottom at around 270°. This is attributed to the buoyancy effect which pushes the near-wall fluid up against the bottom wall. Consequently, the boundary layer thickness is reduced, leading to a large temperature gradient which effectively means enhanced heat transfer as can also be observed in pure natural convection at the stagnation point occurring at the bottom [25]. This trend is clearly seen when comparing the lower half heat transfer profiles in Fig. 5.16 where the bottom heat transfer enhancements are visible in Case-1 whereas Case-3 exhibits a uniform Nusselt number distribution. In terms of heat transfer uniformity, Case-2 lies in between Case-1 and Case-3 as expected considering the fact that Case-2 represents the intermediate Richardson number. The transition from Case-1 to Case-3 in heat transfer profile can also be seen in Fig. 5.17 where the improved HTC uniformity is present in Case-3 at Section 1 circumference. However, it is interesting to note that Case-2 yields a less heat transfer rate than both Case-1 and Case-3 at exactly the bottom at 270°. Case-2 and Case-3 shows relatively uniform heat transfer in the lower half compared to Case-1 which shows a progressive drop in heat transfer at around 240° and 300°. Looking at 210° and 330°, and the region beyond these points towards the top, Case-1 exhibits enhanced and slightly oscillatory heat transfer rates. Recalling the flow field in Case-1 (in Fig. 5.13), this region with heat transfer enhancement on each side marks the location where the formation of longitudinal structures begins, which can also be seen in Fig. 5.17. Similar physical phenomenon with the boundary layer is present in the upper half in Section 1. Heat transfer increases with decreasing Richardson number. This is due to the higher cross-flow speed causing a thinner boundary layer. In contrast, high Richardson number flows (relatively lower cross-flow speeds) exhibit reduced heat

transfer rates with larger boundary layers (smaller temperature gradients). This is clearly seen in the upper half of the heated inner cylinder in Fig. 5.16 where Case-1 and Case-3 yield the lowest and highest heat transfer rates, respectively. Case-1 experimental results show that wall resolved LES is capable of predicting the heat transfer results accurately (particularly at the upper half) with an exception at 330° where the maximum error occurred, reading 21.95 % .

In Section 2, Case-3 continues to exhibit relatively uniform heat transfer in the lower half. This uniform heat transfer profile further expands to the upper half apart from the top region between 60° 120° where the thickening of boundary layer is present as seen with the reduced wall shear stress in Fig. 5.12, which results in higher HTC in the region as seen in Fig. 5.17. Despite the reduction at the top, it is clear that Case-3 yields overall uniform heat transfer around the cylinder circumference. Compared to Section 1, there is an overall heat transfer reduction with Case-3 in Section 2, indicating that the temperature gradient is smaller. Unlike Case-3, Case-1 and Case-2 show diverse flow regimes occurring simultaneously. In the lower half, both Case-1 and Case-2 suggest that the heat transfer profiles are comparable to those in Section 1 with a reduction in magnitude. The heat transfer reduction arises from the increase in boundary layer thickness which has been observed also in Case-3. The heat transfer alternations due to the formation of helical structures occur early in Case-1 compared to Case-2. The influence of formation and development of these structures on heat transfer is clearly seen in the Nusselt number contours in Fig. 5.17. The spatial delay in the formation of helical structures was already discussed in the previous section, and can be seen in Fig. 5.13 and Fig. 5.14. These elongated helical structures along the heat inner cylinder create local impingements and lift-offs after which fresh boundary layer forms. Since fresh boundary layers are thin by nature, they contain large temperature gradients which are responsible for local heat transfer maxima as seen in Fig. 5.17. Similarly, when the flow is detached with a local lift-off, the boundary layer is enlarged, causing a small temperature gradient that is responsible for local heat transfer minima.

Table 5.3: Nusselt number comparison at measurement locations on the heated inner cylinder

	Section 1					Section 2					Section 3				
θ	Exp-1	LES-1	E-1 (%)	LES-2	LES-3	Exp-1	LES-1	E-1(%)	LES-2	LES-3	Exp-1	LES-1	E-1 (%)	LES-2	LES-3
30°	53.29	54.01	1.33	69.99	98.51	69.97	66.81	-4.74	100.87	65.27	86.51	93.88	7.85	99.21	97.35
90°	40.53	41.54	2.43	60.65	90.25	42.01	34.95	-20.19	28.21	46.47	72.34	70.19	-3.07	64.89	89.73
150°	52.85	53.75	1.67	69.27	97.27	90.99	96.80	6.01	117.26	62.93	104.11	106.01	1.78	106.01	99.38
210°	73.88	84.06	12.11	74.93	102.87	65.17	67.35	3.24	67.58	74.71	64.14	64.46	0.49	66.43	78.41
330°	67.82	86.90	21.95	75.15	99.79	68.75	70.02	1.81	67.89	68.83	63.32	64.59	1.97	66.07	67.58

As discussed, it was observed in the wall shear stress contours that the occurrence of the longitudinal coherent structures was more frequent in Case-1 than in Case-2. This, consequently, results in stronger heat transfer alternations in Case-1. This alternating heat transfer profile is not present in Case-3 since the large helical structures did not occur in Case-3. There are commonalities between Case-1 and Case-2, and Case-2 and Case-3 in terms of heat transfer characteristics, which can also be seen in Fig. 5.17.

It is evident from Fig. 5.16 that Case-2 heat transfer profile trend closely matches that of Case-3 in the lower half. On the other hand, Case-2 resembles Case-1 with alternating heat transfer profile in the upper half. However, these heat transfer alternations in Case-2 are not as strong as those in Case-1, which can be identified in Fig. 5.17. More importantly, Case-2 exhibits a sudden heat transfer drop at the top at 90° where Case-1 features the same trend with even more dramatic drop in heat transfer. Significant heat transfer drop at the top of a heated cylinder in a concentric annulus is a well-known characteristic of a pure natural convection. The thermal boundary layer starts developing from the bottom, then is headed towards the top, and finally developing boundary layers meet at the top where separation occurs, which cause a sudden drop in heat transfer with small temperature gradient. This phenomenon confirms that the natural convection is the dominant mode in Case-1. Comparing LES results to the experimental data for Case-1, satisfactory agreement is achieved with a maximum error of 20.19 % occured at 90° as shown in Table 5.3.

Although there are still heat transfer minima/maxima at the upper half of the heated inner cylinder at Section 3 in Case-1, the fluctuations are not as strong as those at Section 2. The Nusselt number contour in Fig. 5.17 also depicts the weakening of alternations in amplitude in Case-1. In the wall shear stress contour in Fig. 5.13, it can be seen that that the number of longitudinal streaks in Case-1 is reduced as the flow progresses to Section 3. This is due to the fact that some of these helical structures entrain the thermal plume development at the top before reaching Section 3. Strong three dimensionality due to the break-up of the coherent structures is present at the top as shown in the same figure with iso-surfaces.

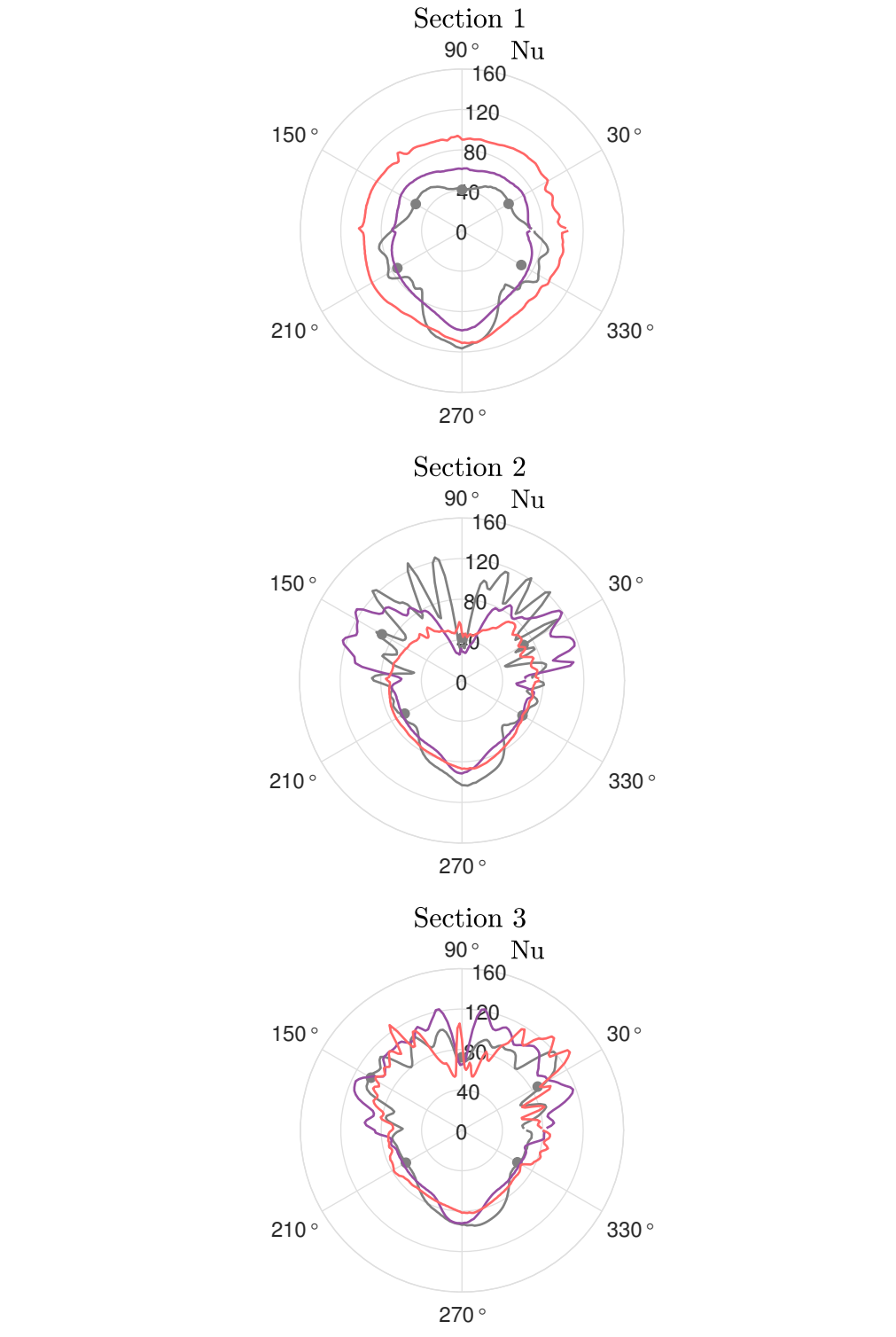

Figure 5.16: Nusselt number distribution around the heated inner cylinder

The developed plume region in Section 3 increases the overall heat transfer at the upper half, particularly at the top at 90°. Interestingly, Case-2 presents a stronger heat transfer reduction at the top than Case-1, resembling Case-1 heat transfer profile in Section 2. In fact, Case-3 also exhibits a reduced heat transfer at around 90°. Turbulent region towards the downstream of the test section in Case-3 yields some oscillations at each side at around 45° and 135°. In the lower half of the cylinder, the heat transfer profile is more uniform in Case-1 compared to the previous sections since the growing helical structures are directed upwards. Conversely, the turbulent region in Case-3 causes the heat transfer oscillations although they are not as strong as those with Case-1 and Case-2 in the previous sections. The reduced heat transfer alternations with decreasing Richardson number are also visible in the Nusselt number contour in Fig. 5.17. Overall, excellent agreement between experimental and LES results for Case-1 can be seen in Table 5.3.

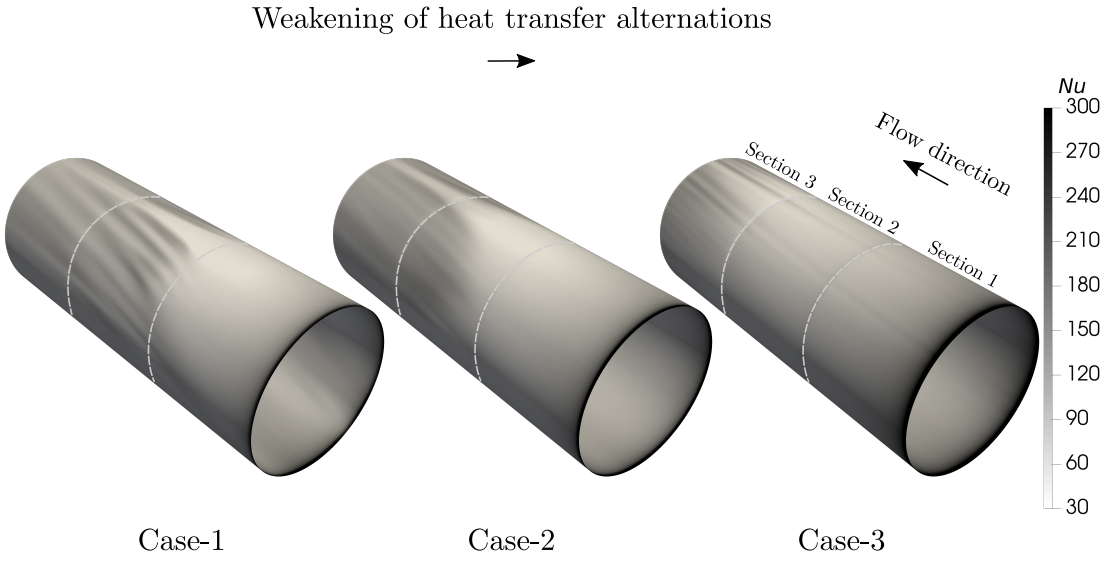

Figure 5.17: Heated inner cylinder time-averaged Nusselt number contours

5.7 Conclusions

The experimental results presented in Chapter 4 have provided the novel, detailed flow field and heat transfer measurements which have enabled the validation of the numerical methods. To this end, wall resolved large eddy simulations (LES) have been performed to better understand the characteristics of the mixed type of convection flows with engine representative conditions.

Detailed information on the LES methodology has been given. In order to ensure that the temporal and spatial resolutions have been adequately determined for wall resolved LES, the Kolmogorov length and time scales, the energy spectra and the amount of resolved turbulent kinetic energy in each case have been provided.

Validations have been performed against the velocity, temperature and heat transfer measurements. It has been found that the present LES methodology agrees well with the experimental data, which increases the confidence in numerical predictions.

The LES results have confirmed that Case-1 represents a natural convection dominant case with a thermal plume at the top of the heated cylinder whereas Case-3 tends to exhibit forced convection dominance. Case-2 has featured some similarities with both Case-1 and Case-3. Development of coherent turbulent structures have been revealed and tracked with their footprints using the wall shear stress contours. Longitudinal helical structures with various magnitudes depending on the dominant convection mode have been identified. These structures have been found to influence the heat transfer characteristics greatly, and be responsible for large alternations in heat transfer which have been confirmed with quantitative and qualitative observations.

Overall, the time-averaged flow field and heat transfer characteristics have been further investigated using the relevant flow structures developing in the test section which are of great importance to better understand the flow regimes in mixed types of flows in turbine casing cavities.

Chapter 6

New Model Development

6.1 Introduction

Although high fidelity scale resolving simulations (i.e., large eddy simulations (LES) and direct numerical simulations (DNS)) have gained a great attention, the RANS based turbulence models are still gold standard in industry due to their low computational resource and time requirements. However, these low order models may not provide a required degree of accuracy since the employed modelling methods may not be adequate for all engineering problems. Of particular interest is mixed convection type of flows occurring inside turbine casing cavities which can be represented by a horizontal concentric annulus as discussed in the previous chapters.

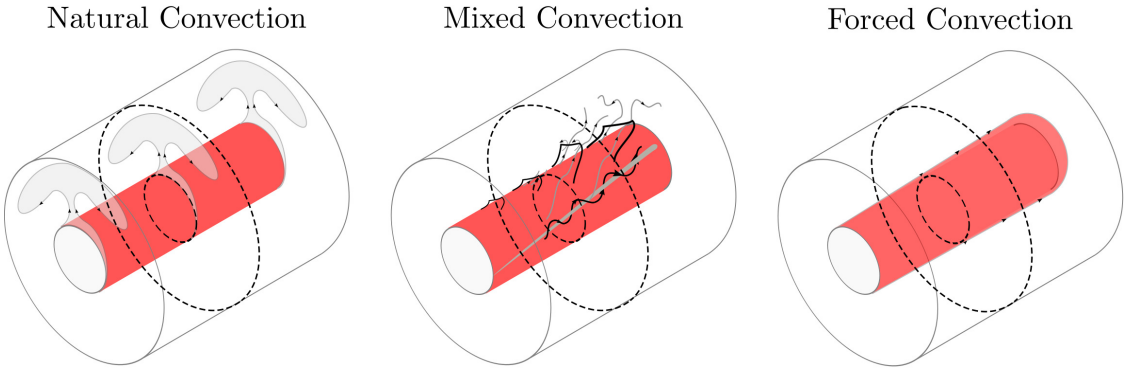

Figure 6.1: Different types of convective flow regimes

Mixed type of flows fundamentally differ from pure natural and forced convective flows. If pure natural convection takes place, the boundary layer starts forming at the bottom of heated cylinder, and progressively thickens as it move towards the top. The thickest boundary layer occurs at the top where thermal plume separation is present. The plume continues to rise until the impingement on the outer cylinder [26]. In this type of flow, the flow movement tends to be two-dimensional with thermal

plume oscillation at radial and circumferential ($r-\theta$) plane. In pure forced convective flows, uniform boundary layer forms around the horizontal cylinder, and gradually gets thicker as the fluid moves along the surface. However, in mixed convection type flows, complex flow interactions occur as the thermal plume region due to buoyancy is now distorted with cross flow. This leads to strong flow instabilities, and the growing vortices trigger early transition to turbulence as shown in Chapter 5. These flow behaviours identified by scale resolving simulations are illustrated in Fig. 6.1. In the literature review, more advanced models for Reynolds stress and turbulent heat flux treatments are reviewed. In this chapter, a new model which incorporates both Reynolds stress and turbulent heat flux treatments will be introduced, and the performance of which in predicting mixed types of flows will be assessed against scale resolving simulations and a widely used turbulence model, $k-\omega\ SST$.

6.2 Reynolds Stress Modelling

The Reynolds stress anisotropy tensor, $a_{ij} = \frac{\overline{u_i{'}u_j{'}}}{k} - \frac{2}{3}\delta_{ij}$, given in the literature review (Chapter 2) can be used for development of a non-linear eddy viscosity model. Recalling the linear eddy viscosity formulation in Eq. 6.1, the Boussinesq hypothesis is based on one term tensor representation with strain rate tensor, S_{ij}.

$$\overline{u_i{'}u_j{'}} = -2v_tS_{ij} + \frac{2}{3}k\delta_{ij} \tag{6.1}$$

Gatski and Jongen [62] stated that the influence of Reynolds stress anisotropy on the mean flow is through the mean strain rate tensor, S_{ij}, and the mean rotation rate tensor, Ω_{ij}, in addition to the characteristic turbulent time scale, τ. Therefore, the anisotropy can be expressed as a function of strain-rate, rotation rate tensors and turbulent time scale as given in Eq. 6.2.

$$a_{ij} = f(S_{ij}, \Omega_{ij}, \tau) \tag{6.2}$$

where the turbulent time scale is defined as $\tau = k/\epsilon$.

Based on Cayley-Hamilton theorem, the anisotropy tensor can be defined as a polynomial, which can be expressed as a tensor polynomial with ten independent terms [63, 132] given in Eq. 6.3.

$$a_{ij} = \sum_{n=1}^{10} \beta_{n-1} T_{ij}^{(n)} \tag{6.3}$$

where β_{n-1} are the coefficients that scale the tensors, and $T_{ij}^{(n)}$ are tensor bases calculated as:

$$\begin{aligned}
T_{ij}^{(1)} &= S_{ij} & T_{ij}^{(6)} &= S_{ik}\Omega_{kl}\Omega_{lj} + \Omega_{ik}\Omega_{kl}S_{lj} - 2IV\delta_{ij/3} \\
T_{ij}^{(2)} &= S_{ik}S_{kj} - II_S\delta_{ij}/3 & T_{ij}^{(7)} &= S_{ik}S_{kl}\Omega_{lp}\Omega_{pj} + \Omega_{ik}\Omega_{kl}S_{lp}S_{pj} - 2V\delta_{ij}/3 \\
T_{ij}^{(3)} &= \Omega_{ik}S_{kj} - S_{ik}\Omega_{kj} & T_{ij}^{(8)} &= S_{ik}\Omega_{kl}S_{lp}S_{pj} + S_{ik}S_{kl}\Omega_{lp}S_{pj} \\
T_{ij}^{(4)} &= \Omega_{ik}\Omega_{kj} - II_\Omega\delta_{ij}/3 & T_{ij}^{(9)} &= \Omega_{ik}S_{kl}\Omega_{lp}\Omega_{pj} - \Omega_{ik}\Omega_{kl}S_{lp}\Omega_{pj} \\
T_{ij}^{(5)} &= S_{ik}S_{kl}\Omega_{lj} - \Omega_{ik}S_{kl}S_{lj} & T_{ij}^{(10)} &= \Omega_{ik}S_{kl}S_{lp}\Omega_{pq}\Omega_{qj} - \Omega_{ik}\Omega_{kl}S_{lp}S_{pq}\Omega_{qj}
\end{aligned} \tag{6.4}$$

The independent scalar invariants are given in Eq. 6.5 [55, 133].

$$\begin{aligned}
II_S &= \{S_{kl}S_{lk}\} & & \\
II_\Omega &= \{\Omega_{kl}\Omega_{lk}\} & IV &= \{S_{kl}\Omega_{lm}\Omega_{mk}\} \\
III_S &= \{S_{kl}S_{lm}S_{mk}\} & V &= \{S_{kl}S_{lm}\Omega_{mn}\Omega_{nk}\}
\end{aligned} \tag{6.5}$$

Since the first tensor in Eq. 6.4 is already included in the linear eddy viscosity model with strain rate tensor, $T_{ij}^{(1)}$ must therefore be excluded (therefore $n = 2$), and the Reynolds stress calculation is updated as:

$$\overline{u_i' u_j'} = -2\nu_T S_{ij} + \frac{2}{3}k\delta_{ij} + \Big[\sum_{n=2}^{10} \beta_{n-1} T_{ij}^{(n)}\Big]k \tag{6.6}$$

The contribution of updated Reynolds stress in Eq. 6.6 is accounted in the turbulence model through the production of turbulent kinetic energy in Eq. 2.14 in Chapter 2 which is re-written as:

$$P_k = -\Bigg[-2\nu_T S_{ij} + \frac{2}{3}k\delta_{ij} + \Big[\sum_{n=2}^{10} \beta_{n-1} T_{ij}^{(n)}\Big]k\Bigg]\frac{\partial u_i}{\partial x_j} \tag{6.7}$$

In the study of Fadhila [55], the same approach was followed, and it was stated that the update of production of specific dissipation rate, ω, with P_k does not affect the solution, and therefore the production of ω in linear eddy viscosity model is retained for numerical stability. In the present study, although the simulations did not suffer from significant numerical instability, the effect of updated P_ω via P_k was found to be negligible, and therefore not included in the model.

In $k-\omega$ *SST* turbulence model [98], the overprediction of the eddy viscosity due to inadequate treatment of turbulent shear stress transport (where the specific dissipation is minimised) with $k-\omega$ model is avoided by a limiter as given in Eq. 2.18 in Chapter 2. The same limiter is retained in the present model development.

Expansion of anisotropy tensor defined in Eq. 6.3 upto four terms, which makes it a quadratic formulation, as also adopted in the study of Fadhila [55], results in:

$$a_{ij} = C_\mu\Bigg[\Lambda_1\left(S_{ik}S_{kj} - \frac{1}{3}II_s\delta_{ij}\right) + \Lambda_2\left(S_{ik}\Omega_{kj} - \Omega_{ik}S_{kj}\right) + \Lambda_3\left(\Omega_{ik}\Omega_{kj} - \frac{1}{3}II_\Omega\delta_{ij}\right)\Bigg] \tag{6.8}$$

where $\Lambda_{1,2,3}$ are the model coefficients, and C_μ is the realisability condition.

In order to ensure that the model does not produce unphysical results with negative turbulent kinetic energy production, a realisability condition should be applied, which was proposed by Schumann [134]. Fadhila [55] calibrated the realisability condition coefficient proposed by Kimura and Hosoda [135] for $k-\omega$ as:

$$C_\mu = \frac{1}{1 + 0.01M^2} \tag{6.9}$$

where M takes the maximum between the nondimensional strain rate, $\tilde{S}$, and rotation rate, $\tilde{\Omega}$, defined as:

$$M = max(\tilde{S}, \tilde{\Omega}), \qquad \tilde{S} = \frac{1}{\omega}\sqrt{2S_{ij}S_{ij}}, \qquad \tilde{\Omega} = \frac{1}{\omega}\sqrt{2\Omega_{ij}\Omega_{ij}} \tag{6.10}$$

Fadhila [55] proposed a scaling function for the anisotropy coefficients, $\Lambda_{1,2,3}$, in Eq. 6.8 to ensure that the isotropy is maintained with the smallest turbulence length scales as the wall is approached. The same scaling function which scales with the specific dissipation rate, ω, is used in the present study as given in Eq. 6.11.

$$\Lambda_n = \frac{C_{\Lambda_n}}{max(\omega, \kappa S)^2} \tag{6.11}$$

where S is the strain rate magnitude which allows the model coefficients to vary depending on the velocity field. The limiter is included to avoid excessive anisotropy production, where κ is a calibrated constant, $\kappa = 2.5$ [63].

The last term in Eq. 6.8 led to convergence difficulties, particularly with ω. The same trend was observed in the original model [63] where the term was found to violate the realisability condition, consequently was set to zero. Similarly, the third term was excluded with $\Lambda_3 = 0$ to maintain numerical stability and realisability condition. C_{Λ_n} in Eq. 6.11 requires a calibration for each Λ. The original formulation

in [55] was calibrated against DNS data, and included damping functions to enable model scale with turbulence Reynolds number which was used in various functional forms representing viscous, buffer and logarithmic regions in the boundary layer. The reader is referred to [55] for further details.

The calibrated C_{Λ_n} values led to serious under and overshooting Reynolds stress predictions in the present study. This is attributed to the fundamental differences between the DNS data (zero pressure gradient flat plate, swirling flow, planar diffuser) used for calibrations in [55] and the mixed types of flows in which the buoyant flows introduce significant changes to the flow field depending on the geometrical feature (e.g. above, below or side of a heated cylinder) and the magnitude of buoyant forces.

A hyperbolic tangent function given in Eq. 6.12 is used as a damping function which monotonically decrease. Interestingly, in the original formulation of Fadhila [55], this function is used for the the logarithmic region in the form of $tanh\frac{Re_T^{1.9}}{70}$.

$$C_{\Lambda_n} = 5\left(1 - tanh\left(\frac{Re_T^{1.9}}{70}\right)\right) \tag{6.12}$$

where Re_T is the turbulence Reynolds number, $Re_T = k/\nu\omega$.

6.3 Turbulent Heat Flux Modelling

As discussed in the literature review (Chapter 2), Pilkington et al. [67] proposed a buoyancy modification to Generalised Gradient Diffusion Hypothesis (GGDH), referred as GGDH+, to enable baseline GGDH turbulent heat flux model to determine whether the flow is below or above a heated surface, and also to identify if the flow is over a vertical surface. The GGDH+ model is re-written here:

$$\overline{u_i'T'} = -C\frac{k}{\epsilon}\overline{u_i'u_j'}\frac{\partial\overline{T}}{\partial x_j} \qquad C = 0.15\left(1 + tanh\left|\frac{u}{v}\right|sgn\left(g_j\frac{\partial T}{\partial x_j}\right)\right) \tag{6.13}$$

Although the term $tanh\left|\frac{u}{v}\right|$ in Eq. 6.13 was proposed to determine whether the flow over a vertical or horizontal surface, it was retained in the present model as it would enable the new model to scale the heat transfer depending on the magnitudes of velocities in streamwise and wall-normal directions. However, since the GGDH and GGDH+ models were developed mainly for pure natural convective flows, it was expected that these models would cause heat transfer overpredictions due to the increased Reynolds stresses in mixed type of flows. Similarly, the Simple Gradient Diffusion Hypothesis (SGDH) model is known to fail in predicting the heat transfer since the turbulent heat fluxes scale only with the mean temperature gradient.

Considering a mixed type of flow, the streamwise components of Reynolds stresses and turbulent heat fluxes are stronger than those in pure natural convection type. Therefore, GGDH based models may not be suitable for mixed type of flows particularly when the cross flow effect is more pronounced. The model constant in GGDH+, 0.15, is reduced to 0.075 in the upper half of the annulus, and further reduced to 0.035 in the lower half to avoid excessive heat transfer predictions. These coefficients have been found to be optimum although some heat transfer overshooting are still present at certain regions which will be discussed in the following sections.

6.4 Model Implementation

The motivation for a more advanced turbulence model treatment for mixed type of flows stems from the fact that these type of flows have not been extensively investigated, and therefore the challenges in modelling for these types of flows have not been revealed. Although, there are various treatments for both pure (or heavily dominant) natural convective flows where the turbulent heat fluxes play a key role in determining heat transfer characteristics, and pure (or heavily dominant) forced convective flows where Reynolds stress treatments are vital for turbulent flows with strong mixing where the isotropy assumption fails.

The model is implemented into a commercial solver ANSYS Fluent 2020 R1 [52] through user defined functions (UDF). With this new non-linear RANS based

turbulence model approach, the aim is to blend turbulent heat flux and Reynolds stress treatments for improved accuracy without increasing the computational expense whilst keeping the proposed model as universal as possible.

In the new model, the Reynolds stresses are calculated as given in Eq. 6.14, which are accounted in the model via a source term for turbulent kinetic energy (TKE) production, S_k, in the transport equation for the TKE. The source term is defined in Eq. 6.15.

$$\overline{u_i{'}u_j{'}} = -2\nu_T S_{ij} + \frac{2}{3}k\delta_{ij} + \left[C_\mu\left[\Lambda_1\left(S_{ik}S_{kj} - \frac{1}{3}II_s\delta_{ij}\right) + \Lambda_2\left(S_{ik}\Omega_{kj} - \Omega_{ik}S_{kj}\right) + \Lambda_3\left(\Omega_{ik}\Omega_{kj} - \frac{1}{3}II_\Omega\delta_{ij}\right)\right]\right]k \tag{6.14}$$

$$S_k = -\left[C_\mu\left[\Lambda_1\left(S_{ik}S_{kj} - \frac{1}{3}II_s\delta_{ij}\right) + \Lambda_2\left(S_{ik}\Omega_{kj} - \Omega_{ik}S_{kj}\right) + \Lambda_3\left(\Omega_{ik}\Omega_{kj} - \frac{1}{3}II_\Omega\delta_{ij}\right)\right]\right]k\frac{\partial u_i}{\partial x_j} \tag{6.15}$$

The turbulent heat flux model is included in the solver via a UDF after setting a high value (10^9) for the turbulent Prandtl number, Pr_t (the turbulent heat flux is inversely proportional to Pr_t), to suppress the the existing SGDH model. The turbulent heat flux is defined in Eq. 6.16 which is used as a source term in the energy equation in the form of $\frac{\partial \overline{u_i{'}T'}}{\partial x_i}$ as given in Eq. 6.17.

$$\overline{u_i{'}T'} = -\left[\alpha\left(1 + tanh\left|\frac{u}{v}\right|sgn\left(g_j\frac{\partial T}{\partial x_j}\right)\right)\right]\frac{k}{\epsilon}\overline{u_i{'}u_j{'}}\frac{\partial \overline{T}}{\partial x_j} \tag{6.16}$$

$$S_E = \frac{\partial}{\partial x_i}\left(- \left[\alpha\left(1 + tanh\left|\frac{u}{v}\right| sgn\left(g_j \frac{\partial T}{\partial x_j}\right)\right)\right] \frac{k}{\epsilon} \overline{u_i' u_j'} \frac{\partial \overline{T}}{\partial x_j}\right) \tag{6.17}$$

where α is the turbulent heat flux model coefficient which is defined as:

$$\alpha = \begin{cases} 0.075, & \text{if} \quad g_j \frac{\partial T}{\partial x_j} > 0 \quad \text{(above a heated surface)} \\ 0.035, & \text{if} \quad g_j \frac{\partial T}{\partial x_j} < 0 \quad \text{(below a heated surface)} \end{cases}$$

6.5 Model Validation and Results

6.5.1 Methodology

ANSYS Fluent 2020 R1 [52] was used to solve the incompressible Navier-Stokes equations with the Boussinesq approximation in the present study. The unsteady Reynolds-averaged Navier-Stokes (URANS) with the $k - \omega$ SST [98] turbulence model was applied to simulate the experimental campaigns for Case-A whilst steady RANS was adopted for the remaining cases presented in Chapter 4.

The SIMPLE scheme was employed for pressure-velocity coupling. Spatial discretisation was performed with the second order upwind scheme and the second order implicit scheme was used for time stepping. A time step of $\Delta t = 0.005$ s was chosen, which yielded the Courant–Friedrichs–Lewy number of $CFL < 0.8$ in the test section.

A structured hexahedral type mesh was created, consisting of 1.92×10^6 nodes which are clustered towards the inner and outer cylinders to maintain $y^+ < 1$, hence no wall function was adopted. The same computational domain used in LES in Chapter 5 was adopted for RANS simulations. The mesh employed in RANS simulations (excluding the entrance region for visual clarity) is shown in Fig. 6.2. The results for the new model, which will be presented in the following sections, will be referred to as New Non-linear RANS (NNR).

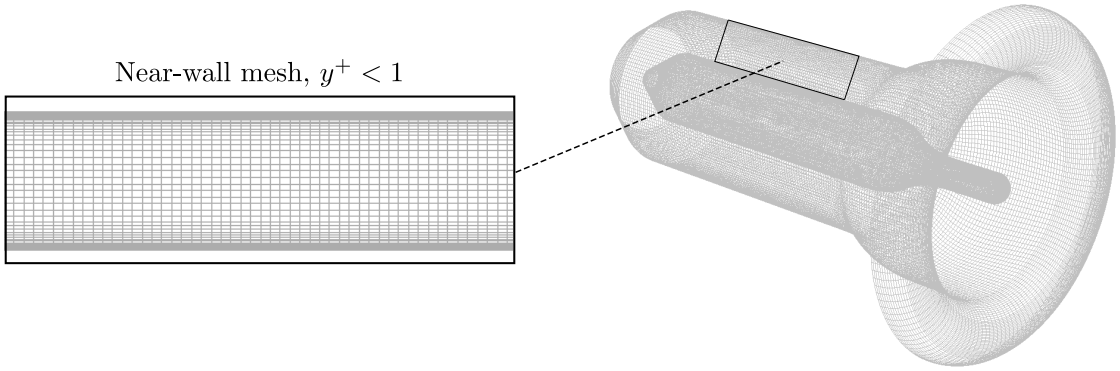

Figure 6.2: Mesh used in RANS simulations

6.5.2 Reynolds Stresses and Turbulent Heat Fluxes

The new model predictions for Reynolds stresses and turbulent heat fluxes which are vital for both flow field and wall heat transfer characteristics are compared against only the LES results due to the unavailability of experimental data. For brevity, Reynolds stress and turbulent heat flux plots will be shown for only Case-1, Case-2 and Case-3. The remaining cases are available in Appendix C.

In Fig. 6.3, the Reynolds stresses, $\overline{u_i{}'u_j{}'}$, in Case-1 are shown. The LES results suggest that the buoyant flows cause stronger turbulent fluctuations in the upper half of the annulus. The buoyant forces are also responsible for the reduced fluctuations since the turbulence is damped out with the flow pushed up against the heated cylinder in the lower half. Similar observations can be made for the turbulent heat fluxes, $\overline{u_i'T'}$, as shown in Fig. 6.4. The conventional RANS consistently underpredicts the Reynolds stresses and the turbulent heat fluxes in the upper half of the annulus. In particular, at 90° in Section 2 where the plume lift-off occurs, the RANS suffers from underpredictions of the turbulent fluctuations the most, yielding nearly no fluctuations. On the other hand, NNR model improves the Reynolds stress predictions significantly in the plume region in Section 2. At 30° and 150°, NNR clearly outperforms RANS particularly for the streamwise components. Despite the underpredictions, NNR still exhibits increased Reynolds stresses compared to the RANS in Section 3. Both RANS and NNR depict underpredictions in turbulent heat

fluxes in Section 3, therefore there is no clear sign of improved predictions with NNR apart from the reduced wall normal heat fluxes which are overpredicted by RANS.

In Fig. 6.5 and Fig. 6.6, the Reynolds stresses and the turbulent heat fluxes in Case-2 are presented, respectively. It is evident that turbulent fluctuations appear to be suppressed compared to those in Case-1. Interestingly, similar Reynolds stress profile at 90° in Section 2 in Case-1 occurs in Section 3 in Case-2. The similar profile delay occurred in the temperature profiles as discussed in Chapter 5. In the lower portion of the annulus at 210° and 330°, the suppression of these turbulent fluctuations is more pronounced as seen from the LES results. Increase in the Reynolds stresses, the streamwise components in particular, with NNR leads to improved accuracy in the upper half in Section 2 where RANS yields virtually no fluctuations. Interestingly, LES results exhibit symmetry between each side at 30° and 150° in Section 3 which RANS fails to capture whereas this trend is predicted by NNR. However, both RANS and NNR yield similar underdpredictions at 90°. Turbulent heat flux underpredictions are still present in the upper half of the annulus in Case-3. In the lower half, the wall normal turbulent heat fluxes are overpredicted by RANS since SGDH scales with the mean temperature gradient which is in the wall normal direction in this region.

In Fig. 6.7 and Fig. 6.8, with further decrease in the Richardson number in Case-3, the turbulent fluctuations are now present in a narrower region close to the heated inner cylinder as opposed to Case-1 where the buoyancy dominated flow exhibits a strong wall normal Reynolds stress and turbulent heat flux at 90°. In this instance, nearly identical Reynolds stresses between RANS and NNR can be observed. This is attributed to the fact that the new model adopts constitutive relation between Reynolds stresses and mean strain-vorticity rate. Therefore, if there is not a strong three dimensional flow, NNR is expected to exhibit similar results to RANS. RANS's persistent wall normal turbulent heat flux overprediction is still present in the lower half of the annulus. Although NNR shows underpredictions in the streamwise turbulent heat fluxes, the suppressed wall normal fluxes are captured in the lower half of the annulus.

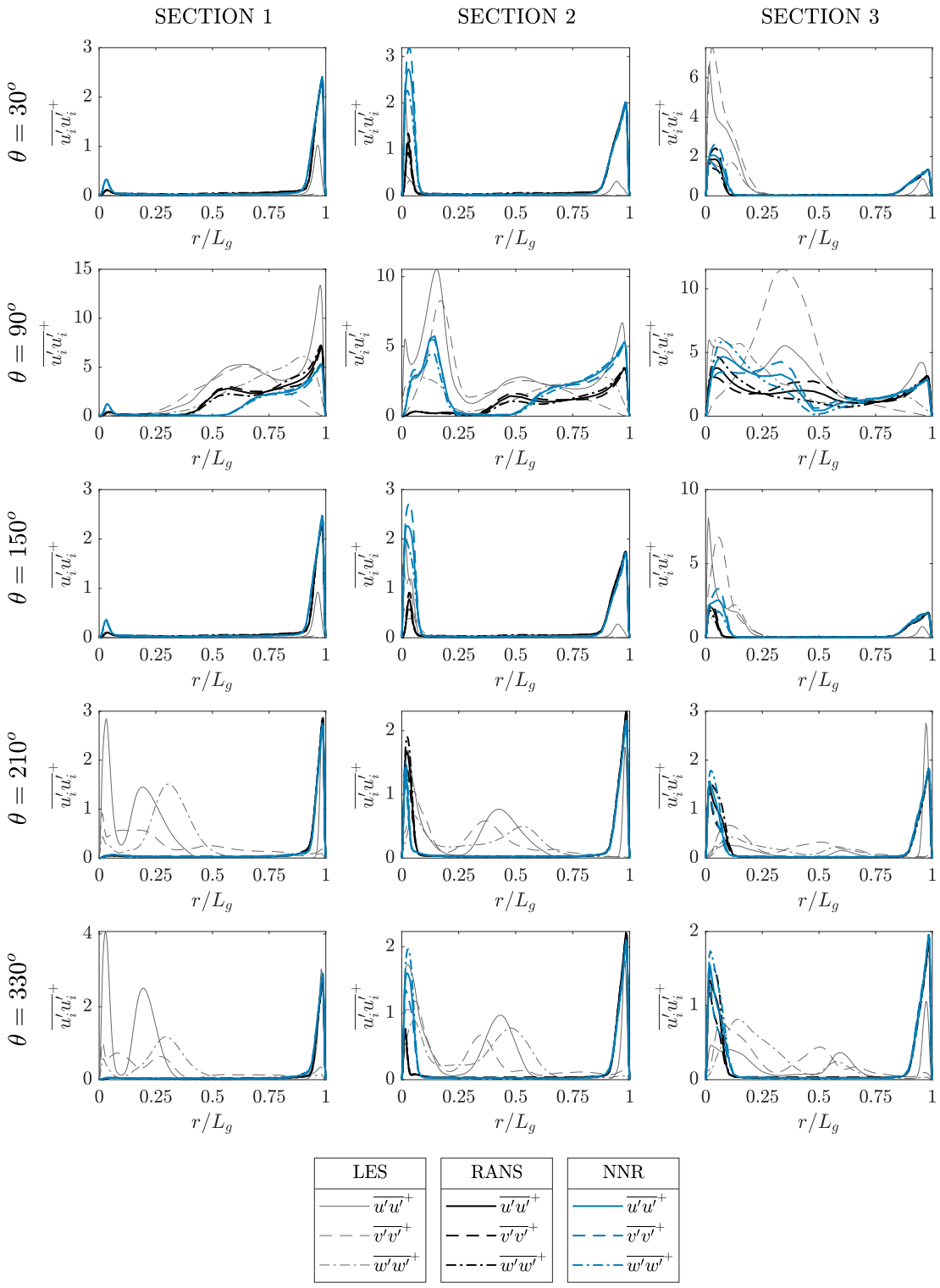

Figure 6.3: Reynolds stresses in Case-1

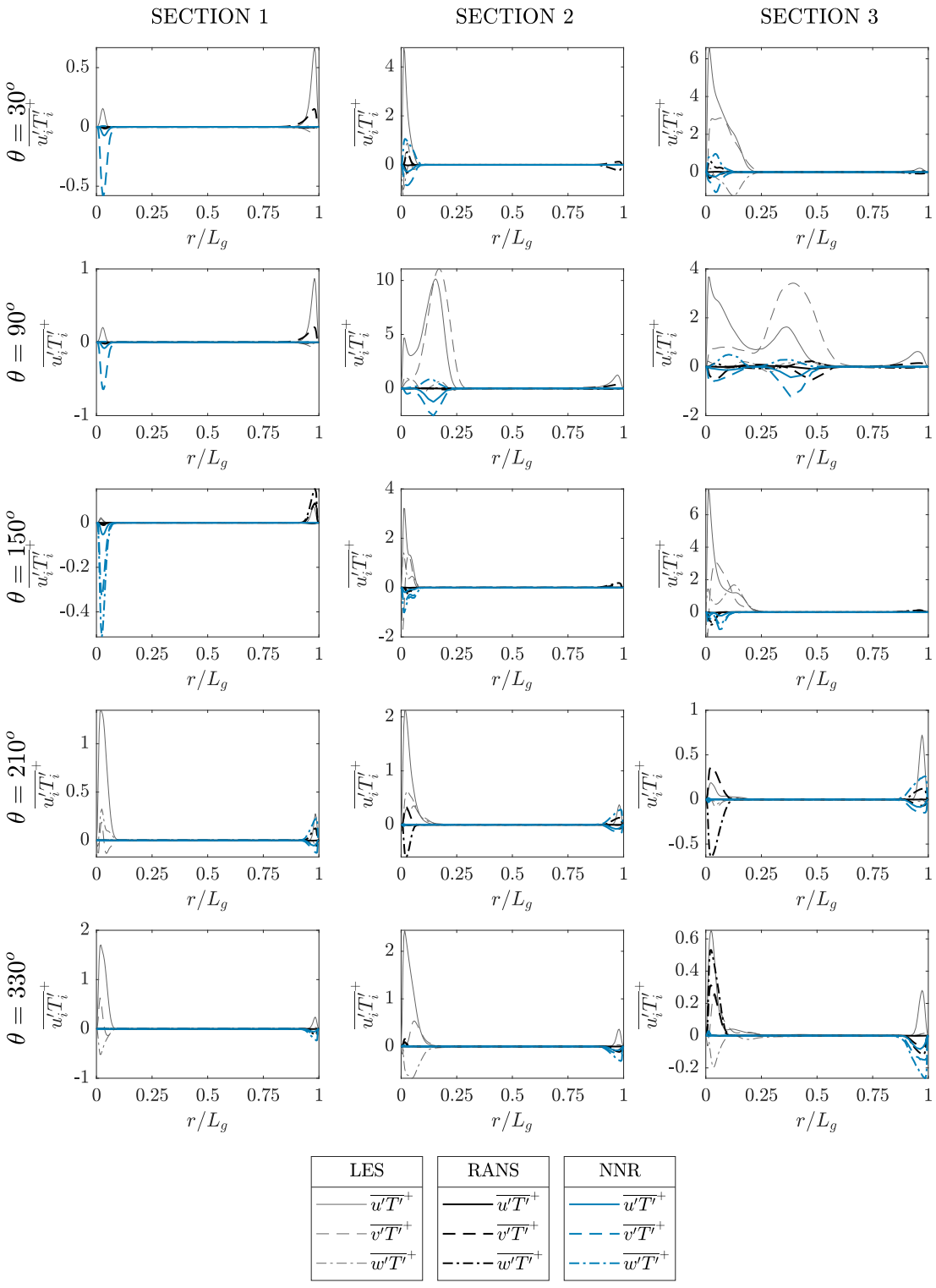

Figure 6.4: Turbulent heat fluxes in Case-1

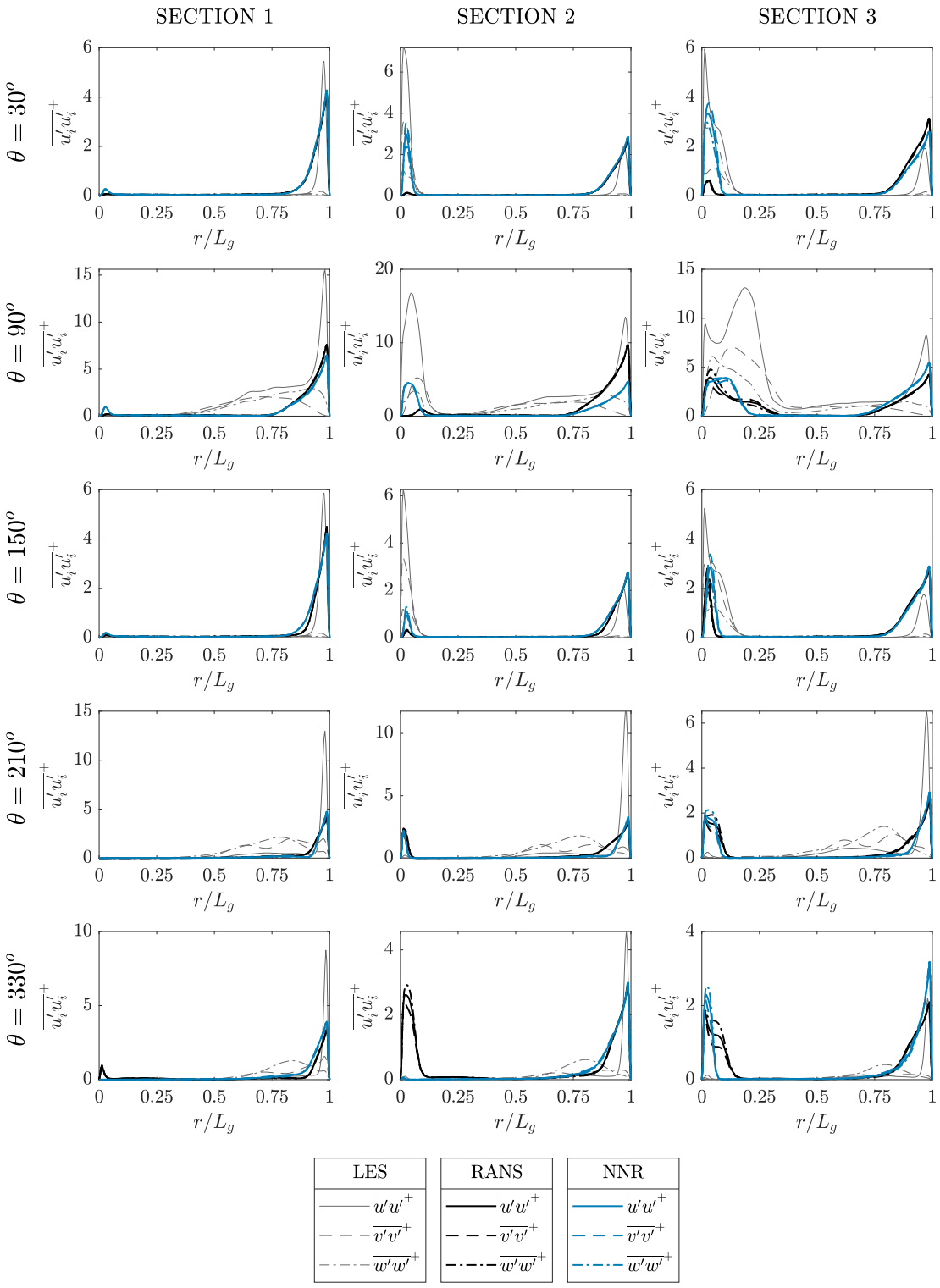

Figure 6.5: Reynolds stresses in Case-2

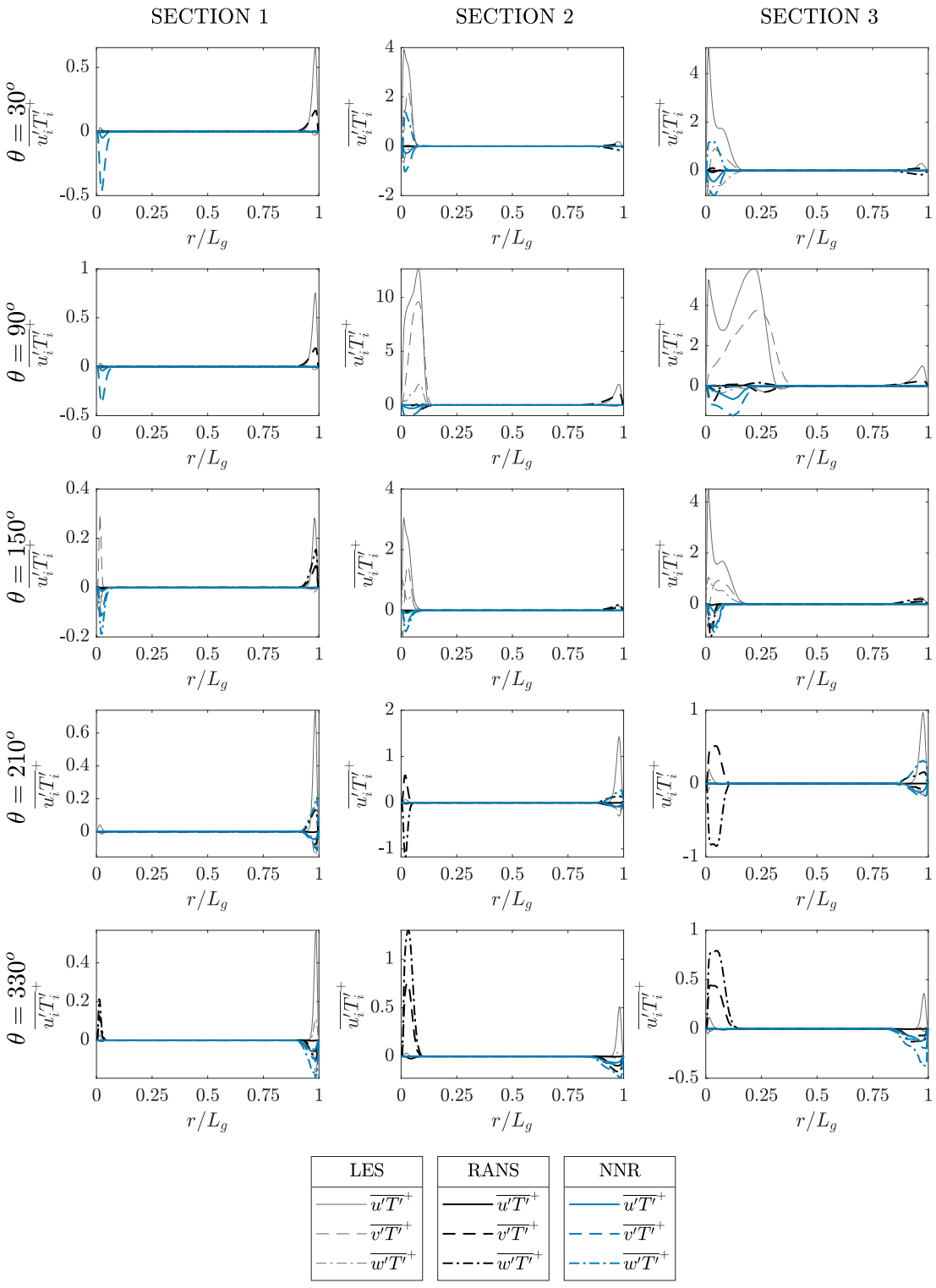

Figure 6.6: Turbulent heat fluxes in Case-2

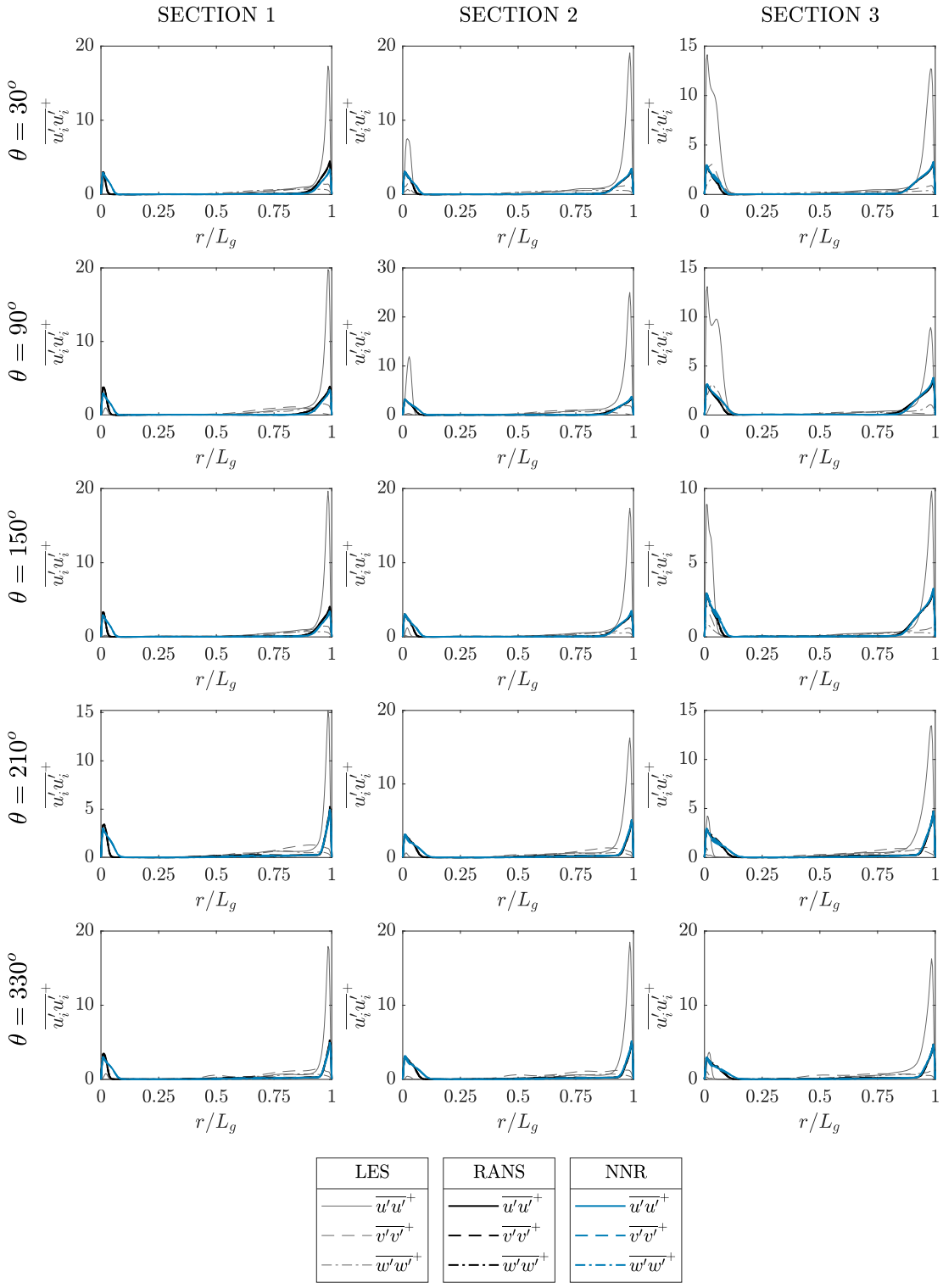

Figure 6.7: Reynolds stresses in Case-3

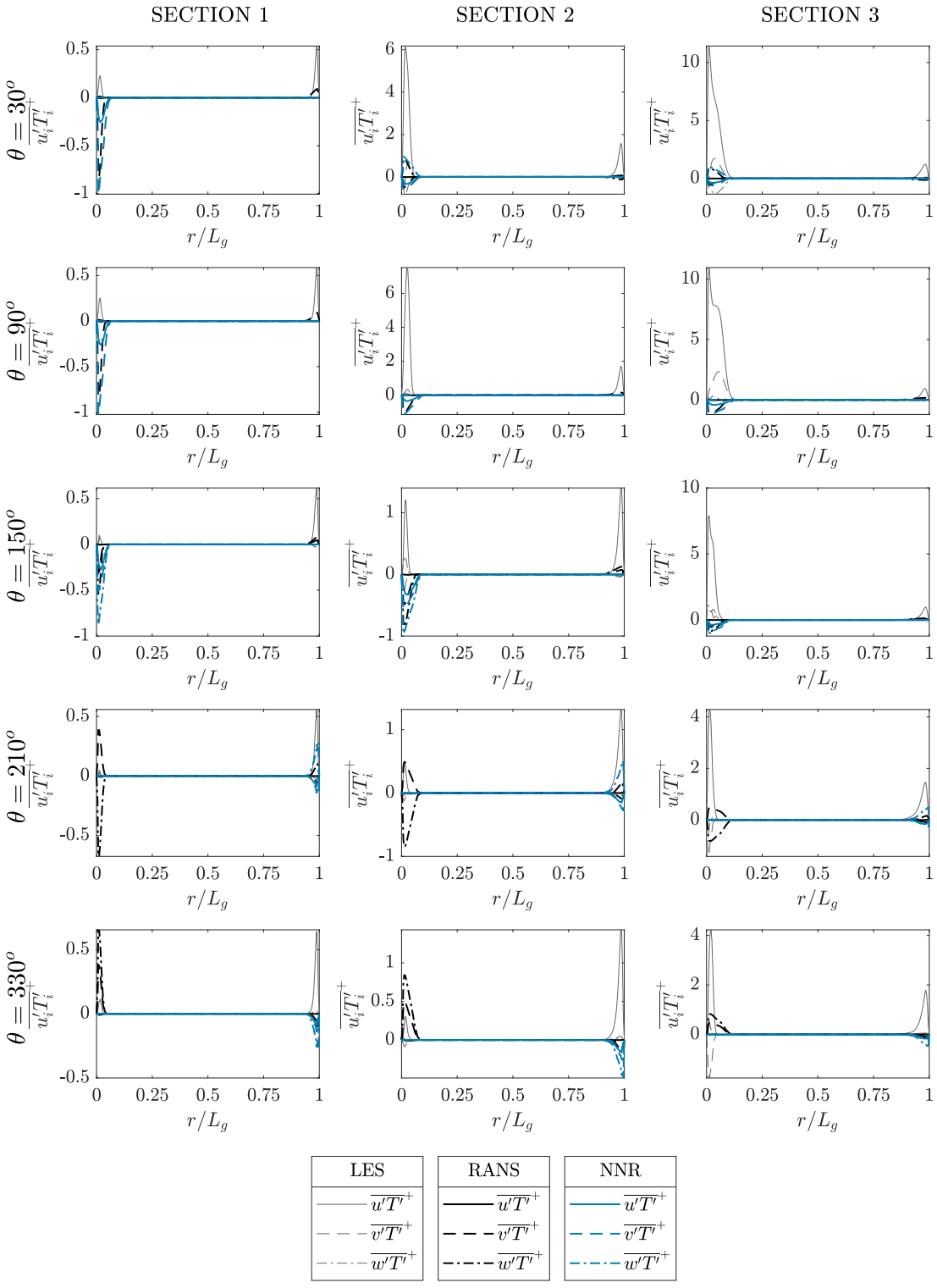

Figure 6.8: Turbulent heat fluxes in Case-3

6.5.3 Temperature Profiles

The nondimensional temperature profiles, $T^* = \frac{\overline{T}-T_\infty}{T_i-T_\infty}$, are presented for the previously selected three cases, namely Case-1, Case-2 and Case-3, as well as Case-D. The remaining cases are given in Appendix B.

The temperature profiles are given for Case-1, Case-2, Case-D and Case-3 in Fig. 6.9, Fig. 6.10, Fig. 6.11 and Fig. 6.12, respectively. It can be seen that RANS is able to capture the thin boundary layer in Section 1 in all cases where NNR also agrees well with the experimental and LES data. In fact, both RANS and NNR are found to predict the flow field accurately in the entire lower portion of the annulus where the flow remains laminar in all sections.

In Fig. 6.9, the temperature prediction comparisons in Case-1 are given. Discrepancies are present between RANS and experimental/LES data in the thermal plume region at $\theta = 90°$ in Section 2. The new model, NNR, appears to outperform the conventional RANS which exhibits a temperature inversion whilst experimental and LES data suggest smoother boundary layer. However, in Section 3 where the thermal plume is further developed, NNR yields temperature overpredictions at the top of the heated inner cylinder. In other measurement locations, all models agree well with the experimental data, managing to capture thin boundary layers.

Fig. 6.10 presents the temperature profiles in Case-2 where the thermal plume development is further delayed at $\theta = 90°$ in Section 3. In fact, RANS is found to overpredict the temperature profiles with temperature inversion in the region. It is evident that NNR model improves the temperature overshooting in the thermal plume region, leading to better accuracy for the flow field predictions. As already discussed with the LES results in Chapter 5, the temperature boundary layer around the heated inner cylinder is thinner than in Case-1 due to the increased Reynolds number, which NNR model is able to capture.

Case-D represents the next instance where the Richardson number is further reduced from that in Case-2. As seen in Fig. 6.11, the same deviation in temperature prediction by RANS is present at $\theta = 90°$. NNR model is able to correct the temperature overprediction in the thickened boundary layer region in Section 3. In

other measurement locations, both NNR and RAN yield satisfactory agreement with the experimental data. Case-D is particularly included in this section since it is clear that beyond this case, $k-\omega$ SST with the conventional Reynolds stress and turbulent heat flux models is able to capture the flow field without any remarkable over/undershootings in the flow field predictions.

Temperature profile comparisons for all models in Case-3 are given in Fig. 6.12. All models yield identical results in this case where the temperature boundary layer is nearly uniform. It is important to note that NNR model is able to adapt itself to predict the flow fields in forced convective dominant cases, which can also be seen in the lowest Richardson number case, Case-G, in Fig. B.3. Therefore, it can be deduced that both conventional RANS and NNR exhibit satisfactory agreement with the experimental data when the forced convection dominance is pronounced with more uniform and thin boundary layer around the heated inner cylinder in all sections.

In general, both RANS and NNR agree well with the experimental and LES temperature profiles in the lower half of the annulus in all cases, where the thin laminar boundary layer is present along the heated inner cylinder at each section. Similarly, it can seen that the RANS perform well in predicting the temperature profiles at each side at 30° and 150° in the upper portion of the annulus where NNR also yields similar results, agreeing well with the experimental data.

The most prominent feature of NNR predictions is seen at the thermal plume region at 90° where the new model improves the temperature predictions with an exception at 90° in Case-1 where the conventional RANS yields better results although the persistent temperature inversion still exists. However, the temperature field results suggest that the new model, NNR, overall improves the temperature predictions compared to the conventional RANS without requiring additional computational resource or time.

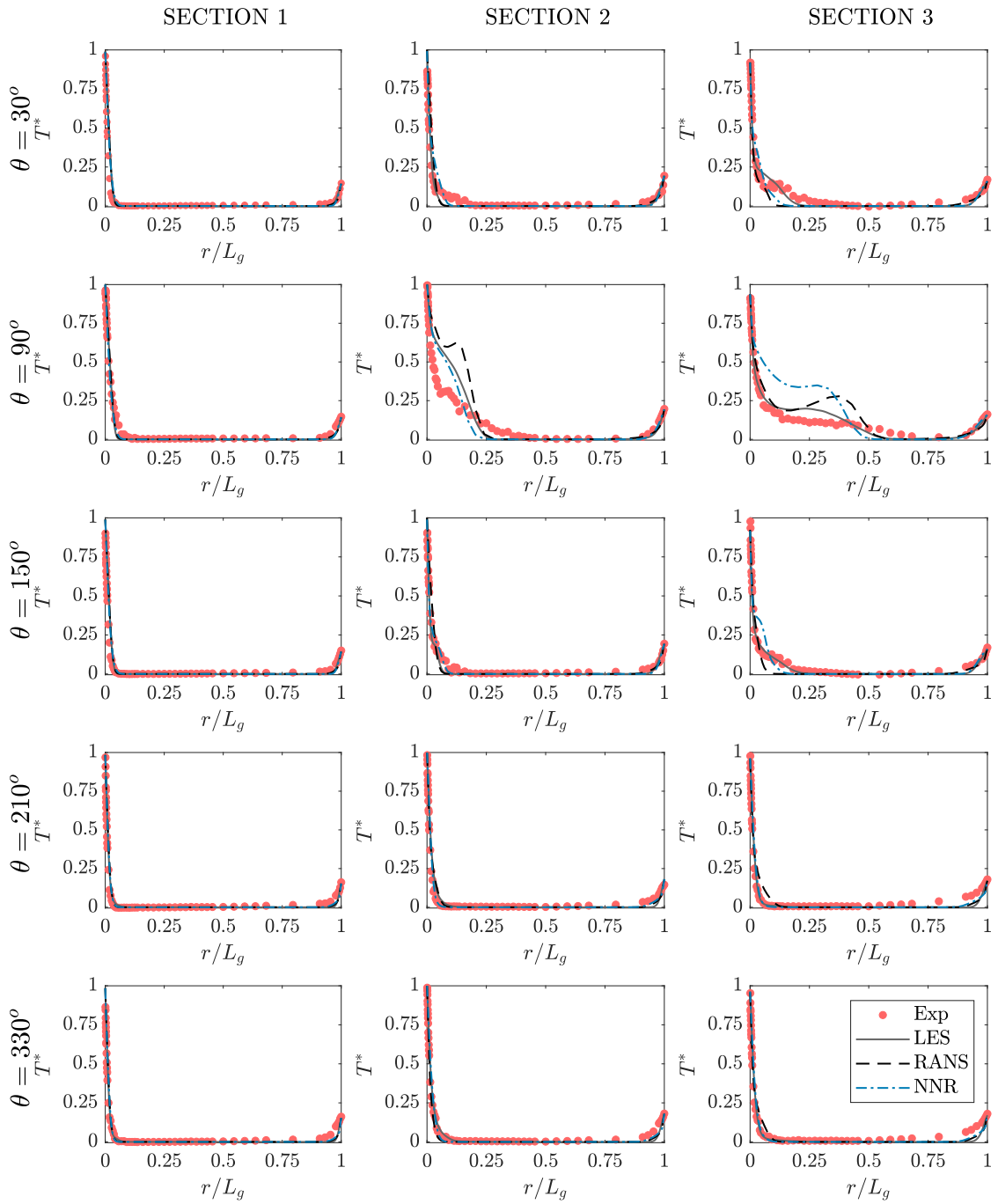

Figure 6.9: Temperature profiles in Case-1

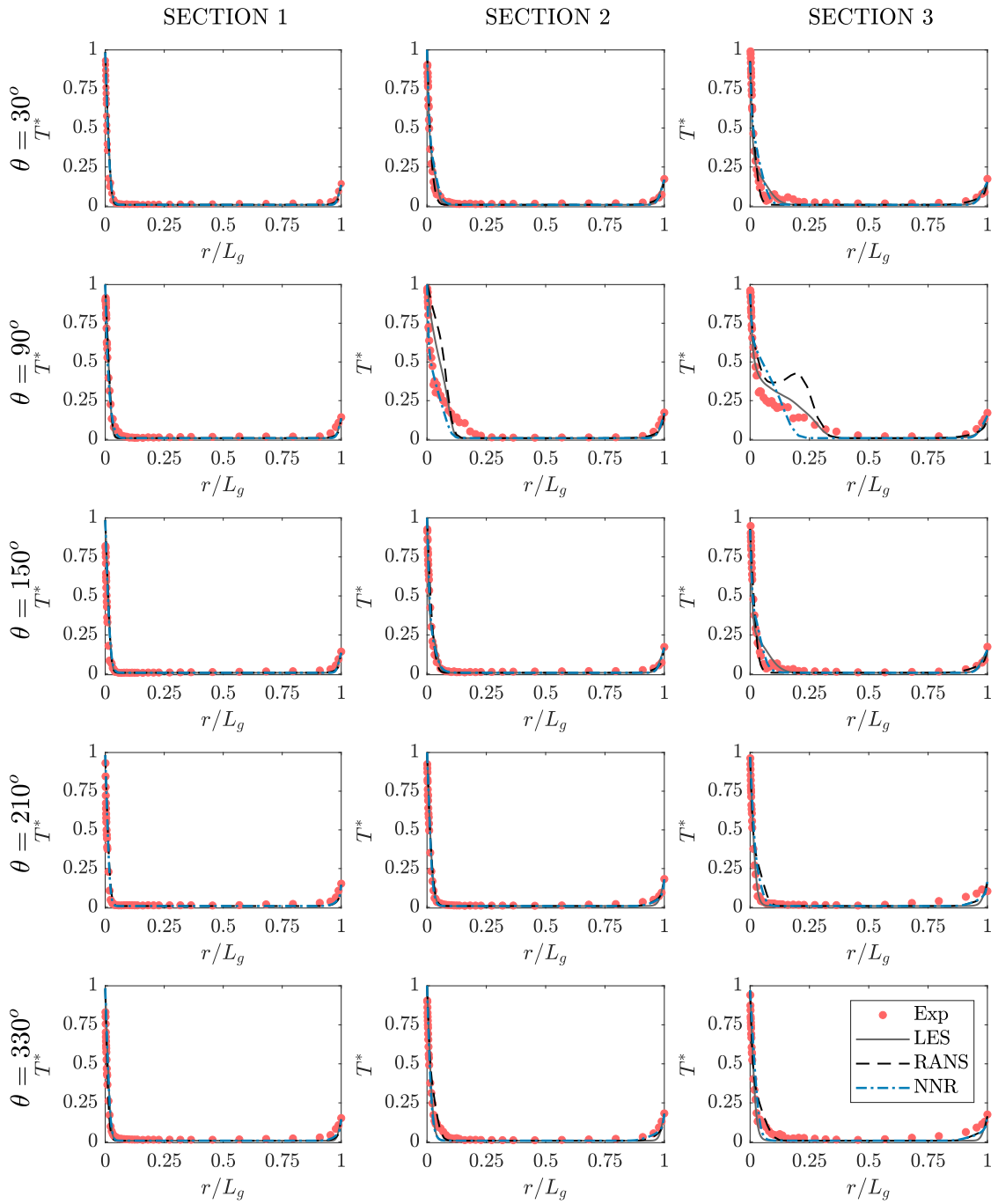

Figure 6.10: Temperature profiles in Case-2

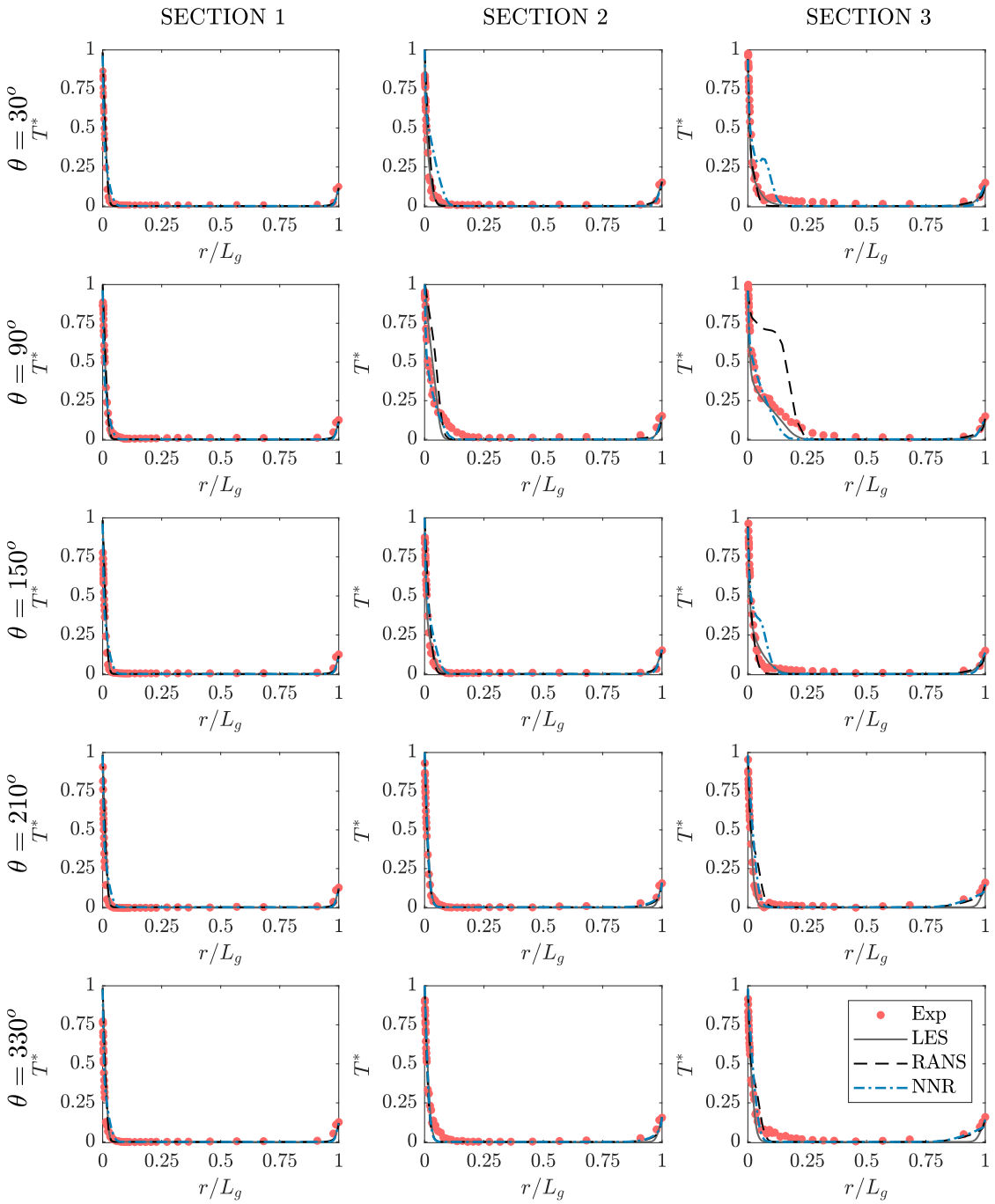

Figure 6.11: Temperature profiles in Case-D

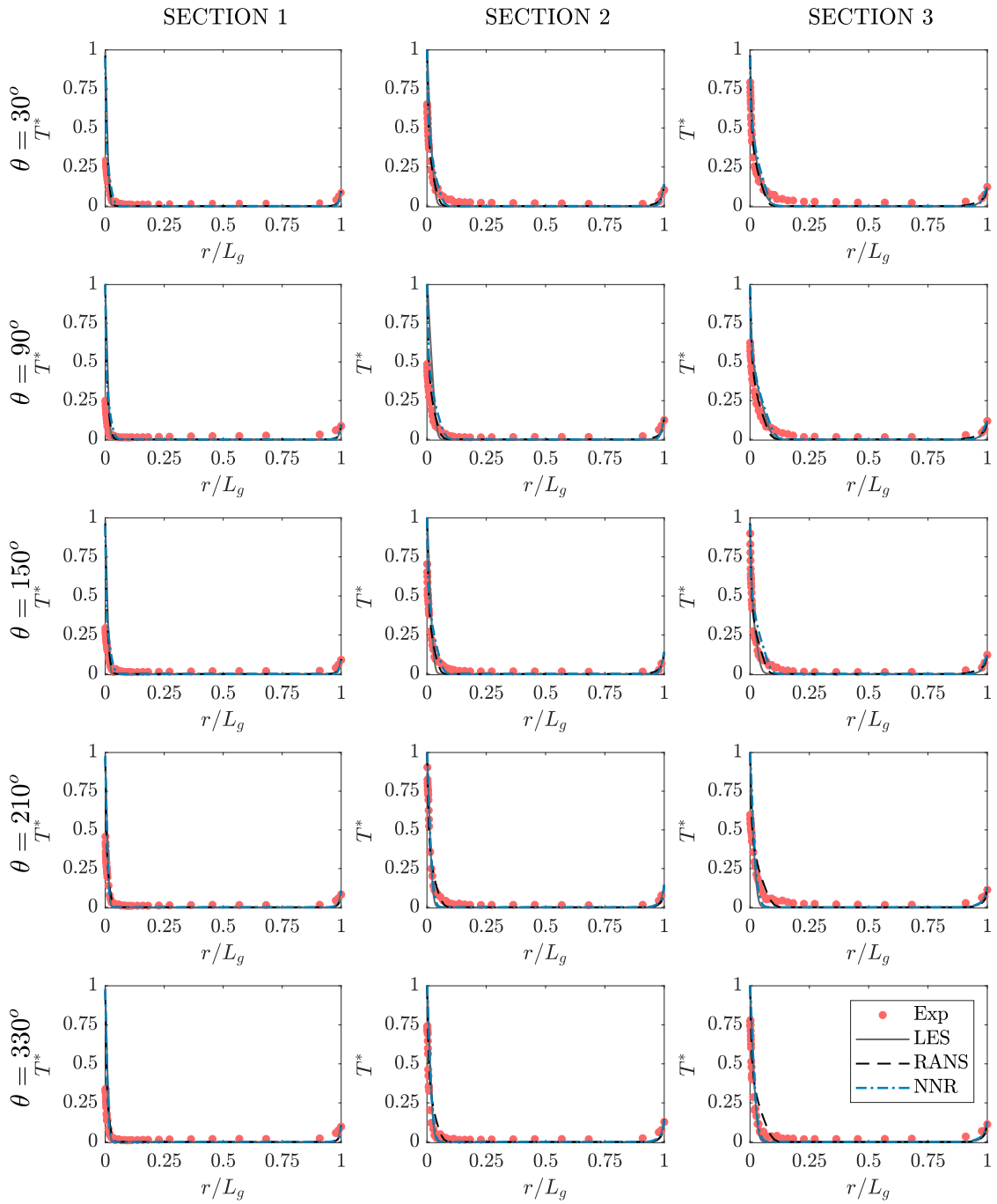

Figure 6.12: Temperature profiles in Case-3

6.5.4 Heat Transfer

The heat transfer predictions by the new model, NNR, will be compared against the two experimental data sets which are available for Case-A and Case-1 where the relatively thick boundary layer allowed a sufficient number of thermocouple measurements to be fitted in the conductive viscous sub-layer for heat transfer measurements as discussed in Chapter 3. The heat transfer results will be presented in Nusselt number form, $Nu = \frac{q'' D_i}{(T_i - T_\infty)k}$.

The experimental and numerical results including the new model, NNR, are presented for Case-A in Fig. 6.13 (a) whilst in Fig. 6.13 (b) the associated errors for each numerical method are shown in polar coordinate system. At Section 1, there is a heat transfer reduction in the upper half compared to the bottom, which is attributed to the buoyant flows which cause large temperature boundary layer leading to small temperature gradient. In general, the heat transfer characteristics are captured by RANS with an underprediction at the top of the heated inner cylinder at 90°. The new model, NNR, improves the underprediction at 90° with increased heat transfer. In the remaining measurement locations, both RANS and NNR model exhibit satisfactory agreement with the experimental data. At Section 2, the influence of buoyant forces becomes more apparent as seen in the heat transfer alternations in the upper half, which are caused by locally impinging and departing buoyant flows. LES results show that the heat transfer is enhanced in the upper half of the heated inner cylinder whereas RANS fails to capture this trend, yielding similar heat transfer rates to the bottom half. NNR is able to capture the increased heat transfer in the upper half. Looking at the error profiles, it is evident that NNR outperform the conventional RANS, leading to much better agreement with the experimental result. At the bottom half, both NNR and RANS are able to capture the heat transfer characteristics. At Section 3, both NNR and RANS show heat transfer maxima and minima which do not agree with the LES results which exhibit more uniform heat transfer distribution in the upper half. Although NNR slightly enhances the heat transfer at 90°, there is still significant heat transfer

underpredictions with both NRR and RANS. In bottom half, both models continue to agree well with the experimental and LES data.

Heat transfer predictions in Case-1 are shown in Fig. 6.14. Similar to Case-A, the heat transfer distribution trend is predicted by RANS and NNR which suggests enhanced heat transfer at the top of the heated inner cylinder, causing an overprediction at 90° in Section 1. At Section 2, there is a sudden heat transfer drop at the top at 90°. As discussed in Chapter 5, the significant heat transfer reduction at 90° arises from the thermal plume lift-off causing a large thermal boundary layer. The cross flow that pushes the hot-rising buoyant flow towards downstream, which causes a strong turbulent heat flux to occur in the streamwise direction as seen in Fig. 6.3. The conventional RANS that employs simple gradient diffusion hypothesis which scales the heat transfer with the mean temperature gradient does not predict the heat transfer in the upper half. On the other hand, NNR model takes into account the streamwise turbulent heat fluxes as well as the Reynolds stresses, which leads to improved predictions in this region. In the lower half of the annulus, all numerical predictions agree with the experimental results. In Section-3, it is interesting to note that the heat transfer profile in the upper half resembles that Case-A Section 2. It is evident in Fig. 6.14 that NNR is able capture the enhanced heat transfer in the upper half which is in better agreement with LES compared to RANS. The improvement is particularly seen at 150° which marks the elongated helical structure location as can be seen in 5.13 in Chapter 5. The conventional RANS yields overpredictions at 210° and 330° in the lower half of the annulus. This is attributed to the overpredictions in wall normal turbulent heat fluxes with RANS as shown in Fig. 6.4.

The heat transfer profiles for Case-D ($Ri = 0.078$) and Case-3 ($Ri = 0.032$) are shown in Fig. 6.15 and 6.16, respectively. As seen in both figures, there is a consistent overprediction of Nusselt numbers with NNR in the upper half of the annulus. These cases represent instances where the forced convection starts to dominate the majority of the flow field. Therefore, the discrepancy with NNR at Section 1 can be attributed to the dominance of streamwise velocity. Considering

the term 6.17 in the turbulent heat flux calculation, overpredictions in heat transfer in this region are expected. This trend can also be observed in other cases in Fig. D.1, Fig. D.2 and Fig. D.3 given in Appendix D, where the Reynolds number is progressively increased. Similarly, RANS also fails to capture the heat transfer profiles in the same region with overpredictions although as not severe as in NNR. At Section 2 in Case-D, the overprediction of heat transfer with NNR continues whilst RANS exhibit undepredictions. At Section 3, NNR yields the improved predictions whereas RANS underpredicts the heat transfer profile and shows alternations which does not agree with the LES results. As opposed to the upper half, NNR is able to capture the heat transfer reductions with increasing Reynolds numbers.

6.6 Conclusions

A new model, NNR, which incorporates and blends a Reynolds stress and a turbulent heat flux model has been developed for $k-\omega$ SST turbulence model and implemented in a commercial CFD package, ANSYS Fluent 2020 R1 [52] through user defined functions. NNR and the conventional RANS simulations employing the linear eddy viscosity for Reynolds stresses and the simple gradient diffusion hypothesis (SGDH) for turbulent heat fluxes have been performed for the experimental campaigns, and the results have been assessed using the data from the experiments and the scale resolving simulations.

NNR model has been developed to account for both strong three dimensional and laminar flow due to the buoyancy forces acting differently depending on geometrical features. It has been found that RANS yields nearly zero Reynolds stresses where the thermal plume creates a large temperature boundary layer whilst the new model, NNR, remarkably improves the predictions with the Reynolds stress profiles resembling the LES results. In the lower half of the annulus, thin temperature boundary layers are predicted by both NNR and RANS. With increased Reynolds numbers (therefore, reduced Richardson numbers), both NNR and RANS have accurately captured the flow field with the thin temperature

boundary layers. Overall, NNR is found to outperform the conventional RANS in the flow field predictions.

For the heat transfer profile results, NNR has increased the accuracy of the predictions, particularly at each side of the upper half of the heated inner cylinder in cases where a distinctive buoyancy influence on the flow field exists. The regions of improvements on each side mark the location of longitudinal enlarging helical structures which were identified with LES. In the lower half, NNR has exhibited similar results to NNR, both of which have been found to agree well with the experimental data.

With increased Reynolds numbers (decreased Richardson numbers) where the buoyancy effect is reduced, NNR has showed tendency to overpredict the heat transfer profiles, particularly at Section 1. This has been attributed to the strong dominance of the streamwise velocity which is used in the turbulent heat flux term with $tanh(\left|\frac{u}{v}\right|)$. Despite the excessive heat transfer at Section 1, NNR has predicted the reduction in heat transfer in the lower half with relatively lower Richardson number cases.

In general, mixed type of flows pose a great challenge to the accurate prediction of flow field and heat transfer characteristics with the RANS based turbulence modelling methods since a number of different flow regimes coexist in various locations. The new model, NNR, promises a great potential for these type of flows. In particular, if the general flow field is of interest, NNR is recommended. However, one should be aware of the shortcomings of both NNR and RANS for relatively higher Reynolds numbers if the heat transfer is the main subject of interest. If the influence of buoyant flow is expected to be pronounced, NNR should be used. Additionally, it is important to emphasize that NNR does not require any additional transport equation to be solved. In fact, NNR has been found to improve the stability of simulations compared to the conventional RANS, therefore faster convergence could be achieved, which is of great importance in industry where the time is a significant constraint.

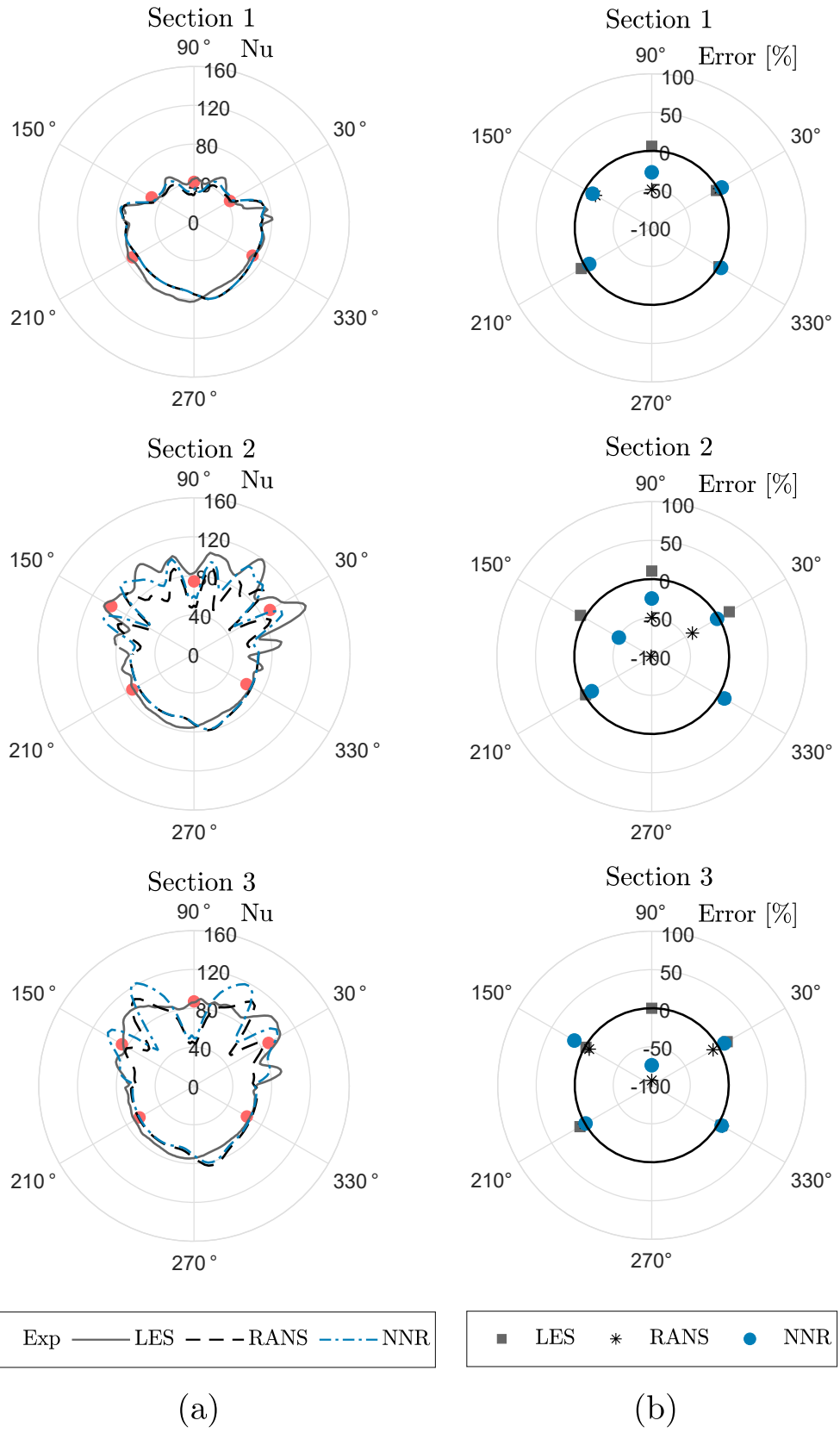

Figure 6.13: Heat transfer distribution in Case-A (a) Nusselt number comparison (b) Error (Solid black line represents 0% error)

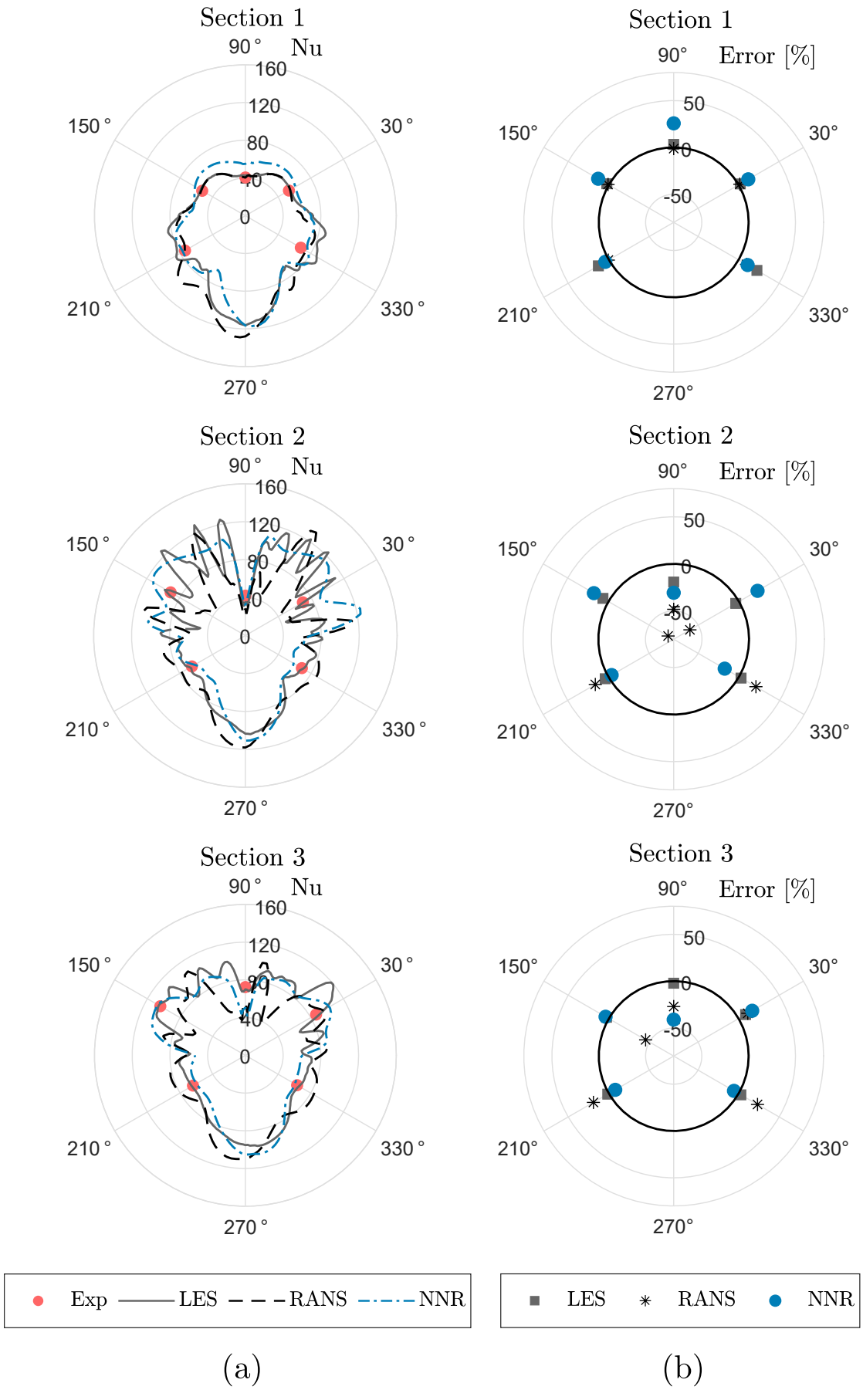

Figure 6.14: Heat transfer distribution in Case-1 (a) Nusselt number comparison (b) Error (Solid black line represents 0% error)

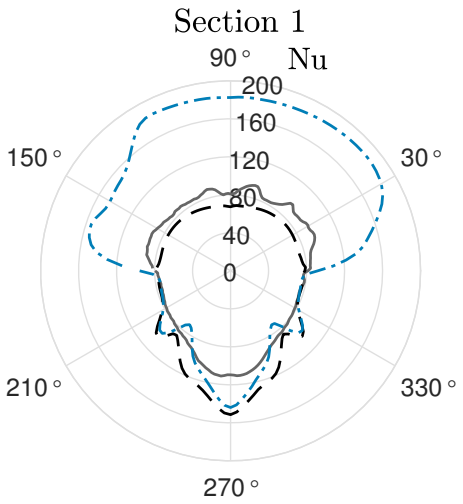

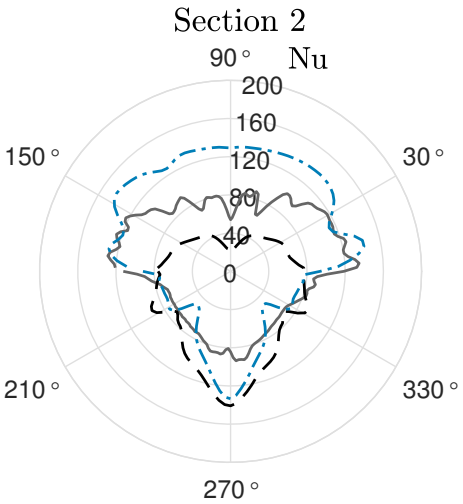

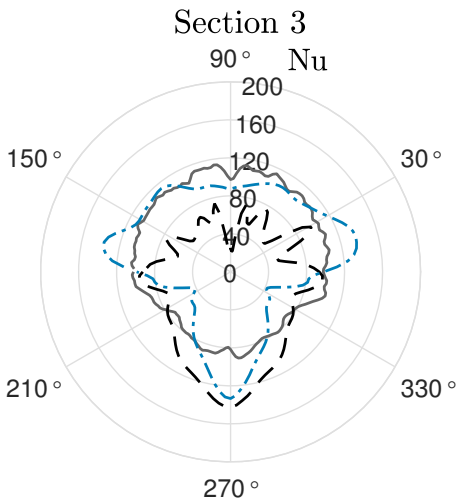



Figure 6.15: Heat transfer distribution in Case-D

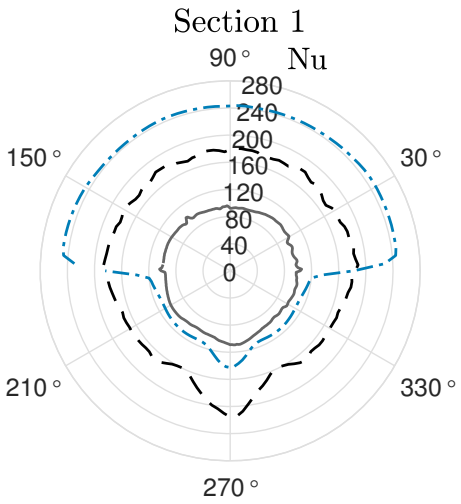

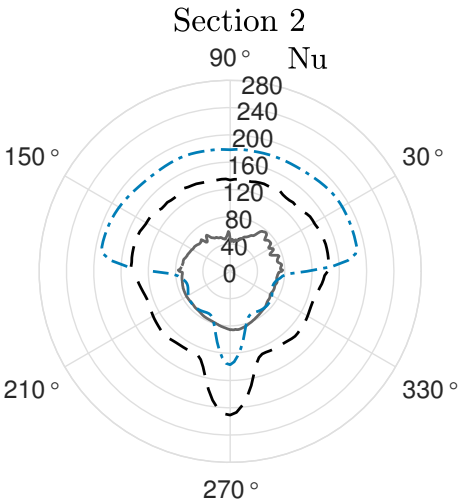

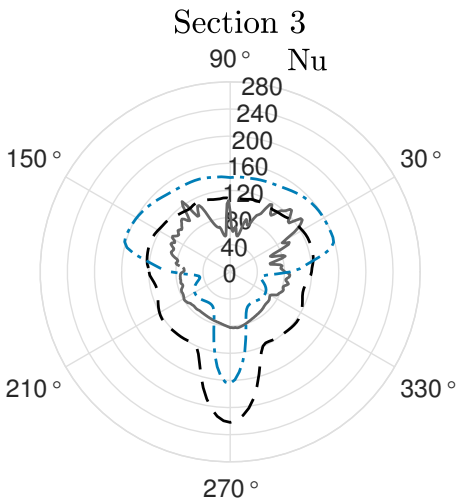



Figure 6.16: Heat transfer distribution in Case-3

Chapter 7

Flow Control

7.1 Introduction

During shut-down regimes, large power generation turbine casing cavities are exposed to various flow regimes with buoyant flows which arise from temperature differences between turbine components. As discussed in Chapter 4 and Chapter 5 with experimental and scale resolving simulations, the casing cavity flow field heavily depends on the dominance of buoyant flows. As highlighted with both quantitative and qualitative scale resolving LES results, heat transfer distribution around the heat inner cylinder is remarkably affected by the presence of turbulent structures which are triggered by buoyant forces. Experimental and numerical observations confirm that thermal boundary layers progressively develop in both axial and circumferential (from bottom to top) directions in all cases.

In cases where natural convection is clearly more dominant mode with a thermal plume at the top of heated cylinder, the temperature field non-uniformity is more severe, which is directly responsible for non-uniform heat transfer distribution with various temperature gradients occurring around the cylinder. Therefore, it would be desirable to suppress the effect of buoyant flows inside turbine casing cavities which take long time to cool-down to reach uniform temperature. Suppression of buoyant flows without increasing the bulk mass flow rate would reduce the time required for uniform cooling, and therefore contribute to enabling power generation turbines to operate more flexibly.

7.2 Design Exercises

7.2.1 Preliminary Design Modifications

Buoyancy driven flows due to temperature differences inside turbine casings with pure natural convection cause enhanced heat transfer on the outer cylinder where thermal plume impingement occurs. In mixed type of convection, the thermal plume may not reach the outer casing cylinder due to streamwise inertial forces depending on the engine operating condition. However, the influence of buoyant flows, even with mixed type of convection, on flow field and heat transfer characteristics is inevitable unless a cross-flow is introduced with sufficiently high mass flow rates which may not be always feasible. Therefore, suppression of buoyant flows, particularly thermal plume, should be investigated without increasing the bulk mass flow rate.

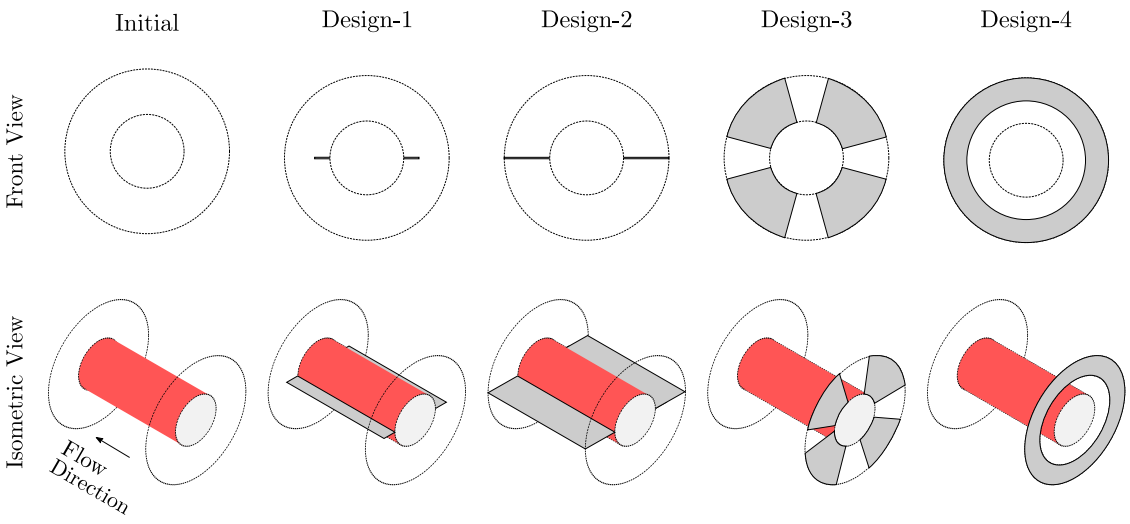

Figure 7.1: Flow control design exercises

In Fig. 7.1, four different design modification is proposed for preliminary numerical investigations. As seen in the figure, the initial design represents plain horizontal concentric annulus. With Design-1 and Design-2, the aim is to prevent

thermal boundary layer development which progressively increase in thickness as it reaches the top. Therefore, winglets of different sizes are placed at each side of the heated inner cylinder to interrupt the boundary layer development. The idea behind Design-3 and Design-4 is to disturb the buoyant flow field and to create a local jet effect, respectively. The plates in Design-3 and Design-4 are placed at the beginning of test section (between Section 1 and Section 0) before the thermal boundary layer starts to develop, the location of plates are illustrated in Fig.7.2.

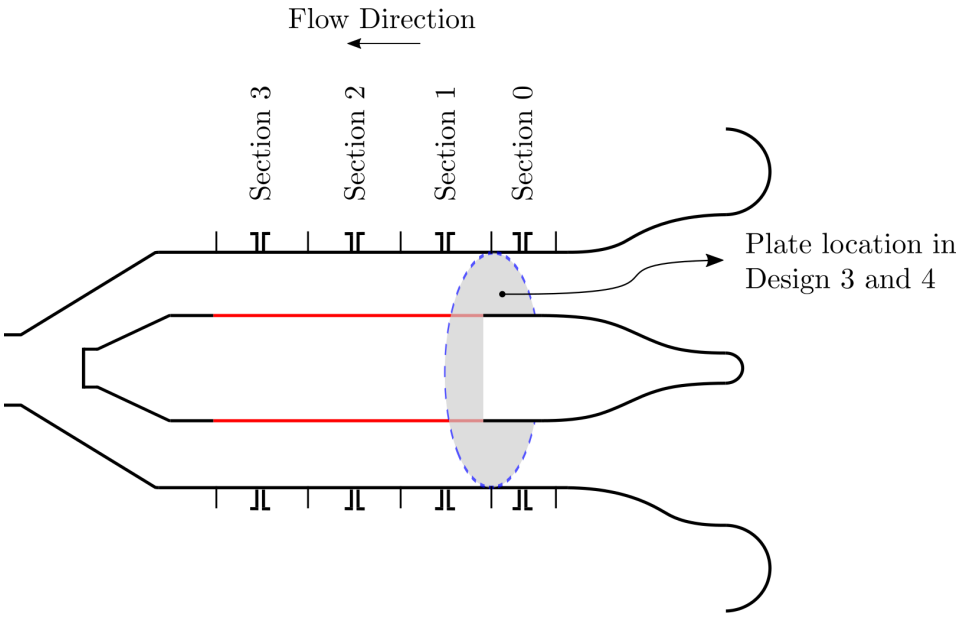

Figure 7.2: Plate location in Design 3 and 4

For preliminary performance tests of each proposed design, the computational domain did not include the entrance region and inlet contraction for faster initial tests. As presented in Chapter 4, Case-A represent the highest Richardson number case among all experimental cases, which exhibits the thickest boundary layer at the top of heated inner cylinder as can be seen in Appendix A. Therefore, Case-A is an ideal instance to evaluate the effectiveness of each design with the strongest buoyancy influence on the flow field.

7.2.2 Preliminary Simulations

Preliminary simulations were performed with ANSYS Fluent 2020 R1 [52]. Pressure based solver with $k-\omega$ SST turbulence model was used with second order upwind scheme for spatial discretisation. The Boussinesq approximation was employed to account for the density changes due to the temperature variation. RANS simulations were performed in a steady manner. The new model presented in Chapter 6 was not used for the flow control simulations since the new model was found to overpredict the Reynolds stresses for flows with weak buoyancy influence in the flow field.

Figure 7.3 shows the streamwise and circumferential (at Section 3) flow field with non-dimensionalised temperature profiles in each design. Initial design which does not include any design modification exhibits a thermal plume region with a large temperature boundary layer at the top of heated inner cylinder. In Design-1, the circumferential thermal boundary layer development is interrupted with short winglets at each side. The upward movement of the boundary layer which starts developing from the bottom is blocked. However, there is a fresh boundary layer forming immediately after the winglet. Subsequently, the boundary layer recovers quickly at the upper half which then causes a thermal plume to occur at the top as if the boundary layer is never interrupted. This can be seen in the streamwise temperature field which is nearly identical to the Initial case with large boundary layer. Similar observations can be made in Design-2 which yields similar streamwise and circumferential flow fields to those in Initial and Design-1.

Although the thermal plume at the top is avoided in Design-3, the temperature field non-uniformity is still present. On the contrary, in Design-4, the thermal plume does not exist at top. In addition, the temperature field in the entire annulus is much more uniform with a thin boundary layer around the heated inner cylinder. It is evident that the influence of buoyant flows on the flow field is significantly reduced compared to both Initial case and the other designs. Therefore, Design-4 is selected to proceed with further experimental and numerical analyses for suppression of buoyancy forces. Design-4 is referred to as blockage plate hereafter.

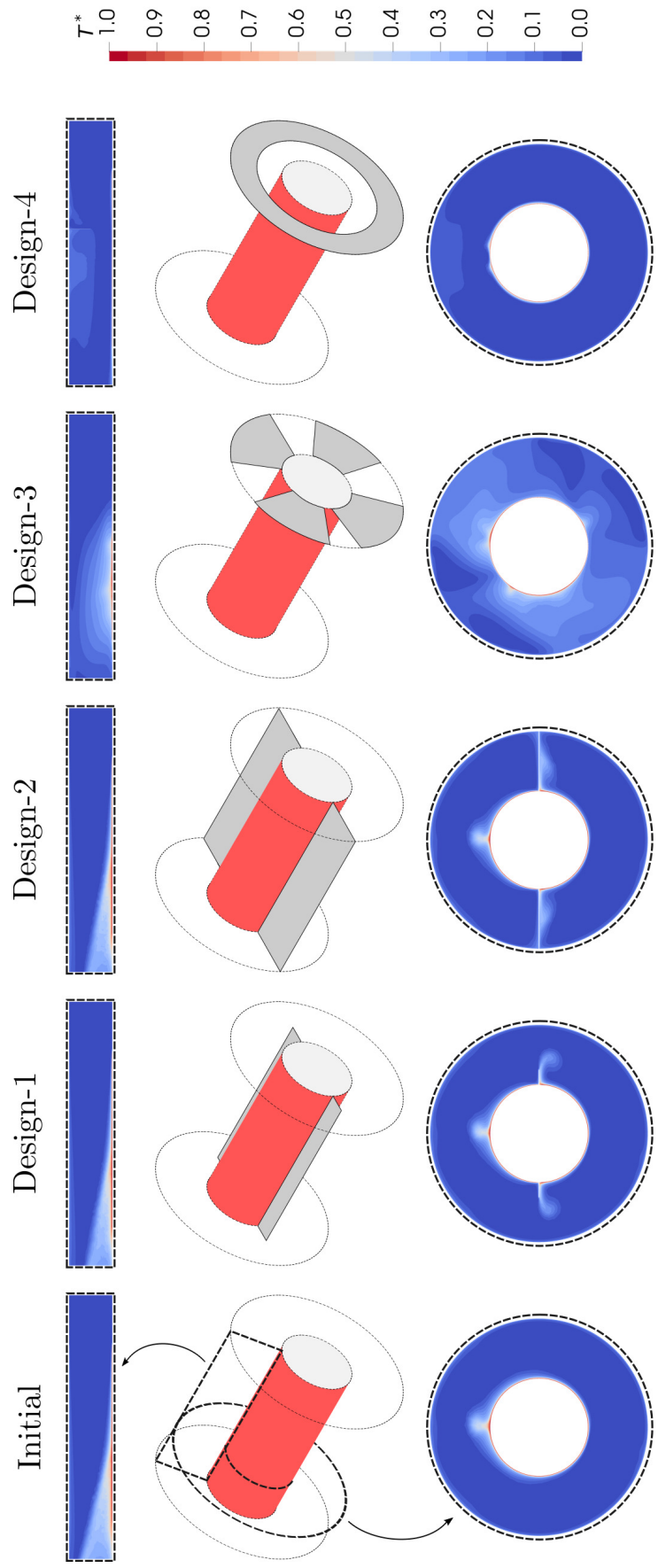

Figure 7.3: Temperature field in each design

7.3 Blockage Plate Experiments

The experimental facility was modified for the blockage plate experiments. Thanks to the modular design of the rig, the blockage plate which is an aluminium sheet with a thickness of 1.5 mm was easily was placed at the upstream of test section between Section 0 and Section 1 as shown in Fig. 7.4. With the blockage plate, the initial gap width, $L_g = 220$ mm, between the inner and outer cylinder is reduced to $L_{gb} = 110$ mm.

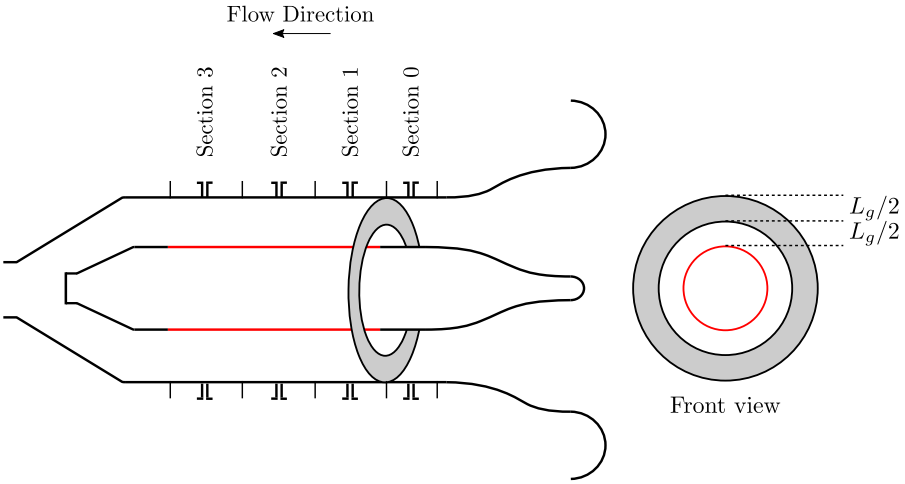

Figure 7.4: Schematic of the modified rig with blockage plate



Figure 7.5: A photograph of the modified rig with blockage plate

Case-A, Case-B (Case-1), Case-C (Case-2) and Case-D were selected to perform the blockage plate experiments since the thermal boundary layer at the top of the heated inner cylinder was discernibly thicker than other circumferential locations, indicating that the buoyancy influence was strong in the selected cases. Similarly, the blockage plate experiments were not conducted for the remaining cases where the buoyant flows were already suppressed, leading to circumferentially uniform boundary layer. In the blockage plate cases, the same mass flow rates as in initial cases were maintained. For each selected case, a suffix "M" (referring to *modification*) is added after the case title to indicate the blockage experiment performed at each corresponding base-line case condition (e.g., Case-AM was run with Case-A operating conditions).

The same experimental methodology as the initial experiments was followed for the blockage experiments. The circumferential temperature measurements at each measurement section are given in Fig. 7.6, Fig. 7.7, Fig. 7.8 and Fig. 7.9 for Case-A, Case-B (Case-1), Case-C (Case-2) and Case-D, respectively.

The experimental results prove that the blockage plate modification successfully suppress the thickening of the boundary layer due to the buoyancy forces at the top of the heated inner cylinder. At each section, particularly at Section 3 where the influence is pronounced the most, circumferentially uniform temperature boundary layer is achieved.

With the blockage plate, the flow is energised at the reduced gap width. In other words, the Reynolds number is locally increased which effectively reduces the Richardson number. Therefore, the flow field resembles that of a forced convection dominant case. It is noticeable that the mid-gap temperature is slightly deviated from the free-stream temperature with elevated values. Before each run, the inner casing was heated with no presence of cross-flow until the outer casing temperature stabilized. When the cross-flow was introduced, the outer casing temperature was dropped to a certain level. However, the outer casing temperature remained relatively warmer with the blockage plate experiments since the plate prevented the incoming flow to cool down the outer casing.

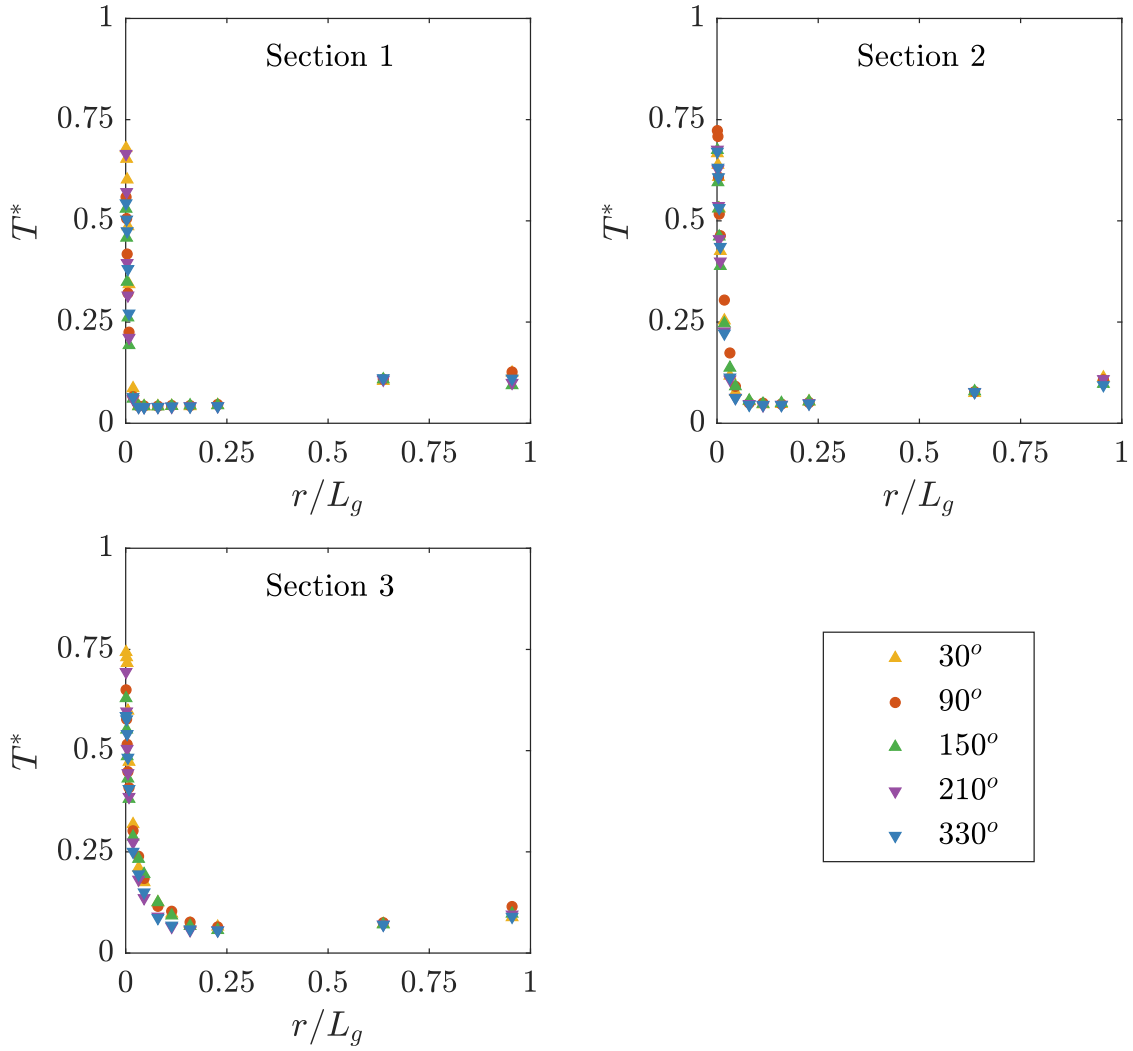

Figure 7.6: Radial temperature profiles in Case-AM

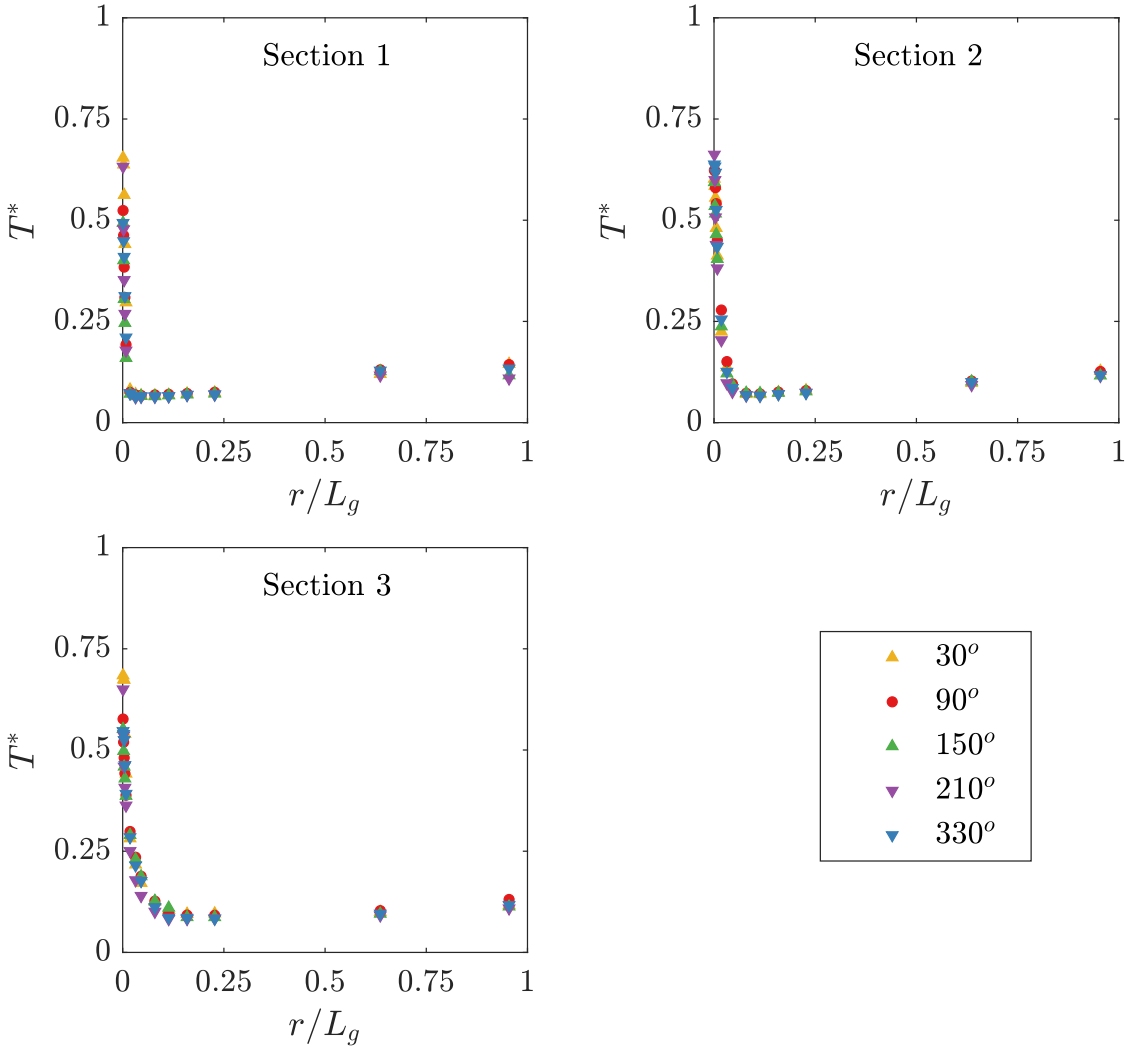

Figure 7.7: Radial temperature profiles in Case-1M

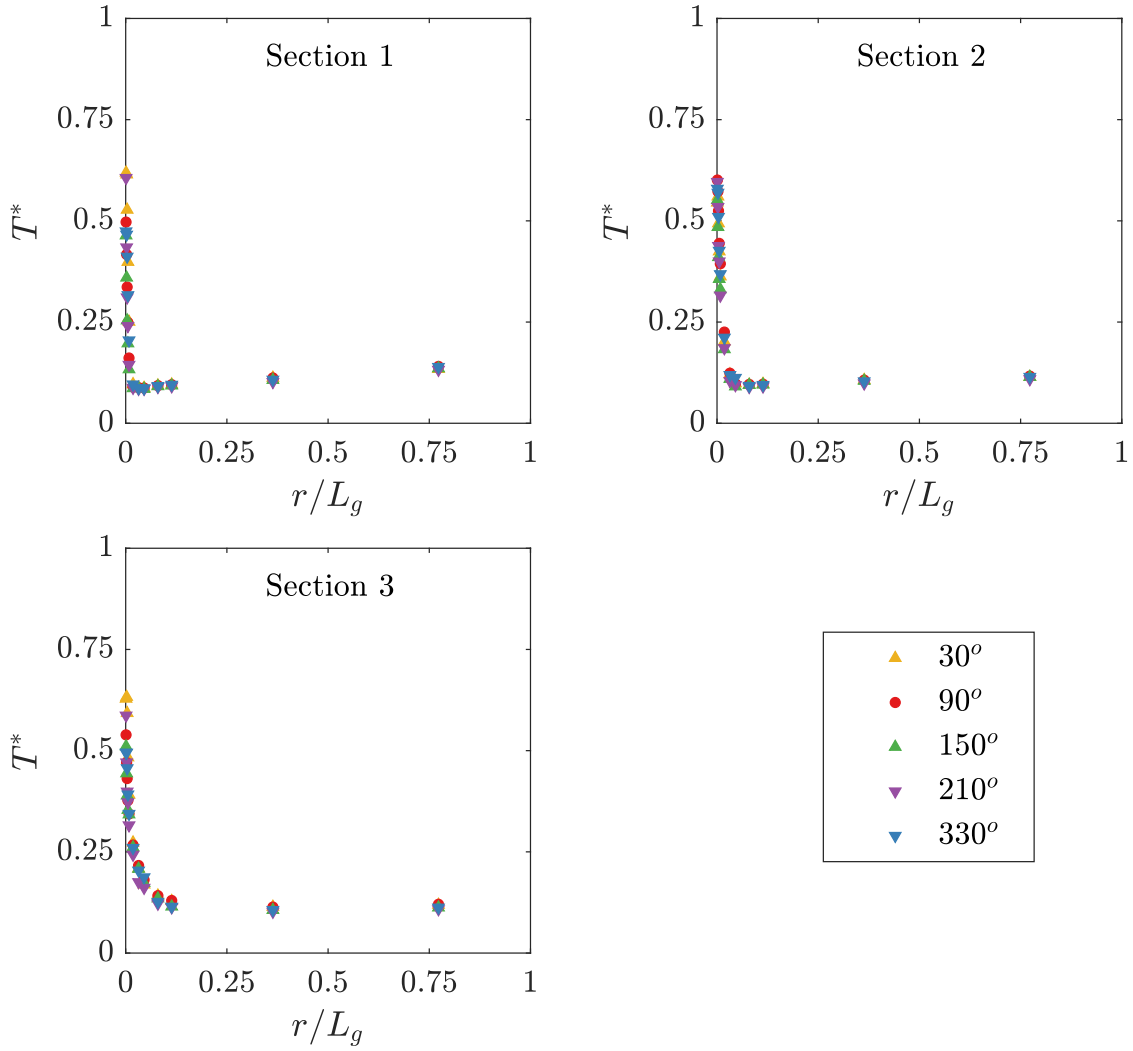

Figure 7.8: Radial temperature profiles in Case-2M

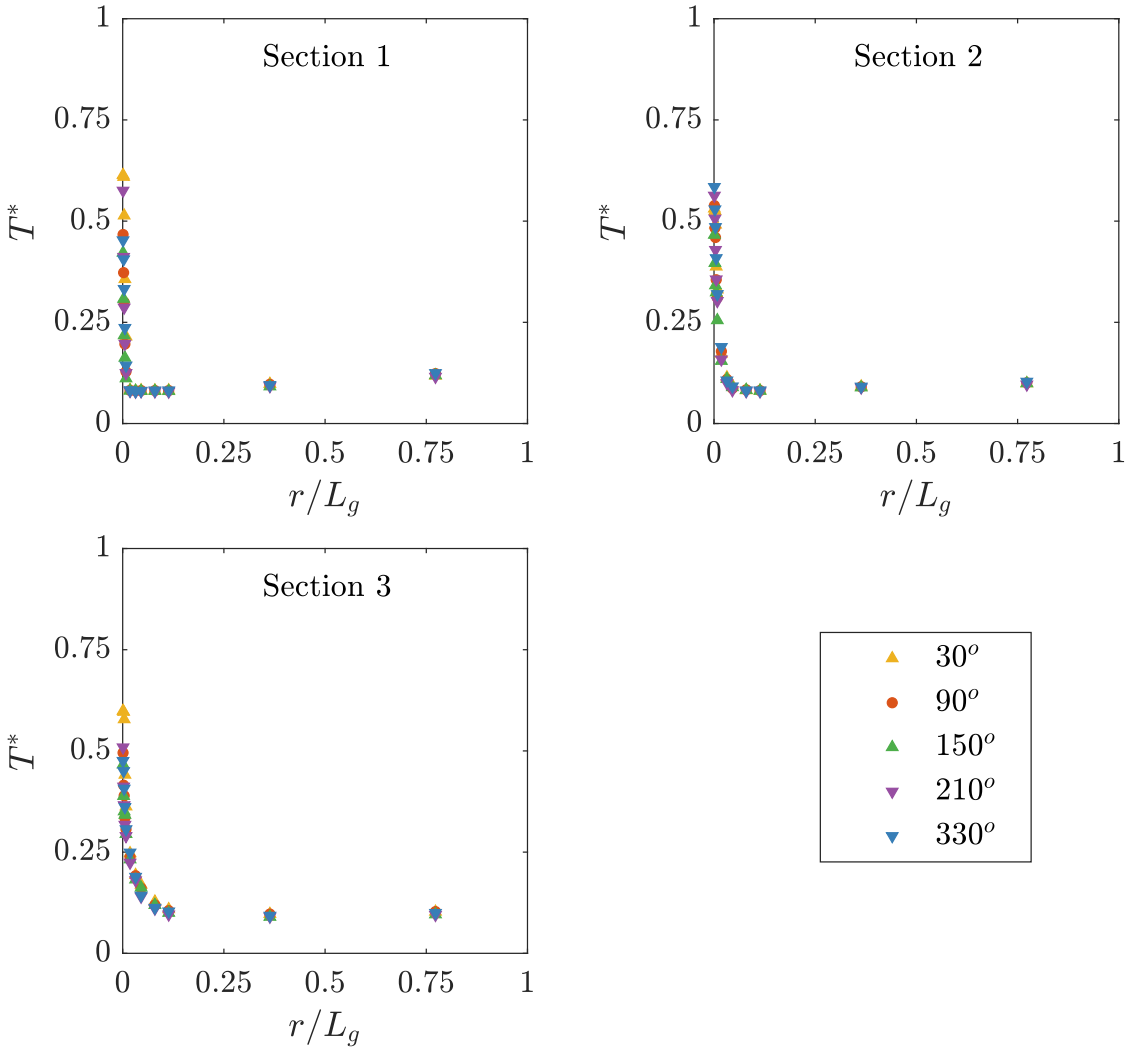

Figure 7.9: Radial temperature profiles in Case-DM

7.4 Blockage Plate Simulations

Steady-state RANS simulations were performed for the blockage plate experiments. The $k-\omega$ SST turbulence model was employed with second order upwind scheme for spatial discretisation. Structured hexahedral type mesh containing 3.3 $\times 10^6$ nodes which are clustered towards the walls to maintain $y^+ < 1$ (without any wall function) was used in the simulations. The computational mesh is shown in Fig. 7.10.

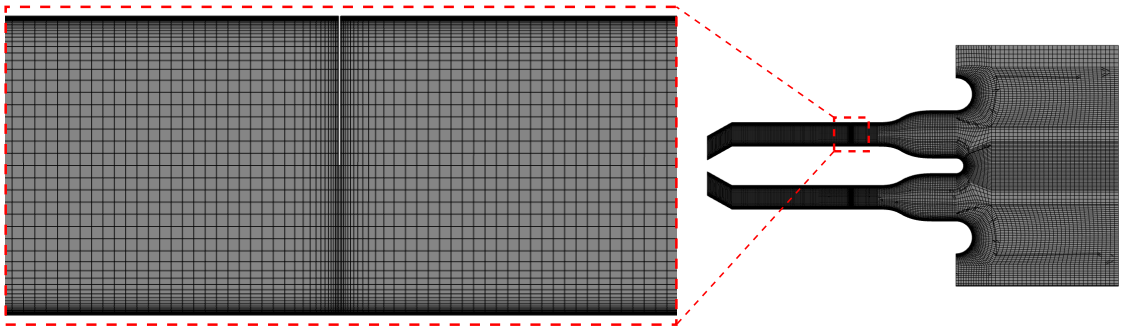

Figure 7.10: Computational mesh for blockage plate

The experimental and RANS temperature profiles are presented here for only Case-AM and Case-1M for brevity, which are shown in Fig. 7.11 and Fig. 7.12, respectively. The results for Case-2M and Case-DM are given in Appendix E. In all simulations, good agreement between experimental and RANS results is observed, which increases confidence in qualitative interpretations for the simulation results.

In Fig. 7.13, temperature field at each measurement section is shown for direct comparison of Case-1 and Case-1M. Case-1 temperature field is from LES study which was presented in Chapter 5. As discussed in LES results, Case-1 represents an instance where the thermal plume region is present at Section 3. The progressive development of thermal boundary layer from Section 1 to Section 3 in Case-1 appears to be interrupted in Case-1M. At Section 1 and Section 2, uniform boundary layer at the cylinder circumference is achieved. The thermal plume at Section 3 is now completely suppressed in Case-1M.

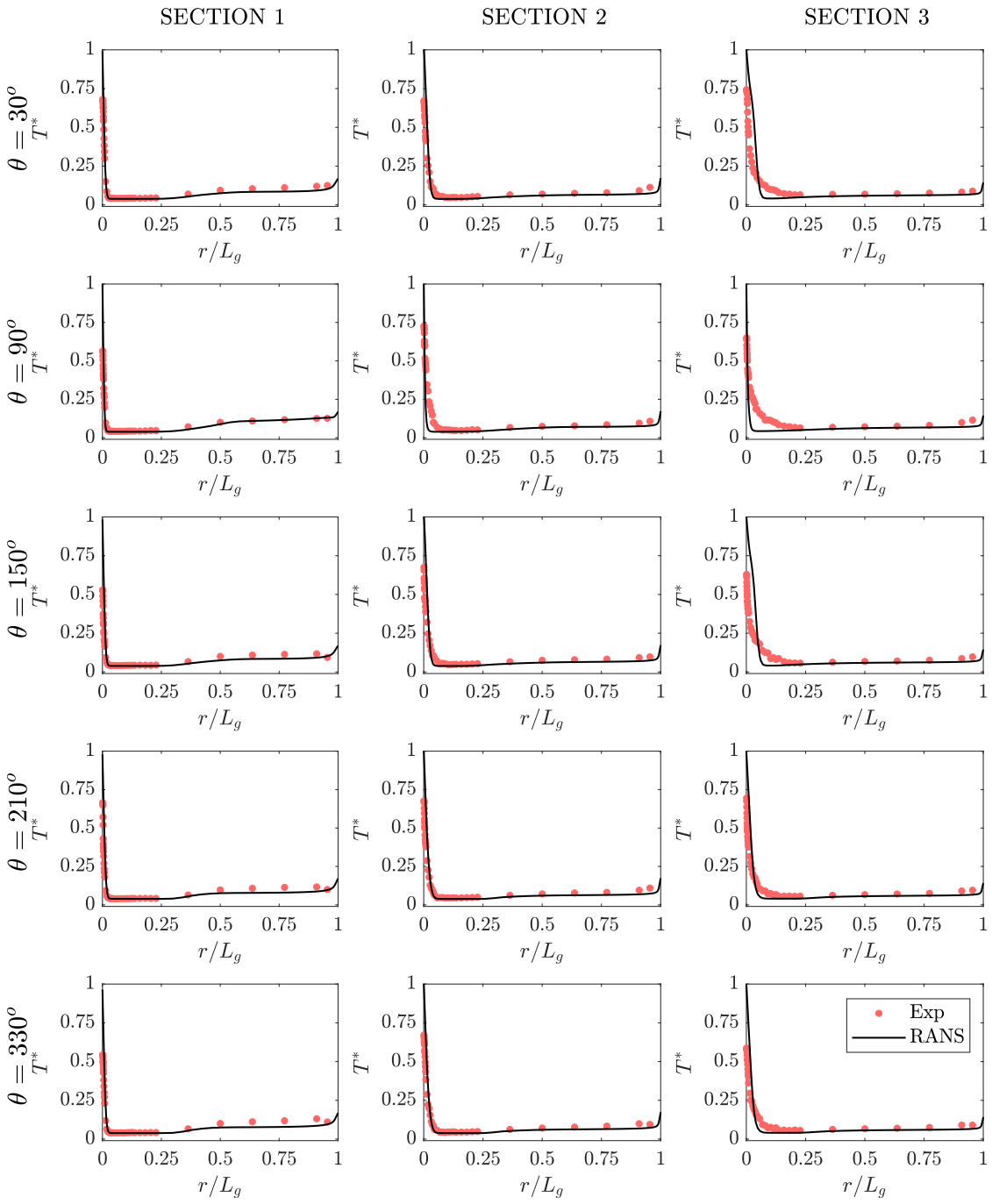

Figure 7.11: Experimental and RANS temperature profiles in Case-AM

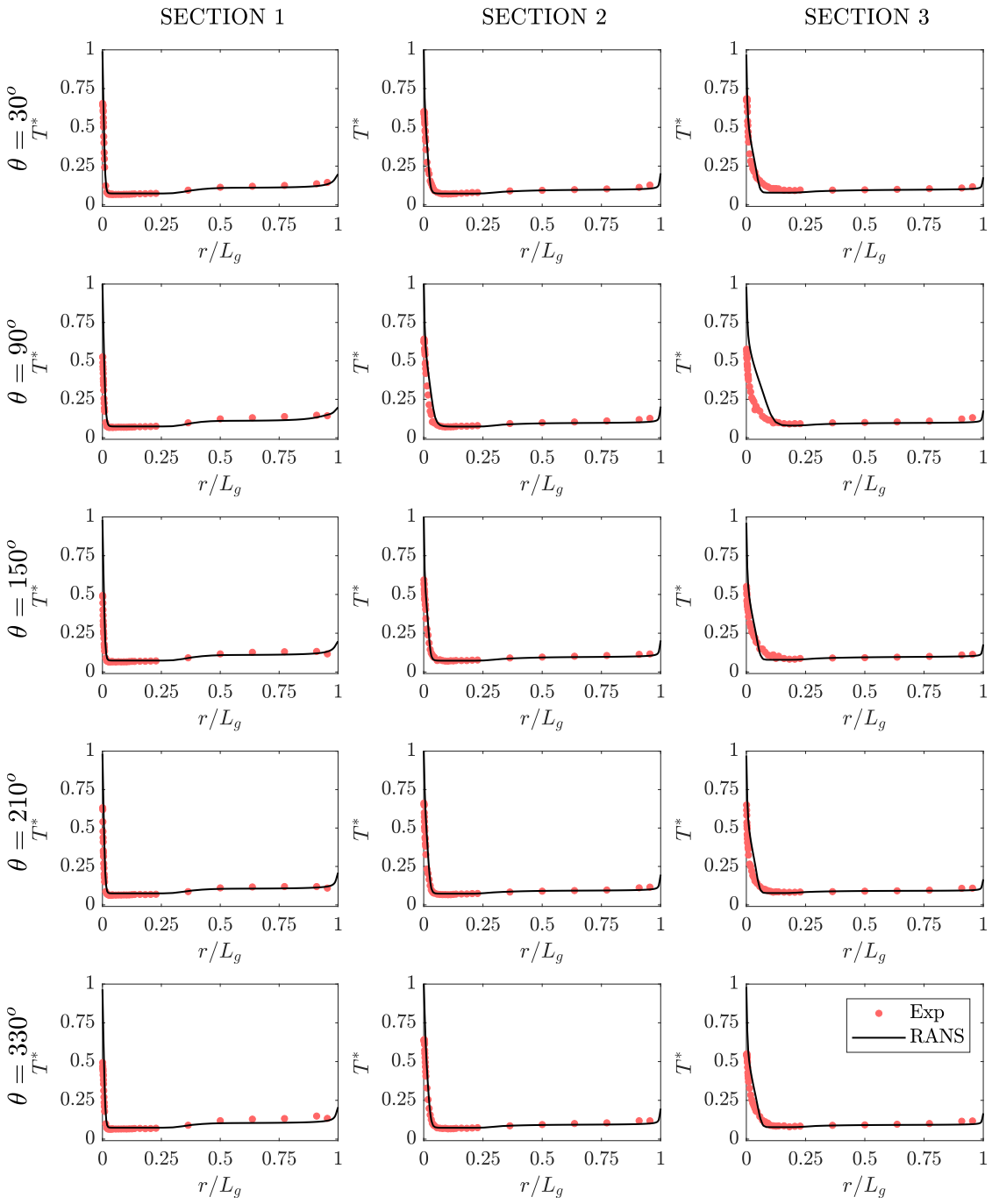

Figure 7.12: Experimental and RANS temperature profiles in Case-1M

Non-dimensional velocity field near the blockage plate region is given in Fig. 7.14 with the arrows that scale with velocity magnitude. It is clear that the flow is accelerated with the reduced gap width due to the blockage plate. The flow acceleration creates a local jet which remains attached to the heated inner cylinder. Consequently, the buoyancy influence is eliminated with strong inertial force that is present along the heated inner cylinder.

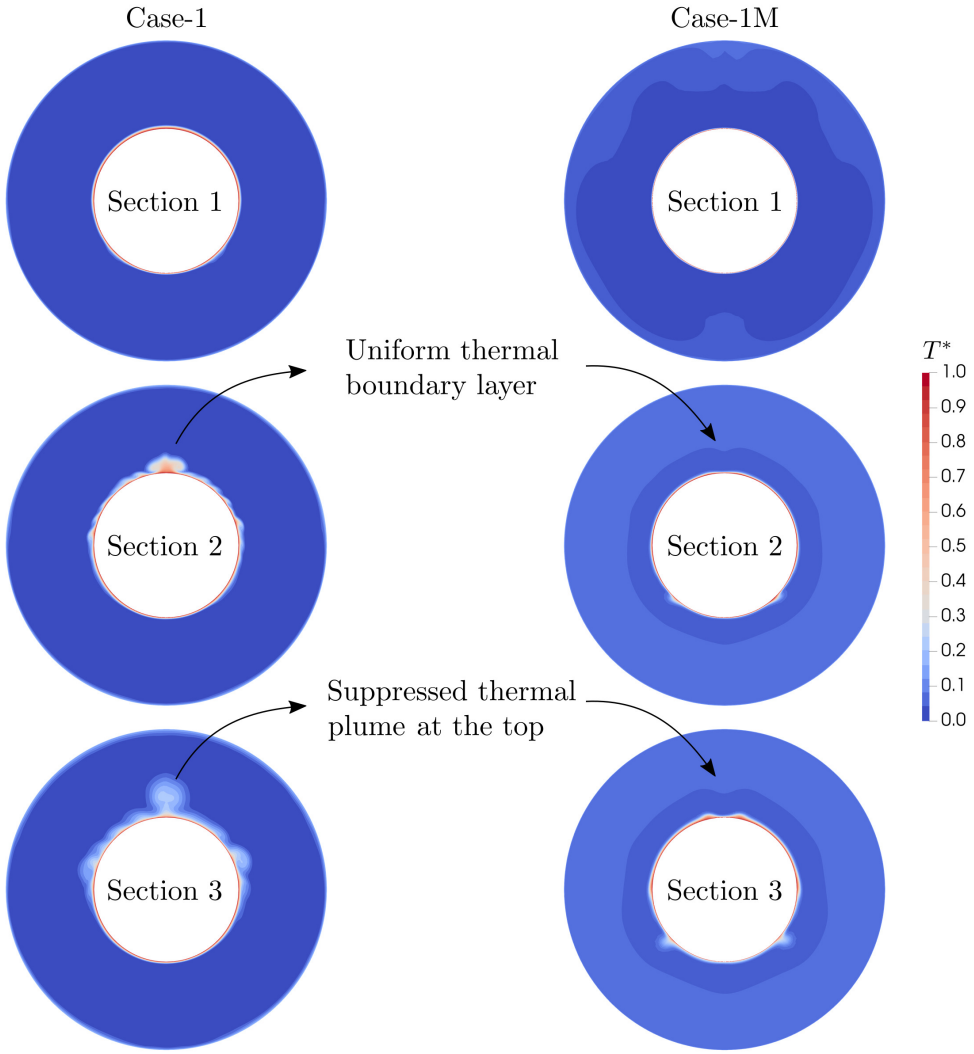

Figure 7.13: Case-1 (no blockage) and Case-1M (blockage) temperature field comparison

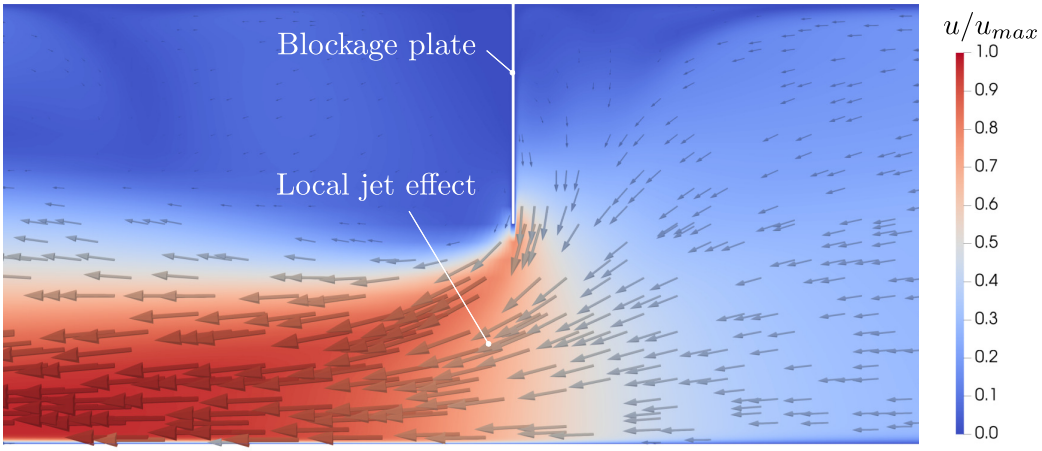

Figure 7.14: Velocity field in the blockage region

7.5 Conclusions

Various design exercises have been performed to modify the experimental facility for suppression of the buoyant dominated flow field. After the preliminary numerical investigations, Design-4 with a blockage plate has been found to decrease the temperature non-uniformity remarkably.

Experiments have been conducted on the modified facility with an aluminium blockage plate which occupies half of the gap width between inner and outer cylinder. The blockage plate experiments have been selected from the initial experimental campaigns where the buoyant field was discernible. The experimental results have confirmed that the circumferentially uniform temperature boundary layer could be achieved with a blockage plate located at the upstream of test section.

Steady-state RANS simulations have been validated against the blockage plate experiments. The flow field contours have highlighted the suppression of the thermal plume developing at the top of heated inner cylinder. Additionally, it has been shown that the non-uniformity in temperature field at the entire test section is achieved due to the local jet created between the heated inner cylinder and the blockage plate.

Overall, the experimental and numerical results suggest that the flow non-uniformity could be improved with a simple modification on turbine casing.

Chapter 8

Turbine Casing Roughness

8.1 Introduction

Casting is a commonly encountered manufacturing process in turbomachinery industry. In particular, large steam and gas turbine casings are casted since machining such large components is not possible. Casting process inevitably results in irregularities on the surface of casted component due to mold and casting temperature, and sandblasting. These surface irregularities may lead to skin friction enhancement, therefore increase in heat transfer [11]. It is therefore important to understand the influence of turbine casing roughness on flow field and heat transfer characteristics.

The objective of the present study is to provide detailed analysis of heat transfer and aerodynamics with the presence of the casting roughness based on a surface scan. Since the cast roughness is rather stochastic by nature, roughness heights may vary at each and every casting process. Therefore, two additional rough surfaces are generated in order to cover a wider range of surface elevation. Although there is a large body of literature available for surfaces with random roughness elements based on detailed surface scans, to the best of author's knowledge, scale resolving simulations of the casting roughness encountered in the turbomachinery industry based on a surface scan to investigate both heat transfer and aerodynamics have not been performed in the literature, and therefore are presented in the present study for the first time.

8.2 Scan of Cast Iron Surface

8.2.1 Scan of Cast Iron Patch

For the surface data acquisition, *Alicona Infinite Focus* 3D Profilometer has been used to scan a patch of cast iron surface as seen in Fig. 8.1 (turbocharger volute surface). The asperities on the surface (in the wall normal direction - y) with corresponding x and z coordinates in the streamwise and spanwise directions, respectively are obtained. Although on visual inspection the scanned surface patch appeared flat, the scanning process revealed that the surface was slightly curved. In order to achieve a flat surface which would then be mapped onto a flat plate to create a computational domain, the surface angle was corrected (flattened) by adjusting the surface normals.

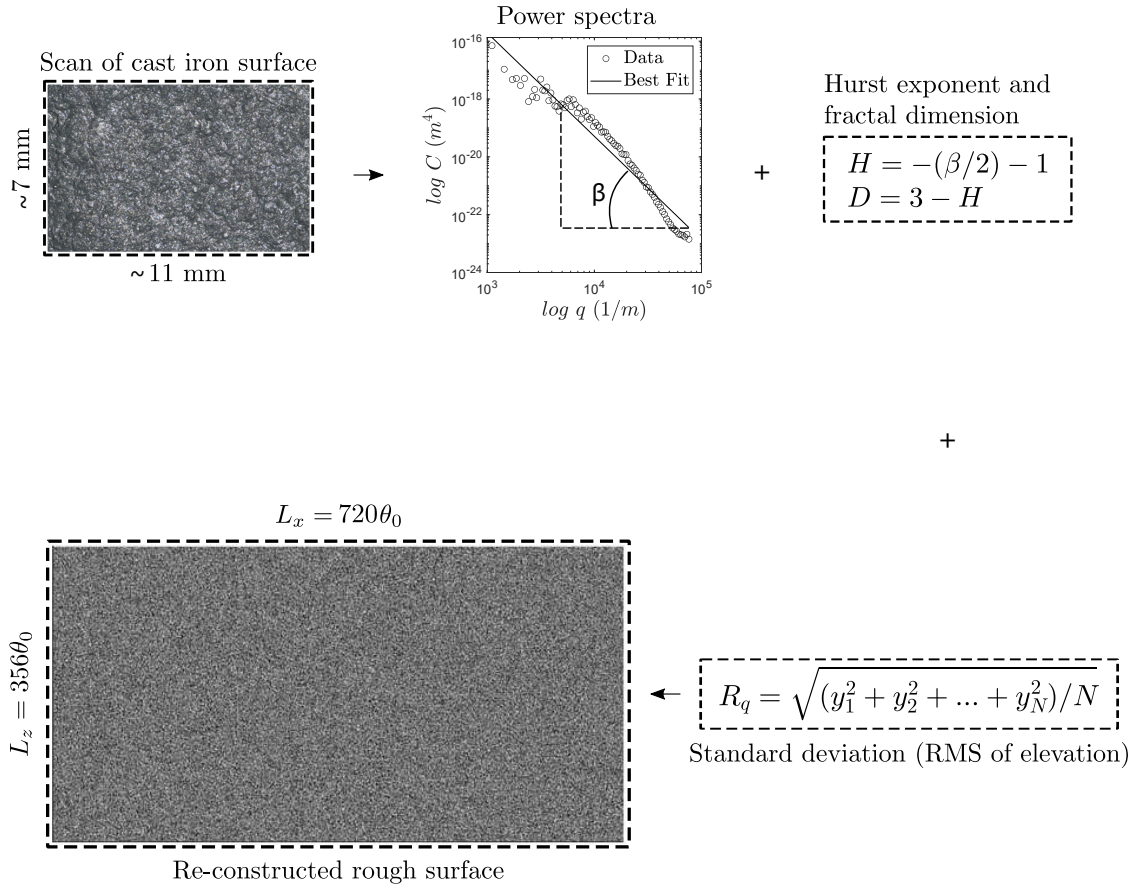

Figure 8.1: Re-construction of rough surface

8.2.2 Reconstruction of Rough Surface

The scanned cast iron patch of a turbocharger volute casing has dimensions of approximately 7 mm × 11 mm as shown in Fig. 8.1. The size of the patch is arguably small in the context of turbomachinery. Therefore, the scanned data was analysed to obtain the topographical information (e.g., power spectra, Hurst exponent, RMS of elevation), then a larger surface which exhibits the similar surface characteristics as the actual patch was created following the methodology in [136].

The dimensions of the generated surface shown in Fig. 8.1 are non-dimensionalised by the momentum thickness at inlet of preliminary simulation which will be discussed in the numerical methodology.

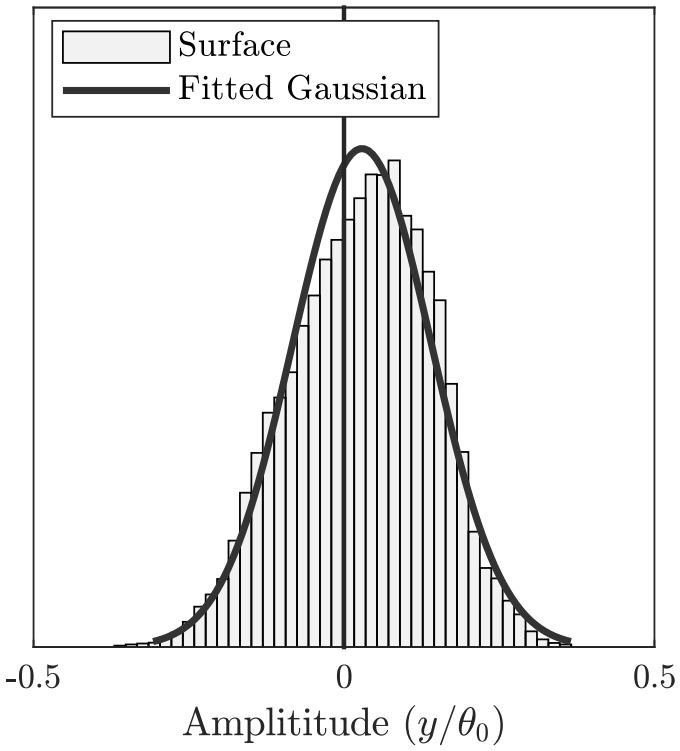

Figure 8.2: Histogram of the scanned rough surface

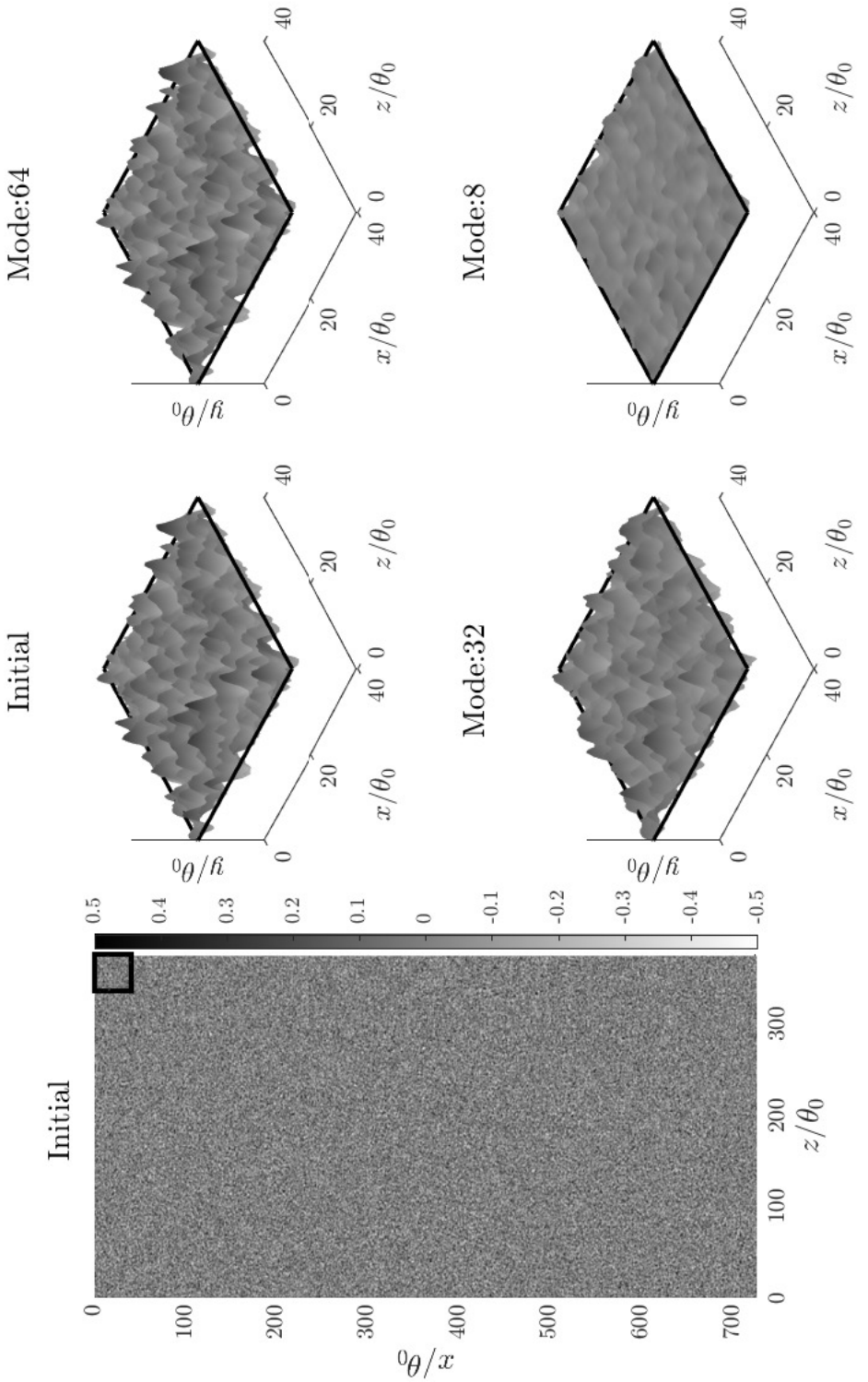

Figure 8.3: Reconstruction of initial rough surface with singular value decomposition

The re-constructed rough surface is, however, still not suitable for the numerical analysis since it inherently exhibits small scales due to the noise in the measurements [137], which cannot be resolved in simulations due to computational constraints. As stated in the study of Mejia-Alvarez and Christensen [138], removing the small surface asperities do not affect the flow field considerably. Once the surface topography is defined as a matrix which contains the height information at corresponding streamwise and spanwise coordinates, the matrix -A can be decomposed by a singular value decomposition (SVD) as seen in Eqn. 8.1.

$$A_{m\times n} = U_{m\times m} \cdot S_{m\times n} \cdot V^T_{n\times n} \tag{8.1}$$

where U and V are orthogonal matrices, and S is a diagonal matrix which contains the dominant mode amplitudes of the surface height information in descending order [139].

The surface height profile closely follow the Gaussian distribution as shown in Fig. 8.2. The re-constructed surface labelled as "Initial" and close-up views of three modes, namely 64, 32 and 8 are shown in Fig. 8.3. Mode:64 is the closest to the initial surface among other modes shown in terms of surface characteristics. Mode:32 has been selected over Mode:64 to be used in the simulations to reduce the stringent computational requirements. Although the average roughness height of Mode:32 is 15% less than that of initial surface, the height difference is indirectly addressed in the additional scaled surfaces (e.g. 25% and 50% scaled-up surfaces). Hereafter, Mode:32 is referred to as Rough surface.

Since the surface quality is affected by the material selection, moulding, shot blasting and other processes when casting turbine casings, roughness height may occur at various levels. To this end, the height map of the rough surface is scaled up to create two additional surfaces, namely, +25% and 50%. This extends the roughness height range investigated in this study. Thus, three surfaces with different roughness heights, the details of which are given in Table 8.1, are used and compared in the simulations. The close-up views at xy plane for each surface are illustrated in Fig. 8.4.

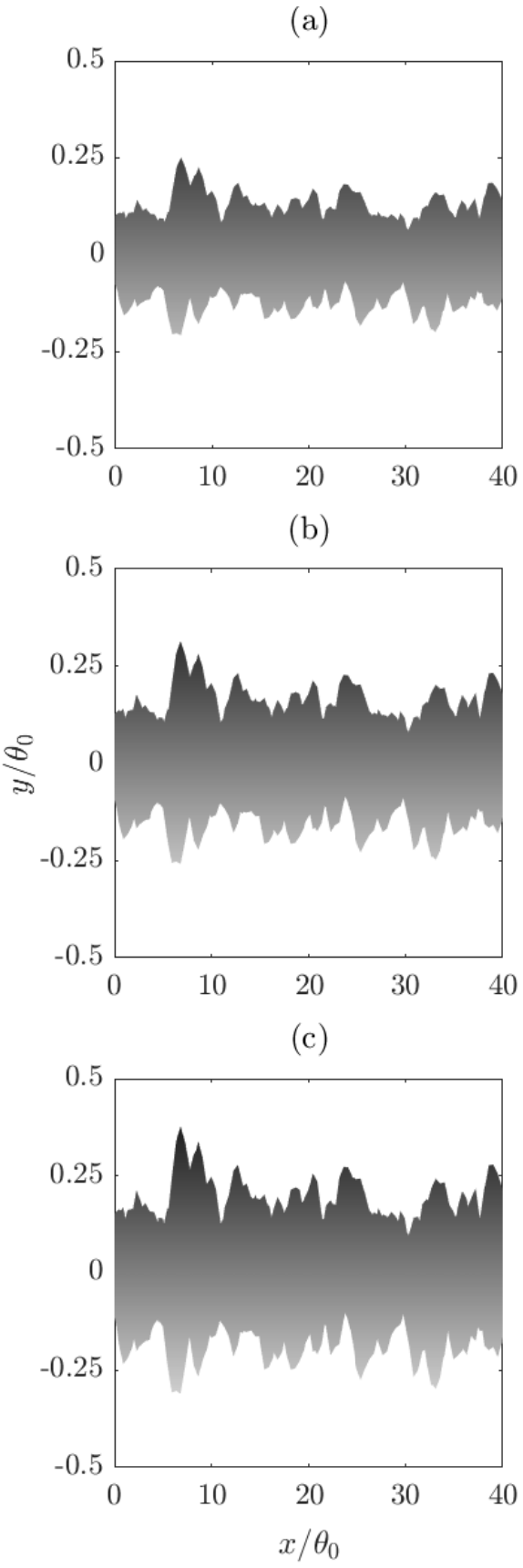

Figure 8.4: Close-up views of (a) Rough surface (b) Scaled +25% (c) Scaled +50%

8.3 Precursor Simulation

8.3.1 Precursor Simulation Methodology

There has been a tremendous progress in realistic inflow turbulence generation techniques for scale resolving simulations to overcome the difficulty of defining the turbulent eddies at inlet as a function of time. Some of them include weak/strong recycling/rescaling, synthetic turbulence generation methods (e.g., Fourier, digital filtering) and precursor simulations. Since it is not in the scope of this work, readers are referred to the review of these methods from [140] and [141].

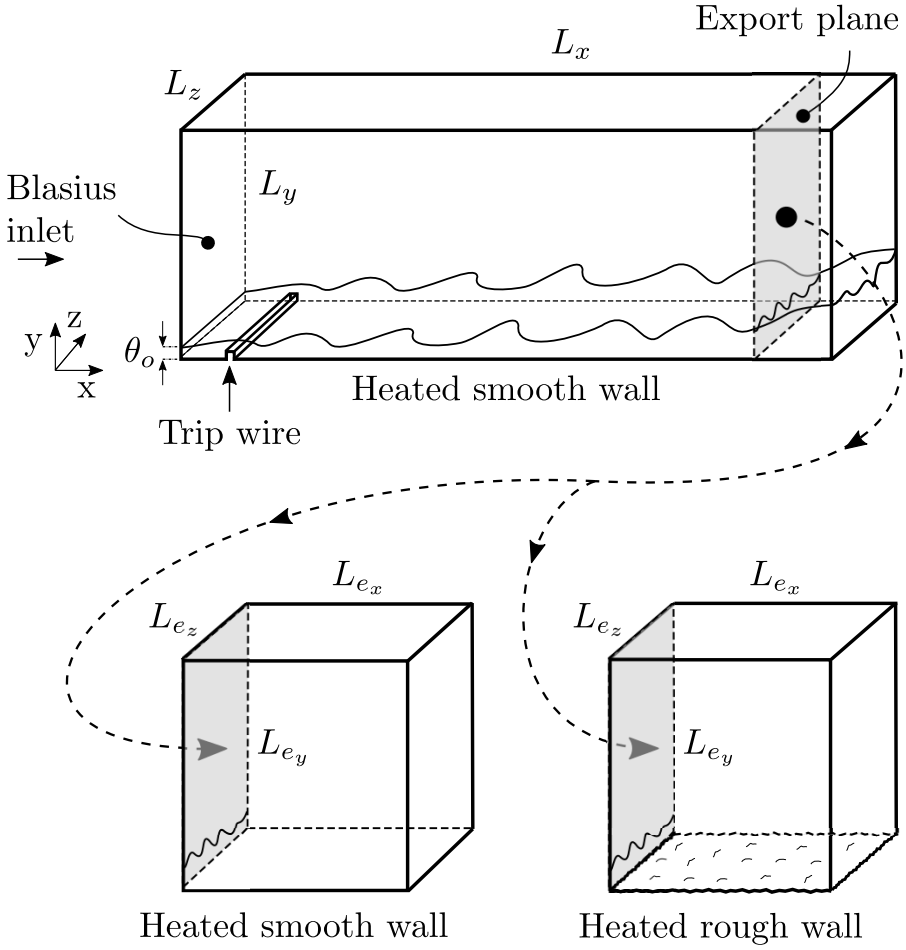

Figure 8.5: Computational domain and methodology

All simulations have been performed with ANSYS Fluent 2020 R1 [52] to solve the incompressible Navier-Stokes equations in the present study. Realistic inflow boundary conditions have been generated using a precursor wall resolved LES of

spatially developing thermal boundary layer over a heated flat plate with $Pr = 0.71$. Unsteady flow field from a recycling/export plane located at $x/\theta_0 = 5440$ has been saved and introduced at the inlet of extension domains which contains smooth and rough surfaces as shown in Fig. 8.5. The precursor computational domain has a dimension of 6053 θ_0 × 1425 θ_0 × 356 θ_0 in the x, y and z directions, respectively. At the inlet of the precursor simulation, laminar Blasius profile (velocity and temperature) is specified, and the corresponding momentum thickness Reynolds number, $Re_{\theta_0} = 85$. The laminar boundary layer is tripped by a numerical square wire along the spanwise, z, direction with a height of 17.65 x/θ_0 to trigger laminar-to-turbulent transition downstream of the domain. The outflow boundary condition was applied at the outlet. In the spanwise direction, periodic boundary conditions were used. At the top of the domain, $u = U_\infty$, $v = V_{Blasius}$, $w = 0$ and $T = T_\infty$ were applied. No-slip boundary conditions were applied at the heated wall with $T_w > T_\infty$.

Dynamic Smagorinsky model was used for the sub-grid scale modelling. The SIMPLE (semi-implicit method for pressure linked equations) algorithm was applied for pressure-velocity coupling in a segregated manner. The momentum and energy equations were discretized with a bounded central differencing scheme, and the second order scheme was used for the pressure discretization. For the transient formulation, bounded second order implicit method was employed with a time stepping of $\Delta t^+ = 3.33 \times 10^{-1}$. A conformal structured hexahedral mesh containing 6.7 × 10^6 nodes was used in the precursor wall resolved LES.

8.3.2 Precursor Simulation Validation

Fig. 8.6 depicts the energy spectra of the streamwise velocity fluctuations monitored at $x/\theta_0 = 5880$ and $y^+ = 145$ which follows the Kolmogrov's -5/3 slope in the inertial subrange. The smooth extension domain has the same mesh density as the precursor simulation case, therefore the mesh resolution details will be given in following section for brevity.

Table 8.1: Roughness details

	Rough	Scaled +25%	Scaled +50%
Scaling	1	1.25	1.50
$R_a\ (m)$	1.1451e-5	1.4314e-5	1.7177e-5
$R_q\ (m)$	1.4428e-5	1.8035e-5	2.1642e-5
R_{ku}	3.1184	3.1184	3.1184
R_{sk}	-1.07e-2	-1.07e-2	-1.07e-2

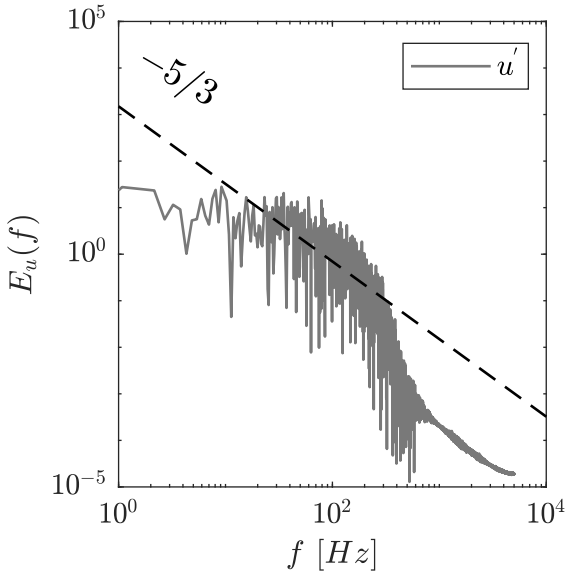

Figure 8.6: Energy cascade at $x/\theta_0 = 5880$ and $y^+ = 145$

The LES was initialized with flow field from steady state RANS simulation, and then run for 8000 $\times$ Δt until the initial transients decay. The unsteady data was sampled for about 18000 time steps which is equivalent of 6 flow-through time.

Stanton number given in Eq. 8.2 is used as a non-dimensional heat transfer coefficient to compare the precursor LES heat transfer results against the turbulent correlation for the Stanton number proposed by Kays and Crawford [142] which is defined in Eqn. 8.3.

$$St = \frac{q_w}{\rho U_\infty C_p (T_w - T_\infty)} \tag{8.2}$$

where q_w is the heat flux from the heated wall to the flow, ρ is the density of fluid, U_∞ is the free stream velocity, C_p is the specific heat capacity of the fluid,T_w is the heated wall temperature, and T_∞ is the free stream temperature.

$$St = 0.287 Re_x^{-0.2} Pr^{-0.4} \left[1 - \left(\frac{\xi}{x}\right)^{\frac{9}{10}}\right]^{-\frac{1}{9}} \tag{8.3}$$

where ξ is the unheated starting length which is taken into account since the Blasius profile defined at the inlet is unheated ($T_w = T_\infty$).

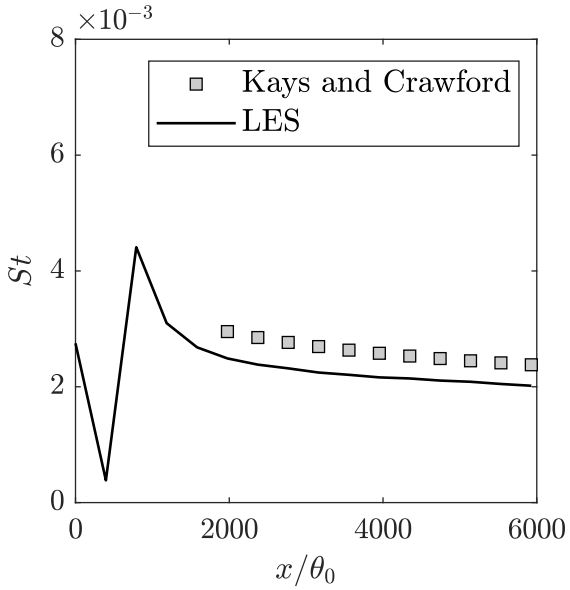

Figure 8.7: Validation case heat flux comparison against Kays and Crawford's correlation [142]

The heat transfer coefficient is plotted in Fig. 8.7. The LES results exhibit underprediction of heat transfer compared to Kays and Crawford's correlation [142]. This can be attributed to the fact that the correlation is for high Reynolds numbers. However, the trend of decreasing heat transfer along the streamwise direction is captured. Mean streamwise velocity $< u >^+$ and temperature $< \theta >^+$ profiles with inner scaling are presented in Fig. 8.8. The DNS results of zero pressure gradient flat plate turbulent boundary layer (ZPGFL) from Li et al. [143] for the velocity and the Zhao et al. [144] for the temperature are also included. Although there exist some discrepancies between the present LES and DNS results from [143, 144] which

can be attributed to the outlet boundary condition treatments and the numerical schemes used, a satisfactory agreement between LES and DNS results is achieved.

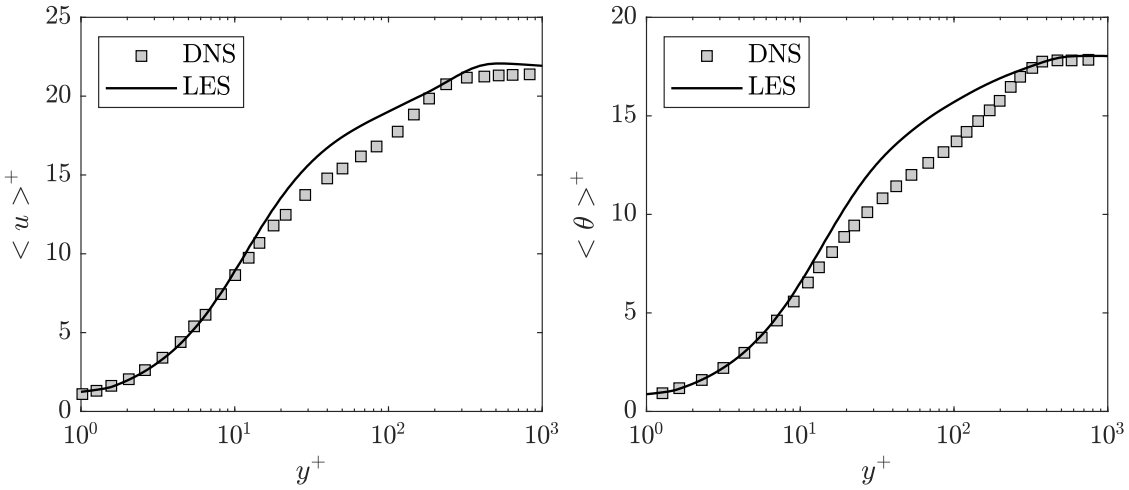

Figure 8.8: Mean velocity $< u >^+$ and temperature $< \theta >^+$ profiles (DNS for $< u >^+$ from [143], DNS for $< \theta >^+$ from [144])

8.4 Wall Resolved LES of Rough Walls

8.4.1 Computational Methodology for Rough Walls

The same numerical scheme as the precursor simulations is used for the extension domains with smooth and rough walls. As mentioned in the previous sections, a datum roughness surface and two additional rough surfaces with scaled up heights are created. The computational domain sizes for rough surfaces are identical. They, as well as the smooth case, can be considered as extension domain of the precursor simulation. The extension domain size is 720 θ_0 × 1425 θ_0 × 356 θ_0 in x, y and z directions, respectively.

It is vital to capture the surface characteristics accurately with sufficiently dense mesh in a scale resolving simulation. Cardillo et al. [90] performed a two-dimensional fast Fourier transform (FFT) to determine the dominant wavelengths in the overall spectrum. The same approach used in the present study to show that the wavelengths which contribute the most to the surface topography. Wavenumber analyses from

two-dimensional FFT are presented in Fig. 8.9 where dark and white areas represent the dominant and weak wavenumbers. The dashed lines indicate the dimensions of required mesh resolution to capture the dominant surface topographical information. $3\pi/2$ mm^{-1} region in streamwise and spanwise directions appears to cover the area where the significant wavenumber contributions are present.

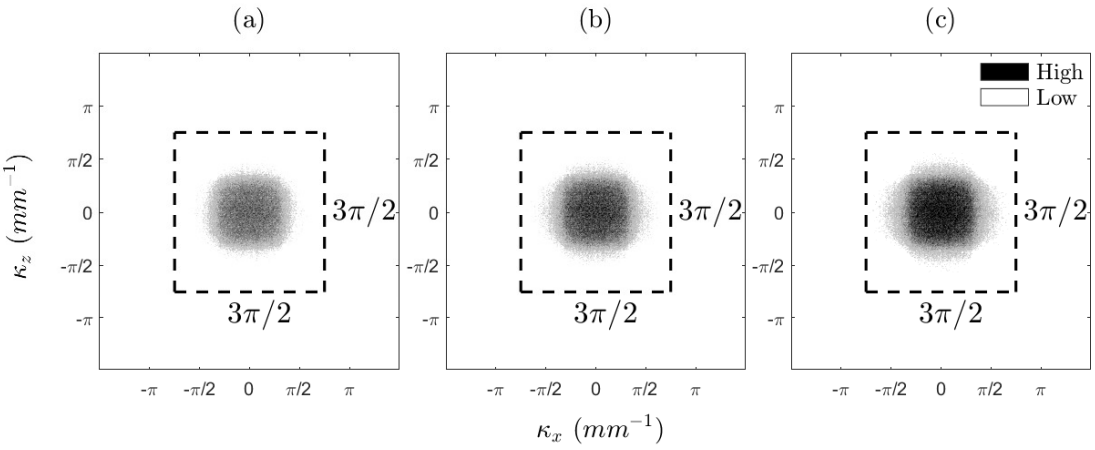

Figure 8.9: FFT of (a) Rough surface (b) Scaled +25% (c) Scaled +50%

Table 8.2: Kolmogorov length and time scales

	Rough	Scaled +25%	Scaled +50%
$\eta_k{}^+$	1.3684	1.3477	1.3544
$\lambda_\eta{}^+$	1.4202	1.3795	1.3921

In order to apply more stringent mesh resolution in the simulations, Kolmogorov length and times scales are considered. The Kolmogorov length and times scales are defined as $\eta_k = (\nu^3/\epsilon)^{0.25}$ and $\lambda_\eta = (\nu/\epsilon)^{0.5}$, respectively. The calculated length and times scales are tabulated in Table 8.2. However, maintaining a grid resolution at these levels in the streamwise and spanwise directions in the entire domain would require extraordinary computational resources. Therefore, non-conformal mesh was used in the scale resolving simulations of rough surfaces.

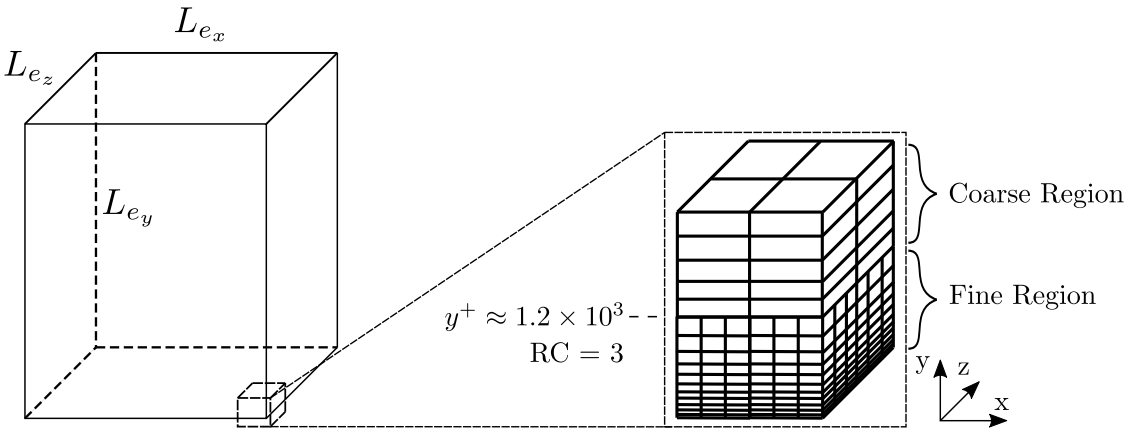

Figure 8.10: Near wall mesh schematic

Fine mesh was created in the near-wall region up to $y^+ \approx 1.2 \times 10^3$. Beyond this point, mesh was substantially coarsened in the streamwise and spanwise directions. For example, the near wall mesh schematic with fine and coarse regions as well as the refinement coefficient (RC) is illustrated in Fig. 8.10.

For the scale resolving simulations, detailed spatial and temporal resolution information for rough cases are given in Table 8.3. The smooth extension case consists 7.8×10^5 nodes with $85 \times 105 \times 87$ (in x, y and z directions, respectively) which results in a grid resolution of $\Delta x^+ = 28.1$, $\Delta y^+_{min} = 0.68$ and $\Delta z^+ = 14.8$. The time stepping for the smooth case is $\Delta t^+ = 0.297$. The time steps maintained the Courant-Friedrichs-Lewy number, CFL<0.75. The time steps used in the simulations are much lower than the Kolmogorov time scales given in Table 8.2. The near wall mesh resolution in all directions resembles a DNS resolution with $\max(\Delta(x, y, z))/\eta_k \approx 2$. In addition, the amount of resolved turbulent kinetic energy (TKE) is plotted in Fig. 8.11, which depicts that the average of more than $k_{resolved}/k_{total} = 98\%$ is resolved. In the same figure, the energy spectra of streamwise velocity fluctuations in each case is presented, all of which agree well with the Kolmogorov -5/3 slope in the inertial subrange which further improves the validity of the simulations.

Table 8.3: LES spatial and temporal resolution

		Rough	Scaled +25%	Scaled +50%
Coarse Region	N_x	384	384	384
	N_y	40	40	40
	N_z	195	195	195
Fine Region	RC	4	3	3
	N_x	1536	1152	1152
	N_y	120	120	120
	N_z	780	585	585
Resolution	Δx^+	1.80	2.37	2.77
	Δy^+_{min}	0.39	0.39	0.39
	Δz^+	1.83	2.41	2.82
Time step	Δt^+	0.135	0.132	0.134
Node Count (M)		145.86	83.37	61.68

8.4.2 Results

Time and spanwise averaged velocity and temperature profiles in wall units are presented in Fig. 8.12 for all extension domain cases with smooth and rough walls. The mean velocity profiles of rough wall cases exhibit a downward shift compared to the smooth wall case. This shift is measured with ΔU^+ referred as the roughness (velocity) function. The ΔU^+ values are seen in the logarithmic region clearly. It is interesting to note that the velocity profiles of all rough surfaces are nearly identical with the same level of $\Delta U^+ \approx 3$. Thakkar et al. [94] performed DNS for transitionally rough engineering surfaces. One of the engineering surfaces considered in their study was a cast surface which yielded a similar downward velocity shift with $\Delta U^+ = 3.39$. The temperature profiles are also shown in Fig. 8.12. Similar to the velocity profiles, the temperature profiles of all rough

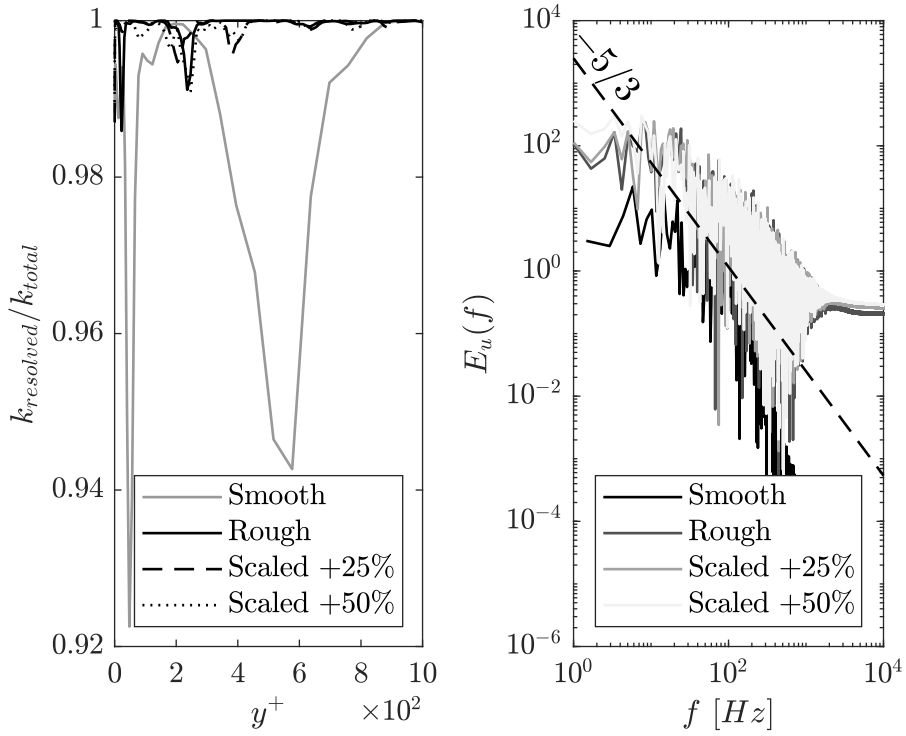

Figure 8.11: Resolved TKE and energy spectra of u'

surfaces exhibit same level of $\Delta\theta^+$.

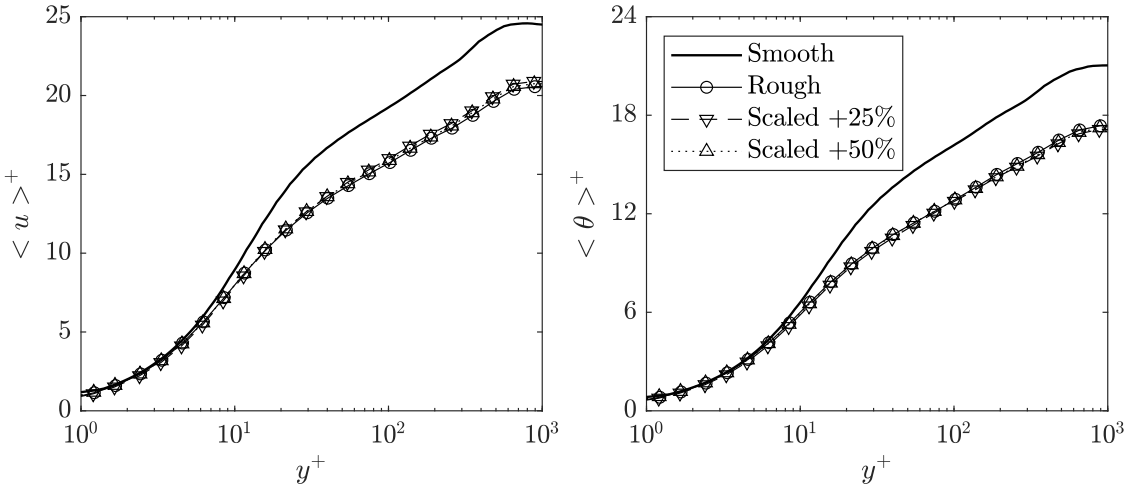

Figure 8.12: Mean velocity and temperature profile comparison

The Reynolds analogy suggests that momentum and heat transfer are related. if skin friction information is available, heat transfer can be approximated with the Reynolds analogy under certain conditions (i.e., no external pressure gradient and unity of Prandtl number). With presence of surface roughness, there is a large

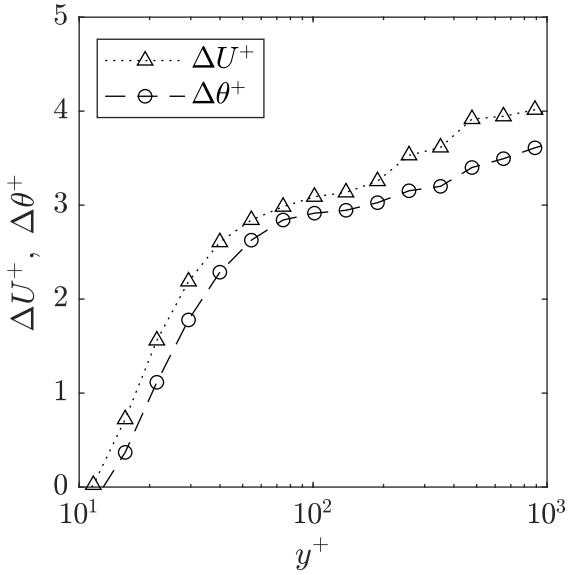

Figure 8.13: Velocity and temperature function ratio for Scaled +50% Case

body of literature with experimental and numerical studies on the dissimilarity between momentum and heat transfer ([145–147] among others) which show that the Reynolds analogy fails with fully rough conditions. Since the momentum transfer is enhanced by pressure gradients stemming from roughness elements while there is no direct mechanism for heat transfer, velocity function becomes greater than temperature function, $\Delta U^+ > \Delta\theta^+$. The similarity between ΔU^+ and $\Delta\theta^+$ can be visually inspected in Fig. 8.12. For further inspection, the velocity and temperature functions in Scaled +50% are plotted in Fig. 8.13 which exhibits that the profiles nearly match in the logarithmic region. The similarity indicates that the case does not represent a fully rough regime.

The mean skin friction coefficient, C_f, and Stanton number, St, are defined in Eq. 8.4, and the profiles of which are shown in Fig. 8.14 and Fig. 8.15, respectively. The enhancement of skin friction and heat transfer can be observed with rough surfaces compared to the smooth case. Similar to the velocity profiles, the heat transfer profiles of rough cases closely match.

$$C_f = \frac{\lambda_w}{0.5\rho U_\infty^2} \quad , \quad St = \frac{q''}{\rho U_\infty C_p \Delta T} \tag{8.4}$$

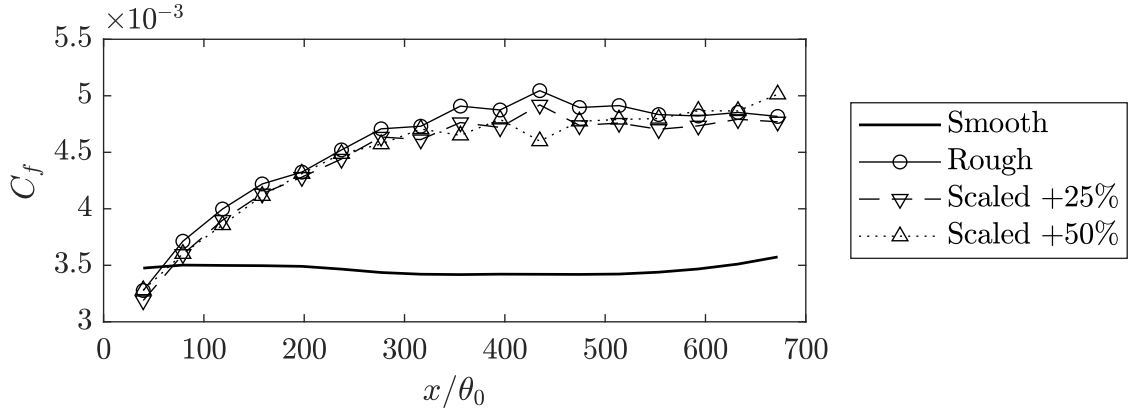

Figure 8.14: Skin friction profile comparison

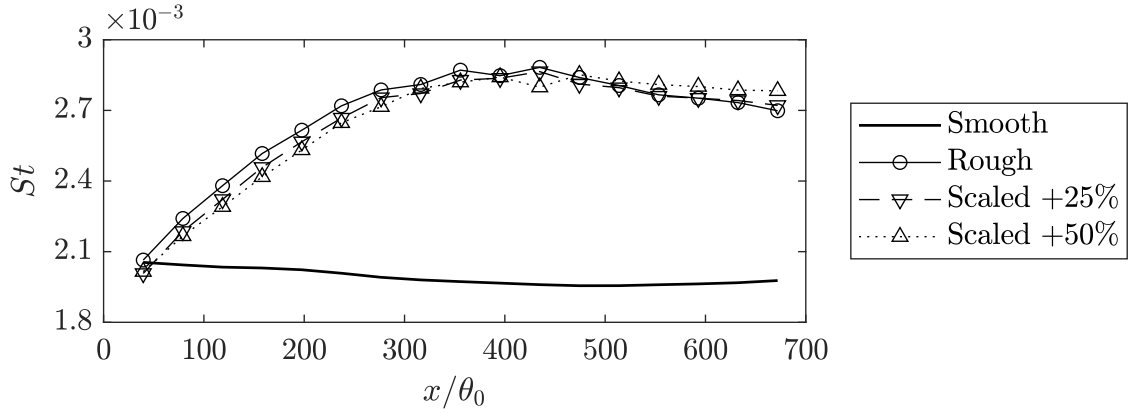

Figure 8.15: Heat transfer profile comparison

Instantaneous near-wall temperature fields of smooth and rough cases in wall normal plane at the centre of the domain are shown in Fig. 8.16 where the temperature is non-dimensionalized as $T^* = (T - T_\infty)/(T_w - T_\infty)$. The figure illustrates the increased mixing due to the local roughness textures present in rough cases compared to the smooth case. It can also qualitatively deduced that the rough surfaces exhibit thicker temperature boundary layer than that of smooth case.

The Reynolds stresses scaled by u_τ^2 and the turbulent heat fluxes scaled by $u_\tau\theta_\tau$ and are shown in Fig. 8.17. All $< u'u' >^+$ profiles exhibit a peak in the near wall region. The $< u'u' >^+$ profiles for the rough cases are nearly identical with a slightly reduced magnitude compared to the smooth case. This phenomenon is explained by the breakdown of the streaky structures occurring in flows over smooth walls. This can be observed at $y^+ = 5$ in Fig. 8.18 where the instantaneous streamwise velocity fluctuations at various wall normal distances are shown. Near

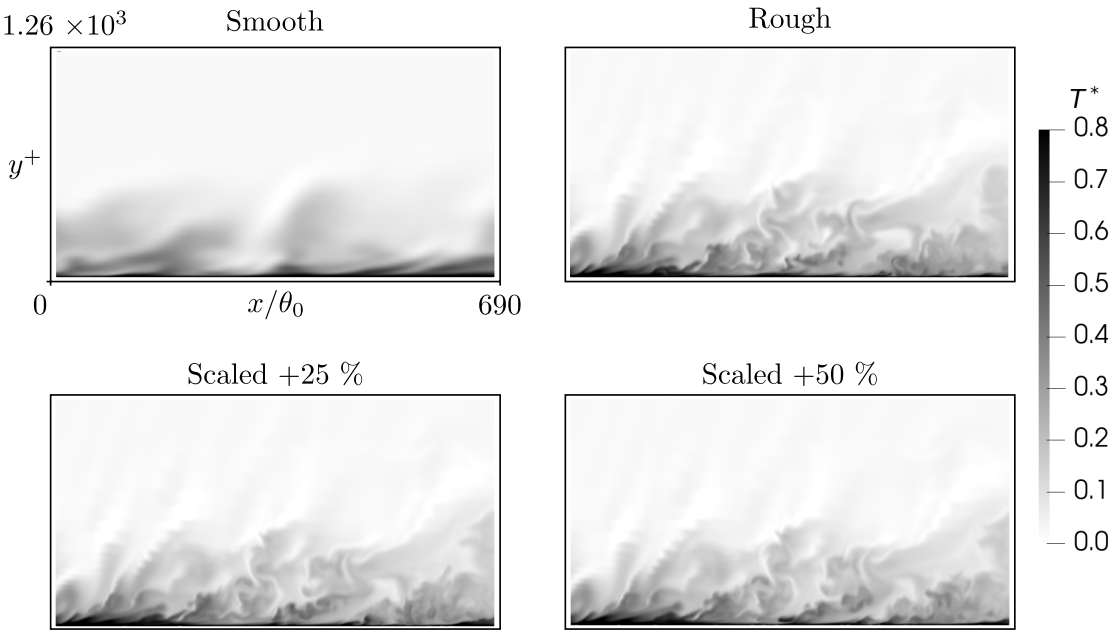

Figure 8.16: Instantaneous temperature field comparison

the rough walls, the local velocity elevations are also seen. However, farther away from the wall, the instantaneous velocity fields of rough surfaces resemble each other. As opposed to the outer layer similarity known as Townsend's hypothesis [148], $< u'u' >^+$ profiles do not coincide in the outer layer.

It is clear that the streamwise Reynolds stresses are much stronger than the spanwise and wall-normal Reynolds stresses. Looking at $< u'u' >^+$ and $< u'\theta' >^+$ which are the most dominant the Reynolds stress and turbulent heat flux components, the decay of fluctuations at $y^+ < 11$ seem to be independent of surface texture. It is important to note that all rough cases exhibit higher the $< v'v' >^+$ and $< w'w' >^+$ peaks than the smooth case, which indicate that the effect of roughness is pronounced in all directions. Streamwise and spanwise Reynolds stress increase appears to occur at the same level with all rough cases. Similarly, the Reynolds shear stress profiles,$< -u'v' >^+$, of all rough cases show a higher peak than the smooth case. All rough wall cases as well as the smooth case exhibit similar $< v'\theta' >^+$ and $< u'v' >^+$ which was also observed in the study of Peeters and Sandham [145]. For all cases, the streamwise turbulent heat fluxes are lower than the streamwise Reynolds stresses.

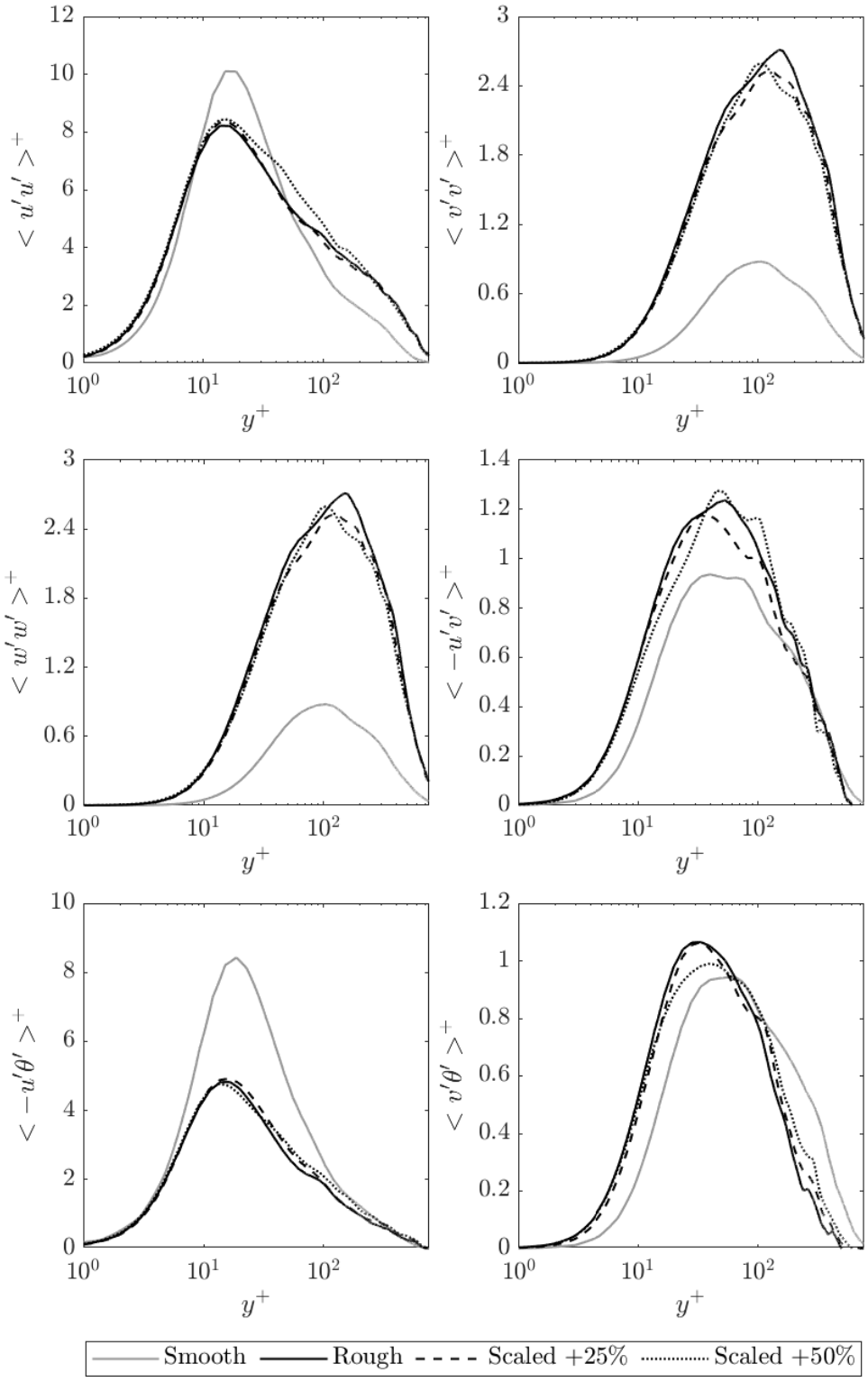

Figure 8.17: Reynolds stresses and turbulent heat fluxes

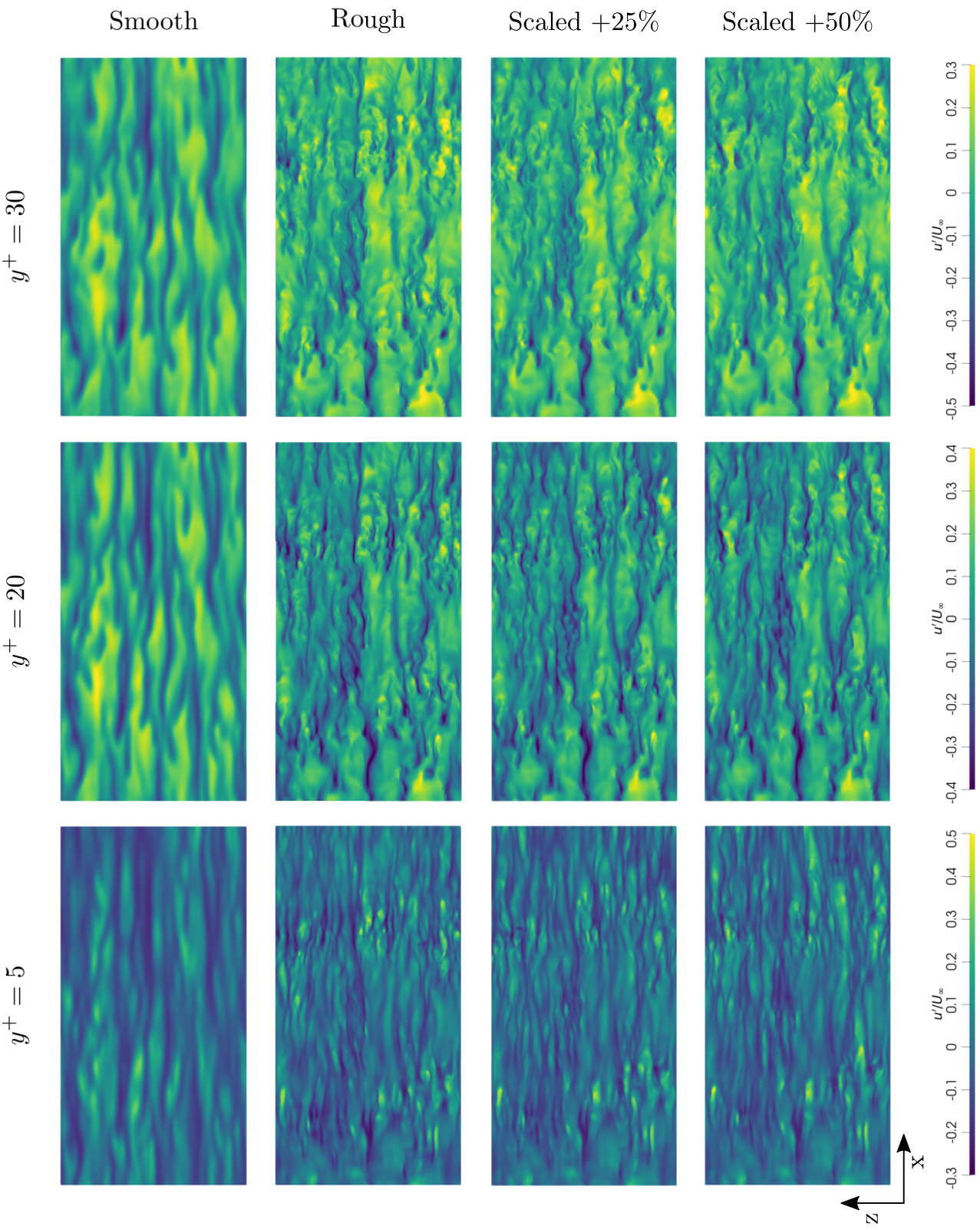

Figure 8.18: Instantaneous streamwise velocity fluctuations at y^+ of 5, 20 and 30

8.5 Conclusions

In the present study, the influence of casting roughness commonly encountered in the turbomachinery industry on heat transfer, flow field and aerodynamics has been investigated. A scan of cast iron patch has been scanned, analysed and the topographical surface information has been used to reconstruct a realistic irregular surface. The height of the reconstructed surface has been scaled up to cover a wide range of roughness to account for the roughness variations due to the different casting processes.

Wall resolved large eddy simulations of spatially developing boundary layer have been performed for various rough and smooth surfaces. In order to generate a realistic inflow boundary conditions and to validate the numerical methodology, a precursor simulation has been performed. A rigorous grid resolution has been used to ensure that the simulation resolves the smallest eddies down to the Kolmogorov scales. The results have revealed that the casting roughness exhibits a downward shift in the logarithmic region at the same level among all rough surfaces considered. Instantaneous temperature and velocity fields have shown that the near-wall mixing is enhanced with the rough wall cases. The skin friction and wall heat transfer are remarkably increased with rough surfaces. Reynolds stresses and turbulent heat fluxes have also suggested that the rough cases exhibit very similar trends among each other.

Hence, the effect of casting roughness appears to consistently occur at the similar level with different roughness heights considered in the present study. These findings suggest that a single roughness model/treatment for computationally cheap low-order turbulence models may potentially reproduce the flow field and heat transfer characteristics accurately for various cast surface topographies. Therefore, the industry would benefit immensely with fast and accurate CFD predictions.

Chapter 9

Conclusions and Future Work

9.1 Introduction

There has been a fast uptake of renewable sources in power generation in the recent years to mitigate the global warming. This trend is expected to continue since more and more countries are joining legally binding treaties which dictate that the targets for reduced emission levels must be met. As the renewables are intermittent by nature, conventional power generation systems will be in use to provide load-levelling capacity depending on the availability of renewables. Therefore, the conventional power generation systems will be required to operate more flexibly with frequent start-ups and shut-downs.

The aim of this work funded by Mitsubishi Heavy Industries (MHI) is to improve our understanding of mixed type of flows occurring inside turbine casings during shut-down regimes by means of extensive experimental and numerical techniques, and also ultimately to form a basis for future power generation systems which can operate flexibly.

9.2 Experimental Campaigns

Since the measurements on real engines are not feasible due to limited access to the flow field and harsh operating conditions, any investigation for shut-down regimes depends solely on numerical predictions which require validation. Mixed type of convection with simultaneous presence of natural and forced convection occurs inside turbine casings during shut-down regimes, for which, to the best of author's knowledge, there is not any detailed experimental flow field data in the literature. Therefore, the confidence in numerical predictions is rather inadequate.

To this end, a novel experimental facility has been designed, built and commissioned at Oxford Thermofluids Institute for experimental investigations of mixed type flows in turbine casing cavities. The facility has been designed to match the real turbine data provided by MHI with relevant non-dimensional numbers.

A number of experimental campaigns have been conducted to cover a wide mixed convection range. Isothermal conditions have been achieved on the heated inner cylinder via a PID control system which adjusts the power for the heater mat installed inside the inner cylinder. In order to achieve different mixed convection scenarios (Richardson numbers), the speed of incoming flow has been varied with an industrial fan which has been placed at the outlet of the facility. A contraction nozzle has been designed to guide the incoming flow towards the test section without any boundary layer separation.

9.3 Wall Resolved Large Eddy Simulations

Wall resolved large eddy simulations (LES) have been performed. Stringent mesh resolutions have been applied to ensure that sufficient amount of turbulence is resolved to improve validity of the simulations which have been validated against each experimental campaign in the thesis.

Unique flow structures which are not conventionally present in the pure natural and pure forced convective flows have been observed. The influence of buoyant forces in the flow field has been found to cause helical structures to occur at each side of the heated inner cylinder. Depending on the magnitude of the cross-flow, these helical structures either stretched along the heated inner cylinder or entrained in the thermal plume region at the top. These structures as well as the thermal plume have been found to affect the heat transfer characteristics significantly. Reynolds stress and turbulent heat flux information have been obtained from wall resolved LES, which are then used to assess the performance of RANS based models.

9.4 New Model Development

A new universal model for $k-\omega$ SST turbulence model has been developed since the conventional RANS has been found to fail in predicting the mixed convective flows. A constitutive relation for Reynolds stress approximations and a modified generalised gradient diffusion hypothesis for turbulent heat flux calculations have been adopted in the new model, NNR, which blends these Reynolds stress and turbulent heat flux treatments. The new model has been implemented into ANSYS Fluent via user defined functions. The new model, NNR, has been tested against the results from experimental and scale resolving simulations for each mixed convection case in the thesis. It has been shown that the conventional RANS suffers from the severe underpredictions of Reynolds stresses at regions where the thermal plume lift-off occurs, whilst NNR is able to reconstruct these stresses which lead to improved accuracy for flow field and heat transfer predictions in mixed type of flows with relatively strong buoyancy influence. Both NNR and RANS have managed to better capture the flow field as the Reynolds number is increased (the Richardson number is decreased) whilst both models have exhibited under and overshootings in heat transfer predictions.

9.5 Flow Control

Since the buoyant flows are directly responsible for the flow field and heat transfer non-uniformities, it would be desirable to completely avoid or minimise the buoyancy influence inside turbine casings during shut-down regimes. To this end, several design ideas on suppression of the buoyant flows have been numerically tested. Upon preliminary numerical observations, the most promising design idea has been found to be *the blockage plate* which is placed upstream of the test section. The experimental facility has been modified to accommodate the blockage plate. The experimental and numerical results have proved that the reduced gap width with blockage plate create a local jet effect which is sufficiently strong to suppress the the influence of buoyant flows on the flow field. These experimental and numerical

observations suggest that a simple modification to turbine casings could reduce the flow field non-uniformity.

9.6 Turbine Casing Roughness

It is not possible to manufacture large casings of steam and gas turbines, therefore these larger components are casted. The casting process results in surface irregularities due to mold/casting temperature and sandblasting, which may cause significant skin friction enhancement, therefore increase in heat transfer To investigate the influence of casting roughness on flow field, heat transfer and aerodynamics, a patch of cast iron turbocharger volute has been scanned to acquire the surface topography. Considering that the generation of surface roughness due to the casting process is random, two additional rough surfaces have been creased by scaling up the roughness height of the scanned surface. Scale resolving simulations with stringent mesh requirements to ensure that the rough surface topography is captured, have been performed for smooth and rough surfaces. Similar velocity and temperature shifts in the logarithmic region have been observed for all rough surfaces. The skin friction and heat transfer enhancements have been found to occur at the same level for the rough surfaces compared to the smooth surface. These findings have indicated that a single low-order model development can reproduce the casting roughness effects on flow field and heat transfer characteristics without having to conduct scale resolving simulations which come at a great computational expense.

9.7 Future Work

There is scope for further research in the following areas:

Experimental campaigns: Further experiments on the facility can be completed to extend the range for mixed convection cases. Additionally, it would be interesting to see how the flow field and heat transfer are effected by varying the Grashof number which has been kept constant in the present study but keeping the

Richardson number constant. The rig has been designed to be modular, therefore further upgrades could de made. For instance, the outer cylinder can be replaced by a thicker casing which houses multiple inlets/outlets at the top/bottom to better represent turbine geometry. In terms of measurement diagnostics, another thermocouple probe can be developed to obtain the temperature gradients on the outer cylinder.

Scale resolving simulations: Detailed investigations in the formation of helical structures and the transition mechanism can be performed to better understand the flow characteristics and how the low order turbulence models can be further developed to account for the effects of these structures.

NNR: Although NNR is found to improve numerical predictions, further research should focus on how to better represent anisotropy in Reynolds stresses and turbulent flux. For instance, the model constants, $\Lambda_{1,2}$ Eq. 6.15 can be further calibrated or switched to non-constant coefficients that vary in the flow field depending on turbulent scales or rotation rates. Additionally, the hyperbolic function in Eq. 6.17 can be replaced by another term which does not cause heat transfer overprediction in forced convection dominant cases.

Flow control: Flow control with a blockage plate has been found to be promising. Further investigations on the required jet effect in terms of local Reynolds number to suppress the buoyant flows would be beneficial.

Turbine casing roughness: Casting roughness on turbine casings could be further investigated since the present study considers a developing flow over a flat plate. The acquired surface topography data could be mapped onto a turbine casing geometry to perform scale resolving simulations, which would further reveal the effects of cast roughness on the flow field and heat transfer inside turbine casing cavities. Additionally, interactions between surface irregularities (i.e., peaks and valleys with various sizes) should be investigated to better understand the roughness influence.

9.8 Final Remarks

The power generation from renewable sources sets new operational realities of frequent start-ups and shut-downs for power generation turbines. Therefore, mixed convective flows are vital in order to understand the shut-down flow regimes which limit the flexible operations.

The developments of experimental and numerical methodologies in this thesis can be used to form a basis for design of future power generation turbines which are capable of operating flexibly.

Appendices

Appendix A

Experimental and LES Results for Remaining Cases

Contents

A.1 Case-A 165

A.2 Case-D 166

A.3 Case-E 167

A.4 Case-G 168

A.1 Case-A

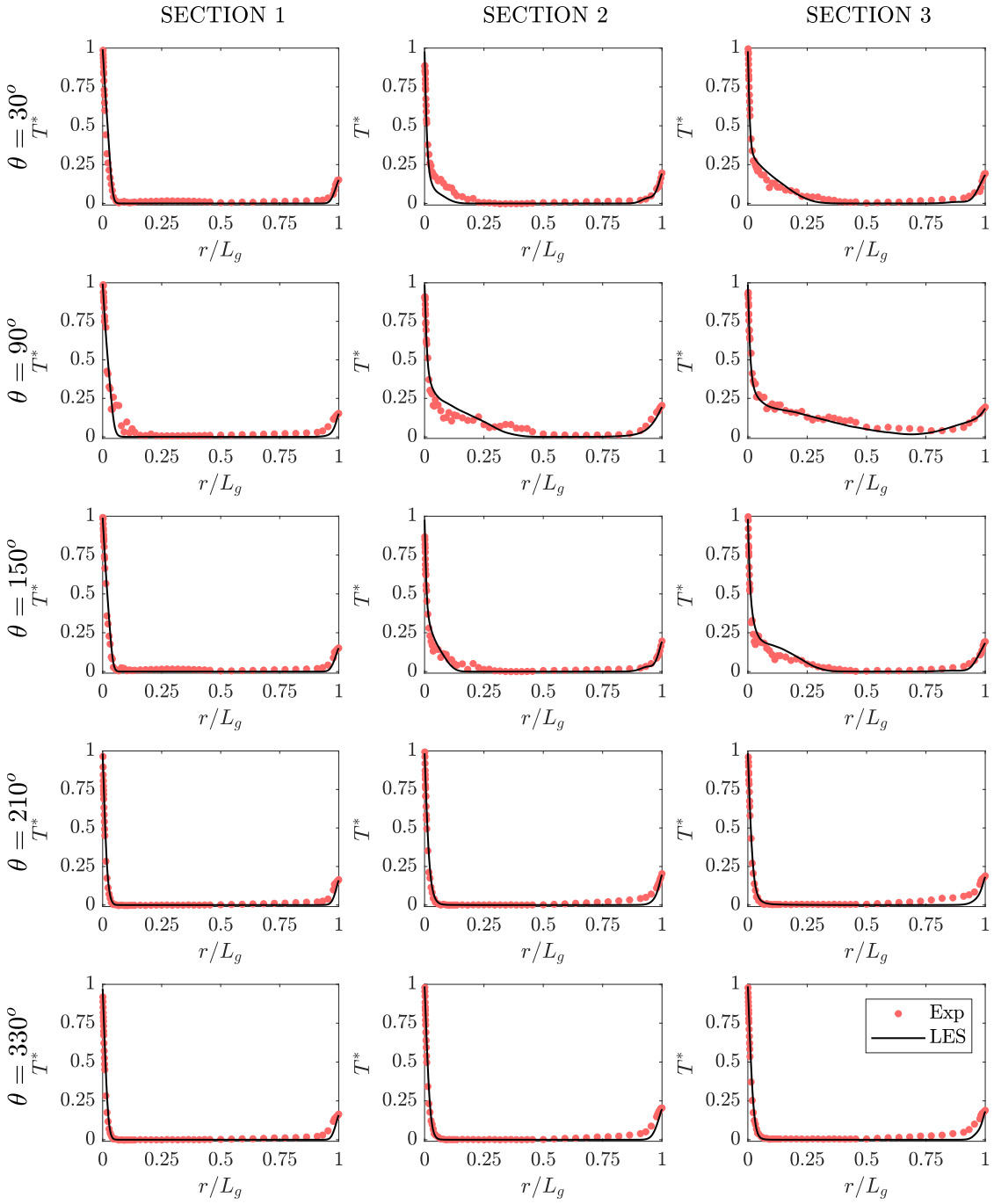

Figure A.1: Experimental and LES temperature profiles in Case-A

A.2 Case-D

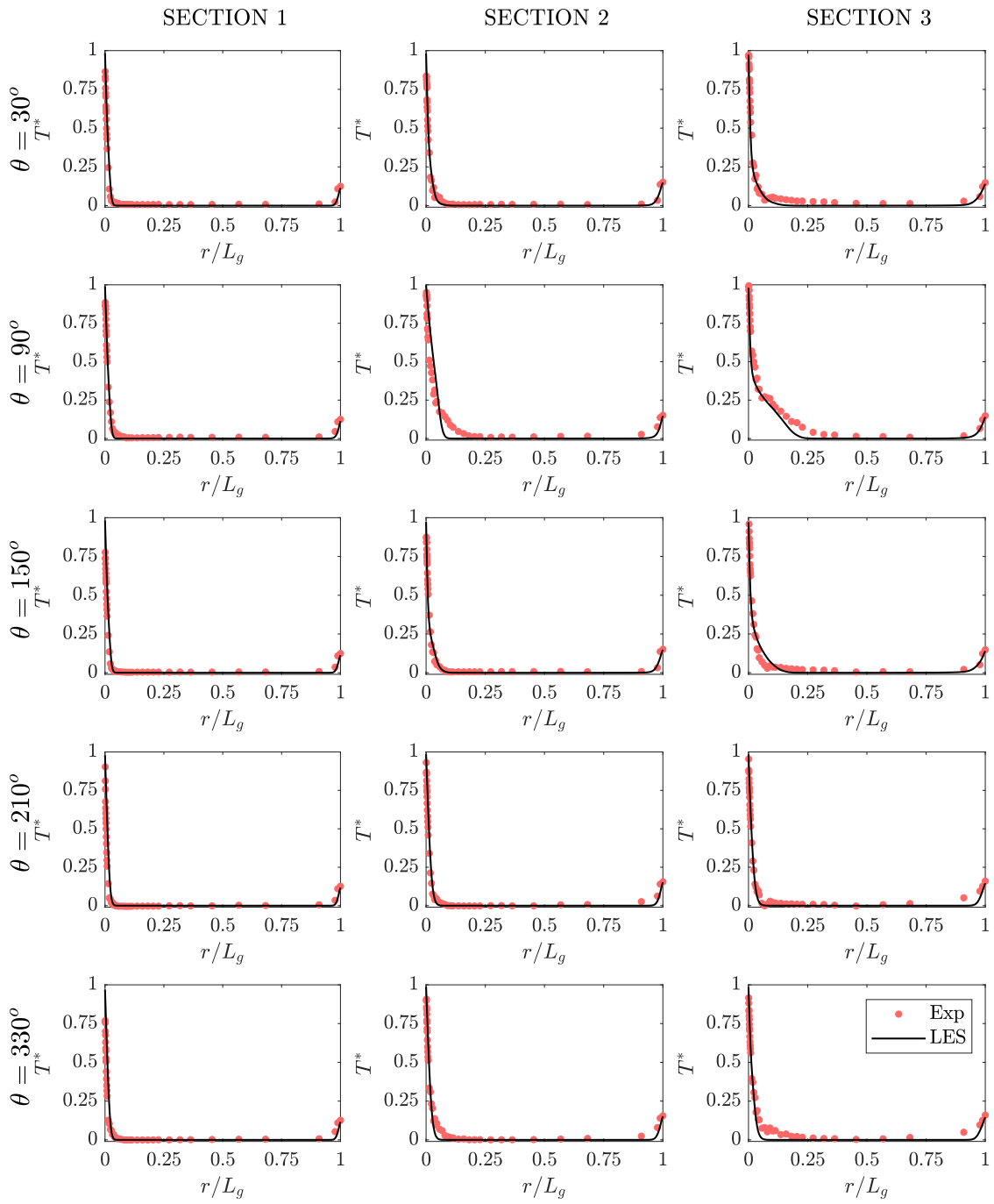

Figure A.2: Experimental and LES temperature profiles in Case-D

A.3 Case-E

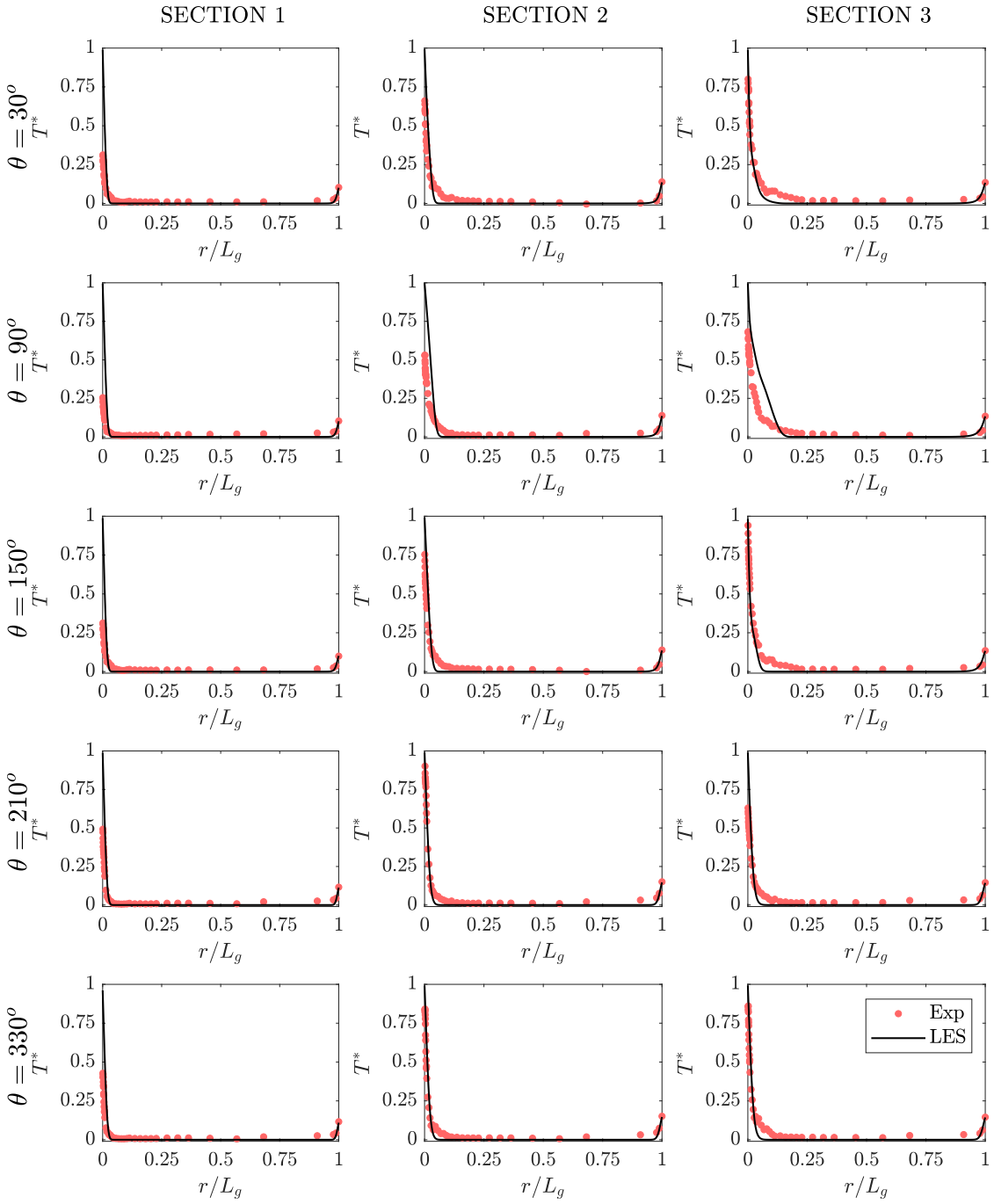

Figure A.3: Experimental and LES temperature profiles in Case-E

A.4 Case-G

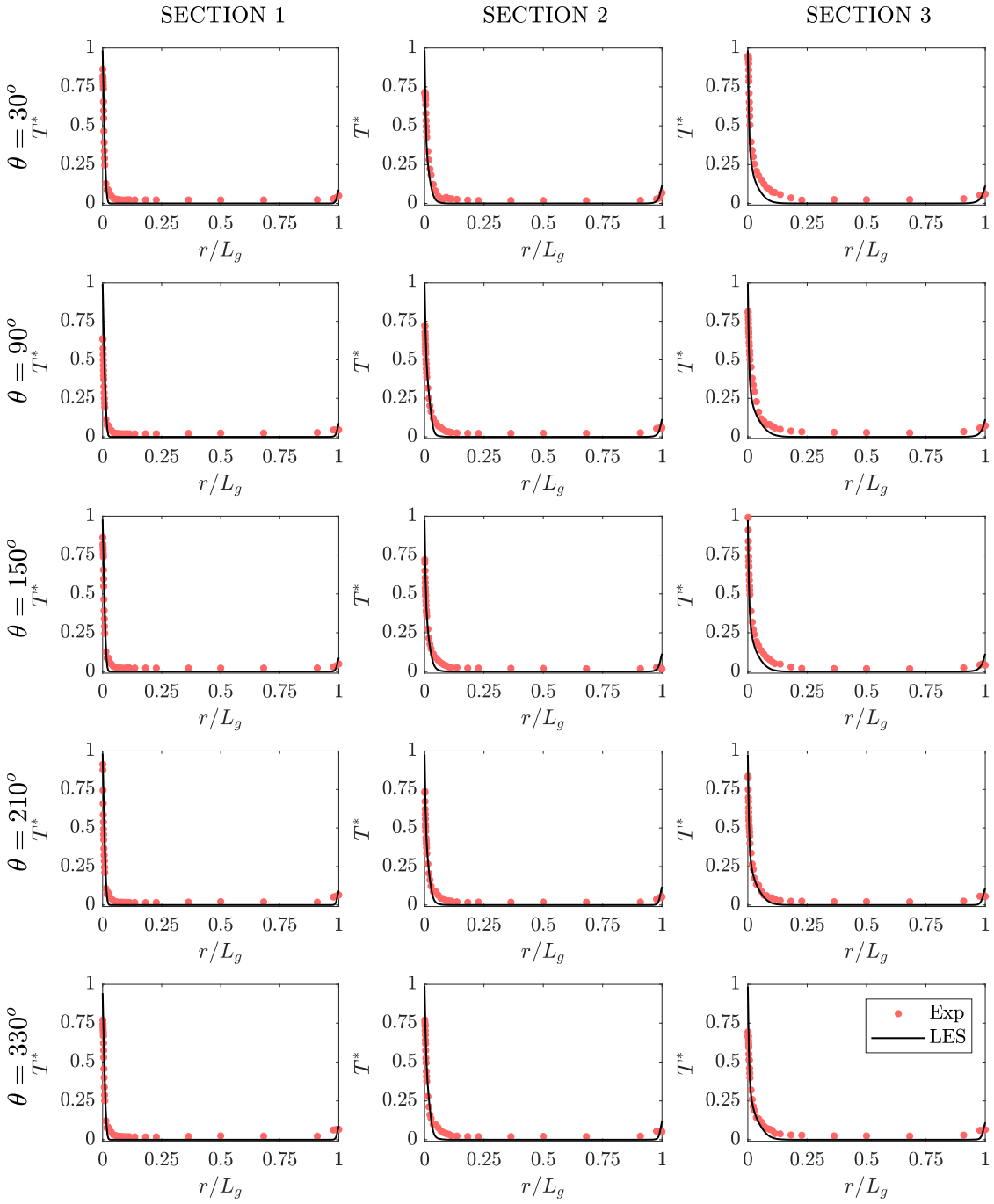

Figure A.4: Experimental and LES temperature profiles in Case-G

Appendix B

NNR Temperature Results for Remaining Cases

Contents

B.1 Case-A 170

B.2 Case-E 171

B.3 Case-G 172

B.1 Case-A

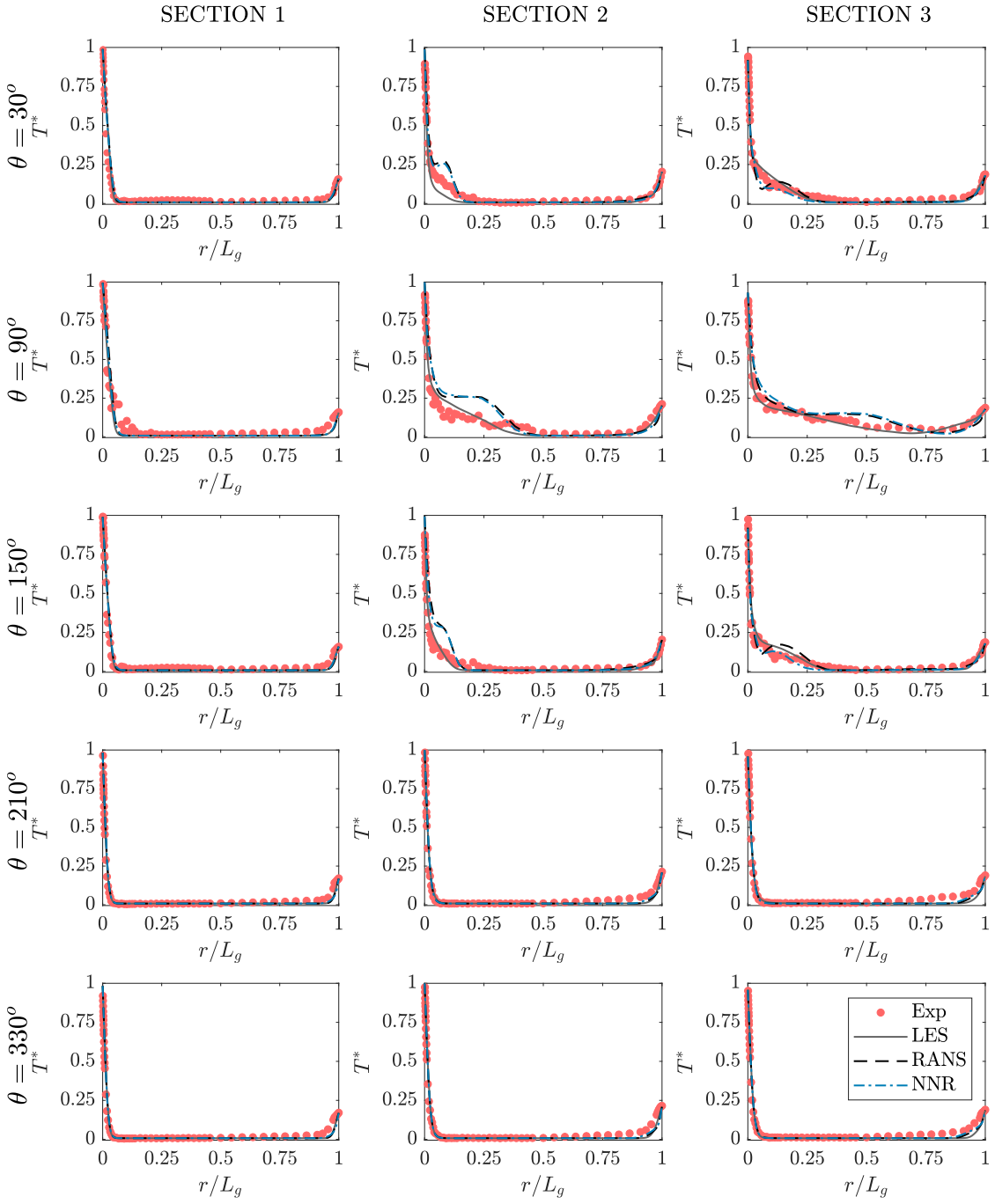

Figure B.1: NNR temperature profiles in Case-A

B.2 Case-E

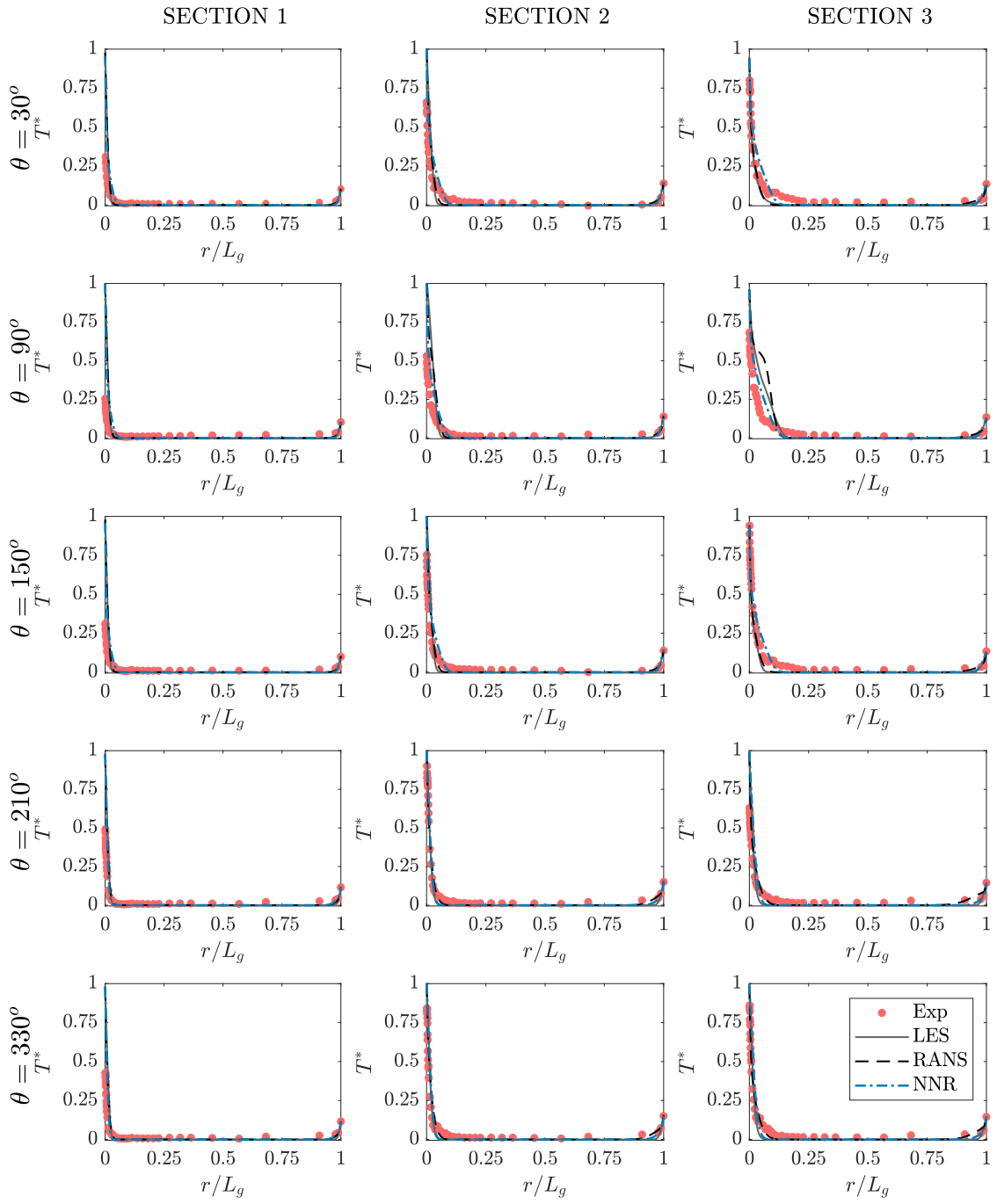

Figure B.2: NNR temperature profiles in Case-E

B.3 Case-G

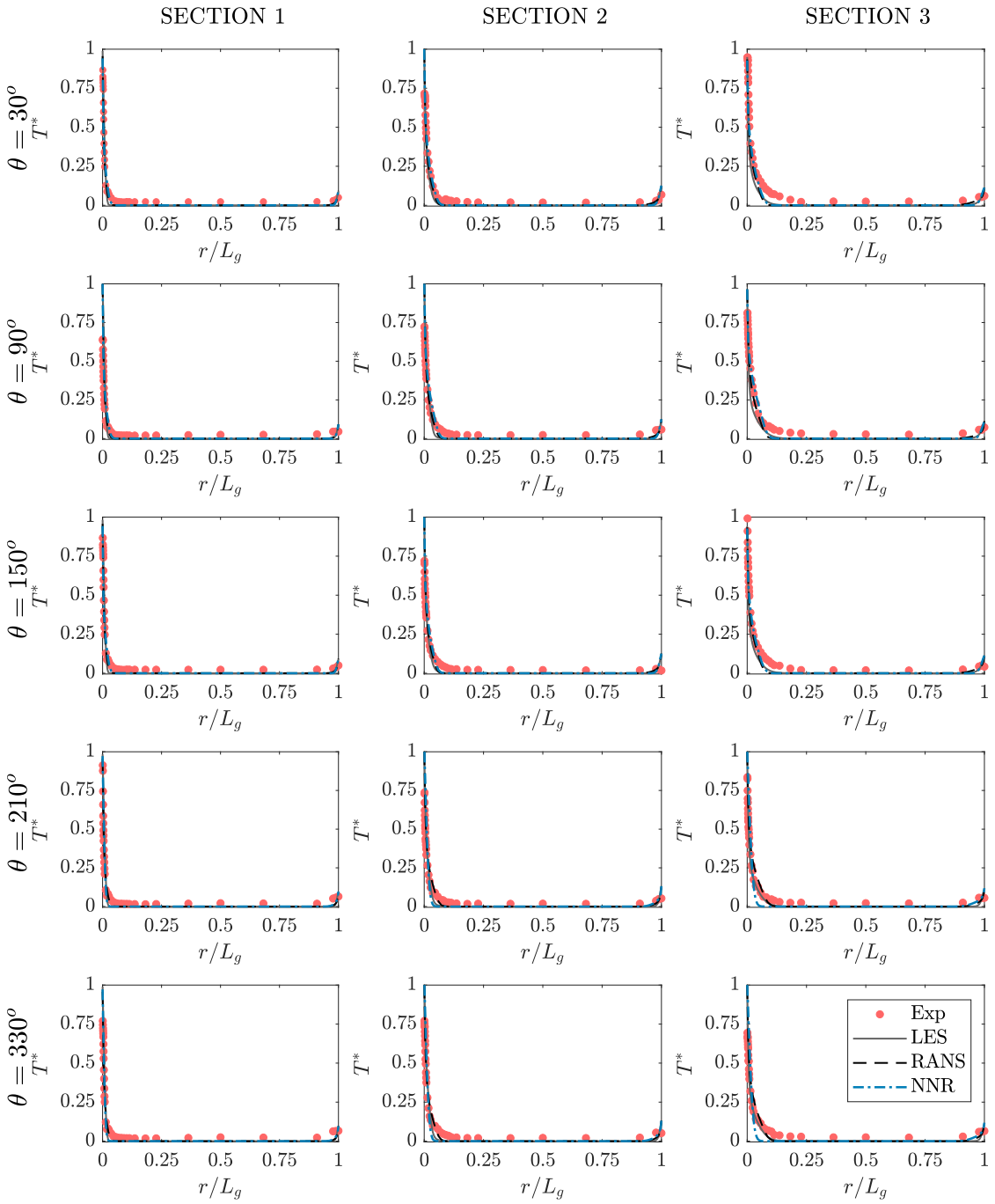

Figure B.3: NNR temperature profiles in Case-G

Appendix C

Reynolds Stresses and Turbulent Heat Fluxes for Remaining Cases

Contents

C.1 Case-A 174

C.2 Case-D 176

C.3 Case-E 178

C.4 Case-G 180

C.1 Case-A

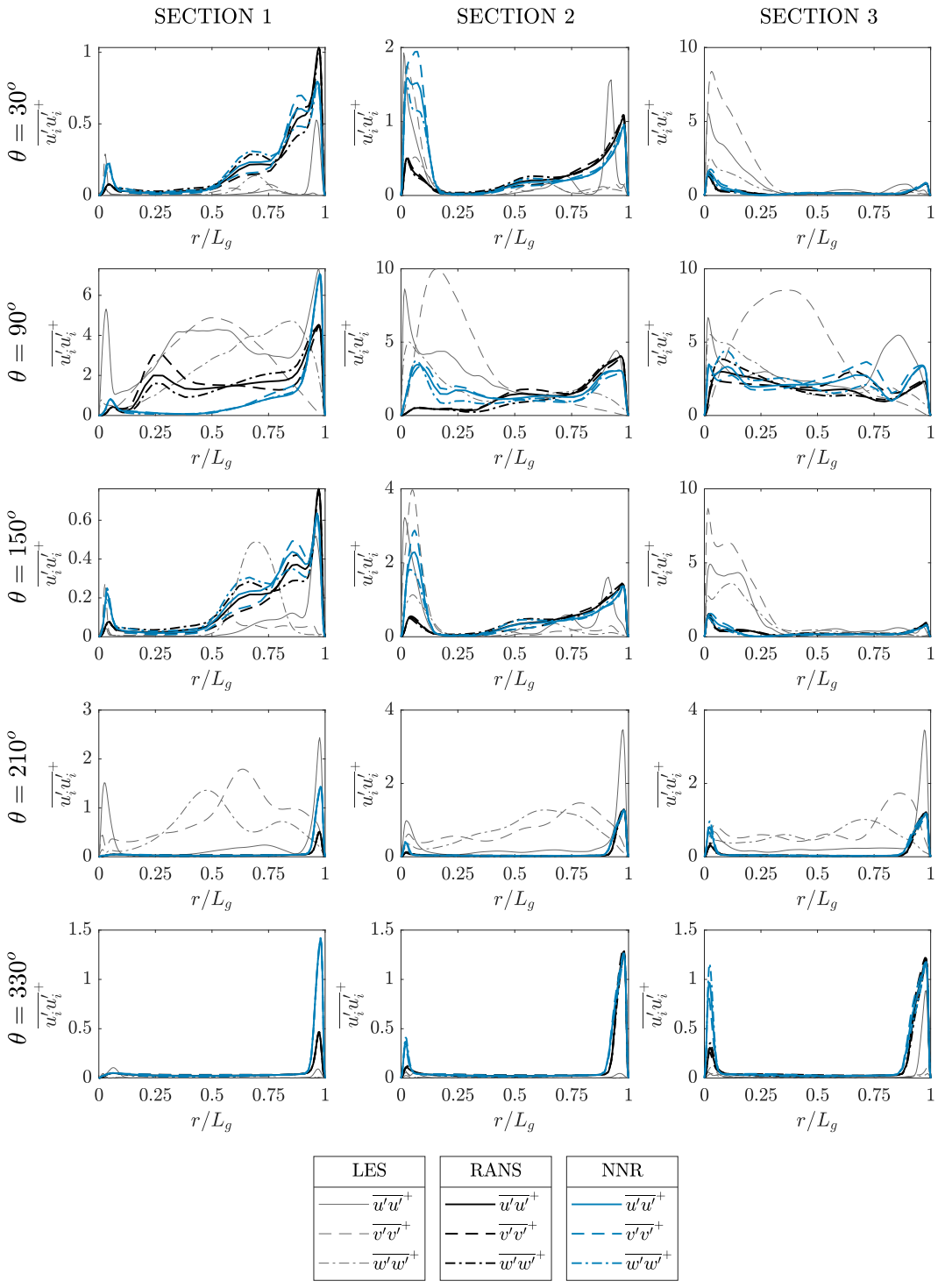

Figure C.1: Reynolds stresses in Case-A

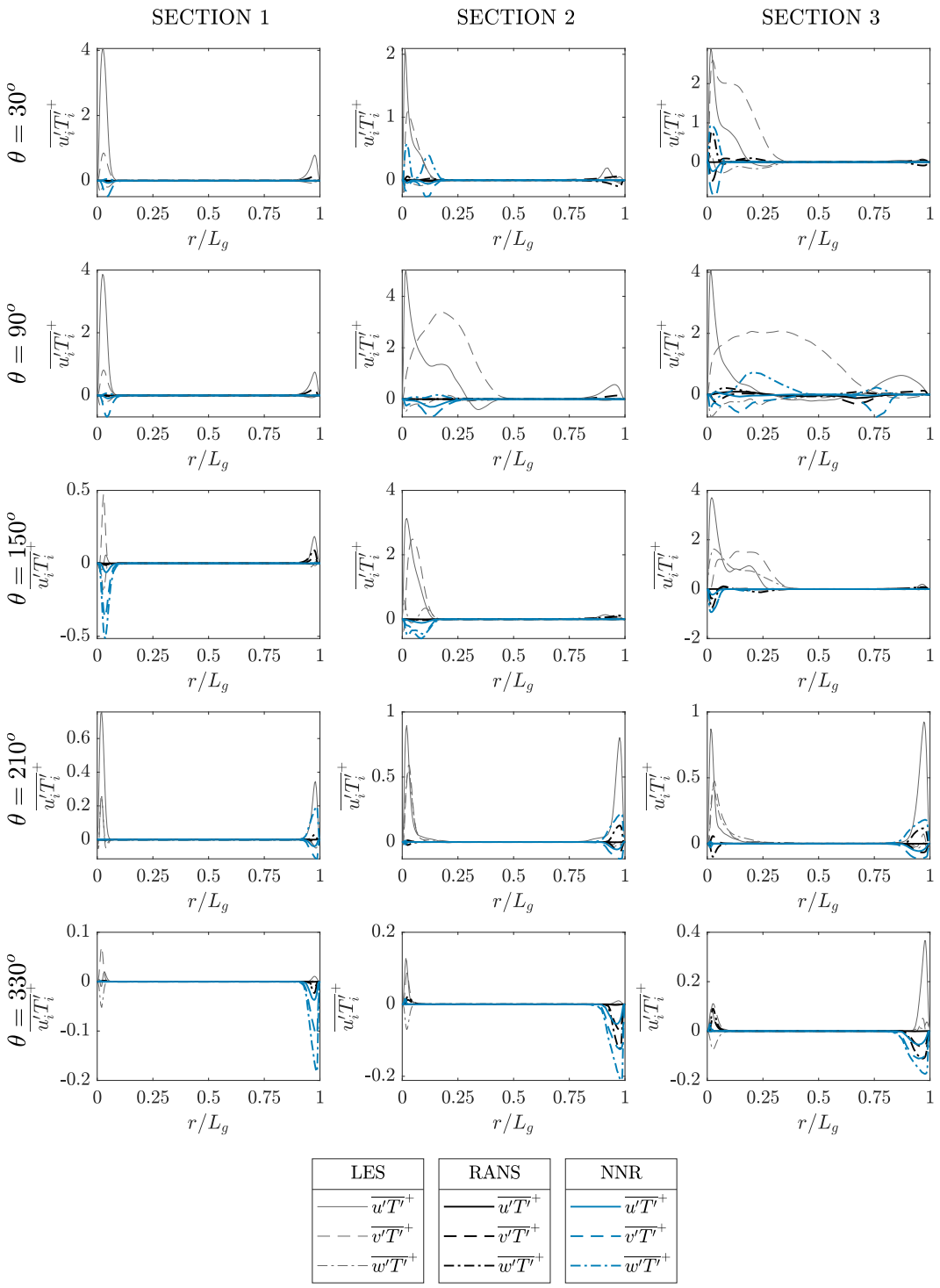

Figure C.2: Turbulent heat fluxes in Case-A

C.2 Case-D

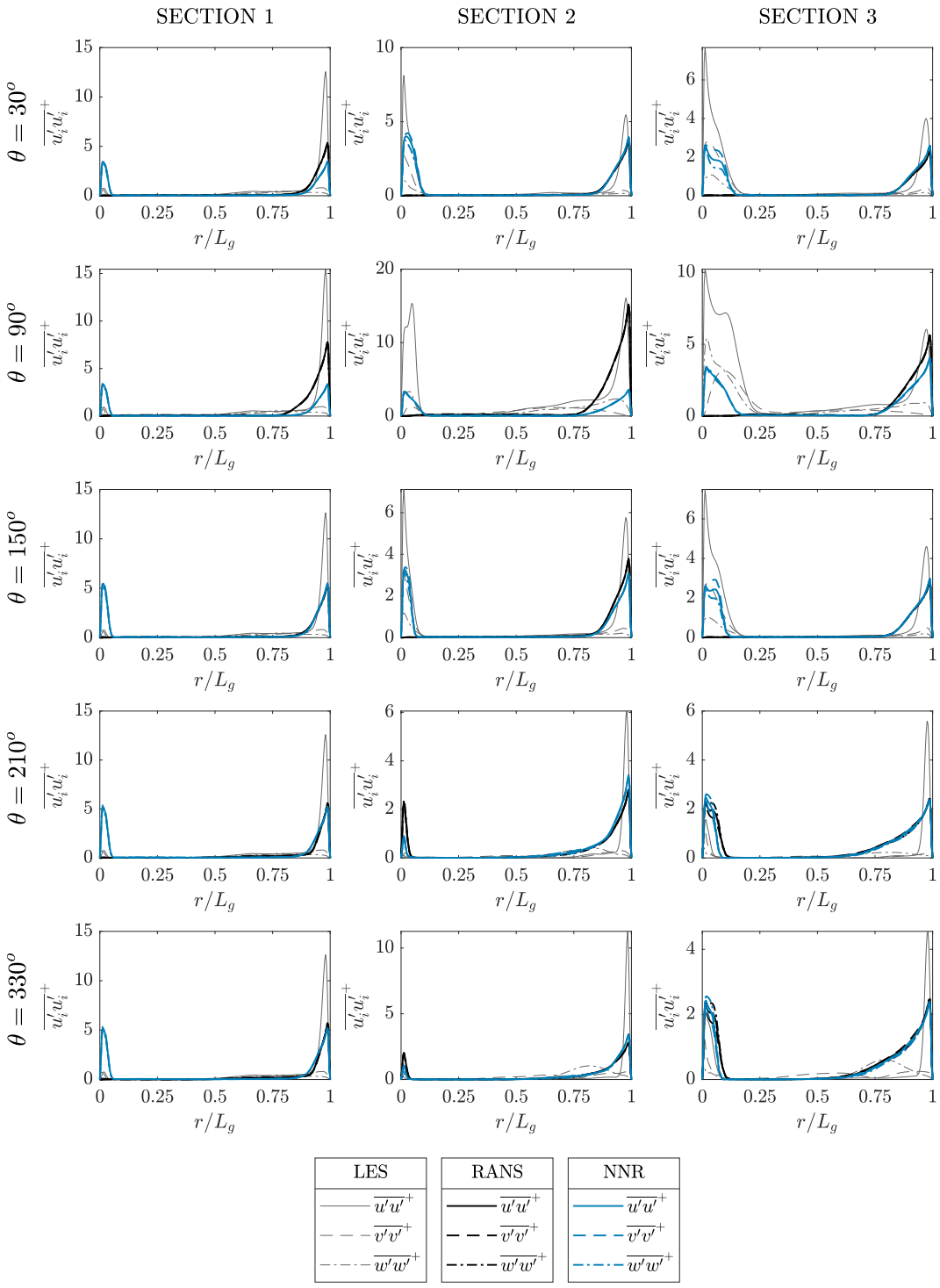

Figure C.3: Reynolds stresses in Case-D

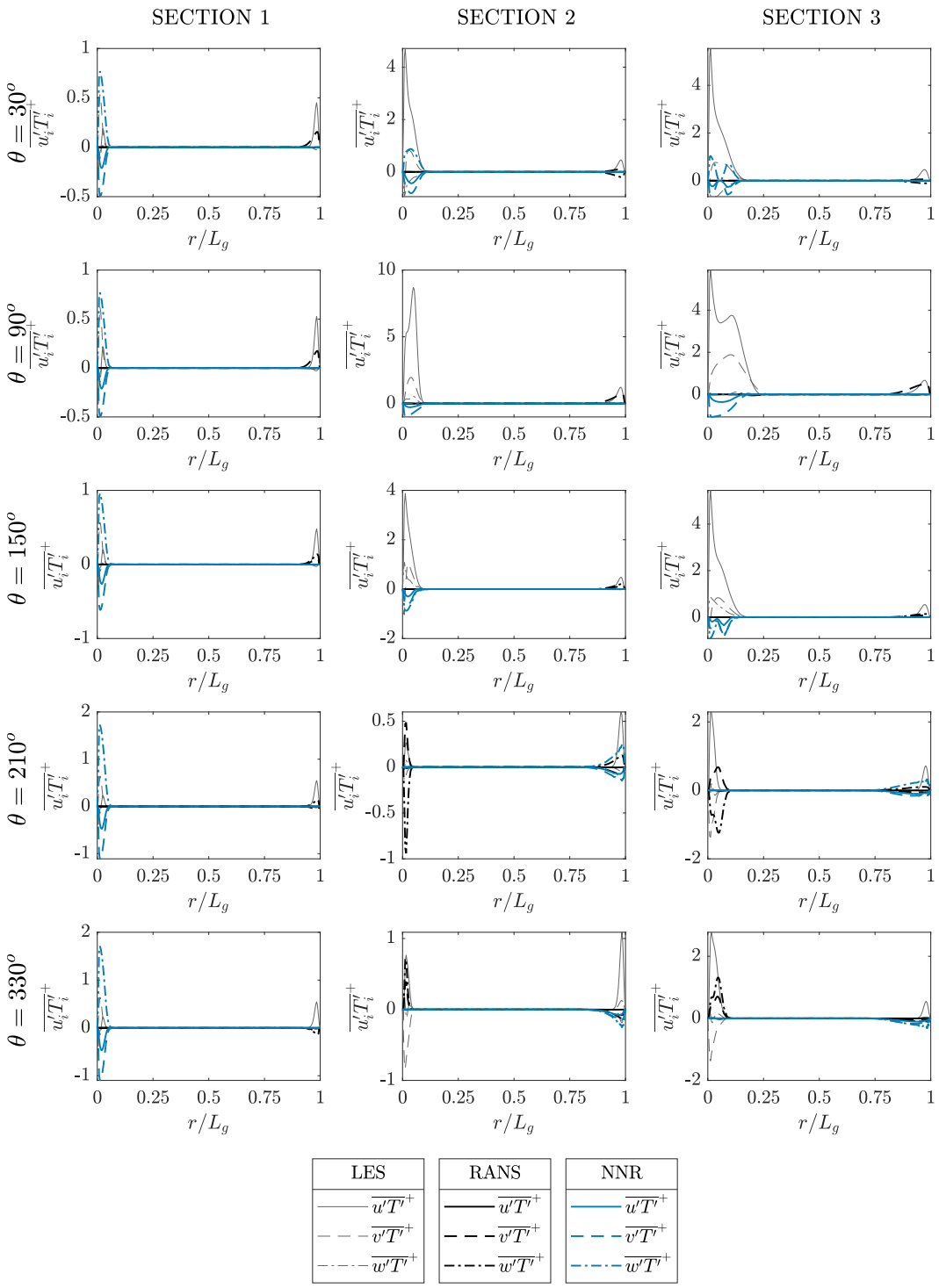

Figure C.4: Turbulent heat fluxes in Case-D

C.3 Case-E

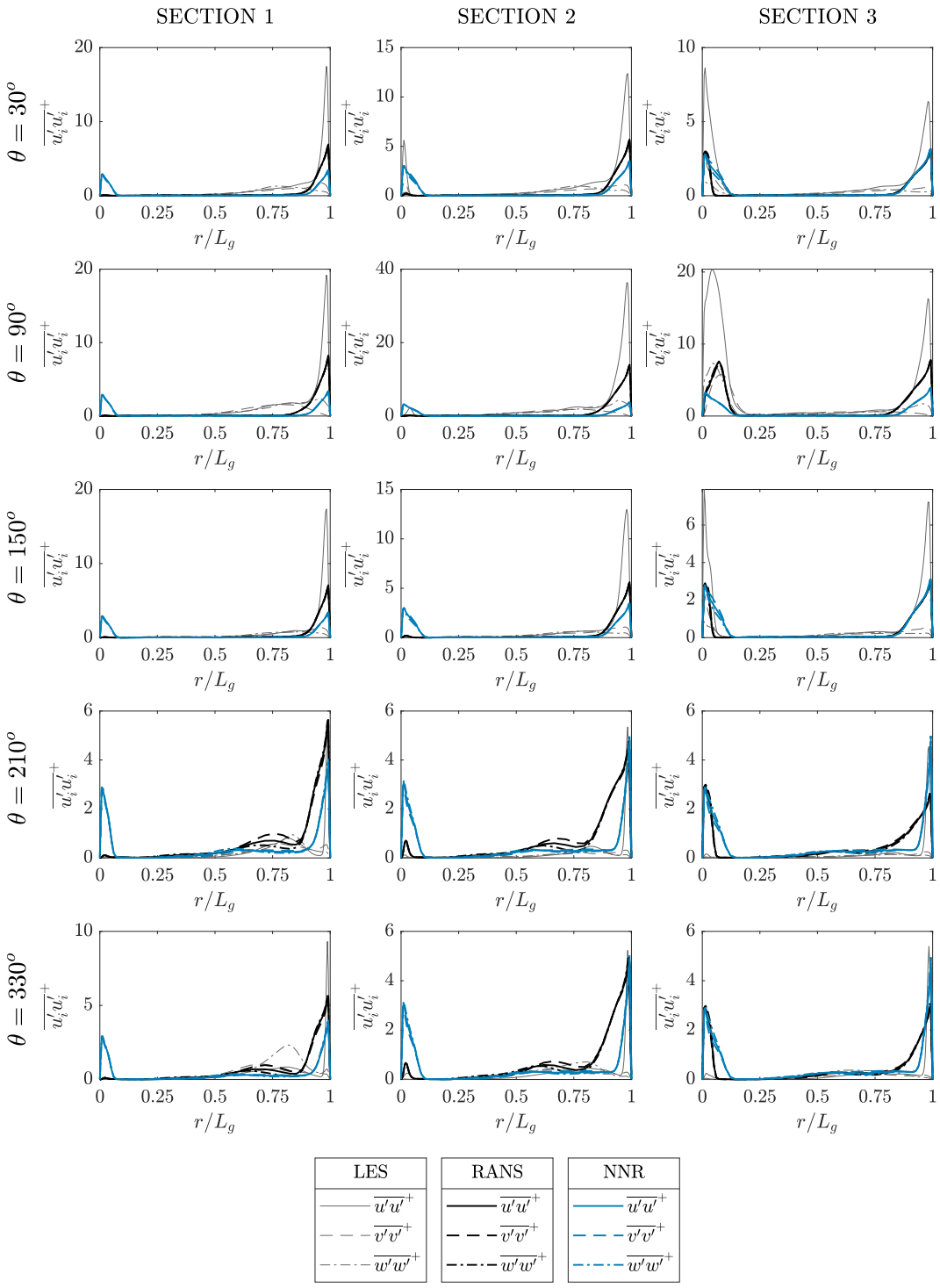

Figure C.5: Reynolds stresses in Case-E

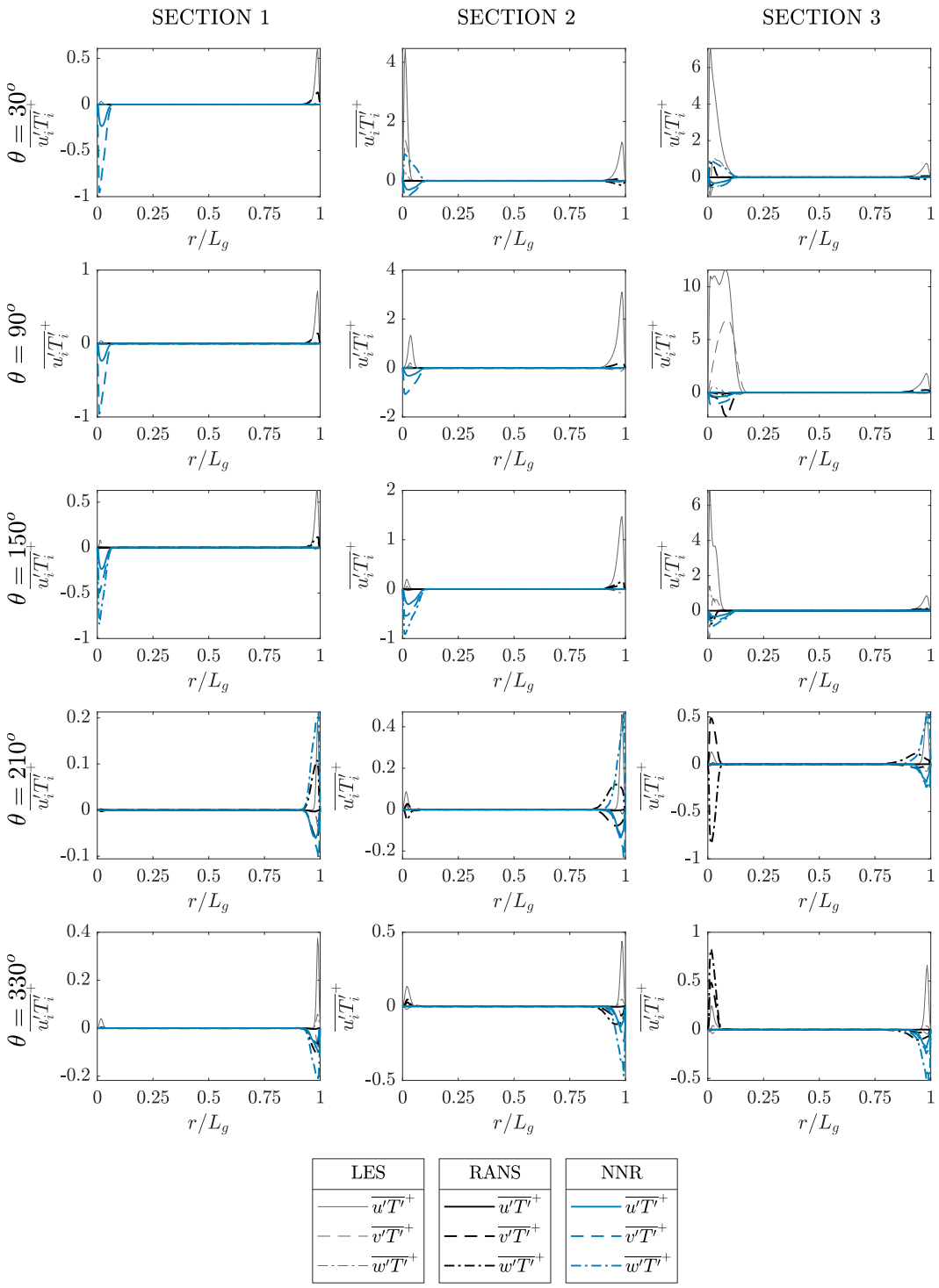

Figure C.6: Turbulent heat fluxes in Case-E

C.4 Case-G

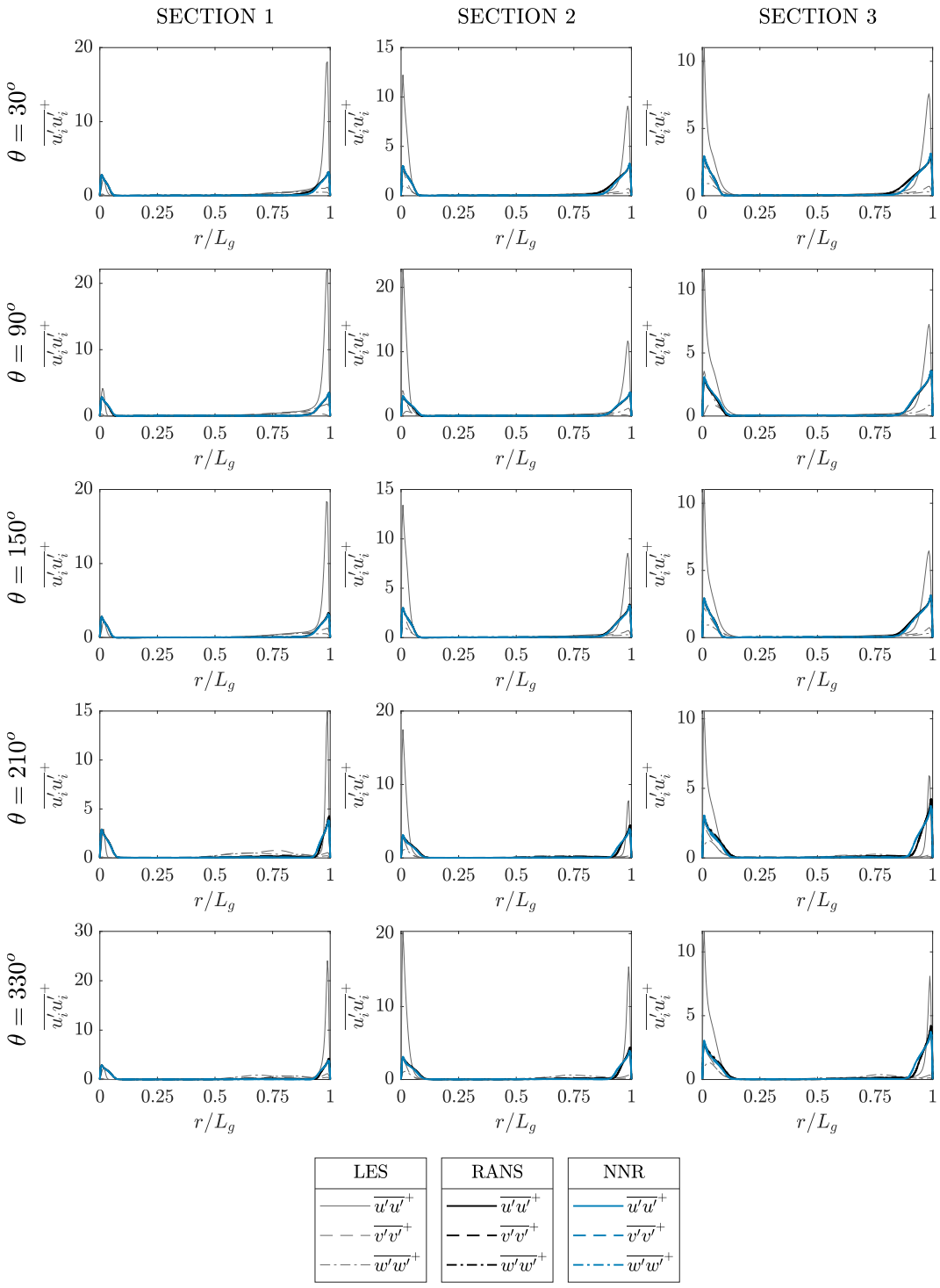

Figure C.7: Reynolds stresses in Case-G

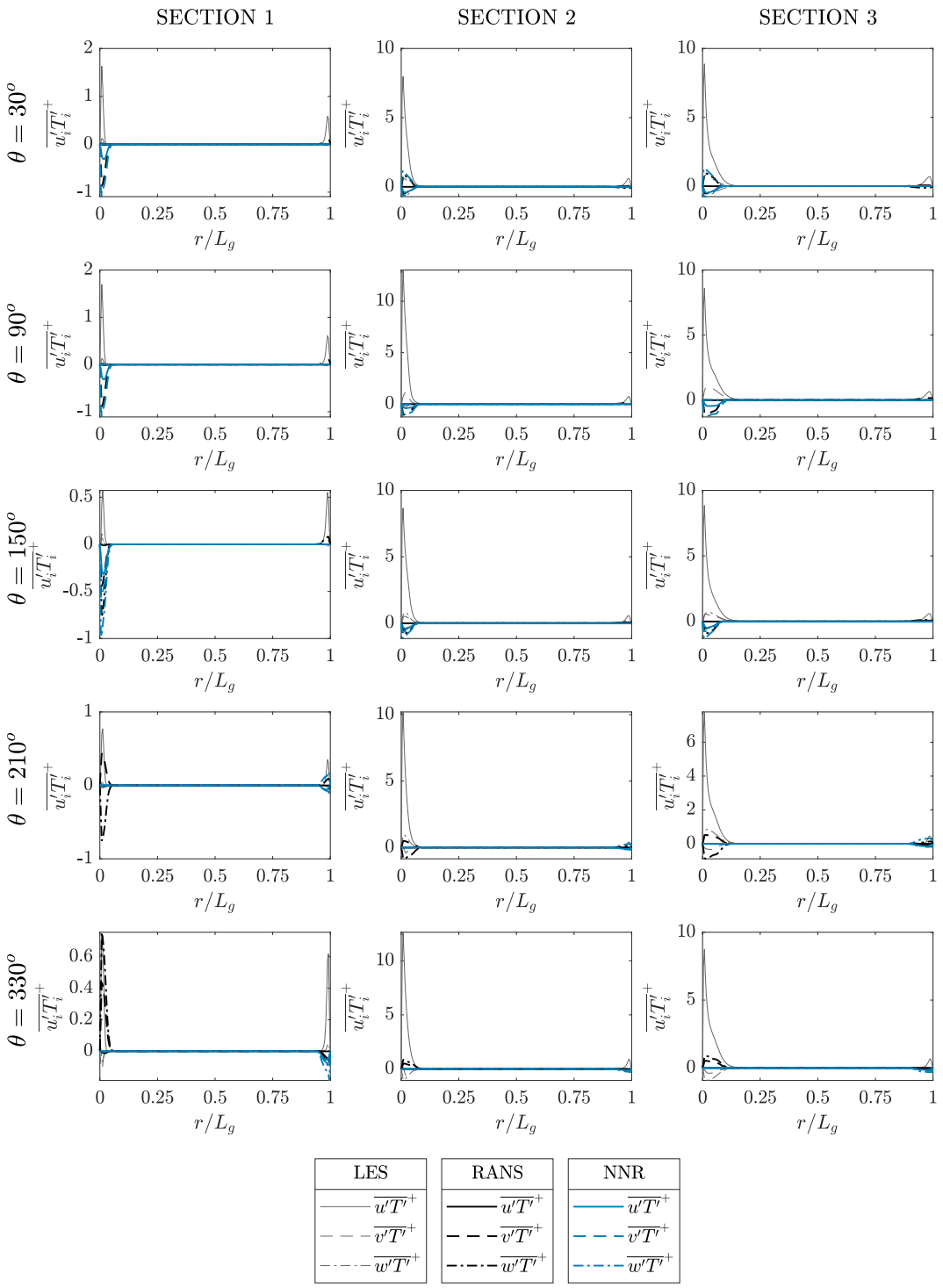

Figure C.8: Turbulent heat fluxes in Case-G

Appendix D

NNR Heat Transfer Profiles for Remaining Cases

Contents

D.1 Case-A 183

D.2 Case-E 184

D.3 Case-G 185

D.1 Case-A

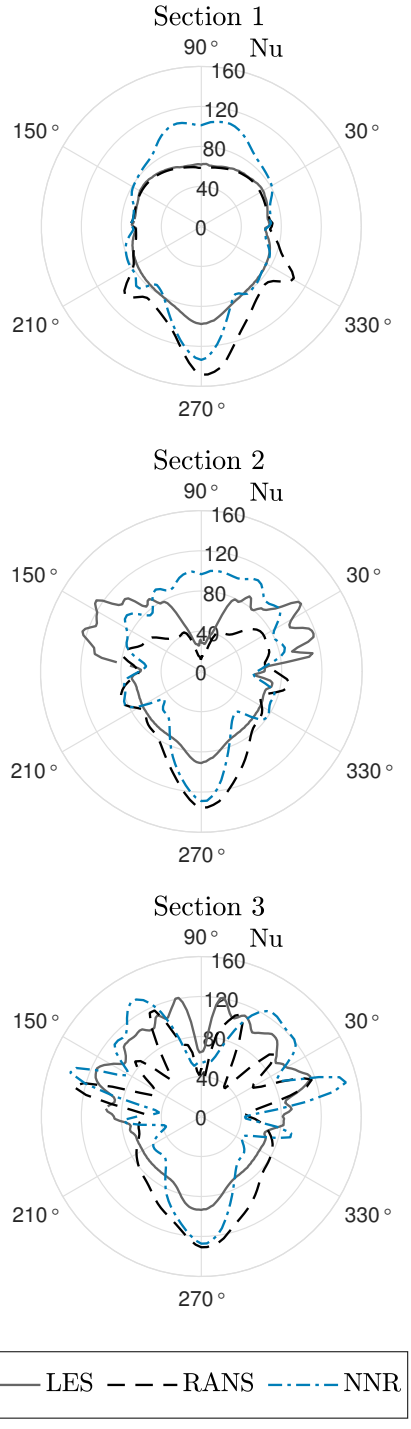

Figure D.1: Nusselt number comparison for Case-2

D.2 Case-E

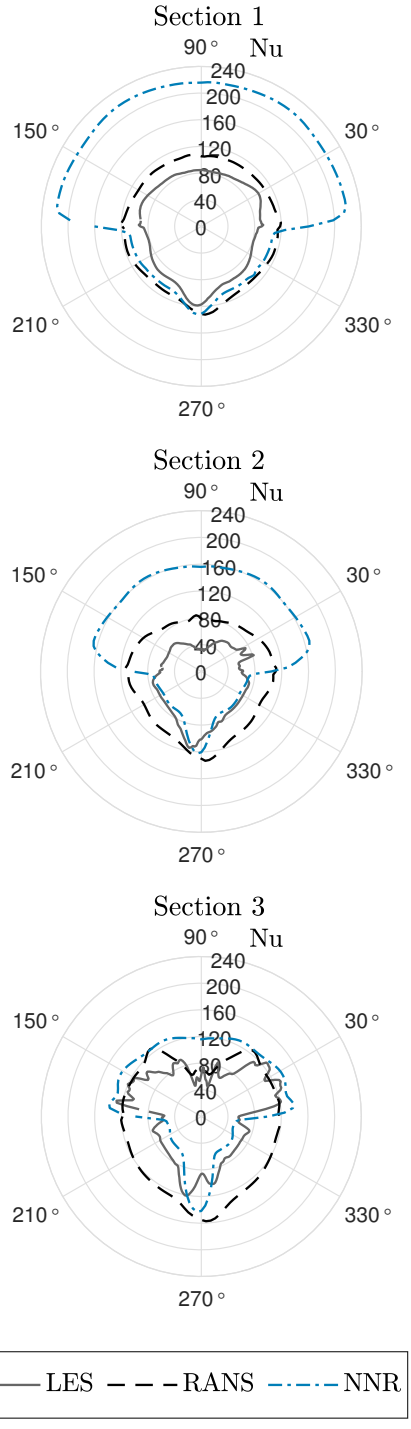

Figure D.2: Nusselt number comparison for Case-E

D.3 Case-G

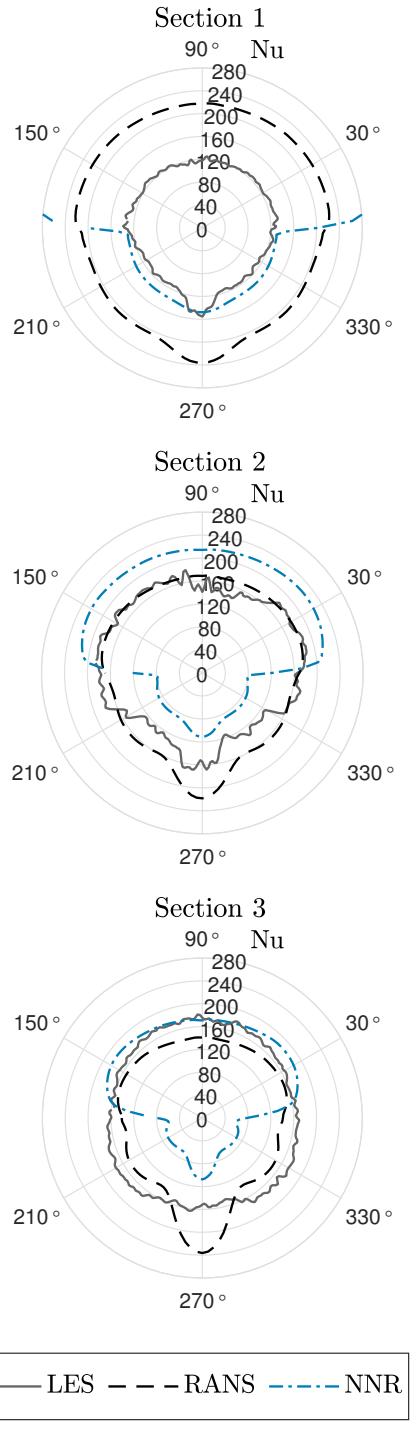

Figure D.3: Nusselt number comparison for Case-G

Appendix E

Experimental and RANS Results for Case-2M and Case-DM

Contents

E.1 Case-2M **187**

E.2 Case-DM **188**

E.1 Case-2M

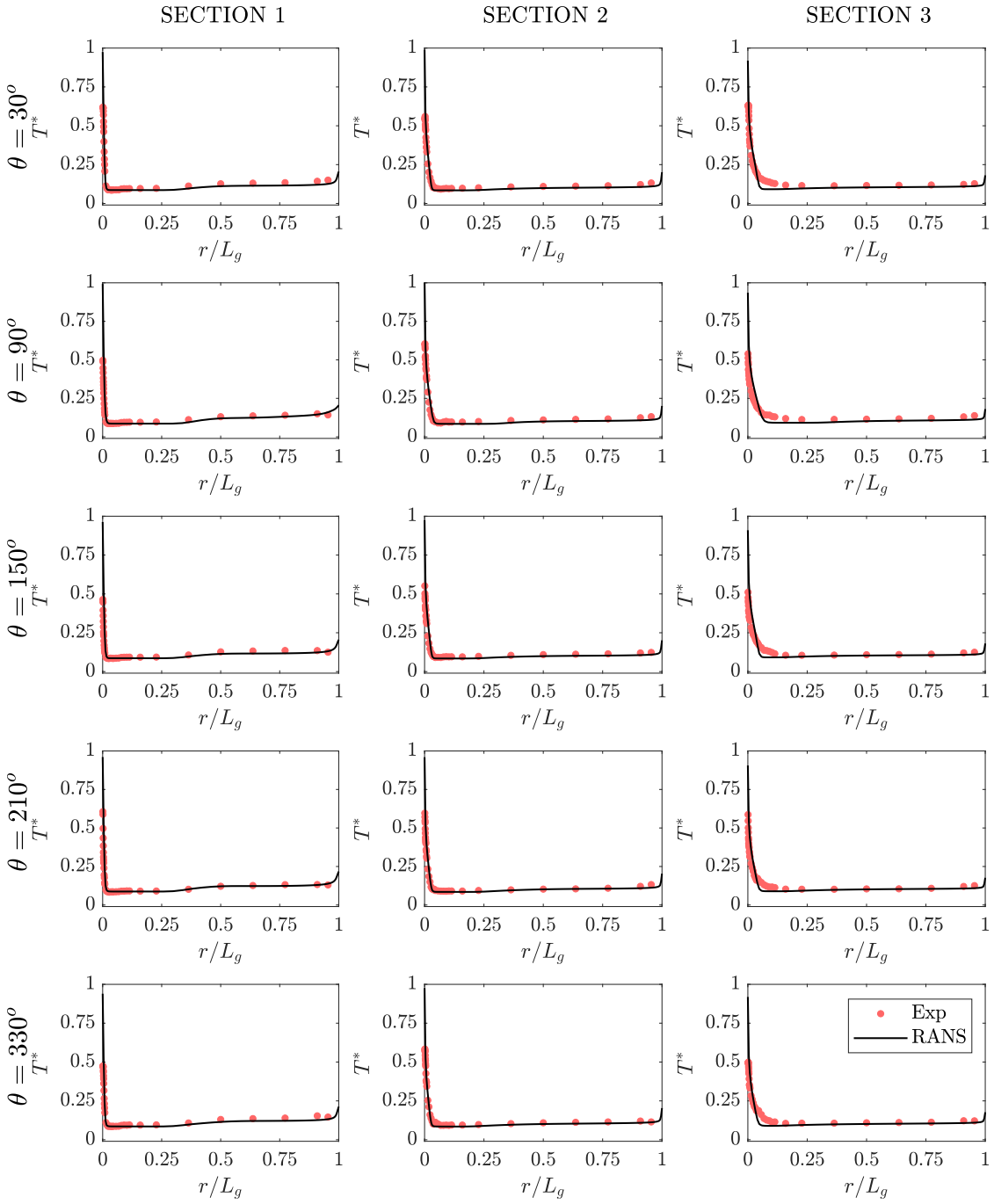

Figure E.1: Experimental and RANS temperature profiles in Case-2M

E.2 Case-DM

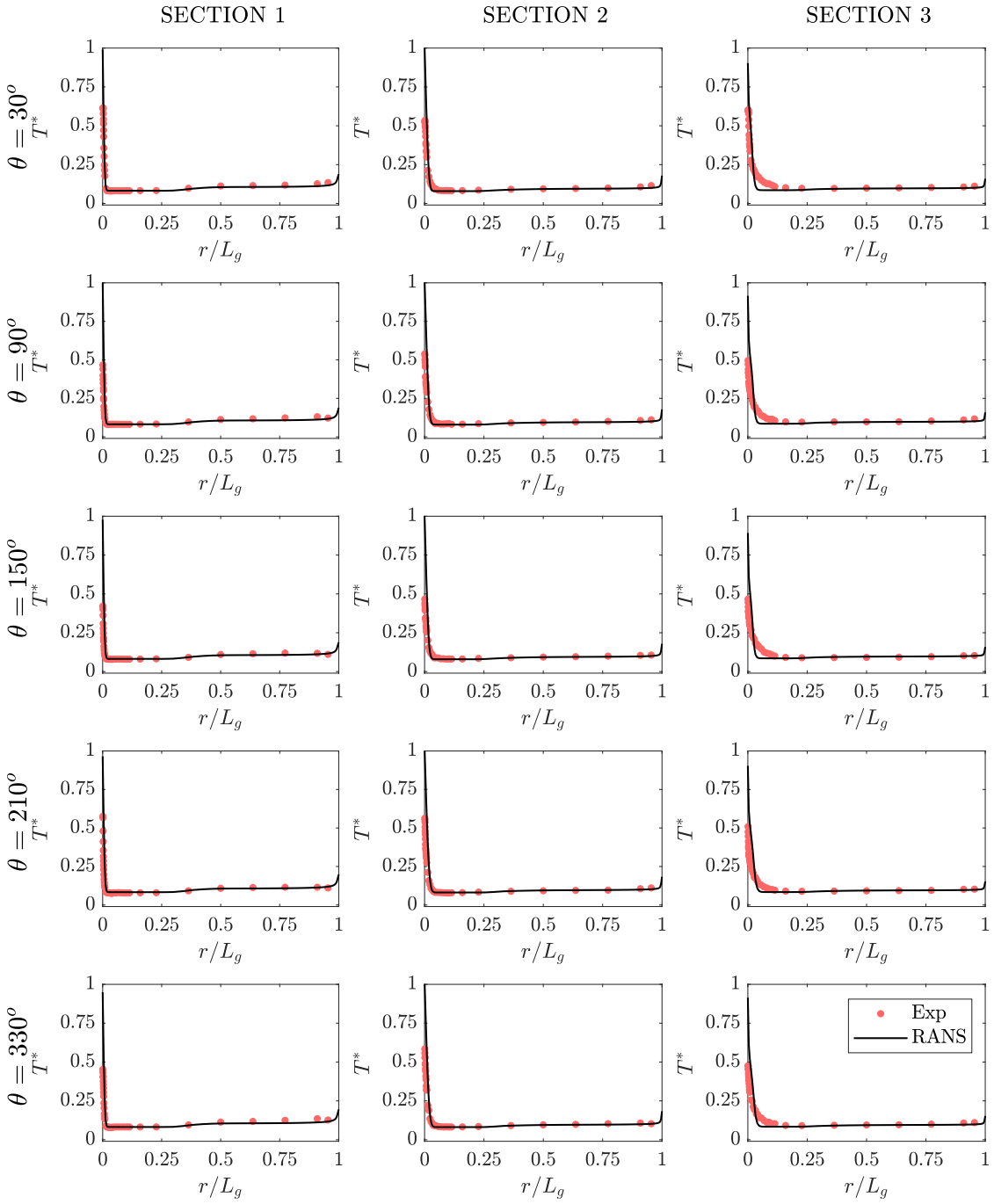

Figure E.2: Experimental and RANS temperature profiles in Case-DM

References

[1] United Nations. *United Nations Net Zero Coalition*. Accessed March 9, 2022. URL: https://www.un.org/en/climatechange/net-zero-coalition.

[2] BP. *BP Energy Outlook 2022*. Accessed March 9, 2022. URL: https://www.bp.com/content/dam/bp/business-sites/en/global/corporate/pdfs/energy-economics/energy-outlook/bp-energy-outlook-2022.pdf.

[3] United Nations. *United Nations Paris Agreement*. Accessed March 9, 2022. URL: https://www.un.org/en/climatechange/paris-agreement.

[4] The Intergovernmental Panel on Climate Change. *IPCC Chapter 1*. Accessed March 9, 2022. URL: https://www.ipcc.ch/sr15/chapter/chapter-1/.

[5] Arne Jungjohann and Craig Morris. "The German Coal Conundrum". In: *Heinrich Boell Foundation, North America, Washington DC, USA* 2014.

[6] Gabriel Marinescu et al. "Experimental Investigation Into Thermal Behavior of Steam Turbine Components—Temperature Measurements With Optical Probes and Natural Cooling Analysis". In: *Journal of engineering for gas turbines and power* 136.2 2014.

[7] Andrew Pilkington. "Numerical prediction of natural convection in gas turbines [PhD thesis]". In: *University of Oxford* 2019.

[8] Mariusz Banaszkiewicz. "Steam turbines start-ups". In: *Transactions of the institute of fluid-flow machinery* 2014.

[9] L. He and M.L.G. Oldfield. "Unsteady Conjugate Heat Transfer Modeling". In: *Journal of Turbomachinery* 133 2011, pp. 031022–1.

[10] Mark Baker. Personal Communication. Jan. 1, 2020.

[11] N. Abuaf, R. S. Bunker, and C. P. Lee. “Effects of Surface Roughness on Heat Transfer and Aerodynamic Performance of Turbine Airfoils”. In: *Journal of Turbomachinery* 120.3 July 1998, pp. 522–529. URL: https://doi.org/10.1115/1.2841749.

[12] E.M. Sparrow, R. Eichhorn, and J.L. Gregg. “Combined forced and free convection in a boundary layer flow”. In: *The Physics of Fluids* 2.3 1959, pp. 319–328.

[13] S. Kotake and N. Hattori. “Combined forced and free convection heat transfer for fully-developed laminar flow in horizontal annuli”. In: *International Journal of Heat and Mass Transfer* 28.11 1985, pp. 2113–2120. URL: http://www.sciencedirect.com/science/article/pii/001793108590105X.

[14] M. Ciampi et al. “Mixed convection heat transfer in horizontal, concentric annuli for transitional flow conditions”. In: *International Journal of Heat and Mass Transfer* 30.5 1987, pp. 833–841. URL: http://www.sciencedirect.com/science/article/pii/0017931087900032.

[15] H.A. Mohammed, Antonio Campo, and R. Saidur. “Experimental study of forced and free convective heat transfer in the thermal entry region of horizontal concentric annuli”. In: *International Communications in Heat and Mass Transfer* 37.7 2010, pp. 739–747. URL: http://www.sciencedirect.com/science/article/pii/S0735193310000904.

[16] S. Kenjereš and K. Hanjalić. “Prediction of turbulent thermal convection in concentric and eccentric horizontal annuli”. In: *International Journal of Heat and Fluid Flow* 16.5 1995, pp. 429–439. URL: http://www.sciencedirect.com/science/article/pii/0142727X9500051Q.

[17] Wilhelm Beckmann. “Die Wärmeübertragung in zylindrischen Gasschichten bei natürlicher Konvektion”. In: *Forschung auf dem Gebiet des Ingenieurwesens A* 2.5 1931, pp. 165–178.

[18] C. Liu, W. K. Mueller, and F. Landis. “Natural convection heat transfer in long horizontal cylindrical annuli”. In: *ASME Int. Develop. Heat Transf.* 117 1961, pp. 976–984.

[19] Ulrich Grigull and Werner Hauf. “Natural convection in horizontal cylindrical annuli”. In: *International Heat Transfer Conference Digital Library*. Begel House Inc. 1966.

[20] J. Lis. “Experimental investigation of natural convection heat transfer in simple and obstructed horizontal annuli”. In: *CHEMICAL ENGINEERING PROGRESS*. Vol. 62. 7. AMER INST CHEMICAL ENGINEERS 345 E 47TH ST, NEW YORK, NY 10017. 1966, p. 83.

[21] E.H. Bishop. “Photographic studies of natural convection between concentric cylinders”. In: *Proceedings of the 1966 Heat Transfer and Fluid Mechanics Institute*. Vol. 63. Stanford University Press. 1966.

[22] E.H. Bishop, C.T. Carley, and R.E. Powe. “Natural convective oscillatory flow in cylindrical annuli”. In: *International Journal of Heat and Mass Transfer* 11.12 1968, pp. 1741–1752.

[23] M. Itoh et al. “A new method of correlating heat-transfer coefficients for natural convection in horizontal cylindrical annuli”. In: *International Journal of Heat and Mass Transfer* 13.8 1970, pp. 1364–1368.

[24] G.D. Raithby and K.G.T. Hollands. “A general method of obtaining approximate solutions to laminar and turbulent free convection problems”. In: *Advances in heat transfer*. 11 1975, pp. 265–315.

[25] T.H. Kuehn and R.J. Goldstein. “An experimental and theoretical study of natural convection in the annulus between horizontal concentric cylinders”. In: *Journal of Fluid mechanics* 74.4 1976, pp. 695–719.

[26] T.H. Kuehn and R.J. Goldstein. “An experimental study of natural convection heat transfer in concentric and eccentric horizontal cylindrical annuli”. In: *Journal of Heat Transfer* 100.4 1978, pp. 635–640.

[27] T.H. Kuehn and R.J. Goldstein. “Correlating equations for natural convection heat transfer between horizontal circular cylinders”. In: *International Journal of Heat and Mass Transfer* 19.10 1976, pp. 1127–1134.

[28] E.H. Bishop. “Heat transfer by natural convection of helium between horizontal isothermal concentric cylinders at cryogenic temperature”. In: *Journal of heat transfer* 110.1 1988, pp. 109–115.

[29] Andrew E. McLeod and Eugene H. Bishop. “Turbulent natural convection of gases in horizontal cylindrical annuli at cryogenic temperatures”. In: *International Journal of Heat and Mass Transfer* 32.10 1989, pp. 1967–1978.

[30] J.W. Fersner. “Natural convection between horizontal isothermal concentric cylinders: the temperature field”. PhD thesis. MS thesis, Clemson University, Clemson, SC, 1986.

[31] Ralph E. Powe, Charles Team Carley, and Samuel Lee Carruth. “A numerical solution for natural convection in cylindrical annuli”. In: *Journal of Heat Transfer* 93.2 1971, pp. 210–220.

[32] S. Shibayama and Y. Mashimo. “Natural convection heat transfer in horizontal concentric cylindrical annuli”. In: *JSME Nat. Symp* 169 1968.

[33] E. Van de Sande and B.J.G. Hamer. “Steady and transient natural convection in enclosures between horizontal circular cylinders (constant heat flux)”. In: *International Journal of Heat and Mass Transfer* 22.3 1979, pp. 361–370.

[34] B. Farouk and S.I. Guceri. “Laminar and turbulent natural convection in the annulus between horizontal concentric cylinders”. In: *Journal of Heat Transfer* 104.4 1982, pp. 631–636.

[35] Brian Edward Launder and Dudley Brian Spalding. “The numerical computation of turbulent flows”. In: 1983, pp. 96–116.

[36] C.P. Desai and K. Vafai. “An investigation and comparative analysis of two-and three-dimensional turbulent natural convection in a horizontal annulus”. In: *International Journal of Heat and Mass Transfer* 37.16 1994, pp. 2475–2504.

[37] K. Fukuda et al. “Direct Simulation and Large Eddy Simulation of Turbulent Natural Convection in Horizontal Annulus”. In: *Memoirs of the Faculty of Engineering* 51.4 1991, pp. 32–49.

[38] Gabriel Marinescu et al. “Experimental Investigation Into Thermal Behavior of Steam Turbine Components—Temperature Measurements With Optical Probes and Natural Cooling Analysis”. In: *Journal of engineering for gas turbines and power* 136.2 2014.

[39] Peter Stein et al. “Thermal Modeling and Mechanical Integrity Based Design of a Heat Shield on a High Pressure Module Solar Steam Turbine Inner Casing With Focus on Lifetime”. In: *Turbo Expo: Power for Land, Sea, and Air*. Vol. 45738. American Society of Mechanical Engineers. 2014, V05CT20A004.

[40] Roberto Maffulli and Li He. “Wall temperature effects on heat transfer coefficient for high-pressure turbines”. In: *Journal of Propulsion and Power* 30.4 2014, pp. 1080–1090.

[41] Roberto Maffulli and Li He. “Impact of wall temperature on heat transfer coefficient and aerodynamics for three-dimensional turbine blade passage”. In: *Journal of Thermal Science and Engineering Applications* 9.4 2017, p. 041002.

[42] Q. Zhang and L. He. “Impact of wall temperature on turbine blade tip aerothermal performance”. In: *Journal of engineering for gas turbines and power* 136.5 2014.

[43] M. Fadl et al. “Assessment of unsteadiness modeling for transient natural convection”. In: *Journal of Engineering for Gas Turbines and Power* 140.1 2018.

[44] L. He and M. Fadl. “Multi-scale time integration for transient conjugate heat transfer”. In: *International Journal for Numerical Methods in Fluids* 83.12 2017, pp. 887–904.

[45] Zixiang Sun et al. “Efficient finite element analysis/computational fluid dynamics thermal coupling for engineering applications”. In: *Journal of turbomachinery* 132.3 2010.

[46] Marc-Paul Errera and Bénédicte Baqué. "A quasi-dynamic procedure for coupled thermal simulations". In: *International Journal for Numerical Methods in Fluids* 72.11 2013, pp. 1183–1206.

[47] M. Fadl and L. He. "On LES based conjugate heat transfer procedure for transient natural convection". In: *Turbo Expo: Power for Land, Sea, and Air*. Vol. 50879. American Society of Mechanical Engineers. 2017, V05AT10A002.

[48] Kemal Hanjalić and Brian Launder. *Modelling turbulence in engineering and the environment: second-moment routes to closure*. Cambridge university press, 2011.

[49] Stephen B. Pope. *Turbulent Flows*. Cambridge University Press, 2000.

[50] Henk Kaarle Versteeg and Weeratunge Malalasekera. *An introduction to computational fluid dynamics: the finite volume method*. Pearson education, 2007.

[51] Philippe Spalart and Steven Allmaras. "A one-equation turbulence model for aerodynamic flows". In: *30th aerospace sciences meeting and exhibit*. 1992, p. 439.

[52] ANSYS. *ANSYS Fluent Theory Guide 2020 R1*. 2020.

[53] Joseph Boussinesq. *Thōrie analytique de la chaleur mise en harmonie avec la thermodynamique et avec la thōrie mccanique de la lumi re: Refroidissement et chauffement par rayonnement, conductibilitdes tiges, lames et masses cristallines, courants de convection, thōrie mccanique de la lumi re. 1903. xxxii, 625,[1] p.* Vol. 2. Gauthier-Villars, 1903.

[54] Hermann Schlichting and Klaus Gersten. *Boundary-Layer Theory*. Jan. 2017.

[55] Hasna Nur Fadhila. "A new non-linear k-w model with enhanced near-wall treatment of turbulence anisotropy [PhD thesis]". In: *Coventry University* 2020.

[56] Christopher L. Rumsey, Thomas B. Gatski, and Joseph H. Morrison. "Turbulence model predictions of strongly curved flow in a U-duct". In: *AIAA journal* 38.8 2000, pp. 1394–1402.

[57] Shoiti Nisizima and Akira Yoshizawa. "Turbulent channel and Couette flows using an anisotropic k-epsilon model". In: *AIAA journal* 25.3 1987, pp. 414–420.

[58] T.J. Craft, B.E. Launder, and K. Suga. “Prediction of turbulent transitional phenomena with a nonlinear eddy-viscosity model”. In: *International Journal of Heat and Fluid Flow* 18.1 1997, pp. 15–28.

[59] T.J. Craft, B.E. Launder, and K. Suga. “Development and application of a cubic eddy-viscosity model of turbulence”. In: *International Journal of Heat and Fluid Flow* 17.2 1996, pp. 108–115.

[60] Charles G. Speziale. “On nonlinear kl and k-ϵ models of turbulence”. In: *Journal of Fluid Mechanics* 178 1987, pp. 459–475.

[61] David Apsley et al. “Non-linear eddy-viscosity modelling of separated flows”. In: *Journal of Hydraulic research* 35.6 1997, pp. 723–748.

[62] T.B. Gatski and T. Jongen. “Nonlinear eddy viscosity and algebraic stress models for solving complex turbulent flows”. In: *Progress in Aerospace Sciences* 36.8 2000, pp. 655–682.

[63] H. Fadhila et al. “A new non-linear RANS model with enhanced near-wall treatment of turbulence anisotropy”. In: *Applied Mathematical Modelling* 82 2020, pp. 293–313.

[64] Kemal Hanjalić. “One-point closure models for buoyancy-driven turbulent flows”. In: *Annual review of fluid mechanics* 34.1 2002, pp. 321–347.

[65] Bart J. Daly and Francis H. Harlow. “Transport equations in turbulence”. In: *The physics of fluids* 13.11 1970, pp. 2634–2649.

[66] Brian Edward Launder. “On the computation of convective heat transfer in complex turbulent flows”. In: 1988.

[67] Andrew Pilkington et al. “Prediction of natural convection heat transfer in gas turbines”. In: *International Journal of Heat and Mass Transfer* 141 2019, pp. 233–244. URL: `http://www.sciencedirect.com/science/article/pii/S0017931019311068`.

[68] Jong Keun Shin et al. “Elliptic relaxation second moment closure for the turbulent heat fluxes”. In: *Journal of Turbulence* 9 2008, N3.

[69] Gotthlif Heinrich Ludwig Hagen. *Über den einfluss der temperatur auf die bewegung des wassers in röhren–*. Druckerei der Königl. akademie der wissenschaften, 1854.

[70] Henry Darcy. *Recherches expérimentales relatives au mouvement de l'eau dans les tuyaux*. Vol. 1. Mallet-Bachelier, 1857.

[71] Cyril Frank Colebrook et al. "Correspondence. turbulent flow in pipes, with particular reference to the transition region between the smooth and rough pipe laws.(includes plates)." In: *Journal of the Institution of Civil engineers* 12.8 1939, pp. 393–422.

[72] Johann Nikuradse. "Laws of flow in rough pipes". In: 1950.

[73] Hermann Schlichting. *Experimental investigation of the problem of surface roughness*. 823. National Advisory Commitee for Aeronautics, 1937.

[74] D. Grinvald and V. Nikora. "Rechnaya turbulentsiya (river turbulence)". In: *Hydrometeoizdat (in Russian)* 1988.

[75] Hong Cheng and Ian P. Castro. "Near wall flow over urban-like roughness". In: *Boundary-Layer Meteorology* 104.2 2002, pp. 229–259.

[76] Paolo Orlandi and Stefano Leonardi. "DNS of turbulent channel flows with two-and three-dimensional roughness". In: *Journal of Turbulence* 7 2006, N73.

[77] Michael P. Schultz and Karen A. Flack. "Turbulent boundary layers on a systematically varied rough wall". In: *Physics of Fluids* 21.1 2009, p. 015104.

[78] R.J. Volino, M.P. Schultz, and K.A. Flack. "Turbulence structure in a boundary layer with two-dimensional roughness". In: *Journal of Fluid Mechanics* 635 2009, pp. 75–101.

[79] Stefano Leonardi and Ian P. Castro. "Channel flow over large cube roughness: a direct numerical simulation study". In: *Journal of Fluid Mechanics* 651 2010, pp. 519–539.

[80] L. Chan et al. “A systematic investigation of roughness height and wavelength in turbulent pipe flow in the transitionally rough regime”. In: *Journal of Fluid Mechanics* 771 2015, pp. 743–777.

[81] L. Chan et al. “Secondary motion in turbulent pipe flow with three-dimensional roughness”. In: *Journal of Fluid Mechanics* 854 2018, pp. 5–33.

[82] Alberto Scotti. “Direct numerical simulation of turbulent channel flows with boundary roughened with virtual sandpaper”. In: *Physics of Fluids* 18.3 2006, p. 031701.

[83] Mauro De Marchis et al. “Large eddy simulations of rough turbulent channel flows bounded by irregular roughness: advances toward a universal roughness correlation”. In: *Flow, Turbulence and Combustion* 105 2020, pp. 627–648.

[84] Nadir Patir. “A numerical procedure for random generation of rough surfaces”. In: *Wear* 47.2 1978, pp. 263–277.

[85] Thomas O. Jelly and Angela Busse. “Reynolds number dependence of Reynolds and dispersive stresses in turbulent channel flow past irregular near-Gaussian roughness”. In: *International Journal of Heat and Fluid Flow* 80 2019, p. 108485.

[86] W. Anderson and C. Meneveau. “Dynamic roughness model for large-eddy simulation of turbulent flow over multiscale, fractal-like rough surfaces”. In: *Journal of fluid mechanics* 679 2011, pp. 288–314.

[87] Jiasheng Yang et al. “DNS-based characterization of pseudo-random roughness in minimal channels”. In: *arXiv preprint arXiv:2106.08160* 2021.

[88] M.P. Schultz and K.A. Flack. “The rough-wall turbulent boundary layer from the hydraulically smooth to the fully rough regime”. In: *Journal of Fluid Mechanics* 580 2007, pp. 381–405.

[89] Brian G. Brzek et al. “Transitionally rough zero pressure gradient turbulent boundary layers”. In: *Experiments in fluids* 44.1 2008, pp. 115–124.

[90] James Cardillo et al. “DNS of a turbulent boundary layer with surface roughness”. In: *Journal of Fluid Mechanics* 729 2013, pp. 603–637.

[91] Guillermo Araya, Kenneth E. Jansen, and Luciano Castillo. “Inlet condition generation for spatially developing turbulent boundary layers via multiscale similarity”. In: *Journal of Turbulence* 10 2009, N36.

[92] J. Yuan and U. Piomelli. “Estimation and prediction of the roughness function on realistic surfaces”. In: *Journal of Turbulence* 15.6 2014, pp. 350–365.

[93] Angela Busse, Mark Lützner, and Neil D. Sandham. “Direct numerical simulation of turbulent flow over a rough surface based on a surface scan”. In: *Computers & Fluids* 116 2015, pp. 129–147.

[94] Manan Thakkar, Angela Busse, and Neil Sandham. “Surface correlations of hydrodynamic drag for transitionally rough engineering surfaces”. In: *Journal of Turbulence* 18.2 2017, pp. 138–169.

[95] T. Morel. “Comprehensive Design of Axisymmetric Wind Tunnel Contractions”. In: *Journal of Fluids Engineering* 97.2 June 1975, pp. 225–233. URL: https://doi.org/10.1115/1.3447255.

[96] Thomas Morel. “Design of Two-Dimensional Wind Tunnel Contractions”. In: *Journal of Fluids Engineering* 99.2 June 1977, pp. 371–377. URL: https://doi.org/10.1115/1.3448764.

[97] Fuh-Min Fang. “A Design Method for Contractions With Square End Sections”. In: *Journal of Fluids Engineering* 119.2 June 1997, pp. 454–458. URL: https://doi.org/10.1115/1.2819156.

[98] Florian R. Menter. “Two-equation eddy-viscosity turbulence models for engineering applications”. In: *AIAA journal* 32.8 1994, pp. 1598–1605.

[99] MakerBot. *Replicator Z18*. Accessed March 16, 2022. URL: https://www.makerbot.com/3d-printers/replicator-z18/.

[100] Zircotec Group. *Zircoflex II*. Accessed March 16, 2022. URL: https://www.zircotec.com/zircoflex-2/.

[101] Par Group Ltd. *Monolux*. Accessed March 16, 2022. URL: https://www.par-group.co.uk/high-temperature-insulation/insulation-boards/monolux/.

[102] Arduino. *UNO R3*. Accessed March 16, 2022. URL: https://docs.arduino.cc/hardware/uno-rev3.

[103] National Instruments Corporation Ltd. *NI-9212*. Accessed March 16, 2022. URL: https://www.ni.com/en-gb/support/model.ni-9212.html.

[104] Glenn E. Daniels. "Measurement of Gas Temperature and the Radiation Compensating Thermocouple". In: *Journal of Applied Meteorology (1962-1982)* 7.6 1968, pp. 1026–1035. URL: http://www.jstor.org/stable/26174404.

[105] M. Tagawa and Y. Ohta. "Two-thermocouple probe for fluctuating temperature measurement in combustion—Rational estimation of mean and fluctuating time constants". In: *Combustion and Flame* 109.4 1997, pp. 549–560. URL: http://www.sciencedirect.com/science/article/pii/S0010218097000448.

[106] S. Brohez, C. Delvosalle, and G. Marlair. "A two-thermocouples probe for radiation corrections of measured temperatures in compartment fires". In: *Fire Safety Journal* 39.5 2004, pp. 399–411. URL: http://www.sciencedirect.com/science/article/pii/S037971120400027X.

[107] Chan Kim et al. "Temperature Measurement With Radiation Correction for Very High Temperature Gas". In: vol. 4. Jan. 2010.

[108] L.G. Blevins and W. M. Pitts. "Modeling of bare and aspirated thermocouples in compartment fires". In: *Fire safety journal* 33.4 1999, pp. 239–259. URL: http://dx.doi.org/.

[109] Stephen Whitaker. "Forced convection heat transfer correlations for flow in pipes, past flat plates, single cylinders, single spheres, and for flow in packed beds and tube bundles". In: *AIChE Journal* 18.2 1972, pp. 361–371. URL: https://aiche.onlinelibrary.wiley.com/doi/abs/10.1002/aic.690180219.

[110] Elmar Achenbach. "Heat transfer from spheres up to Re= 6× 10 6". In: *International Heat Transfer Conference Digital Library*. Begel House Inc. 1978.

[111] Joseph Fourier et al. *The analytical theory of heat*. The University Press, 1878.

[112] William K. George Jr and Steven P. Capp. "A theory for natural convection turbulent boundary layers next to heated vertical surfaces". In: *International Journal of Heat and Mass Transfer* 22.6 1979, pp. 813–826.

[113] Daniel D. Fahy. "On natural convection in a large civil gas turbine". In: *University of Oxford* 2020.

[114] Alireza Ebadi, Faraz Mehdi, and Christopher M. White. "An exact integral method to evaluate wall heat flux in spatially developing two-dimensional wall-bounded flows". In: *International Journal of Heat and Mass Transfer* 84 2015, pp. 856–861.

[115] Dantec Dynamics. *Boundary Layer Probe*. Accessed March 16, 2022. URL: `https://www.dantecdynamics.com/product/miniature-wire-probe-boundary-layer/`.

[116] National Instruments Corporation Ltd. *NI-9209*. Accessed March 16, 2022. URL: `https://www.ni.com/en-gb/support/model.ni-9209.html`.

[117] Dantec Dynamics. *Streamline Pro*. Accessed March 16, 2022. URL: `https://www.dantecdynamics.com/solutions-applications/solutions/fluid-mechanics/constant-temperature-anemometry-cta/streamline-pro/`.

[118] Yunus A. Çengel and John M. Cimbala. *Fluid Mechanics: Fundamentals and Applications*. McGraw-Hill Higher Education, 2010.

[119] John F. Kenney and E.S. Keeping. "Linear regression and correlation". In: *Mathematics of statistics* 1 1962, pp. 252–285.

[120] Howard J. Seltman. *Experimental design and analysis*. 2012.

[121] Robert J. Moffat. "Describing the uncertainties in experimental results". In: *Experimental thermal and fluid science* 1.1 1988, pp. 3–17.

[122] Joseph Smagorinsky. "General circulation experiments with the primitive equations: I. The basic experiment". In: *Monthly weather review* 91.3 1963, pp. 99–164.

[123] Jiri Blazek. *Computational fluid dynamics: principles and applications*. Butterworth-Heinemann, 2015.

[124] Massimo Germano et al. "A dynamic subgrid-scale eddy viscosity model". In: *Physics of Fluids A: Fluid Dynamics* 3.7 1991, pp. 1760–1765.

[125] Osborne Reynolds. "XXIX. An experimental investigation of the circumstances which determine whether the motion of water shall be direct or sinuous, and of the law of resistance in parallel channels". In: *Philosophical Transactions of the Royal society of London* 174 1883, pp. 935–982.

[126] Peter G. Baines, Sharan J. Majumdar, and Humio Mitsudera. "The mechanics of the Tollmien-Schlichting wave". In: *Journal of fluid mechanics* 312 1996, pp. 107–124.

[127] Ephraim M. Sparrow and R.B. Husar. "Longitudinal vortices in natural convection flow on inclined plates". In: *Journal of Fluid Mechanics* 37.2 1969, pp. 251–255.

[128] Andrew Pilkington et al. "An investigation into the formation of buoyancy driven streamwise vortices". In: *International Journal of Heat and Mass Transfer* 162 2020, p. 120348.

[129] Theodore Theodorsen. "Mechanisms of turbulence". In: *Proceedings of the 2nd Midwestern Conference on Fluid Mechanics, 1952*. 1952.

[130] Giancarlo Alfonsi. "Coherent Structures of Turbulence: Methods of Eduction and Results". In: *Applied Mechanics Reviews* 59.6 Nov. 2006, pp. 307–323.

[131] Abdelkader Mojtabi and J.P. Caltagirone. "Analyse du transfert de chaleur en convection mixte laminaire entre deux cylindres coaxiaux horizontaux". In: *International Journal of Heat and Mass Transfer* 23.10 1980, pp. 1369–1375.

[132] Anthony James Merrill Spencer and Ronald S. Rivlin. "Further results in the theory of matrix polynomials". In: *Archive for rational mechanics and analysis* 4.1 1959, pp. 214–230.

[133] S.B. Pope. "A more general effective-viscosity hypothesis". In: *Journal of Fluid Mechanics* 72.2 1975, pp. 331–340.

[134] Ulrich Schumann. "Realizability of Reynolds-stress turbulence models". In: *The Physics of Fluids* 20.5 1977, pp. 721–725.

[135] Ichiro Kimura and Takashi Hosoda. "A non-linear k-ϵ model with realizability for prediction of flows around bluff bodies". In: *International Journal for Numerical Methods in Fluids* 42.8 2003, pp. 813–837.

[136] M.M. Kanafi. "Surface generator: artificial randomly rough surfaces". In: *File Exchange, MathWorks,[online] https://www. mathworks. com/matlabcentral/fileexchange/60817-surface-generator–artificial-randomly-roughsurfaces* 2016.

[137] I. Sherrington and G.W. Howarth. "Approximate numerical models of 3-d surface topography generated using sparse frequency domain descriptions". In: *International Journal of Machine Tools and Manufacture* 38.5-6 1998, pp. 599–606.

[138] R. Mejia-Alvarez and K.T. Christensen. "Low-order representations of irregular surface roughness and their impact on a turbulent boundary layer". In: *Physics of fluids* 22.1 2010, p. 015106.

[139] Anindya Chatterjee. "An introduction to the proper orthogonal decomposition". In: *Current science* 2000, pp. 808–817.

[140] Gavin R. Tabor and M.H. Baba-Ahmadi. "Inlet conditions for large eddy simulation: A review". In: *Computers & Fluids* 39.4 2010, pp. 553–567.

[141] Xiaohua Wu. "Inflow turbulence generation methods". In: *Annual Review of Fluid Mechanics* 49 2017, pp. 23–49.

[142] W. M. Kays and M. E. Crawford. *Convective heat and mass transfer*. 3rd ed. McGraw-Hill Education, 1993.

[143] Qiang Li et al. "DNS of a spatially developing turbulent boundary layer with passive scalar transport". In: *International Journal of Heat and Fluid Flow* 30.5 2009. The 3rd International Conference on Heat Transfer and Fluid Flow in

Microscale, pp. 916–929. URL: https://www.sciencedirect.com/science/article/pii/S0142727X09001040.

[144] Hui Zhao et al. “Direct numerical simulation of turbulent boundary layer with heat transfer”. In: *International Journal of Heat and Mass Transfer* 99 2016, pp. 10–19.

[145] J.W.R. Peeters and N.D. Sandham. “Turbulent heat transfer in channels with irregular roughness”. In: *International Journal of Heat and Mass Transfer* 138 2019, pp. 454–467.

[146] Kenji Katoh, Kwing-So Choi, and Tsuneo Azuma. “Heat-transfer enhancement and pressure loss by surface roughness in turbulent channel flows”. In: *International Journal of Heat and Mass Transfer* 43.21 2000, pp. 4009–4017.

[147] Y. Kuwata. “Direct numerical simulation of turbulent heat transfer on the Reynolds analogy over irregular rough surfaces”. In: *International Journal of Heat and Fluid Flow* 92 2021, p. 108859.

[148] A.A.R. Townsend. *The structure of turbulent shear flow*. Cambridge university press, 1980.